UNIVERSITY
OF
JOHANNESBURG

RESEARCH DISSERTATION

INVESTIGATING MECHANICAL PROPERTIES OF MIG REINFORCED STEEL SHEETS USING TITANIUM ALLOY POWDER

By

Odiaka, TN

Submitted in partial fulfilment for the requirements of the degree

Masters in Engineering

In

Mechanical Engineering
Department of Mechanical Engineering Science
Faculty of Engineering and the Built Environment

Student Number: 218085764

At the

UNIVERSITY OF JOHANNESBURG

Supervisor: Dr S.A. Akinlabi
Co-supervisor: Dr N. Madushele

January 2020

DECLARATION

I, **Odiaka Timothy Nkemasom**, hereby declare that this dissertation is wholly my own work and has not been submitted anywhere else for academic credit either by myself or another person.

I understand what plagiarism implies and declare that this dissertation is my own ideas, words, phrases, arguments, graphics, figures, results and organization except where reference is explicitly made to another's work.

I understand that any unethical academic behaviour, which includes plagiarism, is seen in a serious light by the University of Johannesburg and is punishable by disciplinary action.

Signed:

Date: January, 2020

ACKNOWLEDGEMENT

Special thanks go to my supervisor, Dr S.A. Akinlabi for conceptualizing this research study and providing all the research materials and for his immense patience, guidance and contribution to this research work. You were always readily available and eager to help in the accomplishment of this work. Heartfelt thanks also go to my co-supervisor, Dr N. Madushele for your frankness, immense contribution and priceless guidance. I'm grateful to the MAMS (Modern and Advanced Manufacturing System) research group leader, Prof. E.T. Akinlabi, for being a source of inspiration to me and the entire research team.

I would like to acknowledge Mr Willie Williams at South Africa Institute of Welding, for his gracious help during the experimental phase of this work. I'm also grateful to my research colleagues, Mr Simeon Okwudili, Mr Pardon Baloyi, Mr Opeoluwa Dada, Mrs Cynthia Abima, Pastor Olatunji Abolusoro, Dr Olajide Abdulrahman, Mr Paul Adedeji, Mr Victor Aladesanmi, Dr Damilare Baruwa and all distinguished members of MAMS Research group. Your help and friendship made research fun.

I remain indebted to my parents, Prof. and Dr (Mrs) Odiaka for their invaluable support and inspiration.

Above all, I'm thankful to God. All we discover is only but a minute fraction of what you already know.

RESEARCH OUTPUT

Journal Manuscripts Submitted

1. Investigating the Role of Titanium Alloy Powder Reinforcement in MIG Mild Steel Lap Joints
2. Effect of Titanium Alloy Powder Reinforcement on the Mechanical Properties and Microstructural Evolution of GMAW Mild Steel Butt Joints.

Conference Paper - Published

3. Odiaka Timothy, Madushele Nkosinathi and Akinlabi Stephen. "Improvement of Joint Integrity in MIG Welded Steel: A Review." *Proceedings of the ASME 2018 International Mechanical Engineering Congress and Exposition*. *Volume 2: Advanced Manufacturing*. Pittsburgh, Pennsylvania, USA. November 9–15, 2018. V002T02A099. ASME. https://doi.org/10.1115/IMECE2018-86788

ABSTRACT

Mild steel is one of the commonest materials used in the metal industry due to its weldability, malleability and hardness properties. Consequently, there is always a need for joining processes of mild steel, with welding techniques such as Metal Inert Gas (MIG) welding being a popular choice. However, the complex physics involved in welding such as phase changes, metal deposition, and inhomogeneous heating and cooling rates across the weld zone often results in the compromise of structural integrity in mild steel welds. Improving weld integrity has since become an area of interest, with process parameter optimization and post-weld heat treatment being the most popular solutions as discovered in the literature.

This study explores the prospects of titanium powders as weld reinforcements in improving the structural integrity of AISI 1008 mild steel welds. Using Taguchi's design of experiment method, butt and lap joint weldments reinforced with titanium powders were optimized for tensile strength in the first welding phase. In the second welding phase, the optimum parameters obtained were used to make two sets of weldments for comparison; one with titanium reinforcement and the other without any reinforcement. The weldments were characterized using optical microscopy, x-ray diffraction (XRD) analysis, energy dispersive spectroscopy (EDS) and scanning electron microscopy (SEM). Mechanical tests for tensile strength and for microhardness were carried out. A three-dimensional transient thermal numerical analysis was used to predict the temperature field and weld pool geometry of the reinforced and unreinforced weldments. The temperature histories obtained, and the simulated weld pool geometries were correlated with the microstructure evolution observed across the weld zones.

The optimum parameters obtained from the optimization process were 24V and 220 A for butt joints and 26 V, 215 A for lap joints. Ti 6-2-2-2-2 alloy powder was also selected as the preferred titanium powder reinforcement. It was discovered that microhardness in the weld metal was higher in the reinforced weldments due to the formation of an iron-titanium intermetallic compound and martensite microphases. There was no significant improvement in the tensile strength of the reinforced joints. However, it was observed that acicular ferrite formation was more prominent in the titanium-reinforced weldments, suggesting an improvement of impact toughness. Failure analysis revealed that all reinforced welds underwent predominantly ductile failure. The temperature histories at selected points away from the weld centre were estimated for the

weldments using numerical analysis. These temperature histories correlated well with the microstructures observed across the weld zones. The weld pool geometry prediction obtained through the numerical analysis agreed with experimental results.

It was concluded that the reinforcement of steel welds with titanium particles improved the hardness property of the weldments. It also promoted the dominance of acicular ferrite microstructure in the weld zone. Acicular ferrite is desired in mild steel welds to improve material toughness.

TABLE OF CONTENT

LIST OF FIGURES

LIST OF TABLES

GLOSSARY OF TERMS

A

Allotropes: a structurally different form of an element

Alloy: A metallic solid or liquid that is composed of a homogeneous mixture of two or more metals or of metals and non-metal or metalloid elements, usually for the purpose of imparting or increasing specific characteristics or properties

Ambient Temperature: the outside temperature at any given altitude, preferably expressed in degrees centigrade

Annealing: To subject metal to a process of heating and slow cooling in order to toughen and reduce brittleness

Austenite: a solid solution of carbon in face-centred-cubic gamma iron, usually existing above 723°C

B

Characterization: description of distinctive characteristics or essential features of a material.

Cleavage Fracture: The splitting or tendency to split, of a crystallized substance along definite crystalline planes, yielding smooth surfaces.

Corrosion: a process in which a solid, especially a metal, is eaten away and changed by a chemical action

Crystal: A homogenous solid formed by a repeating, three-dimensional pattern of atoms, ions, or molecules and having fixed distances between constituent parts.

D

Dendrite: a crystal that has branched during growth and has a treelike form

Depth of penetration: the distance from the original surface of the base metal to the bottom of the pool of fused metal.

Ductility: the property of something that can be worked or hammered or shaped without breaking.

E

Electrode (welding): used to conduct current through a workpiece to fuse two pieces together

Epitaxial growth: a type of crystal growth or material deposition in which new crystalline layers are formed with a well-defined orientation with respect to the crystalline substrate

Equiaxed grain: having approximately equal dimensions in all directions - used especially of a crystal grain in a metal

Equilibrium: The state of a system in which more than one phase exists and exchange between phases occurs at equal rates so that there is no net change in the composition of the system

Eutectoid: relating to or denoting an alloy which has a minimum transformation temperature between a solid solution and a simple mixture of metals.

F

Failure analysis: the process of collecting and analyzing data to determine the cause of a failure.

Ferrite: any of the body-centred cubic allotropes of iron, such as alpha iron, occurring in steel.

Filler wire: In welding, it is a joining material is placed at the point of welding to help better connect the weld.

Fusion zone: the portion of materials that have undergone melting due to heat input during welding.

G

Gas flow rate: the volume of gas that is supplied to the welding arc in a particular period.

Grain boundaries: the interface between two grains, or crystallites, in a polycrystalline material

H

Hardness: resistance of a material to deformation, indentation, or penetration by means such as abrasion, drilling, impact, scratching, and/or wear,

I

Impact toughness: the ability of a weld to permanently deform while absorbing energy before fracturing, specifically when stress is applied rapidly

M

Martensite: is a body-centred tetragonal form of iron in which some carbon is dissolved

Microstructure: the fine structure (in a metal or other material) which can be made visible and examined with a microscope.

N

Nucleation: the initial process that occurs in the formation of a crystal from a solution, a liquid, or a vapour, in which a small number of ions, atoms, or molecules become arranged in a pattern characteristic of a crystalline solid, forming a site upon which additional particles are deposited as the crystal grows

P

Parameter: a numerical or other measurable factor forming one of a set that defines a system or sets the conditions of its operation.

Parametric optimization: the selection of parameter values, which are optimal in some desired sense

Pearlite: a finely laminated mixture of ferrite and cementite present in cast iron and steel, formed by the cooling of austenite

Percentage elongation: a measurement that captures the amount a material will plastically and elastically deform up to fracture

Plastic deformation: a permanent deformation or change in the shape of a solid body without fracture under the action of a sustained force.

Porosity: a measure of the voids or spaces in a material

R

Recrystallization: a process by which deformed grains are replaced by a new set of defect-free grains that nucleate and grow until the original grains have been entirely consumed

T

Tempering: To harden or strengthen metal by the application of heat or by heating and cooling

Tensile Strength: the resistance of a material to breaking under tension.

Transient: lasting only for a short time

Travel speed: the linear rate that the arc moves along the workpiece.

W

Weld bead: a deposit of welding metal on the surface of a metal workpiece, often used to examine the structure of the weld zone

Weld pool: the dime-sized workable portion of a weld where the base metal has reached its melting point and is ready to be infused with filler material

Welding: to join metal parts together by heating the surfaces to the point of melting

Welding current: the current that flows through a circuit while a weld is being made

Welding voltage: an electromotive force or potential difference between the workpiece and the welding torch.

Y

Yield strength: the stress at which a specific amount of plastic deformation is produced, usually taken as 0.2 per cent of the unstressed length.

ABBREVIATIONS

AISI - American Iron and Steel Institute
ANOVA - Analysis of Variance
ANSYS - Analysis System Software
ASTM - American Society for Testing Materials
BCC - Body Centred Cubic
CGHAZ - Coarse Grain Heat Affected Zone
CMC - Ceramic Matrix Composites
CWM - Computational Welding Mechanics
DoE - Design of Experiments
DOF - Degree of Freedom
EDS - Energy Dispersive Spectroscopy
FEA - Finite Element Analysis
FEM - Finite Element Method
FGHAZ - Fine Grain Heat Affected Zone
FSW - Friction Stir Welding
GMAW - Gas Metal Arc Welding
GTAW - Gas Tungsten Arc Welding
HAZ - Heat Affected Zone
HCP - Hexagonal Close Packing
HRC - Rockwell Hardness
HV - Vickers Hardness
MIG - Metal Inert Gas
MMC - Metal Matrix Composite
PAW - Plasma Arc Welding
PMC - Polymer Matrix Composites
PWHT - Post Weld Heat Treatment
RSM - Response Surface Methodology
RSW - Resistance Spot Welding
S/N - Signal to Noise Ratio
SAW - Submerged Arc Welding
SEM - Scanning Electron Microscopy
SMAW - Shielded Metal Arc Welding
TIG - Tungsten Inert Gas
UTS - Ultimate Tensile Strength
WM - Weld Metal
WZ - Weld Zone
XRD - X-Ray Diffraction

1. Introduction

1.1 Background

The industrial world is constantly in pursuit of high-quality materials. Where these high-quality materials are in use, the technologies applied in forming or joining these materials are constantly being pushed to their limits to deliver quality. One of the most common materials in the metal industry is steel, and an even more commonly used type of steel is Mild Steel. It is widely known that steel is favoured for its high tensile and yield strength. Mild steel combines this strength with good malleability, weldability, hardness and wear resistance properties [1]. These properties make Mild Steel a widely used industrial material. Mild steel finds applications in construction, machine ware, cookware, pipelines amongst others [2]

As earlier said, the technology used in forming or joining materials such as mild steel is just as important as the material itself. For instance, in the case of welding, the integrity of the welded material itself is compromised when subjected to welding processes, especially in the heat-affected zone because the metal in this area undergoes changes [3]. This means that welded materials are usually weakest at their welded joints. It is primarily because of this, that some structures, which are subjected to certain degrees of stress, are designed without any kind of joints as is seen in some aerodynamic designs [4]. Such design luxuries are usually complex and expensive and are typically reserved for specialized cases such as military applications and space explorations.

However, for simpler design demands, where welding is unavoidable, the search to maintain or optimize weld joint integrity continues. Engineers and researchers want to produce welded joints that are just as strong, if not stronger than their base material. With respect to these pursuits, welding engineers have come up with ingenious technological methods to improve mechanical integrity in welded joints. In the case of steel as well as other materials, technological methods such as Post weld heat treatment, hybrid welding and pulsed current welding are becoming more common. [5][6] [7]

Common drawbacks, however, with innovative technologies are costs and difficulty of use. While more research is constantly being undertaken to improve such technology, perhaps conventional welding methods could still be efficiently applied in producing quality welds. Considering this view, many scholars, engineers and researchers have studied the optimization of process parameters to improve weld quality and have obtained significant results. Various welding methods from the well-used Shielded Metal Arc welding to the relatively new Friction Stir welding have been optimized to produce quality welds for various materials. [8] [9]

Metal Inert Gas welding is one of the most popular welding methods and is widely used for the welding of mild steel. It makes use of a consumable electrode to create an electric arc between itself and the workpieces. This electric arc causes the workpieces to melt, resulting in a permanent joint of the workpieces. MIG is different from other welding processes in that it makes use of inert gases to shield the weld pool from atmospheric contamination. These shielding gases could be argon, helium, helium-argon mixture [10] and sometimes CO_2. The important process parameters in MIG include electrode size, welding current, arc voltage, arc travel speed, welding position, gas flow rate, shielding gas composition and electrode extension or electrode stick-out [10]. Figure 1-1 shows the schematics of the MIG welding process.

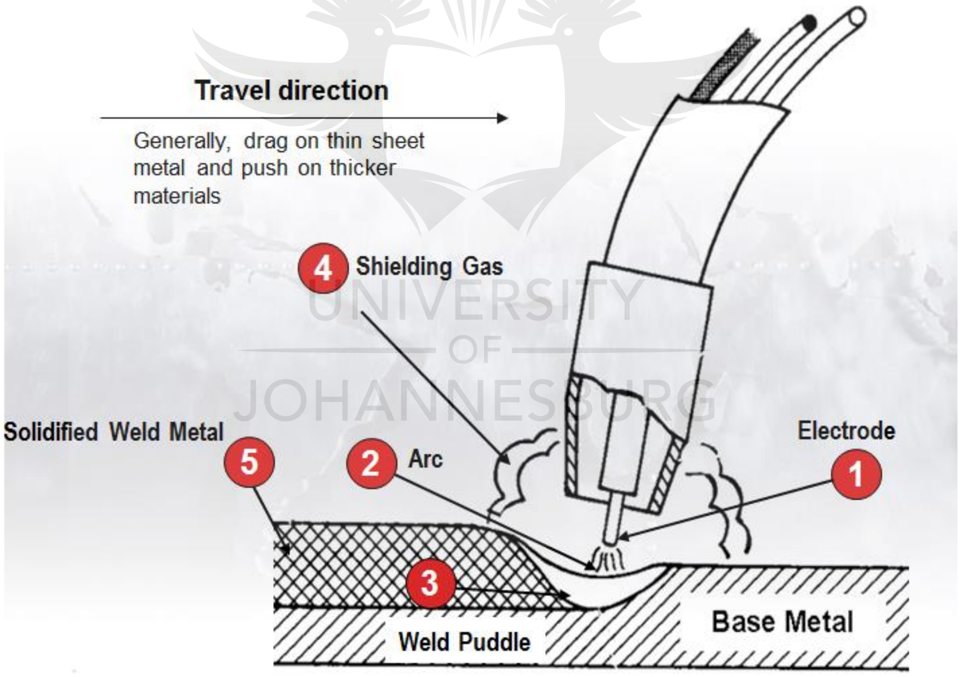

Figure 1-1: MIG Welding [11]

As with other methods, there has been substantial research on optimizing the process parameters in the MIG welding of mild steel plates. Still, there is a substantial suggestion in the literature that mild steel welded joints could be further improved beyond the optimization of process parameters.

The application of metallic powders to improve joint integrity is a suggestion worth investigating. Titanium alloy powders, for instance, are well known for their strength and hardness and can be applied as reinforcement to mild steel joints in MIG welding considering the melting points of mild steel and these titanium powders are not too far apart. This suggestion could provide a relatively easy solution to improving welded steel joints and thus make structures such as building frames and steel pipes more structurally robust.

This idea forms the basis on which this study was carried out. The study investigates what effect titanium powders have on the integrity of welded mild steel joints, and the degree to which these powders contribute to the mechanical properties of the joints.

1.1.1 Keywords

i) Mechanical Properties: are the responses of a material(s) to specified external load. These properties include tensile strength, fracture toughness, hardness, fatigue, ductility amongst others.

ii) MIG: This is an abbreviation for Metal Inert Gas welding. It is a fusion welding process that employs the use of inert gases to protect the weld pool while a consumable electrode melts together with the work pieces to form a fused joint.

iii) Reinforced Steel Sheets: In this study, a welded steel joint into which metallic powders have been added before welding, is referred to as a reinforced steel sheet.

iv) Titanium Alloy: This is a mixture of titanium (as the primary element) with other suitable chemical elements. The most common alloying elements used with titanium include Aluminium, Vanadium, Zirconium, Tin, Manganese amongst others.

1.2 Problem Statement

Materials such as steel, are selected for their desirable properties. In the case of mild steel, its mechanical properties, especially its high tensile strength, makes it a material of choice for various applications. It is well known that in the joining of steel sheets using MIG welding, the fused material undergoes microstructural changes due to the heat energy applied for fusion to take place [3]. These microstructural changes have a direct impact on the mechanical properties of the welded joint.

This poses a problem to engineers who must devise methods to either reduce the degree of the compromise of integrity in the welded joint or increase the desirable properties in the weld joint.

To tackle this problem, engineers have come up with the idea of optimizing the process parameters of the welding process, with successful results recorded [12],[13]. However, there could be other ways to improve weld joint integrity beyond the optimization of process parameters.

To address this challenge, this study seeks to explore the application of titanium powders as reinforcements in welded joints to improve the mechanical properties of welded mild steel joints.

1.3 Rationale and Motivation for the Study

This research will push the frontiers in the improvement of weld joint integrity. It will contribute substantially to the knowledge of the viability of titanium powders in improving weld integrity in mild steel. The study also serves as a platform for further improvement on the methodology of the application of metallic powders in the industry.

1.4 Aim of Research

The aim of this research is to investigate the effect of the use of titanium alloy powder to reinforce the weld joint of MIG welded steel sheets, with attention to the tensile stress and hardness of the welded sheets.

1.5 Objectives of Research

The objectives of the research study are as follows:

1. Explore the properties of Titanium alloy powder and steel sheets through elemental composition analysis.
2. Adopt Taguchi's Design of Experiment method to plan and execute welding experiments.
3. Conduct MIG welding of steel sheets with and without the reinforcement of titanium powder with both Butt and Lap Configurations.
4. Conduct Microstructural analysis, failure analysis and mechanical testing of both parent material and MIG welded joint with and without titanium reinforcement.
5. Analyze tests results for mechanical properties using Taguchi's Signal-to-Noise S/N ratio and Analysis of Variance (ANOVA)
6. Adopt the Finite Element Method to simulate and predict the temperature field and weld pool geometry obtained due to heat input during welding.

1.6 **Research Methodology**

The base material used for this research was 3 mm mild steel sheet. The powder reinforcements applied in the welded joints were commercially pure titanium and titanium 6-2-2-2-2 alloy powders. Taguchi's Design of experiment method was used to plan and execute the research experiments. The research procedure is outlined as follows;

1. A thorough literature review was conducted to gain insight into the method of parametric optimization to improve the mechanical properties of steel in MIG welding. Process parameter ranges were obtained from the literature for experimentation.

2. Taguchi's design of experiment method was used to plan the welding experiment. This was preferred to other design methods because of its economic and efficient advantages.

3. A butt joint configuration with mild steel sheets of 100 mm x 40 mm x 3mm; and lap joint configuration with mild steel sheets of 150 mm x 40 mm x 3 mm were prepared and welded using MIG. Samples of the steel sheet joints were reinforced with commercially pure titanium powder and titanium alloy powder. The welding experiments were carried out at South Africa Institute of Welding Johannesburg, Johannesburg, South Africa.

4. The welded specimens were prepared for microstructural examinations and characterization tests. The characterization tests conducted were optical microscopy and XRD.

5. The welded specimens were also tested for mechanical properties. The tests conducted were tensile and microhardness tests.

6. Failure analysis was conducted using SEM and EDS.

7. The tensile test results were analyzed using Taguchi's signal-to-noise ratios and ANOVA. These statistical analyzes produced results for optimum parametric settings of the experimental procedure.

8. Using the optimum parameters from Taguchi's DoE, final welding was carried out for a set of reinforced samples, and another set of unreinforced samples. This was done for both butt and lap joints.

9. Tensile testing, hardness testing, XRD analysis and failure analysis were carried out on each set of samples and a comparison was done between the reinforced and unreinforced weldments to ascertain the effect of titanium reinforcement.

10. ANSYS Software - Workbench was used to simulate and predict the temperature field and weld pool geometry of the reinforced and unreinforced butt and lap welds.

1.7 Delimitation

The experimental work was limited to mild steel sheets of 3mm thickness. Only lap and butt joint configurations were considered during the experimental stage. The experimental work also focused on MIG welding alone.

1.8 Research Expectation

Due to the highly favourable mechanical properties of titanium powders, it is expected that using these powders as joint reinforcement in the MIG welding of mild steel sheets, will substantially affect the tensile strength and/or hardness of the steel sheets. It is expected that proper experimental design, characterization and analysis will test this prediction and confirm its validity. The FEA is expected to predict the temperature field and weld pool geometry of the weldments to acceptable levels of precision.

1.9 Overview of Dissertation

This dissertation has been structured into five chapters (Figure 1-2).

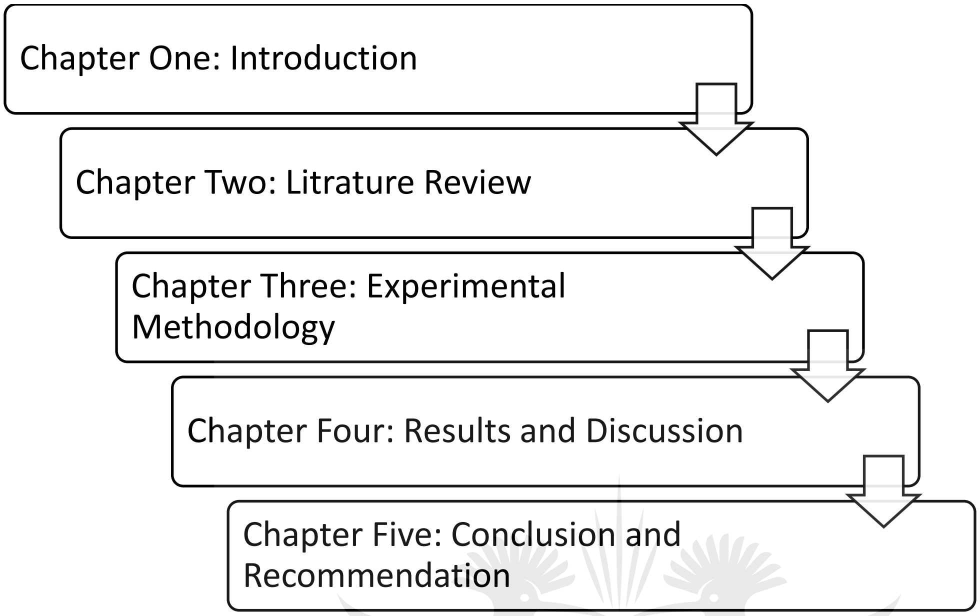

Figure 1-2: Workflow of Dissertation

Each chapter begins with an introduction into its content, followed by its body of content and a summary. The thesis also contains a collection of references for all cited works, as well as appendices of other useful information. The reference list and appendices occur at the end of the dissertation. The chapters in this dissertation are outlined as follows:

- Chapter one gives the introduction and overview of the entire research work.
- Chapter two covers the review of literature in the related field of research. The emphasis of the review is on the scholarly works done in improving joint integrity of welded materials, with special attention to MIG welding of steel materials.
- Chapter three details the experimental research methodology adopted for this study. It describes the successful adoption of Taguchi’s design of experiment method and the characterization tests carried out on the welded samples.
- Chapter four is a thorough analysis and discussion of the experimentation results. It gives a comprehensive explanation of the effect of the titanium powders on the welded mild steel sheet joints through the interpretation of the results from statistical analysis.

- In chapter five, conclusions and recommendations were made regarding the research work.

1.10 **Summary**

In this chapter, a background of the research study has been given which identifies the need for this research. The problem that this research intends to solve was identified and the aims and objectives that will guide this solution were given. A brief overview of the methodology of the research was also captured and the structure of the dissertation was explained.

2. Literature Review

2.1 Introduction

This chapter is a theoretical review of scholarly literature on the improvement of the mechanical properties of welded steel joints. The chapter opens with a look at the background information on steel as a material, its properties, forms and applications. This is followed by a broad look at welding as a material joining process. The review goes further into MIG welding and how it compares with other welding processes. The improvement of mechanical properties of steel welds in MIG welding through parametric optimization is reviewed after which parametric optimization with and without Taguchi's Design of Experiment method is thoroughly considered. This section is followed by a review of alternative means of improving weld integrity of steel materials and is concluded with the suggestion of Titanium alloy powder as a viable material for the reinforcement of welded steel joints in MIG welding.

2.2 Steel

Steel is arguably the world's foremost construction material. It is an iron alloy which contains between 0.2 and 2 per cent carbon by weight [14]. Steel is an integral part of building and construction due to its strength and durability [15]. These properties of strength and durability make it a great choice for structures exposed to high amounts of stress which could be due to weather, heat, large amounts of applied forces and prolonged usage. The use of steel is not limited to building and construction. It is largely used in the construction of ships, railroads, cars, machines, appliances and weapons. [15]

According to the World Steel Association, there are over 3, 500 different grades of steel [16] [17]. These various grades of steel vary in physical, chemical and environmental properties. Since steel is basically a composition of iron and carbon, varying the amount of carbon gives rise to these different grades of steel. The properties of these grades of steel are also affected by the level of impurities and additional alloying elements [18].

The various grades of steel can be broadly categorized into four types [18]. The first are carbon steels which account for 90% of total steel production [19]. Carbon steel is further categorized into three sub-categories based on their carbon content. First is low carbon or mild steel which contains up to 0.3% carbon. Second is medium carbon steel which contains 0.3-0.6% carbon and finally, high carbon steel which contains more than 0.6% carbon. Alloy Steel is another type of steel. It contains alloying elements such as manganese, silicon, nickel, titanium, copper, chromium and aluminium. These alloys could be mixed in various proportions to manipulate the properties of steel.

Stainless Steels is a class of steels that generally contains between 10-20% chromium as the main alloying element. This presence of chromium makes stainless steel highly resistant to corrosion and improves weldability [20]. Stainless steel is further divided into three groups based on their crystalline structure. These groups are Austenitic steels (18% chromium, 8% nickel and less than 0.8% carbon), Ferritic steels (12-17% chromium, less than 0.1% carbon, trace amounts of nickel and other alloying elements such as molybdenum, aluminium or titanium) and Martensitic (11-17% chromium, less than 0.4% nickel and up to 1.2% carbon). Both ferritic and martensitic sheets of steel are magnetic while austenitic steels are not. [21]

The last class of steel is called Tool Steel. It contains tungsten, molybdenum, cobalt and vanadium in varying quantities specifically to increase heat resistance and durability. These properties make them ideal for cutting and drilling equipment [16].

Another way of classifying steel is by their shapes and related applications. Using this system of classification, there are long/tubular Products which include bars and rods, rails, wires, angles, pipes, and shapes and sections. These products are commonly used in the automotive and construction sectors [15]. Flat Products include plates, sheets, coils, and strips. These materials are mainly used in automotive parts, appliances, packaging, shipbuilding, and construction. Other Products include valves, fittings, and flanges and are mainly used as piping materials. [16]

2.3 Welding

Welding has been used extensively in the last several decades and is widely accepted as one of the most commonly used joining techniques for various metallic structures including ships, aeroplanes, automobiles, bridges, pressure vessels, etc. It is said to provide better performance in comparison to other joining techniques in terms of joint efficiency, mechanical properties, and applications [22]. Welding is the most vital and most common operation used for the joining of two similar or dissimilar parts [22]. Other joining techniques apart from welding include brazing and soldering.

By simple definition, fusion welding is a fabrication or sculptural process that joins materials, usually metals or thermoplastics, by causing coalescence. This is often done by melting the workpieces and adding a filler material to form a pool of molten material, also known as the weld pool, that cools to become a strong joint. The pressure is sometimes used in conjunction with heat to produce the weld [23].

There are more than 80 different types of welding and associated processes [24]. Some of the most common types of welding include arc welding, which includes shielded metal arc welding (SMAW), the gas-shielded methods of metal inert gas (MIG) and tungsten inert gas (TIG), plasma arc welding (PAW), and submerged arc welding (SAW). Some of the welding processes may use oxy-acetylene gas, electrical current, lasers, electron beams, friction, ultrasonic sound, chemical reactions, heat from fuel gas, and robots to carry out different operations [24].

Friction stir welding (FSW) stands out on its own as a relatively new welding process that may have significant advantages compared to the fusion processes. It involves the joining of conventionally non-fusion weldable alloys, which reduces distortion and improves mechanical properties of weldable alloys joints due to the pure solid-state joining of metals [25]. The solid-state joining process of friction stir welding implies that similar or dissimilar metals are joined without melting the metals. This is achieved through friction which generates heat between the metals.

2.3.1 Types of Welding Joints

There are five (5) basic types of welding joints; butt joint, lap joint, tee-joint, edge-joint and corner joint. These joint types are illustrated in Figure 2-1. The choice of welding joint is dependent on the application, material, ease of welding, amongst other factors.

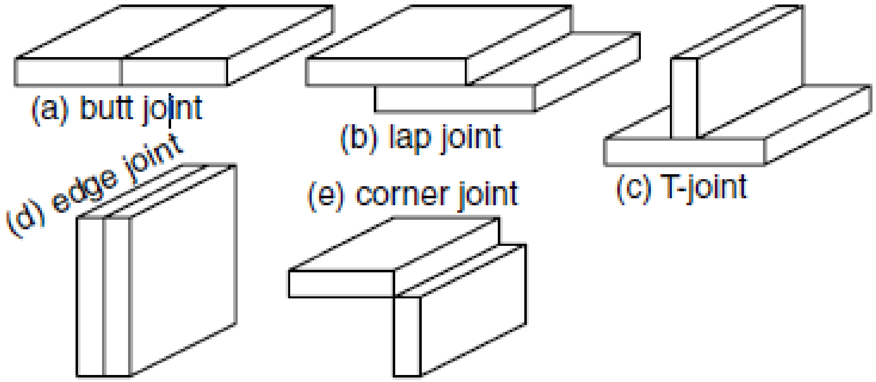

Figure 2-1: Types of Weld Joints [26]

2.3.2 Gas Metal Arc Welding or Metal Inert Gas (MIG) Welding

Gas metal arc welding is one of the conventional and traditional methods to join materials. A wide range of materials may be joined by Gas metal arc welding—similar metals, dissimilar metals, alloys, and non-metals [27]. Being arguably the most widely used welding process in the industry, it is worth taking a closer look at gas metal arc welding.

GMAW is a broad term used to describe Metal Inert Gas (MIG). GMAW welding is used because of its advantages over other welding techniques like high welding speeds, less distortion, absence of slag removal, high weld metal deposition rate, high weld quality, precise operation, etc. [27]

MIG welding is one of the most important, easiest & strongest welding techniques used in industries. It is very useful because it can be used to weld many different types of metals like carbon steel, aluminium, stainless steel, nickel etc. [28]

The welding process of MIG consists of transferring the material of filler wire in the form of molten liquid to the workpiece. The heat produced by the short circuit, along with a non-reactive gas locally melts the metal and allows them to mix together. Once the heat is removed the metal begins to cool and solidify and forms a new piece of fused metal [28]. This non-reactive gas, which is often Argon or a mixture of Argon and CO_2, protect the weld pool from atmospheric contaminants while the welding process takes place [28].

Figure 2-2 shows a schematic of the working relationships between the components of typical MIG equipment set up. Inert gas flows from the gas cylinder into the welding torch. The wire feed unit feeds the wire electrode into the welding torch at a specified rate. A power source connects the welding torch to the workpiece, between which the electric arc is created. This electric arc is responsible for the melting of the workpiece. The legend for the illustration in Figure 2-2 is given below;

1-Welding Torch, 2-Work Piece, 3-Power Source, 4-Wire feed unit, 5-Electrode source,
6-Shielding gas supply

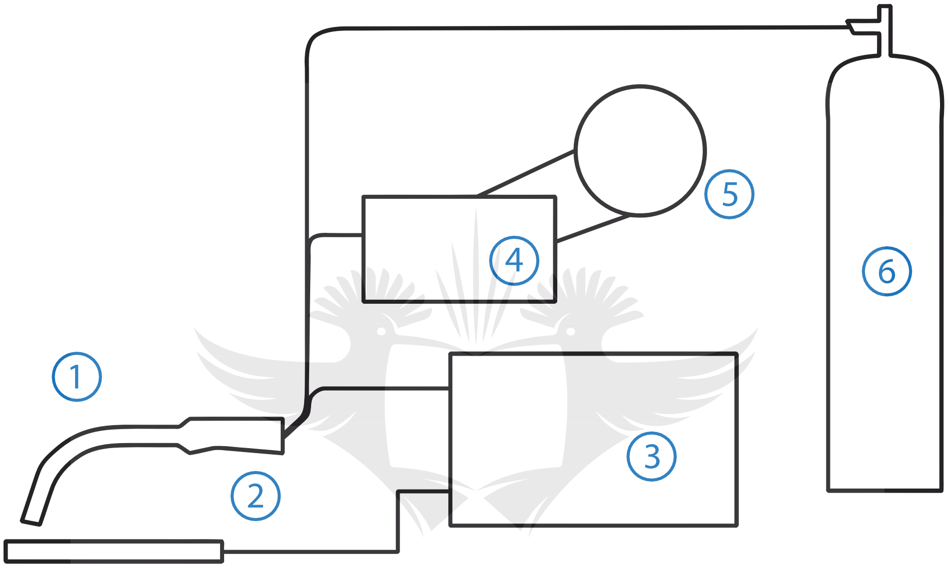

Figure 2-2: Schematic of the MIG Equipment Circuit Diagram [11]

In Figure 2-3, the science behind the MIG welding of a workpiece is depicted. The electric arc formed between the welding torch and the workpiece causes the workpiece to melt, creating a molten weld pool. The fusion of the metals occurs in this weld pool. The shielding gas protects the weld pool from atmospheric contamination which could result in poor weldments with defects such as porosity.

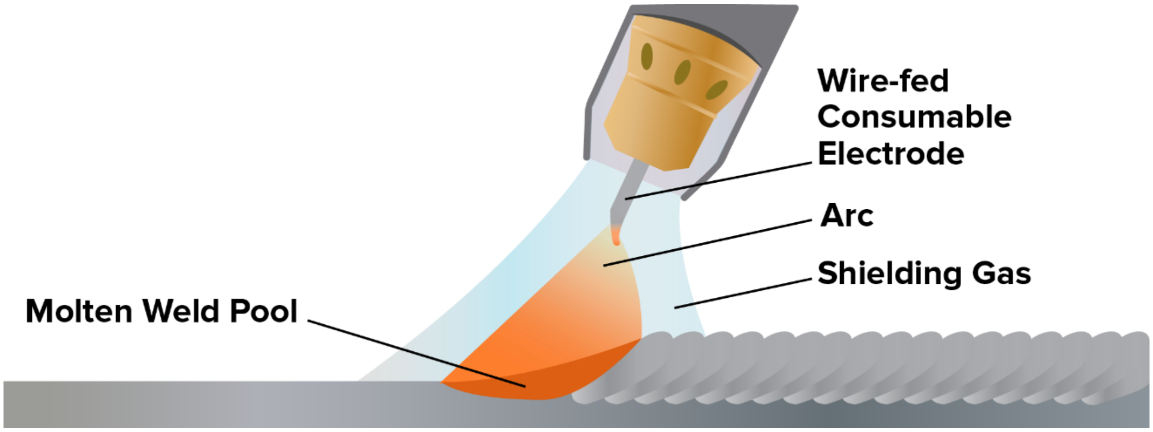

Figure 2-3: MIG Welding [11]

2.3.3 Modes of Metal Transfer in MIG Welding

Metal transfer in welding refers to the process by which molten metal travels from the tip of the electrode to the molten pool. There are three basic ways that this occurs: globular, spray and short-circuiting [26].

Globular transfer occurs when the molten metal droplet from the electrode is same in size or larger than the diameter of the electrode, a globular transfer occurs as the metal travels across the electric arc into the molten pool under the effect of gravity. This form of metal transfer usually occurs at relatively low currents and produces spatter with welds that are not smooth. [26]

In spray transfer mode, small molten metal drops travel across the electric arc at a much higher frequency than in globular transfer. As opposed to the gravitational influence in the case of globular transfer, spray transfer occurs due to electromagnetic forces around the weld pool. Spray transfer usually results in spatter-free welds and the metal transfer process is said to be more stable. This type of metal transfer occurs when the current is above the critical level. The critical current level is dependent on the material, the electrode size and the shielding gas used during the welding process. [26]

Unlike in the cases of globular and spray transfer modes where the metal droplets travel across the arc, in short-circuiting, molten metal is transferred from the electrode to the weld pool when the electrode touches the pool surface. This metal transfer mode occurs across the lowest range of welding currents and the smallest electrode diameters. Fast-freezing weld pools are said to be produced by this transfer mode. [26]

2.3.4 **How MIG compares to Other Fusion Welding Techniques**

Amongst the variety of choices available in terms of welding processes, the question arises on which welding process is the best. This question clearly does not have a straightforward answer. This is because the suitability of a welding process depends on a range of factors, beginning from the base metal to be welded to whether the welding will be done indoors or outdoors, where the weld pool will be exposed to atmospheric elements. Notwithstanding, there are scholars who have compared the performance of various welding processes and given noteworthy contributions.

In 2007, Yayla *et. al.* [29] conducted experiments to determine the best welding method for HY-80 Steel. These experiments were conducted using shielded metal arc welding (SMAW), gas metal arc welding (GMAW) and submerged metal arc welding (SAW). Following these experiments, the specimens were subjected to mechanical tests for tensile strength and Charpy impact tests for impact toughness. It should be noted that optimum welding parameters were obtained for these experiments from industrial experience and literature. The impact test results showed that SAW and SMAW had better heat-affected zone (HAZ) toughness than GMAW and this, according to the scholars, is due to higher heat input in the other welding methods. SAW and SMAW also showed slightly better results for hardness than GMAW. However, it was also noted that despite the variation of hardness profiles from one method to another, the maximum hardness reaches up to the maximum values of 425 HV at the HAZ in all the methods.

It, therefore, appears that while SAW and SMAW methods give slightly better values for impact toughness and hardness, these values are relative, and the values obtained for GMAW do not necessarily rule out the use of GMAW method for HY-80 steel. While SAW and GMAW may give better mechanical results other factors should be considered when selecting a suitable welding process, such as ease of use and economic factors.

Another comparative study proved a bit more favourable for MIG welding. Nathan *et. al.* [30] carried out a comparative evaluation of mechanical properties and microstructural features of Shielded metal arc welding (SMAW), Gas metal arc welding (GMAW), and Friction stir welding

(FSW) on naval grade steel joints. The mechanical properties considered were tensile strength, impact toughness and hardness. They discovered that the friction stir welding process eliminated the problems related to fusion welding processes and produced superior properties compared to gas metal arc and shielded metal arc welding techniques. FSW weld produced the highest values for strength which was due to grain refinement in the weld metal, unique weld metal composition and strain-induced deformation during FSW. The GMAW joint showed a 28% and 10% higher impact toughness than FSW and SMAW respectively. The authors put this down to the presence of martensite-austenite (M-A) constituents and the ferrite laths in a bainitic matrix in the weld zone microstructures. The hardness of the FSW joint was shown to be higher than the SMAW and GMAW joints. The authors affirmed that this was due to severe plastic deformation and continuous dynamic recrystallization in the stir zone as well as localized heating and fast cooling rate of the FSW process. This study indicates a good degree of superiority of FSW over other fusion welding techniques.

However, attention should be drawn to a key difference between Yayla *et. al.* [29] and Nathan *et. al.'*s [30] works. While Yayla *et. al.* [29] reported better toughness in the heat-affected zones for SAW and SMAW over GMAW, Nathan *et. al.* [30] reported that GMAW showed 10% better impact toughness values than SMAW. This discrepancy might be due to the different materials worked with; HY-80 steel in Yayla *et. al*.'s [29] case and naval grade steel in Nathan *et. al*.'s [30] case. While both materials are quite similar but will vary slightly in chemical composition, this discrepancy shows that the composition of the weld metal is a vital factor in determining the suitability of a welding process. Another well-known factor in both the suitability of welding processes and the obtainment of desirable weld quality is the consideration of process parameters.

2.4 **Significance of MIG Welding Parameters**

In the use of MIG welding, there are certain parameters that are often considered. Tewari *et. al.* [31] showed that these parameters influence the weld quality significantly. These parameters include welding current, welding voltage, welding speed and wire feed rate. Welding current is simply the amount of current supplied to the welding gun. Tewari *et. al.* [31] explain that the current affects the electrode burn-off rate, the depth of fusion and the geometry of weldments. Welding voltage is the electric potential difference between the tip of the welding wire and the surface of the molten weld pool. It is said to determine the shape of fusion and weld reinforcement [31]. Welding speed is defined as the rate of travel of the electrode along the seam or the rate of the travel of the work under the electrode along the seam. Wire Feed Rate is the rate at which the electrode or filler wire is supplied to the weld joint. This is usually regulated in IPM or inches per minute [32].

Amongst these parameters are others such as gas flow rate and distance from the nozzle to workpiece. In the classification of these parameters, Ramos-Jaime *et. al.* [33] recalled the classification of process parameters given by D.A Dornfeld in 1982. Some parameters that can be changed online i.e. during the welding process; these include welding voltage, wire feed rate, welding current and travel speed. Some Parameters are set prior to the beginning of the process; these include composition and protective gas flow, torch angle, electrode distance to the workpiece and the composition and diameter of the electrode A few parameters cannot be modified; these include the thickness of base metal, the joint geometry and the physical properties of the base metal.

The importance of these variables is further highlighted in a problem that Ramakrishna *et. al.* [34] discuss in their paper. Ramakrishna *et. al.* [34] assert that the welding processes affect the metallurgy of the welded components. While welding takes place, there is an intense heat input on the weld material which causes the regions near the weld to undergo severe thermal cycles. This leads to inhomogeneous plastic deformation in the weldment and an inevitable reduction in the strength of the weld joint. What happens is that despite the permanent joining of similar or dissimilar metals, the weld joint often turns out to be the weakest point of the fused metals.

This compromise of the structural integrity of the weld joint has led to a pursuit of numerous techniques employed to improve mechanical properties of weld joints. One prominent solution to this problem lies in the optimization of process parameters. Investigations into the relationship between process parameters and mechanical properties go as far back as the mid-1900s [31]. Lee [35] and Raveendra [34] applied regression analysis to welding geometry as far back as the late 20th century. Ever since, there has been thorough research and development of proven techniques used to improve the integrity of steel welds. It is important that an extensive and detailed review of the work done so far in improving weld integrity is considered.

In the following portions of this review, a very thorough look at the various methods used to improve weld joint quality is carried out. The objective of the review is to discover the extent to which experimental research has been carried out while understanding the limitations and areas of possible improvement.

2.5 Improving Weld Integrity through Parametric Optimization

There is a vast amount of scholarly research majoring on optimizing process parameters of welding operations in a bid to improve the integrity of welded joints. A good number of these studies have been discussed in the following sections.

2.5.1 Parametric Optimization Done on TIG, MIG and others

MIG and TIG welding processes are two of the most popular welding processes in the industry. Both processes are very similar in that, they both employ the use of inert gases to shield the weld pool from atmospheric contaminants which could easily compromise the integrity of the welds. However, they also differ, in that TIG uses a non-consumable Tungsten electrode while MIG uses a consumable wire electrode, and this major difference amongst others creates advantages and disadvantages of each process over the other. A closer look at some scholarly work done on the optimization of both processes follows.

Kazi *et. al.* [23], Patel and Gandhi [36], Kumar *et. al.* [37] and Kishore *et. al.* [38] are just a few scholars who conducted simultaneous studies on TIG and MIG process parameter optimization. Kazi *et. al.* [23] first carried out an extensive literature review on the various methods adopted by several researchers to explain the effect of process parameters on mechanical properties, weld bead geometry, depth of penetration etc.

Following this scholarly review, a brief look at various welding techniques was also done with an aim to suggest the best welding technique for steel. They emphasized specifically on TIG and MIG welding.

Kazi *et. al.* [23] welded type 304 stainless steel under varied conditions of current, voltage and speed. The authors further proceeded to test for mechanical properties such as percentage elongation, reduction in area, yield strength, hardness and corrosion resistance. These characterization tests were carried out on hardness testing machines and universal testing machine for properties such as strength, hardness, modulus of rigidity, ductility, breaking point and percentage elongation.

Following these experiments, Kazi *et. al.* [23] concluded that hardness in MIG welding was higher than in TIG welding. They also submitted that ductility in MIG welding was higher than in TIG welding of 304 stainless steel. The authors reported that the TIG welding specimen could bear a higher load and had higher yield stress and tensile stress.

Kazi *et. al.* [23] concluded that TIG welding was a better option for 304 stainless steel ahead of MIG welding. Patel and Gandhi's [36]study on the effect of different input parameters of TIG and MIG welding on weld quality was geared towards application in pipe welding. Kazi *et. al.* [23] commented on Patel and Gandhi*'s* [36] work by predicting that gas shielded metal arc welding was beginning to make inroads in pipe welding and was set to overtake shielded metal arc welding as the popular choice for pipe welding, owing to the advancement in welding technology.

Kumar *et. al.* [37] appear to agree with Kazi *et.al.* [23] on the suitability of TIG over MIG. In their work, Kumar *et. al.* [37] extensively studied the mechanical properties of austenitic steel for TIG and MIG processes. Their goal was to determine the impact of welding voltage on the mechanical properties of austenitic steel. The mechanical properties considered were the strength, hardness, ductility, grain structure, modulus of elasticity etc. They concluded that TIG welding is more suitable for austenitic steel. They also pointed out that hardness property was more prominent in MIG welding of austenitic steel.

In another simultaneous study on MIG and TIG processes, Kishore *et. al.* [38] analyzed the defects in gas shielded metal arc welding of AISI1040 steel plates using Taguchi's method. They conducted a survey across a few parametric variables which include arc voltage, arc current, welding speed, nozzle to work distance, and gas pressure to confirm that these parameters have varying degrees of influence on the quality of welds. An orthogonal array was adopted for experimentation. The weldments were properly tested, and the results were analyzed using ANOVA. Data in the work was collected using ultrasound testing of the specimens. The testing specimens were found to possess defects such as blowholes, cracks, lack of penetration and lack of fusion.

Kishore *et. al.* [38] suggested that to avoid lack of penetration in the specimen optimized values for current should be 150 A and 180 A for 3 mm and 5 mm plates respectively for MIG welding. Also, for TIG welding, optimum current values for current were given as 65 A and 80 A for 3mm and 5 mm plates respectively. The welding speed was advised to be less than 0.45 m/min for 3 mm plates and 0.35 m/min for 5 mm plates in MIG welding. In the study the optimum nozzle to tip distance given for MIG welding of 3 mm plates was 10 mm; and 12 mm distance for 5mm plates of AISI1040 steel plates. The study also validated Taguchi's method as a robust method for the design of experiments and for quality evaluation. Rather than pick one welding process over the other, Kishore *et. al.*'s [38] work showed that both MIG and TIG can be used for welding steel if optimum parameters are employed. According to Kou [26], TIG welding is more suited to thinner materials due to its relatively low heat input.

In another example to illustrate the effectiveness of optimizing process parameters, Patel and Rahul [39] conducted a review on the effect of TIG welding parameters on mechanical properties such as hardness and tensile strength using optimization philosophy. They discovered how welding parameters such as welding current, gas flow rate and welding speed can be optimized and how they influence output parameters such as hardness of welding and tensile strength. Following their review, they proposed research experiment was on austenitic type stainless steel with grade E310, to test the optimization of parameters.

Parametric optimization is also popularly used in other welding techniques. In 2009, Esme [40] investigated the effect and optimization of welding parameters on the tensile shear strength of SAE 1010 steel sheets in Resistance Spot Welding (RSW) process. Esme [40] carried out parametric studies by varying electrode forces, welding currents, electrode diameters and welding times. He adopted Taguchi's experimental design method. Optimum welding parameters were obtained using the analysis of signal-to-noise ratio while the degrees of the contribution of the welding parameters were determined by using the analysis of variance (ANOVA). It was discovered that welding current was the most significant contributor to the improvement of tensile shear stress in the RSW process. Esme [40] carried out confirmation tests and concluded that is possible to significantly increase tensile shear strength by using Taguchi's method. His experiments also confirmed the validity of using Taguchi's method to enhance welding performance and to optimize welding parameters in resistance spot welding process.

While Esme [40] optimized process parameters in Resistance spot welding, Kathuria and Gupta [41] carried out research work on IS 2062 mild steel plates using the submerged arc welding process. They investigated the effect of the addition of titanium powder to Submerged Arc Welding (SAW) of mild steel plates on the tensile stress of the material. To carry out this experiment, Kathuria and Gupta [41] used Taguchi's method to formulate the experimental design. A total number of 9 experimental runs were conducted using an L9 orthogonal array, after which the optimum parameters required to achieve the best values of tensile strength, were determined. The varied parameters for the experiment were voltage, electrode stick out and flux. Three levels of flux were used for the experiment, two of which were 10% titanium powder addition to the normal AUTOMELT B31 flux, and 20% titanium powder addition to the AUTOMELT B31 flux. The results were further analyzed using ANOVA. These results showed that the flux containing 20% titanium powder had a significant contributing effect of 83.77% on the tensile strength of the material. The optimum values derived from the experiment were current of 350 A, electrode stick out of 25mm and flux of AUTOMELT B31 with 20% titanium powder. This experiment strongly suggests the significant effect of titanium powder in improving mechanical properties of mild steel plates.

In another parametric optimization study on mild steel plates, Tewari *et. al.* [31] studied the effect of various welding parameters on the weldability of Mild Steel specimens using shielded metal arc welding. They conducted their experiments on 18 specimens of Mild steel with dimensions of 50 mm x 40 mm x 6 mm with a closed butt joint weld geometry. The arc time was varied for each specimen. The value of each arc time was then used to calculate the welding speed and the heat energy input rate. The depth of penetrations for each specimen was measured and the effects of welding speed and heat input rate on the depth of penetration were investigated. It was discovered that the deepest penetration of 5.41 mm was obtained at a welding speed of 110.39 mm/min as shown in Figure 2-4. The maximum depth of penetration was obtained when the heat input rate was 1369.68 J/mm (Figure 2-5). It was therefore concluded that increasing the speed of travel and maintaining constant arc voltage and current will increase penetration until an optimum speed is reached where penetration is at its maximum. If the speed is further increased beyond this value, a resulting decrease in penetration follows.

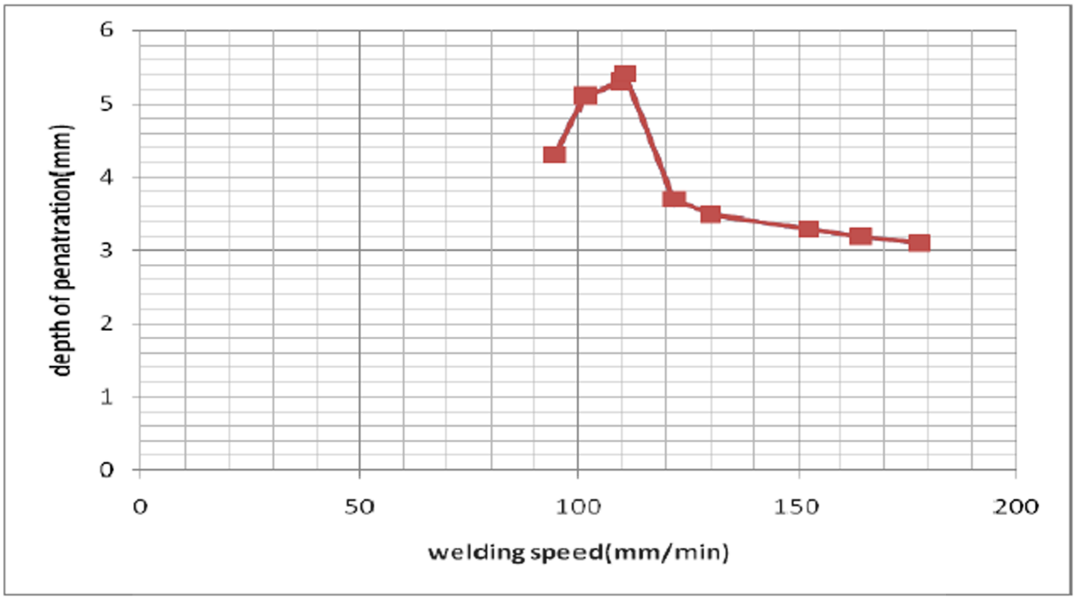

Figure 2-4: Relationship between depth of penetration and welding speed in MIG welding of 6mm thick mild steel plates [31]

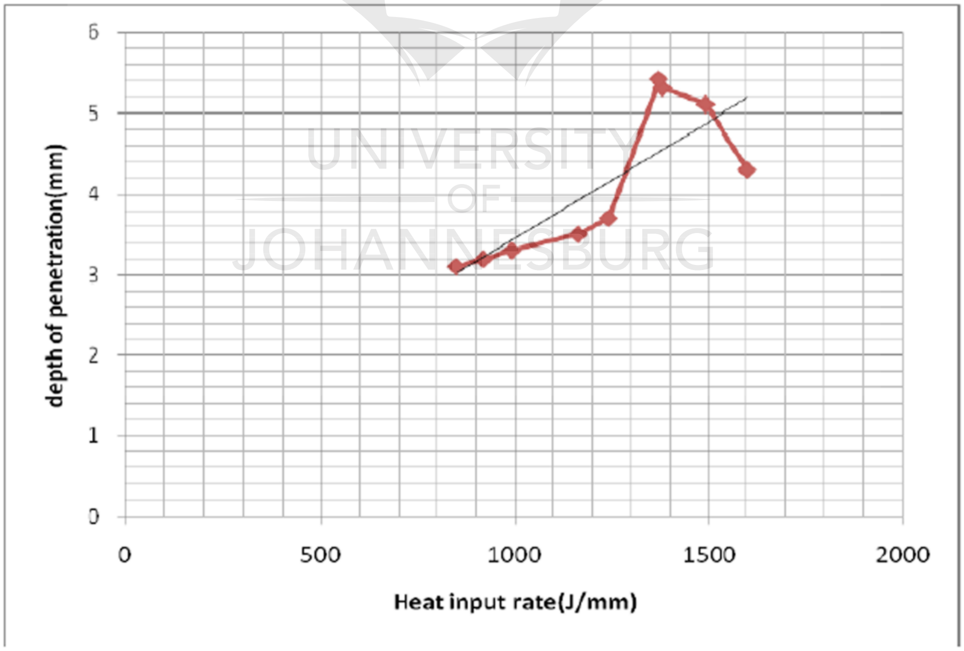

Figure 2-5: Relationship between heat input rate and depth of penetration in MIG welding of 6 mm thick mild steel plates [31]

These scholarly works clearly show that optimizing process parameters in a welding process substantially improves the quality of the weld as reflected in its physical and mechanical properties. Another subject worthy of note is the methodology employed in carrying out these optimization experiments.

Kathuria and Gupta [41], Esme [40] and Kishore *et. al.* [38] all adopted Taguchi's method of Design of Experiments. The significance of this method will be discussed further in the review. However, it will be helpful to consider other experimental design methods used in the optimization of process parameters for MIG welding.

2.5.2 **Parametric Optimization Research Done on MIG Welding**

In this section, parametric optimization methods different from Taguchi's Design of Experiment method is first considered, then Taguchi's method is squarely reviewed.

2.5.2.a Using Design of Experiment Methods Different from Taguchi's Method

As this review continues, the popularity and efficiency of Taguchi's method of Design of Experiments (DoE) in parametric optimization will become apparent. However, to avoid any impulsive conclusion that Taguchi is the most effective method of DoE, other methods of design of experiments in conducting parametric optimization experiments should be considered.

In 2016, Pandhare *et. al*, [42] studied the effect of significant factors on the bending strength of weld joints prepared by Gas Metal Arc Welding. With the consideration of welding current, welding voltage and welding speed as variable process parameters, Pandhare *et. al.* [42] conducted experiments on weld joints of low carbon steel, medium carbon steel and die steels. They suggested that analyzes be done using Design of Experiment on ReliaSoft DOE++ software to determine the significant factors affecting the bending strength and of the weld joint, which at the time of execution, was a novel idea at least according to the authors. ANOVA was also employed in their parametric analysis. Their studies showed that welding voltage was the most significant factor affecting the bending strength of the weld joints and that welding speed and welding current do not individually have significant roles on the bending strength of the weld joints.

The use of ReliaSoft DOE++ software for the design of their experiments by Pandhare *et. al.* [42] is worth noting. In the course of reviewing the literature on parametric optimization, this software was hardly mentioned. Pandhare *et. al.'s* [42] work has opened the door for another proven design of experiment tool. Another group of scholars used a different design approach in their optimization experiment.

One of the more common design of experiments method is Response Surface Methodology (RSM). RSM involves the use of statistical and mathematical methods to model and analyze a given problem such that the interactions between the independent variables are studied and their effect on the output responses are quantified or even predicted. [43], [44]

Srivastava and Garg [44] adopted Response surface methodology to optimize process parameters in the MIG welding of 6mm mild steel plates. The selected factors for consideration were wire feed rate, voltage, gas flow rate and travel speed. Regression models were developed for Bead Height, Bead width and Depth of penetration. The developed models were tested using ANOVA and found to be adequate to a 95% degree of confidence level. Study design expert 9.0 was used to carry out parametric optimization using response surface methodology. This generated easy to read response surface plots where the effects of the input parameters on the output responses can clearly be read. The response surface plots are given in Figure 2-6, Figure 2-7 and Figure 2-8.

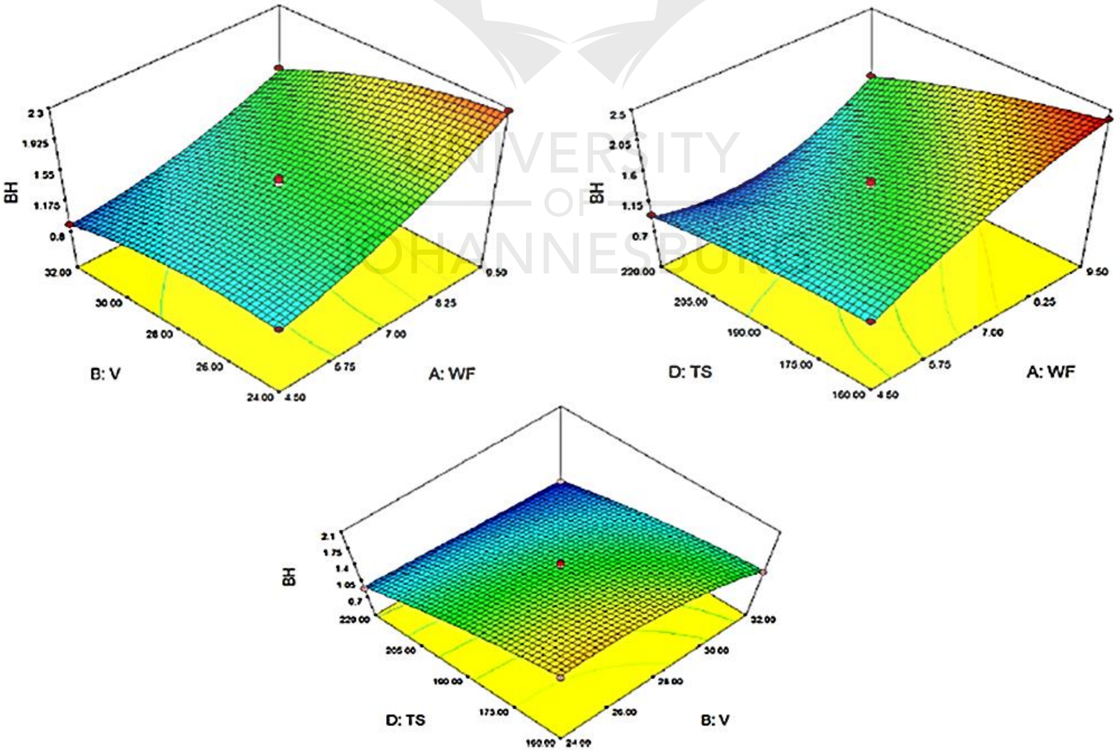

Figure 2-6: Combined effects of (A) Voltage and Wire Feed rate on Bead Height (B) Travel Speed and Wire Feed rate on Bead Height (C) Travel Speed and Voltage on Bead Height. [44]

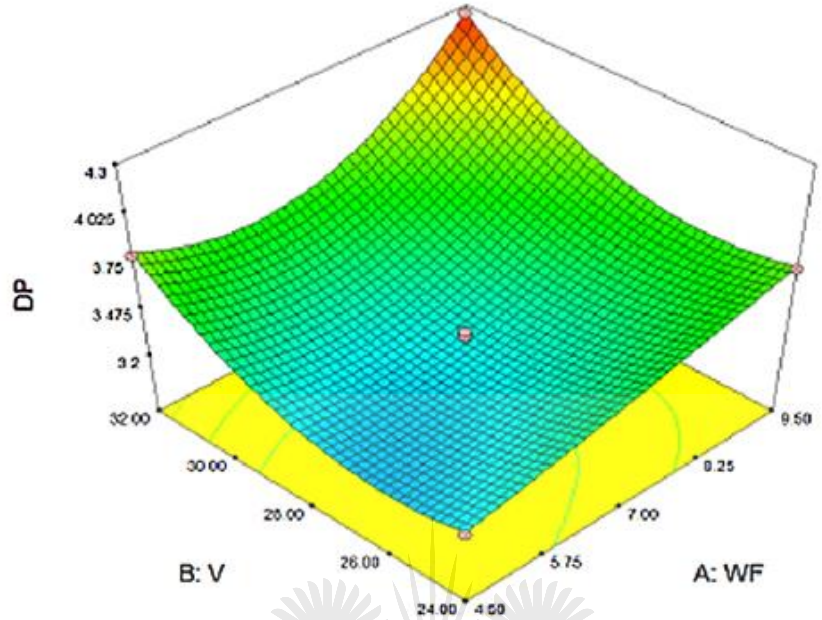

Figure 2-7: Combined effects of Wire Feed rate and Voltage on Depth of Penetration [44]

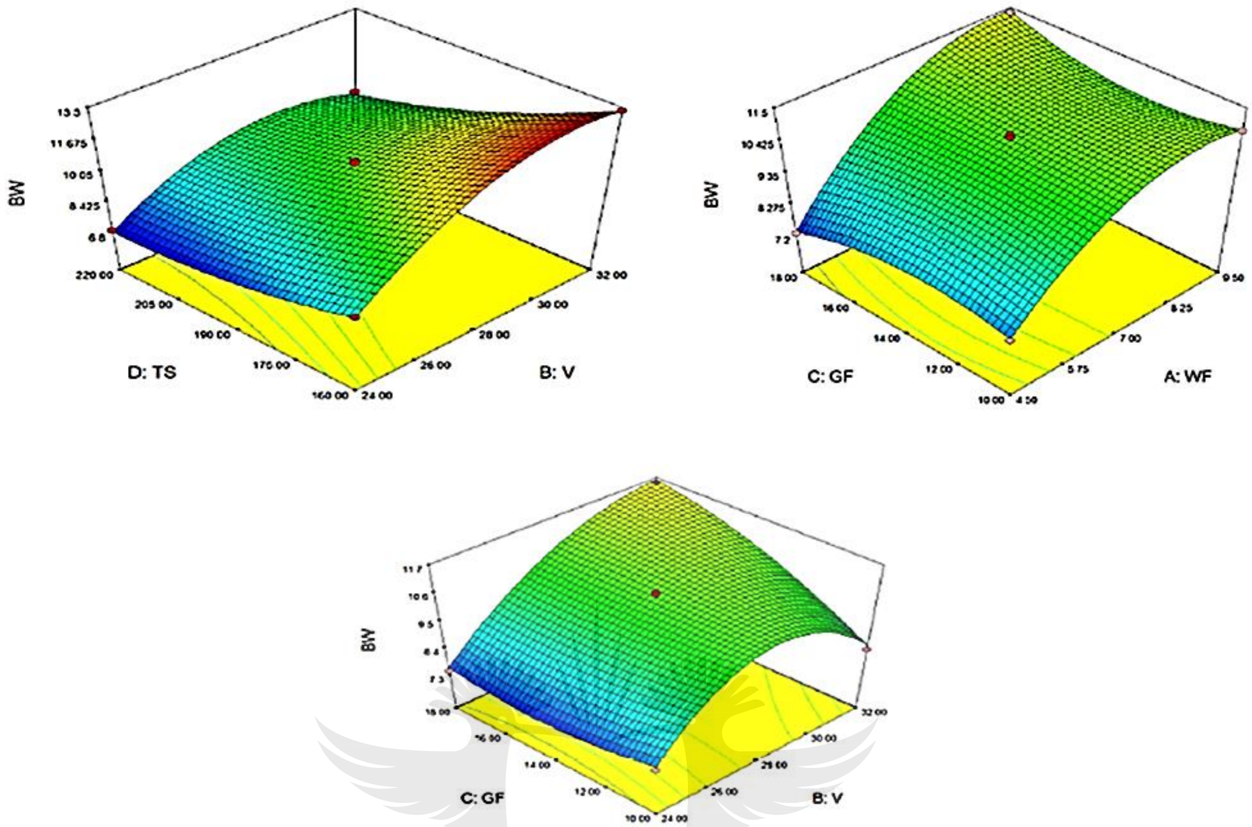

Figure 2-8: Combined effects of (A) Travel Speed and Voltage on Bead Width (B) Gas Flow rate and Wire Feed rate on Bead Width (C) Gas Flow rate and Voltage on Bead Width. [44]

Optimum values at wire feed rate 4.5 m/min, voltage 32V, gas flow rate 10.3 lpm, and travel speed of 160 mm/min were observed. These values gave optimum desired responses of bead height, bead width and depth of penetration. A confirmatory experiment was conducted using the derived optimum parameters. Figure 2-9, below compares the results; Figure 2-9a gives the experimental weld pool geometry while Figure 2-9b shows the predicted weld pool geometry. The confirmatory results were found to have less than 2% error when compared to the predicted results

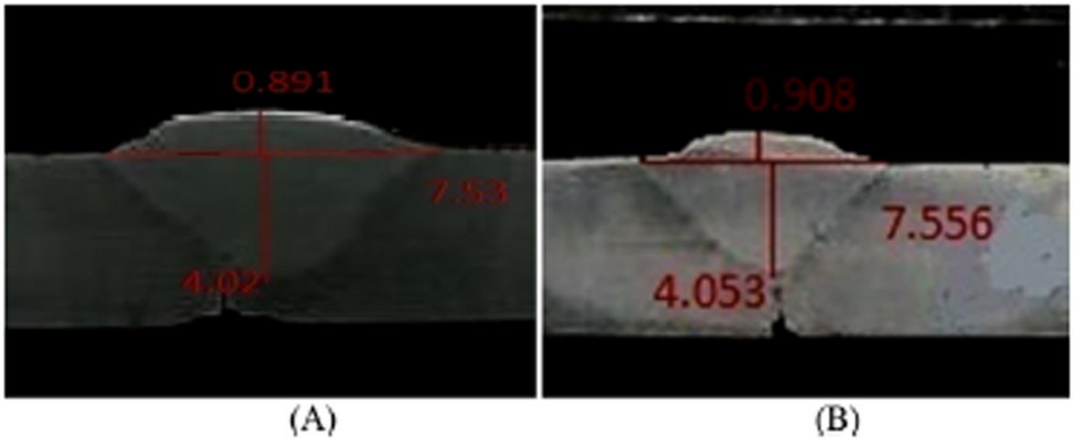

Figure 2-9: (A) Experimented vs (B) Predicted Results. [44]

Hooda *et. al.* [27] attempted to develop a response surface model to predict the tensile strength of MIG welded AISI medium carbon steel joints. They carried out experiments on a 4-factor, 3-level, face centred composite design matrix. The process parameters selected for the study were welding voltage, current, wire speed and gas flow rate. Response surface methodology was applied to optimize the process parameters to achieve maximum yield strength of the joint. Following a run of 28 experiments, Hooda *et. al.* [27] determined optimum parameters for the weld at 22.5 V, 190 A, 2.4 m/min and 12 l/min for welding voltage, welding current, wire feed rate and gas flow rate respectively. These optimum parameters produced a weld joint with a maximum transverse yield strength of 374.57 MPa and maximum longitudinal yield strength of 398.9 MPa. The authors finally concluded that longitudinal yield strength was always higher than the transverse yield strength.

Response surface methodology was also used by Shukla and Phafat [45] in their work. They investigated the effect of welding parameters on CO_2 arc welding with a view to maximizing weld strength for AISI 1022 steel plates. They adopted Response surface methodology for this experiment. They considered welding current, welding voltage, wire feed rate and gas pressure as selected input parameters. It was discovered the square of the wire feed rate (R^2) is directly proportional to the quality of the weld. Welding current, voltage and gas pressure were considered significant terms as well, in maximizing the weld strength.

It should be noted that both Hooda *et. al.* [27] and Shukla and Phafat [45] worked on very similar specimens using the same welding process and design approach. The optimum parameters derived by Hooda *et. al.* [27] can be easily combined with Shukla and Phafat's [45] discovery on the effect of wire feed rate in any experimental work on the MIG welding of medium carbon steel plates.

Another design approach was adopted by Singla *et. al.* [46]. They used the Factorial Design Approach to investigate the optimization of process parameters of Gas Metal Arc Welding Processes. The parametric variables considered for the study were welding voltage, welding current, welding speed and nozzle to plate distance. They carried this out by developing a mathematical model for sound weld deposit area of a mild steel specimen. Using the factorial design approach to establish a relationship between various process parameters and weld deposit area, the study showed that increase in welding voltage and nozzle to plate distance directly resulted to an increase in the weld deposit area. On the other hand, the weld deposit area was shown to reduce with a corresponding increase in welding current and welding speed.

A number of other scholars conducted parametric optimization experiments without necessarily defining their design of experiment method but still conducted research without using Taguchi's methods. Some of these scholars include Ibrahim *et. al*. [47]

Ibrahim *et. al.*, [47] in their study of different parameters on welding penetration, microstructural and hardness measurement in mild steel, conducted an experiment using robotic gas metal arc welding. They specifically picked arc voltage, welding current and welding speed as variable parameters and conducted a total of twenty-seven (27) experimental runs to determine how these variables affected the quality of the weld. They found out that an increase in welding current corresponded to an increase in the value of depth penetration. They also concluded that both arc voltage and welding speed also influenced the value of depth penetration. There was a clearly noticeable increase in penetration with an increase in welding speed for each voltage category. Also, a slight decrease in penetration was recorded as voltage values were increased.

Consequently, the highest value of penetration was achieved at 22V and 210 A for all selected speeds of 20, 40 and 60cm/min. With regards to hardness, Ibrahim *et. al.* [47] showed that higher values of hardness were observed at a voltage of 26V, current of 90A and welding speed of 60cm/min. They concluded that this occurred because the higher speeds at medium voltage reveal the best formation of martensite grain. Microstructurally, the grain boundaries were shown to change for bigger to smaller sizes when the welding parameters were changed. For some given parameters of welding current and welding voltage at 210A and 22V respectively, the microstructural grains were shown to reduce in size as welding speeds increased.

A few scholars have even employed computer modelling software to conduct parametric optimization as Harshal *et. al.* [48] have shown. They used finite element modelling to predict residual stresses in MIG welding. They achieved this by using the finite element software ANSYS. In their study, Harshal *et. al.* [48] investigated the effects of varying heat input and welding speed on the thermal-mechanical properties of the weldment after the specimens were cooled to room temperature. The authors concluded that strain changes corresponded to heat input changes. They discovered that as heat input increases, the temperature in the plates build-up, resulting in a decrease in stresses generated. Finally, their study showed that the faster the welding speed, the less heat is absorbed by the base material and consequently induced stresses decrease.

2.5.2.b Taguchi's Orthogonal Array Method

Now that it has been shown that parametric optimization can be successfully carried out with various experimental design methods to improve the quality of steel welds, a closer look at scholars who employed Taguchi's design method will follow. But first, it is important to understand what Taguchi's method really is.

Taguchi's method is an alternative to the classical statistical experimental design, where each variable factor is investigated one at a time, by keeping other variables constant. The statistical experimental design leads to conducting many experiments. Taguchi's method allows for a more efficient way to conduct experiments. Pipavat *et. al.* [49] took the time to explain the use of Taguchi's method.

They explained that Taguchi's method makes use of a special design of orthogonal arrays to study the entire process parameter space with a small number of experiments, as opposed to the classical statistical experimental method. Taguchi Technique has become a powerful tool for improving productivity during research and development so that high-quality products can be produced quickly at low cost [50]. Dr Taguchi of Nippon Telephones and Telegraph Company, Japan, is credited with developing this technique [50] [51]. The technique is based on predefined orthogonal arrays which are adopted for experiments with much-reduced variance and optimum settings of control parameters [50].

These orthogonal arrays help designers to study the effect of multiple controllable factors on the average of quality characteristics and variations in a fast and economical way. It also employs the signal-to-noise ratio to analyze the experimental data, from which designers can select optimum parametric combinations. Taguchi's method adopts the use of a loss function to determine the deviation of the quality characteristic from the desired value. This is used to determine the S/N ratio. A larger S/N ratio usually corresponds to a better-quality characteristic [43].

There are three categories of quality characteristics in the analysis of S/N ratio. They are: the lower-the-better, the larger-the-better and the nominal-the-better.

The required category is dependent on the output response characteristic in consideration. In using Taguchi's method, analysis of variance (ANOVA) is used to determine which of the process parameters are statistically significant. Taguchi's method requires that a confirmatory experiment should be conducted after optimum parameters have been determined [40].

There are some critics of Taguchi's Orthogonal Array method. One of the main criticisms of Taguchi's method is that it does not test all the variable combinations since it adopts an orthogonal array. The method has therefore been criticized for its difficulty in accounting for interactions between parameters. One other limitation is that Taguchi's methods are done offline and are consequently inappropriate for a dynamically changing process such as a simulation study. This limitation is responsible for applying Taguchi's methods mostly at the early stages of a design process since the method deals with designing for quality rather than correcting poor quality [51]

Notwithstanding, Taguchi's design of experiment method has proven to be largely successful in the optimization of process parameters for various types of welding processes. Esme [40] and Kishore *et. al.* [38] notably validated the use of Taguchi's method for the optimization of process parameters in welding, after confirming the predicted optimum parameters experimentally and getting improved output responses.

A closer look at various scholars who adopted Taguchi's design of experiments methods in parametric optimization of MIG welding is vital to this study. Several researchers specifically studied welding current, speed and voltage exclusively as parametric variables, to determine their effect on the mechanical properties of various forms of steel.

2.6 **Scholarly Works on Parametric Optimization using Taguchi's Method**

Pipavat *et. al.* [49] and Sapakal and Telsang [50] in their separate works, selected welding voltage, welding current and welding speed as the three parameters to be studied. They set out not only to optimize the parameters but to determine which of the parameters contributed most significantly to the desired mechanical property.

Pipavat *et. al.* [49] studied the influence of welding parameters on the mechanical properties of austenitic stainless steel. In their work, Taguchi's method was adopted to optimize parameters as well as analysis of variance (ANOVA), to determine the contribution of each factor. According to their research, welding current had the highest contributing factor for tensile strength, with a percentage contribution of 50.16%. The optimum process parameters were put at 32 V for voltage, 180 A for current and 300 mm/min welding speed.

Sapakal and Telsang [50] studied the optimization of welding parameters for MIG welding by employing Taguchi's Design of Experiment method. They also studied the influence of welding parameters such as welding current, welding voltage and welding speed on the depth of penetration of Mild Steel C20. Sapakal and Telsang [50] successfully carried out experiments based on Taguchi's Orthogonal Array design method combined with the signal to noise (S/N) ratio and analysis of variance to investigate and optimize welding parameters. It was well noted that Taguchi's Design, combined with the S/N ratio and ANOVA successfully predicted the optimum parameters required for MIG welding of C20 steel. A confirmatory experiment was carried out in line with the predicted parameters from Taguchi's design and improvement of S/N ratio on initial parameters was 2.13. This confirmed that Taguchi's optimization method did, in fact, help to improve weldability. The confirmatory experimental values obtained from optimal welding parameters arrived at through Taguchi's method gave penetration of 5.25 mm and S/N ratio of 14.40. These values were close enough to the predicted optimum values of 6.45 mm and 16.19 for penetration and S/N ratio respectively.

Sapakal and Telsang's [50] work also showed that welding voltage was the highest contributing factor to the penetration of the mild steel C20 specimen. This discovery can be compared with

Ibrahim *et. al.*'s [47] work which has been discussed earlier. First, it should be noted that both Ibrahim *et. al.* [47] and Sapakal and Telsang [50], worked on mild steel. However, while Ibrahim *et. al*. [47] appears to conclude that welding current played the most significant role in weld penetration, on the other hand, Sapakal and Telsang [50] submit that welding voltage had the highest contributing factor of 84.4 %.

It is fairly obvious that Sapakal and Telsang's [50] submission is the more accurate of the two. This is because they obtained their conclusion through the analysis of variance (ANOVA), while Ibrahim *et. al.* [47] made their submission by merely observing data results, where they kept the voltage constant at each level, and increased current to see its effect on penetration. In other words, Ibrahim *et. al.* [47] experiment could not sufficiently confirm which factor contributed the most to weld penetration. By going through their work, there is a tendency to conclude that current is the most significant factor, however, Sapakal and Telsang's [50] work gives us clarity on this matter thanks to Taguchi's method and the use of ANOVA.

In 2015, Patil and Kavade [52] carried out parametric studies on the effect of current, voltage and welding speed on the tensile strength of S355J2N steel material. Using the popular Taguchi method by employing an L9 orthogonal array, calculating the signal-to-noise ratio to obtain optimum levels for each input parameter and determining the significant coefficients for each parameter with ANOVA, the parametric effects on tensile strength was defined. They concluded that tensile strength increases with a corresponding increase in voltage. Their work also showed that there is a corresponding increase in tensile strength with an increase in welding current and speed, but only up an optimum level, after which a decrease in tensile strength follows. The optimum values for current, voltage and speed, were given as 200A, 26V and 5.5 IPM respectively.

While Patil and Kavade [52], Sapakal and Telsang [50], and Pipavat *et al.* [49] all worked on different materials of S355J2N Steel, Mild Steel C20 and austenitic stainless steel respectively, a common thread is seen in all three works, that welding speed has little effect in the chosen mechanical properties. As a matter of fact, only Pipavat et. al. [49] shows welding current to play a key role in the tensile strength of austenitic stainless steel. The other two authors show voltage to be the key determining factor for mechanical properties in their respective chosen steel materials. However, it remains to be seen if this trend continues in other works.

In 2014, Utkarsh *et. al.* [53] studied the effect of current, arc voltage, gas flow rate and welding speed on the Ultimate Tensile Strength of st-37 low allow steel material. The experiments were designed using an L9 orthogonal array, after which confirmatory experiments were conducted. Utkarsh *et. al.*'s [53] work concluded that arc voltage had the most effect on the tensile strength of the specimen. This conclusion was based on results gotten from ANOVA. Welding voltage gave a contributing factor of 86.2%, which was followed very closely by welding speed of 84.1 %, then welding current with 78.6%. The scholars successfully conducted a confirmatory test using optimum parameters of 110 A for current, 22 V for voltage, 5.5 m/min for wire feed rate, and 9 l/min for gas flow rate. This experiment yielded a maximum ultimate tensile strength of 454.25 N/mm^2.

Once again, we see voltage playing a major role in the tensile strength of ST-37 low alloy steel. However, it must be noted that in this work welding speed and welding current are shown to contribute substantially as well, with values of 84.1% and 78.6% respectively. The significant contribution of welding current in Utkarsh *et. al's* [53] work contrasts with the less significant role welding current plays in Patil and kavade [52], and Sapakal and Telsang's [50] works earlier discussed. This suggests that the percentage contribution of parameters is mostly down to the composition of the base metal to be welded.

Other scholars have worked on varying other parameters along with voltage, current and speed, and have succeeded in obtaining optimum process parameters. One of these works includes the study carried out by Raut and Shelke [32] who undertook an investigation to find the design optimization for special purpose MIG welding. They worked on the effects of welding current, welding voltage, welding speed, gas flow rate, the rotational speed of workpiece and filler wire feed rate on MIG welding. Raut and Shelke [32] adopted Taguchi's method of experimental design. Consequently, they employed an orthogonal array, signal to noise (S/N) ratio and analysis of variance to determine welding characteristics and optimization parameters. They showed that improvement of S/N ratio was 2.13. The experimental value observed from optimal welding parameters gave a good penetration value of 5.23 mm.

Raut and Shelke [32] are not alone in their optimization of gas flow rate. Rajagopal *et.al.* [54] investigated the effect of voltage, wire feed rate and gas flow rate in the gas metal arc welding of AISI 1042 Steel. The work was done with the view to optimize these parameters to produce welds of high strength and hardness. Taguchi's methods were adopted for experimental analysis. Rajagopal *et. al.* [54] concluded from their work that welding voltage most significantly affected the process. The optimum values obtained from the experiment were 26 V, 3.4 m/min and 14 l/min for voltage, wire feed rate and gas flow rate respectively. A confirmatory test was carried out which yielded 700 N/mm^2 for tensile strength and 76 HRC for hardness.

Despite successfully optimizing values for gas flow rate in their work on AISI 1042 Steel, Rajagopal *et. al.* [54] still concluded that welding voltage had the most significant contribution to the process. However, contrary to these works that put welding voltage in the forefront of determining factors, Dinesh *et. al.* [55] in their work showed welding current to also be the most significant contributing factor.

Dinesh *et. al.* [54], in their paper on parametric optimization of MIG process parameters using Taguchi's and Grey analysis also studied grey analysis method for operating parameters for alloy steel. They concluded that higher penetration was directly proportional to weld strength. They also concluded that the most significant factor in MIG welding of steel is the welding current. It should be noted that other parameters like wire diameter, arc voltage, welding speed and gas flow rate were studied in this work. This study was done to derive optimum parameters for achieving desired results in tensile strength, bead width, bead height, penetration and heat-affected zone.

Another set of scholars included the optimization of wire feed rate and nozzle distance to their process. Meshram and Pohokar [56], used Taguchi's optimization technique along with grey relational analysis to carry out studies on the effect of process parameters on penetration, reinforcement and bead width in GMAW process of stainless steel. They considered voltage, wire feed rate, welding speed, nozzle to plate distance and gas flow as variable parameters. Using analysis of noise (S/N) ratio, Meshram and Pohokar [56] obtained optimum welding parameters for every input factor in the GMAW of stainless steel, which had dimensions 70 mm x 25 mm x12 mm thickness. Analysis of Variance (ANOVA) was employed to check the adequacy of the developed model and significant coefficients for each input factor on weld bead geometry were determined.

Also, Kocher *et. al.* [57] in their experimental analysis in MIG welding considered welding speed as a variable process parameter while leaving other parameters such as arc voltage, welding current, wire feed rate, and distance between the nozzle and the plates as fixed parameters. The effects of weld speed on the weld bead profile, fusion angle and wetting angle were discussed. The effect of weld speed on penetration and reinforcement areas was also discussed.

Singh [51] investigated the optimum parameters required for mild steel AISI 1016 in gas metal arc welding, using Taguchi’s method. This also included the use of an orthogonal array, signal to noise ratio and analysis of variance. An interesting part of this study was the effect of the welding gap position on the tensile strength of the weld joint. Singh [51] showed that welding gap position had a contribution of 67.05% to the tensile strength of the weld joint ahead of gas flow rate and arc voltage, with contributions of 15.3% and 10.6% respectively. A confirmation experiment was conducted, and the validity of Taguchi’s optimization method was established.

Singh’s [51] work showed how parameters such as welding gap position, though typically overlooked, had a significant influence on the tensile strength of the weld. Two other works draw attention to other parameters that have a significant effect on the mechanical properties of steel welds but haven’t quite received as much attention.

Firstly, Pal [28] presented the effect of different welding parameters on the strength of weld joints and the elongation produced during tensile tests. The parameters considered in his study were welding voltage, filler wire rate and v-butt angle. Taguchi’s orthogonal arrays were adopted, alongside ANOVA to predict the percentage effect of each parameter on results. The welding material used was medium carbon steel slabs. An L9 array was designed to carry out the experiment. Pal’s [28] work showed that v-butt angle was the highest contributing factor to the Ultimate tensile strength and percentage elongation of the specimens. This is a noteworthy experimental result considering many other research works didn’t take the v-butt angle into account. Pal [28] obtained optimum values for tensile strength at 5.2 m/min wire feed rate, 35 V arc voltage and 70^0 v-butt angle.

While Pal [28] has drawn attention to the effect of v-butt angle, Rakesh [58] conducted a study to determine the most significant parameter between welding current, welding voltage and root gap in the MIG welding of mild steel 1018 grade by adopting Taguchi’s method and analysis of variance (ANOVA). The mechanical properties observed in the study were hardness and tensile strength of the specimens. The study made use of an L9 orthogonal array to carry out the experiments. The work showed that the root gap had the greatest effect on the tensile strength of the specimen with a percentage contribution of 38%, which was followed by a welding current with 32%. For hardness, arc voltage gave the highest contribution with 62%, followed by the root gap with 28%. Welding current showed to have the least effect on both tensile strength and hardness. The highest tensile strength obtained in the experiment was 482.2 N/mm^2 at 180 A, 35 V and root gap of 4 mm. The maximum hardness was obtained at 180A, 40V and root gap of 3 mm.

All these scholars have shown without a doubt, that using Taguchi's method of parametric optimization to achieve optimum output characteristics is reliable. Their various works, done on various materials, and other various conditions prove that Taguchi's method is a powerful tool for improving the mechanical properties of steel welds.

This review thus far has heavily addressed the success associated with the optimization of parameters to improve the mechanical integrity of steel welds. However, researchers have come up with other innovative methods to improve weld integrity. A number of these methods will be discussed in the next section.

2.7 Other Methods of Improving Weld Joint Integrity

Taguchi's methods have proven successful over the decades as a resourceful tool in improving the mechanical properties of weld joints. In this section, however, alternative means of weld integrity improvement are considered.

Ramakrishna *et. al.* [34] undertook an extensive review on developments of other technologies to improve weld integrity. They first considered the adoption of Post Weld Heat Treatment to improve the mechanical properties of joints. Ding *et. al.* [59] and Ahmed *et. al.* [60] had adopted this method on aluminium alloy joints and Chromium-Molybdenum welded joints respectively with considerable success. Ibrahim *et. al.* [61] applied PWHT on gas metal arc welded joints to improve the mechanical properties of duplex stainless steel. Ahmad *et. al.* [62] applied PWHT to AA6661 welded joints to successfully enhance its tensile strength and hardness. He recorded a 3.8% increase in tensile strength and a 25.6% increase in hardness for the welded joints. An *et. al.*[63] also successfully adopted PWHT in the laser-welded joint of stainless steel and significantly improved the hardness and tensile strength of the joints. These are just a few researchers amongst others mentioned in Ramakrishna *et. al.'s* [34] review on the subject.

The second proposed solution to improve the mechanical properties of welded joints given by Ramakrishna *et. al.* [34] was the use of Pulsed Current. Ramakrishna *et. al.* [34] explained pulsed current welding as a process of “pulsing” the current during the welding process. They explained that this method was useful in controlling the metal transfer at low mean current levels by imposing short durations of high current pulses. This is said to improve the mechanical properties of the weldments and is confirmed by several scholars.

For instance, Mao *et. al.* [64] used this technique their work with Gas tungsten welds of titanium matrix composites. They noticed an improvement in hardness, tensile strength and ductility in pulsed current gas tungsten welds compared to non-pulsed current welds.

Balasubramanian *et. al.* [65] found out that pulsed current welding in both gas tungsten arc welding (GTAW) and gas metal arc welding (GMAW) led to an increase in tensile strength when compared to conventional continuous welding. These scholars were convinced that this was due to the fine grain structure attained in pulsed current welding.

While Raveendra and Kumar [66] discovered an improvement in the hardness of welded joints produced with pulsed current, they also noted that tensile strength was found to have decreased when a pulsed current was applied on stainless steel sheet SS304.

Hybrid welding was the next solution proffered by Ramakrishna *et. al.* [34] According to Ramakrishna *et. al.* [34], hybrid welding combines the principles of one type of welding to another type of welding to enhance the properties of the weldments. Ramakrishna *et. al.* [34] pointed out three main types of hybrid welding which are; TIG laser welding, Plasma arc-laser welding and MIG augmented-laser welding.

Numerous scholars including Dai *et. al.* [67] have adopted hybrid welding techniques with considerable success. Dai *et. al.* [67] discovered an improvement in tensile shear strength of a weld joint between 1 mm thick Mg AZ31B and A16061 alloy sheets when gas tungsten arc welding – assisted hybrid ultrasonic seam welding was carried out. Another set of scholars, Leo *et. al*. [68] in their investigation into hybrid-laser arc welding of Al-Mg alloy welded joint, discovered that tensile strength and microhardness increased when welding voltage and current were decreased.

Li *et. al.* [69] discovered a 90% improvement of the shear strength of T-joints of base metal in the hybrid welding of laser-gas tungsten arc welding when compared to joints produced with only laser welding or only gas tungsten arc welding.

Despite the well-documented improvements of the mechanical properties of weld joints by employing Post Weld Heat Treatment, Pulsed Current welding and Hybrid welding, Ramakrishna *et. al.* [34] did not fail to point out some drawbacks commonly associated with these methods. They listed these drawbacks as follows;

Firstly, Post Weld Heat Treatment requires special tools and consumes more time when compared to other methods. Secondly, high pulsed current reduces the mechanical properties of welded joints compared to low pulsed currents. It was pointed out that if the thickness of the sheet is increased mechanical properties of the weld joints are known to be reduced as a result. Thirdly, in hybrid welding, many parameters must be carefully adjusted otherwise there is a risk of reducing the strength of the joint.

These drawbacks clearly show that these techniques are not straightforward and would require a mastery of proper welding skills to successfully utilize them. To counter these drawbacks, Ramakrishna *et. al.* [34] finally suggest adopting Vibratory welding as a method of improving the mechanical properties of weld joints.

In vibratory welding, mechanical vibrations are given to the weldments with a periodical force during the welding operation. This method is said to have advantages over PWHT, pulsed current and hybrid welding due to its flexibility in use, less manufacturing time and the absence of environmental pollution.

Because of these factors, Ramakrishna *et. al.* [34] claim that vibratory welding techniques have been implemented effectively with varying degrees of success. A vibratory set up was used by Singh *et. al.* [70] to improve the mechanical properties of mild steel butt welded joints in shielded metal arc welding (SMAW). The idea of introducing vibrations to the setup is to stir the molten weld pool before solidification takes place. A vibratory wave with a resonance frequency of 300Hz and amplitude of 0.5 mm was transmitted to the weld pool. Figure 2-10 is the graphical representation of the welding set up;

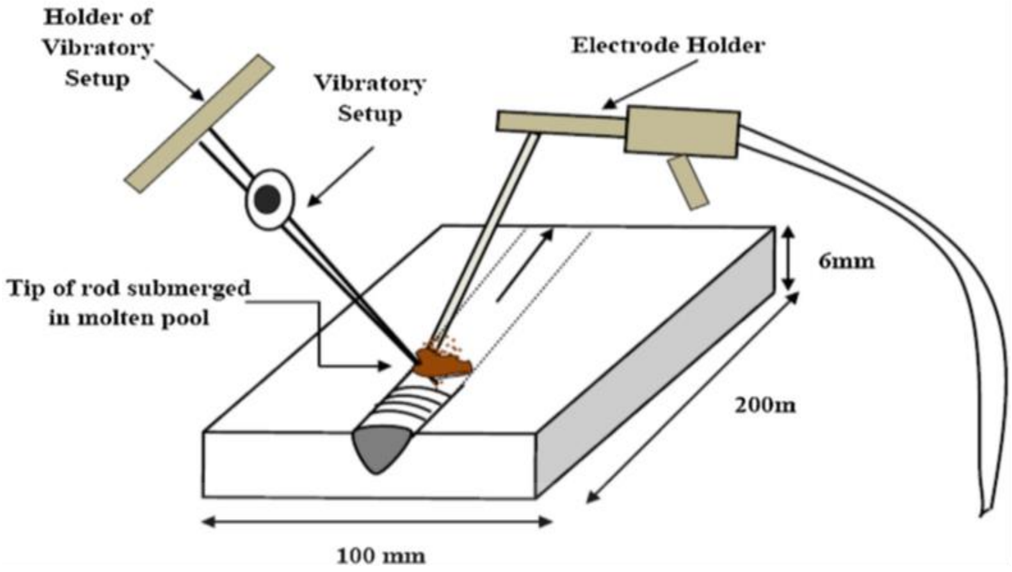

Figure 2-10: Vibratory welding set up for SMAW of mild steel plates [70]

The process parameters were optimized for output responses of yield strength and microhardness, using Taguchi's method. The study showed an increase in the microhardness of the weld metal. A small motor was used to introduce vibration into the system, this was conceived using the principle of rotation of an unbalanced motor. An offset weight was attached to the drive shaft of the motor, which rotates when the motor was switched on, thereby causes resonance and delivers vibrations in the weld pool. This simple but ingenious idea was preferable to other vibratory techniques because it is very efficient. The optimized parameters were welding current, welding speed and frequency. The frequency of vibration gave the highest contribution to both hardness and yield strength values with percentage contribution of 90% and 95% respectively. The yield strength was found to be maximum at a current of 110 A, welding speed of 8 cm/min and induced vibration of 250 Hz [70]. The vibration was directly responsible for causing fine grain structures in the weld pool by inhibiting the solidifying dendrites and forming new nucleation sites and was also responsible for the increase in microhardness [70]. A direct relationship between the increase in vibration frequency and consequent increase in yield strength was identified [70]. This was also due to the fine grain structures produced because of the induced vibrations [70]. The S/N ratio effect plots are shown in Figure 2-11 and Figure 2-12;

Figure 2-11: Main effects plot for S/N ratios of Hardness of mild steel plates subjected to vibratory welding [70]

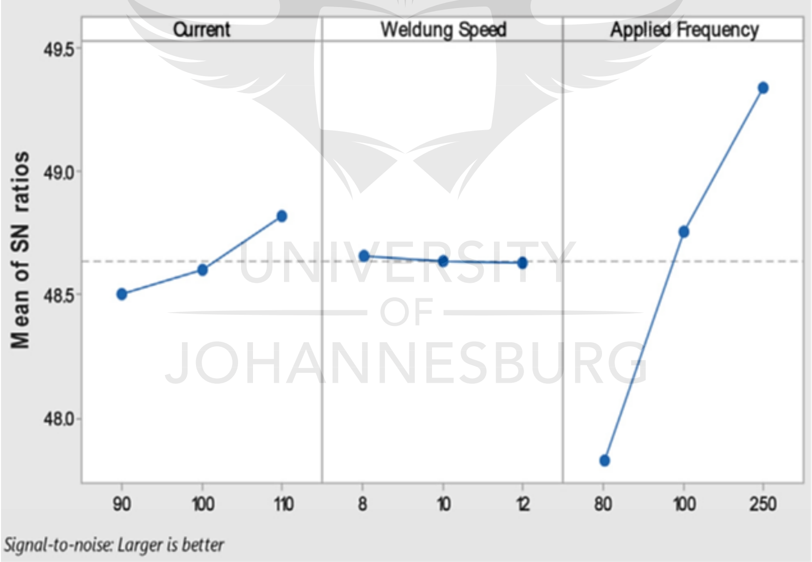

Figure 2-12: Main effects plot for S/N ratios of Yield strength of mild steel plates subjected to vibratory welding [70]

The main effects plots clearly show that the introduction of vibration to the weld pool of the materials significantly affected the mechanical properties of the material.

Vibrations were applied during submerged arc multi-pass welding to improve the quality of welded valves [71]. There were significant reductions in residual stresses and welding deformation when vibratory welding techniques were applied. There was a 21% increase of the Charpy v-notch impact toughness in the weld metal region and a 0.9% decrease in the HAZ [71]. There was a substantial improvement in the microstructure of the welded specimens as the vibratory energy significantly reduced the broke up the growth of dendritic grains in the weld and HAZ [71]. The vibrations contributed to a higher cooling rate and smaller grain size which generally improves mechanical properties [71].

In their review, Ramakrishna *et. al* [34] also discussed the proposition of Dynamic solidification technique during welding to kick-start the vibrations especially during the welding of butt-welded joints. They noted that there is a presumption that butt-welded joints arranged under vibratory conditions had high hardness with no loss of ductility. However, no specific work was discussed in this regard by Ramakrishna *et. al.* [34]

Ramakrishna *et. al.* [34] concluded their report by strongly advocating for the use of vibratory assisted welding as it was more advantageous over the other discussed techniques. They, however, remarked that more research will need to be done to firmly establish the influence of vibratory parameters on the mechanical properties of weldments.

This review conducted by Ramakrishna *et. al.* [34] opens the door for more research and developments of these methods amongst others. There are other innovative suggestions to improve properties of steel welds, one of which is submitted by Ambroza *et. al.* [72]

Ambroza *et. al.* [72] analyzed the microstructure and properties of the steel metal obtained in welding and overlaying welding using waste material. In other words, they set out to determine the effect of waste materials elements on the weld. The scholars concluded that the use of waste material powders in the welding process due to alloying elements in the powder allows for the production of weld joints with required microstructure and properties. For instance, their work showed that welds produced using glass powder or glass and cast-iron powder mixture have a higher tensile strength than the main metal. To further prove this, their study showed that Cт3 steel subjected to overlaying welding with 60% P6M5 chips, 20% grinding wheel SiC and 70% Fe-70% Mn powder mixture in comparison with hardened tool steel (0.9% C; 1.5% Cr) was 3-4 times more abrasive wear-resistant.

In another work, Singh *et. al.* [73] evaluated the effects of CaF_2, FeMn and NiO additives on impact strength and hardness of low carbon steel plate welds using submerged arc welding. In the study, fluxes containing CaO, SiO_2 and Al_2O_3 as base fluxes were designed and developed through agglomeration technique. Afterwards, CaF_2, FeMn and NiO were added to these fluxes in varying amounts. Results showed that CaF_2 and FeMn significantly affected the impact strength of the welds while the interaction of CaF_2 and NiO significantly affected the hardness of the weld. This work gives us an insight into the addition of suitable materials to improve the mechanical structure of steel welds.

The addition of suitable materials to the welding of steel materials was also explored by Lin *et. al.* [74] who studied the influence of Titanium on weld microstructure and mechanical properties in large heat input welding of high strength low alloy steel. The work showed that moderate amounts of Titanium are effective for grain refinement. They, however, remarked that the toughness of the weld metals severely reduces when Titanium content is over the optimum range of 0.028% - 0.038%. It has already been shown that applying moderate amounts of titanium powder in the welding of high strength low-alloy steel improved grain refinement [74]. A practical way of introducing titanium powders in submerged arc welding has already been carried out and proven to improve arc efficiency, deposition rate and productivity, while also reducing consumption of shielding flux [75].

Perhaps even more enlightening is the adoption of the idea of introducing titanium powder into steel welds by Kathuria and Gupta [41] in 2016. Their work has been discussed earlier in this review. Their success in introducing titanium powder to the steel welds of mild steel plates to improve tensile strength strongly suggests the potential of titanium alloy powder in improving steel weld integrity. It is also worth considering the properties of titanium alloy powder, to see how it can potentially weld joint integrity.

2.8 **Microstructure of Steel**

2.8.1 **Iron**

Steel is primarily an alloy of iron and carbon, commonly containing other alloying elements such as nickel, manganese, chromium, vanadium, molybdenum amongst others, depending on the required properties of steel [19]. To understand the microstructure of steel, we must first understand that of its primary material; iron.

There are three common allotropes of iron which occur naturally in bulk form; There is the Body-centred cubic α-iron which is also known as Ferrite. There is the Face-centred cubic γ-iron which is also known as Austenite. Thirdly, there is the Hexagonal-closed packed ε-iron [76].

The phase diagram of iron is given in Figure 2-13 below;

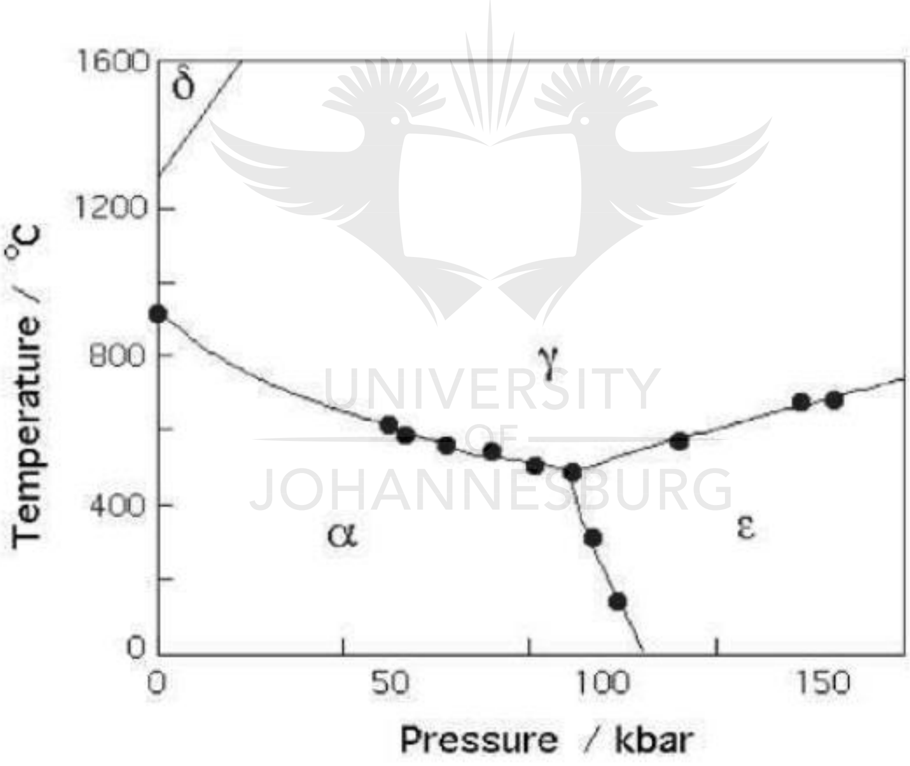

Figure 2-13: Phase diagram of Iron [77]

Iron, at ambient temperature, is in the form of α-iron (ferrite) and remains stable as the temperature increases up to 910 ^{0}C (A3 point). At this point, it transforms into γ-iron (austenite). Austenite reverts to ferrite at 1390 ^{0}C (A4 point) [77]. However, ferrite at this temperature is usually called δ-ferrite. Notwithstanding, δ-ferrite still possesses the same crystal structure as α-iron. δ-ferrite remains in a stable phase until melting occurs at 1536 ^{0}C [78].

2.8.2 Steel – Phases and Microstructure

The microstructure of a crystalline material refers to the type, shape, structure and topographical arrangement of phases and lattice defects which are mostly not related to the thermodynamic equilibrium structure [79]. In a metallic material, the microstructure depicts the distribution and topological arrangement of phases, grains, interfaces and other defects [80]. The alloy chemistry and processing history of a metal are directly responsible for its microstructure. Furthermore, the microstructure determines the properties and performance of the metal or any other material made from it [80]. In view of this, the most common microstructures related to steel will be discussed.

Majority of steels rely mostly on the ferrite and the austenite phases of iron. The many varieties of microstructures in steels is largely due to the α↔γ allotropic transition which can occur in numerous ways, where the atoms move to create changes in the crystal structure [81]. The transformation from one phase to another occurs primarily via two mechanisms. In reconstructive transformation; all the atomic bonds are broken and rearranged into different patterns. During displacive or shear transformation, the original atomic pattern is homogenously deformed into a new crystal structure [77].

All phase transformation in steel can be explained using these two forms of transformation. Figure 2-14 summarizes the various phases that could arise due to these transformations in steel; the decomposition of austenite.

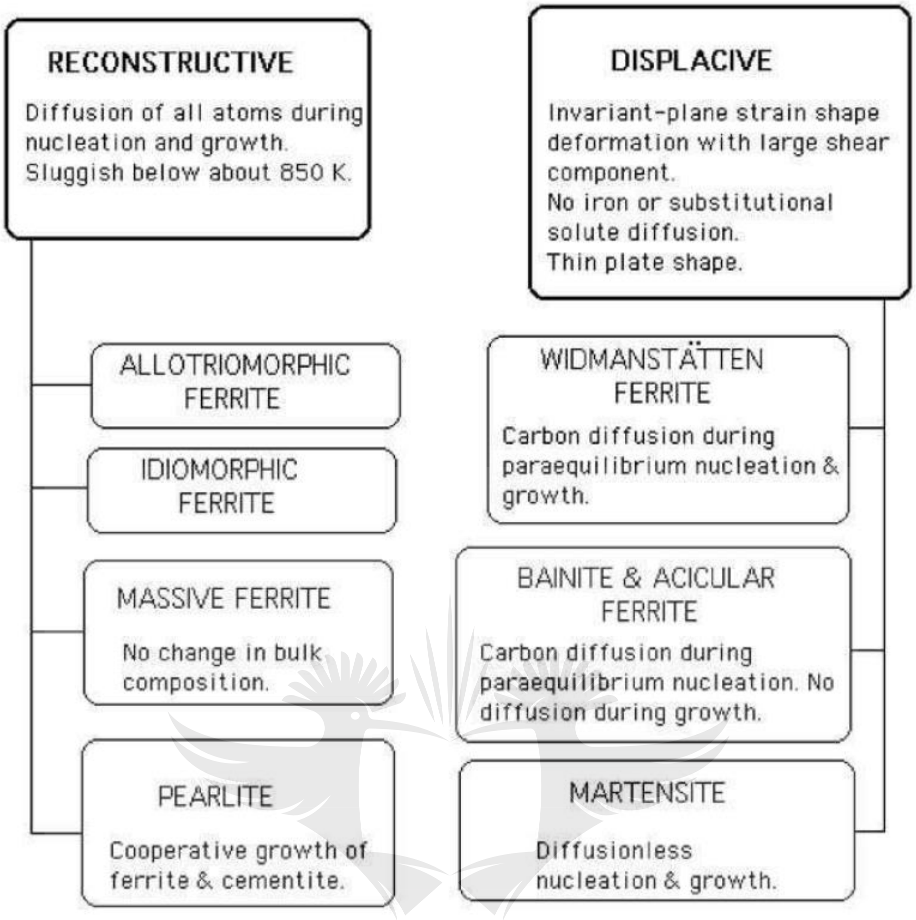

Figure 2-14: summary of phases generated by the decomposition of austenite via reconstructive and displacive transformations [77]

The phase transformations that occur in steel materials is best explained in the Carbon-Iron Equilibrium diagram (Figure 2-15). The basic features of this diagram are known to influence the behaviour of even the most complex alloys.

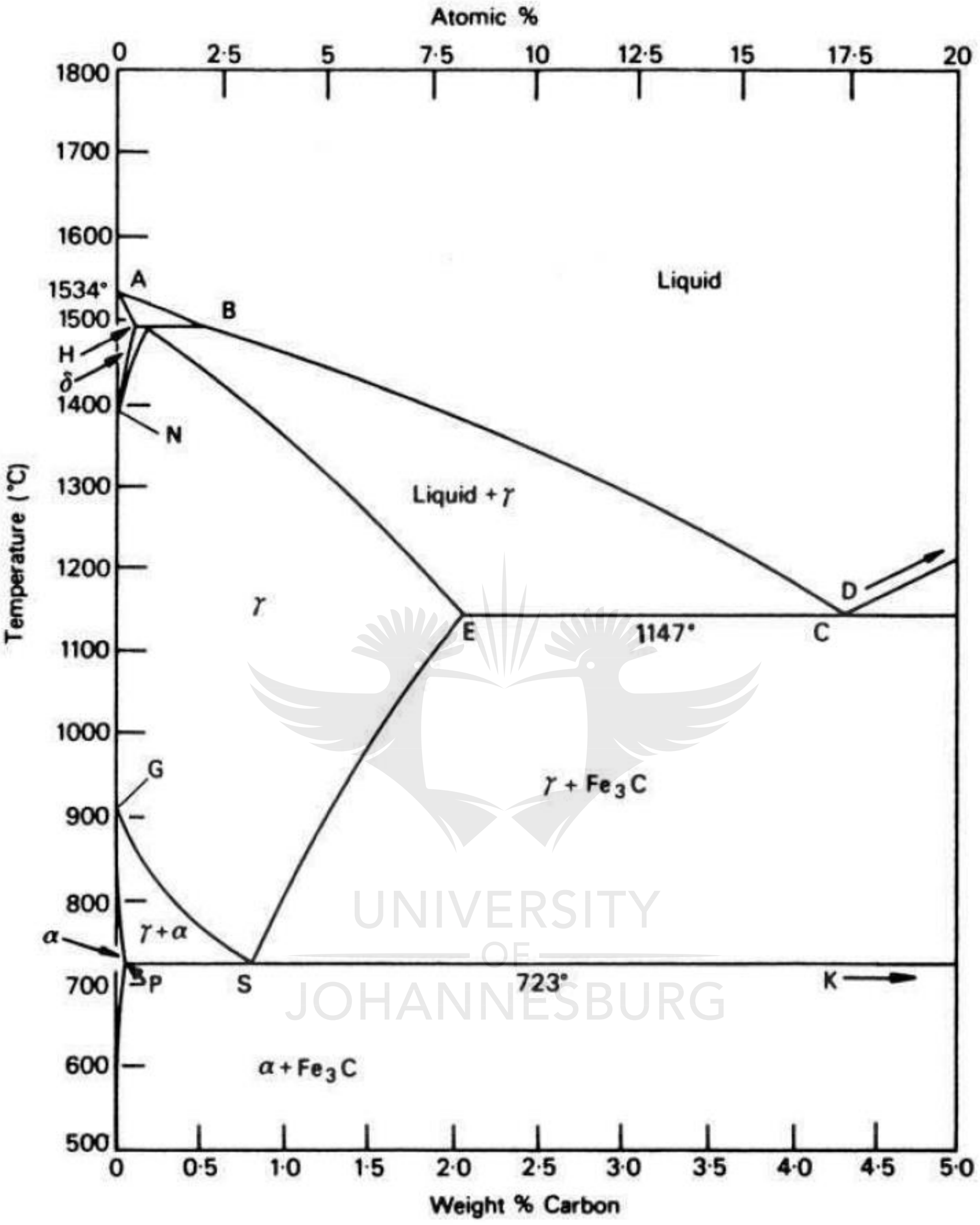

Figure 2-15: Carbon-Iron Equilibrium Diagram [82]

The Carbon-equilibrium diagram shows the relationship between percentage Carbon by weight in steel and its corresponding phases at various temperatures. In the diagram, the much larger γ-iron (austenite) field phase than the α-iron (ferrite) field phase, owes to the higher solubility of carbon in the austenite phase [78]. The carbide Fe_3C present in the ferritic phase is also known as cementite. This combination of α-iron + Fe_3C is present in steel at temperatures up until 723 ^{0}C, which is called the critical temperature point called A1 (P-S-K in the diagram) and is the point at which eutectoid (solidification) reaction occurs [78]. At the A3 temperature, α-iron (ferrite) transforms to γ-iron (austenite) [81]. For pure iron, this occurs at 910 ^{0}C, however, this critical temperature point is lowered by the addition of carbon. This is seen along the line G-S in the carbon-equilibrium diagram in Figure 2-15. A third critical temperature point is called A4, which is the temperature at which γ-iron transforms to δ-iron [78]. In pure iron, this occurs at 1390 ^{0}C but with an increase in carbon, this critical temperature point is raised [78] . Line N-H in Figure 2-15, defines this point. Another critical temperature point is A2, also called the curie point. At this temperature, ferritic iron changes from ferromagnetic to paramagnetic conditions. It occurs at 769 ^{0}C for pure iron. During this transformation, crystal structural changes are not involved [77].

The α-iron phase field is restricted. It possesses a maximum carbon solubility of 0.04 wt. % at 723 ^{0}C, described at point P in Figure 2-15 [83]. The δ-phase field is also very restricted between 1390 ^{0}C and 1534 ^{0}C. This phase disappears completely when the carbon content is at 0.4 wt. %, as seen at point B in Figure 2-15 [83].

In alloys containing less than 0.8 wt. %, when cooling takes place, hypo-eutectoid ferrite is formed from austenite between 910-723 ^{0}C. This ferritic phase is enriched with residual austenite until it reaches 723 ^{0}C, at which point, the carbon-contained austenite phase transforms to pearlite [83]. Pearlite is a lamellar mixture of ferrite and iron-carbide (cementite) (Figure 2-16).

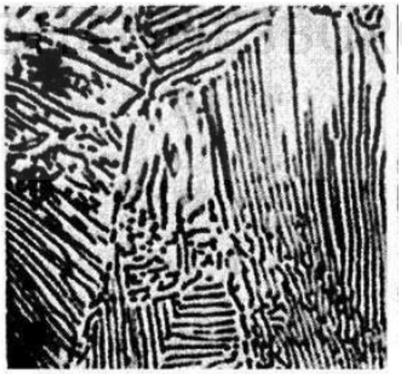

Figure 2-16: Pearlite in 0.8 wt. % C-Steel [77]

In the austenite phase with 0.8-2.06 wt. % carbon, as it slowly cools from 1147 to 723 ^{0}C, cementite forms gradually depleting the austenite in carbon until the austenite contains 0.8 wt. % carbon at 723 ^{0}C and transforms to pearlite [83].

Steels with less than 0.8 wt. % are therefore called hypo-eutectoid alloys which are primarily made up of ferrite and pearlite [84] (Figure 2-17)

Figure 2-17: Ferrite and pearlite in 0.4 wt. % C steel [77]

According to the lever rule, an increase in carbon content is said to be directly proportional to the volume percentage of pearlite until it reaches 100 % at the eutectoid composition [85]. The ferrite, cementite and pearlite phases are therefore the principal constituents in the microstructure of plain carbon steel. These carbon steels, however, must have been forged at relatively slow cooling rates to prevent the formation of metastable phases [77].

2.8.2.a Martensite

Martensite is one of the most remarkable technologically important constituents of steel, because it can combine very high strength (> 3500 MPa) with toughness (> 200 MPa √m) [86]. Martensite is a hard phase where the carbon which was formally in solid solution in the austenite phase is retained in solution in the new phase. The formation of martensite can occur when austenite in steels is quenched at room temperature [86]. The formation of martensite is said to be a diffusionless shear transformation because the during the deformation of the austenitic lattice, diffusion of atoms does not occur as it does in the case of pearlite and ferrite formations [86]. Figure 2-18 shows the martensite phase of Fe-0.16 C wt. %. The alloy formed by quenching from 1050 ^{0}C. The morphology of martensite phases in low carbon steel is plate-like or laths. The laths are usually long at about 0.5 μm wide [77]

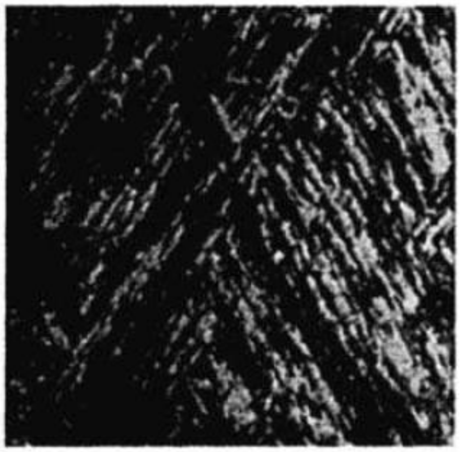

Figure 2-18: Martensite in Fe- 0.16C wt.%. quenched at 1050 ^{0}C [77]

2.8.2.b Bainite

Bainite is a structure where fine aggregates of ferrite plates and cementite particles are formed. It is known to occur during athermal treatments at cooling rates that are too quick for pearlite structures to form and yet too slow for martensite structures to form [86]. Two forms of bainite phases exist; upper bainite and lower bainite. Upper bainite forms at a higher level of transformation temperature between 550 - 400^{0}C. It is typically made up of fine plates of ferrite, 0.2 µm thick and about 10µm long. These plates are called sheaves, and they grow in clusters [87] (Figure 2-19).

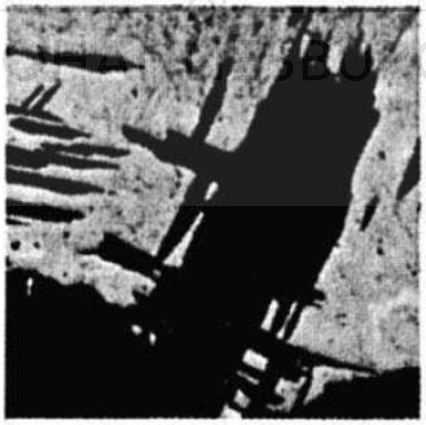

Figure 2-19: Microstructure of upper bainite in Fe – 0.8C wt.% Steel, transformed 20 secs at 400 ^{0}C. [77]

Lower bainite occurs at transformation temperatures between 400 – 250 ^{0}C and contains cementite particle precipitated within ferrite plates [87] (Figure 2-20). This is the major distinction between upper and lower bainite.

Figure 2-20: Microstructure of lower bainite in Fe – 0.8C wt.% steel, transformed at 300 ^{0}C [77]

2.8.2.c Acicular Ferrite

“Acicular” means shaped and pointed like a needle. This microstructure is characteristically disorganized and better described as chaotic. Acicular ferrite plates nucleate heterogeneously on non-metallic inclusions and propagate in many different directions from these nucleation sites, giving it its characteristic chaotic look (Figure 2-21) [77].

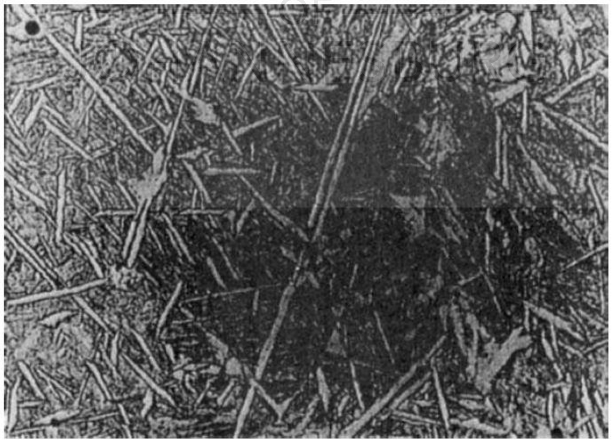

Figure 2-21: Replica of a transmission electron micrograph of acicular ferrite plates in martensite matrix, in a steel weld deposit [77]

The transformation mechanisms of both bainite and acicular ferrite are quite similar [87]. The major difference is that bainite sheaves grow in a series of parallel platelets originating from austenite grains, however, acicular ferrite platelets undergo intragranular nucleation [88] (Figure 2-22). This nucleation occurs at ‘point’ sites, thus hindering the development of parallel plates formations [77]. Although acicular ferrite grows without diffusion, the excess carbon is not retained in the supersaturated ferrite, rather, shortly after growth, it is partitioned into the residual austenite grain.

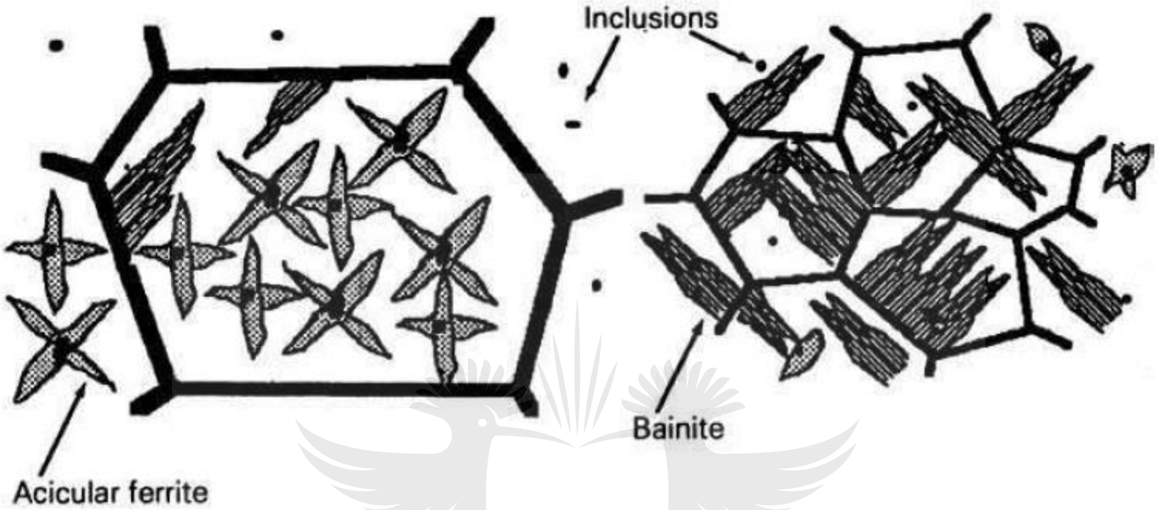

Figure 2-22: Acicular ferrite and bainite formation [77]

2.9 Effect of Gas Metal Arc Welding Process on the Microstructure of Steel

Naturally, weld joints are heterogeneous in terms of microstructure. Consequently, there is a gradual change in properties across the zones of the weldment from the base metal to the fusion zone [88]. The understanding of the formation of microstructures in these regions, as well as the effect of the microstructural evolution on the properties of the material, is critical. For instance, is has been shown that grains close to the line of fusion typically act as origins of nucleation [89]. This is due to the ‘wetting’ of the weld pool on the grains of the substrate. In the process of solidification, these grains appear to have columnar growth perpendicular to the weld pool boundary. This is largely due to the temperature gradient being at its maximum in this region [89], [90]. Typically, high heat input and low cooling rates increase nucleation and recrystallization which is responsible for grain growth in the HAZ [91]. Weld pool stirring, arc oscillation and arc pulsation are some grain refining techniques used to counter the effects of increased nucleation and recrystallization in this region [26].

Microstructural evolution of this sort has a significant effect on the structural integrity of the weldment.

2.9.1 The microstructure of Steel Welds

When it comes to the microstructure of steel welds, all the aspects of phase transformation in steel are relevant. This is because a series of phase transformation in steel occurs due to the fusion welding process as the weld cools and solidifies [77]. It is critical to understand the formation of these microstructures in the fusion and heat-affected zones.

2.9.1.a Microstructural Evolution in the Fusion Zone

Most steel welds undergo very similar microstructural evolution as iron. When the weld deposits began to solidify, epitaxial growth of columnar δ-ferrite occurs. This results from the hot-grain-structure of the parent material at the fusion surface [92] (Figure 2-23).

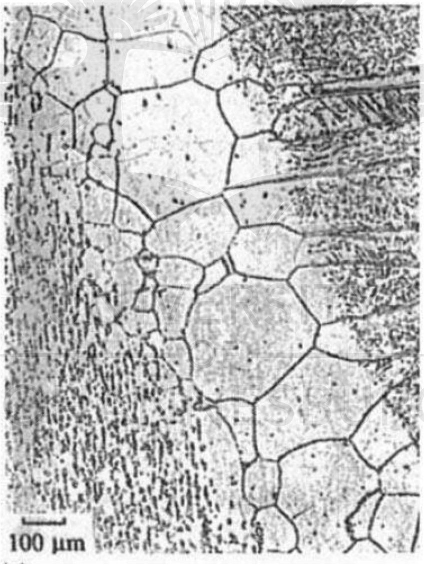

Figure 2-23: Epitaxial growth of columnar grains from the fusion boundary of a stainless-steel weld [77]

As the temperature decreases, the δ-ferrite phase undergoes solid-state transformation to austenite. This austenite nucleates at the δ-δ grain boundaries, where it further develops into columnar austenite grain structure [92] (Figure 2-24).

Figure 2-24: Prior-columnar austenite grain structure in the weld deposit of steel welds [77]

The chemical composition of the weld deposit is quite complicated. It is typically determined by the variables involved in the welding process such as plate, wire and flux compositions [93]. Also, oxide particle entrapment within the fusion zone, could, during solidification, serve as heterogeneous nucleation sites. This has significant effects on microstructural evolution in the fusion zone [88]. As the weld cools from the liquid phase to ambient temperature, the primary microstructure formed predominantly consists of allotriomorphic ferrite, Widmanstatten and acicular ferrite [93] (Figure 2-25).

In the weld deposit microstructure, there could also be some martensite, retained austenite or degenerate pearlite. However, an occurrence of these will only be in very small fractions and are thus collectively called microphases [77]. Bainite, however, is hardly formed in properly designed weld alloys. Rather, acicular ferrite is induced to nucleate heterogeneously on non-metallic inclusions [88].

In situations where multi-run welds are required, the resulting microstructure is rather complicated. As the weld layers are successively deposited, originally deposited layers undergo reheating, sometimes up to temperatures high enough to cause re-formation of austenite [77].

When the reformed austenite undergoes cooling, a different microstructure is formed. This sort of microstructure is called reheated or secondary microstructure [77].

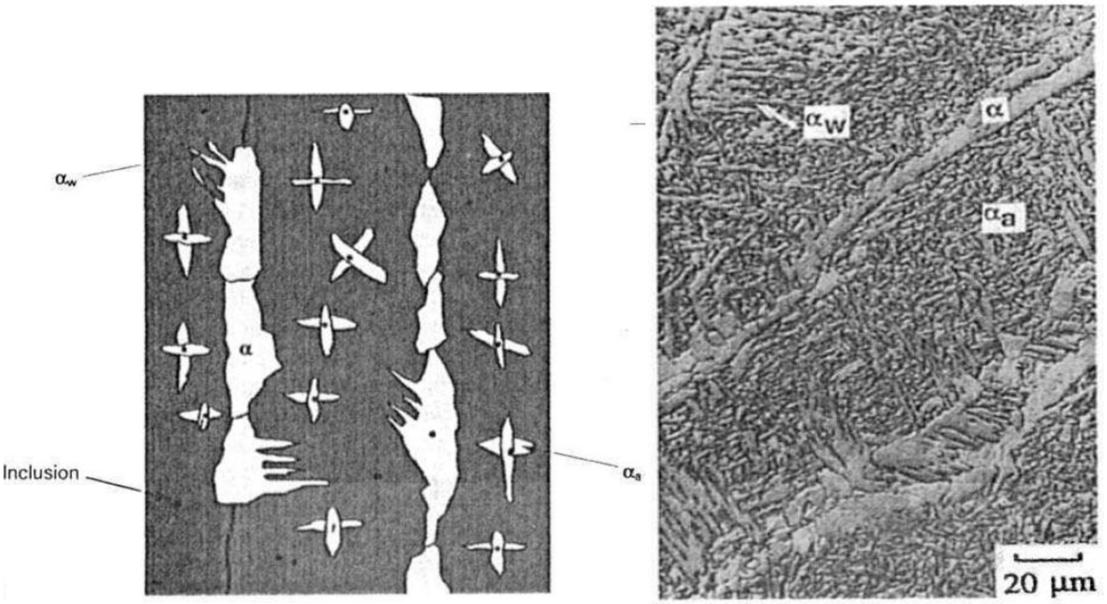

(a) (b)

Figure 2-25: (a) schematic illustration of the predominant constituents of the primary microstructure in steel weld deposits. (b) Scanning electron micrograph of the primary microstructure of a steel weld deposit [77] α_w, α, and α_a represent Widmanstatten ferrite, allotriomorphic ferrite and acicular ferrite respectively.

2.9.1.b Effect of Carbon on Microstructural Evolution in the Fusion Zone.

Changes in carbon concentration significantly influence the weld's microstructure [77]. The rate of ferrite growth sharply increases as the carbon concentration of steel approaches solubility (Figure 2-26). This happens because of the absence of carbon diffusion ahead of the austenite-ferrite interface due to the increased solubility of carbon in ferrite [77].

This sensitivity to carbon concentration is reflected in the mechanical properties of steel materials as shown in Figure 2-26. There is a more rapid change of mechanical properties at low carbon concentration

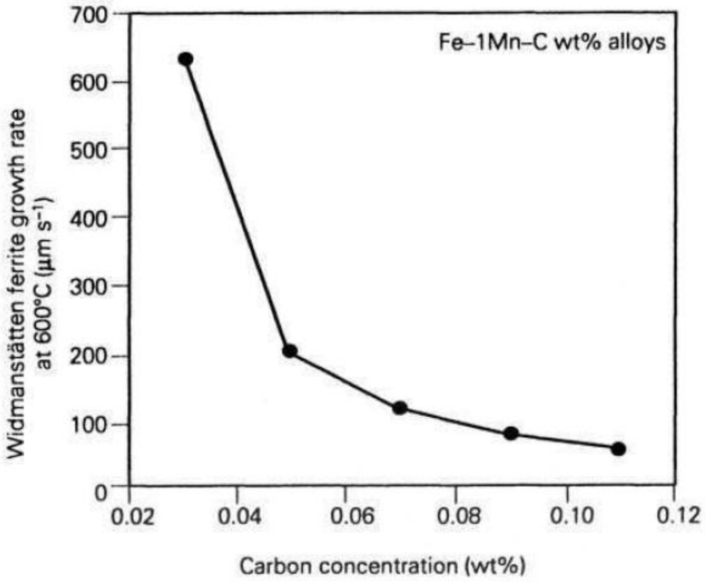

Figure 2-26: Isothermal growth rate of Widmanstatten ferrite in a series of Fe–1Mn–C wt. % alloys with respect to carbon concentration [77]

2.9.1.c Microstructural Evolution in the HAZ

As heat diffuses from the fusion zone into the adjacent parent material, heating and cooling cycles occur in the HAZ. The severity of these cycles largely depends on the distance away from the fusion boundary. The peak temperature and heating rate naturally decrease with distance away from the fusion boundary (Figure 2-27) [77].

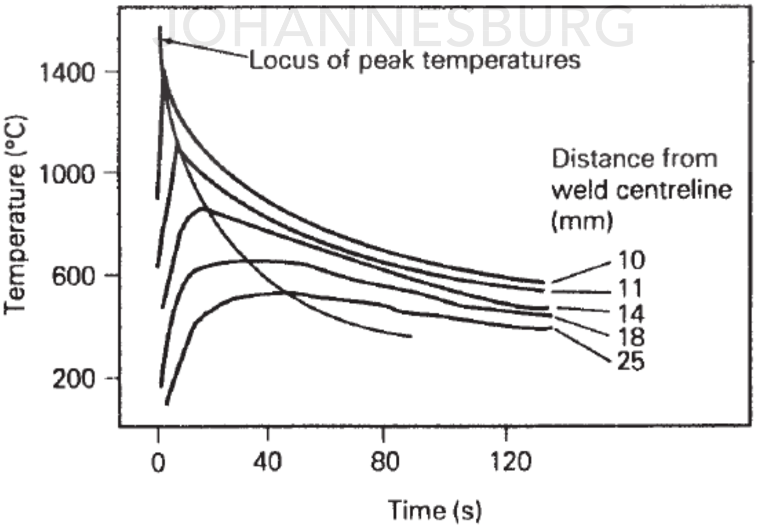

Figure 2-27: Temperature-time curves typically obtained in the HAZ of steel welds

The cooling rate, however, which is defined as the time, Δt_{8-5}, taken to cool over the range of 800 - 500 ^{0}C, is less sensitive to the distance away from the fusion boundary [94]. So, using the peak temperature, T_p and the time-period, Δt_{8-5}, the thermal cycle at any point in the HAZ can be characterized.

2.9.1.d Microstructural Zones in the HAZ

The microstructures in the HAZ are well graded along the distance away from the fusion boundary as shown in Figure 2-28. The areas adjacent to the fusion boundary completely transform to austenite due to very high heat input and high temperatures. Austenite begins to form at $A_{c1} \cong 800$ ^{0}C. The region becomes fully austenitic at $A_{c3} \cong 950$ ^{0}C [77].

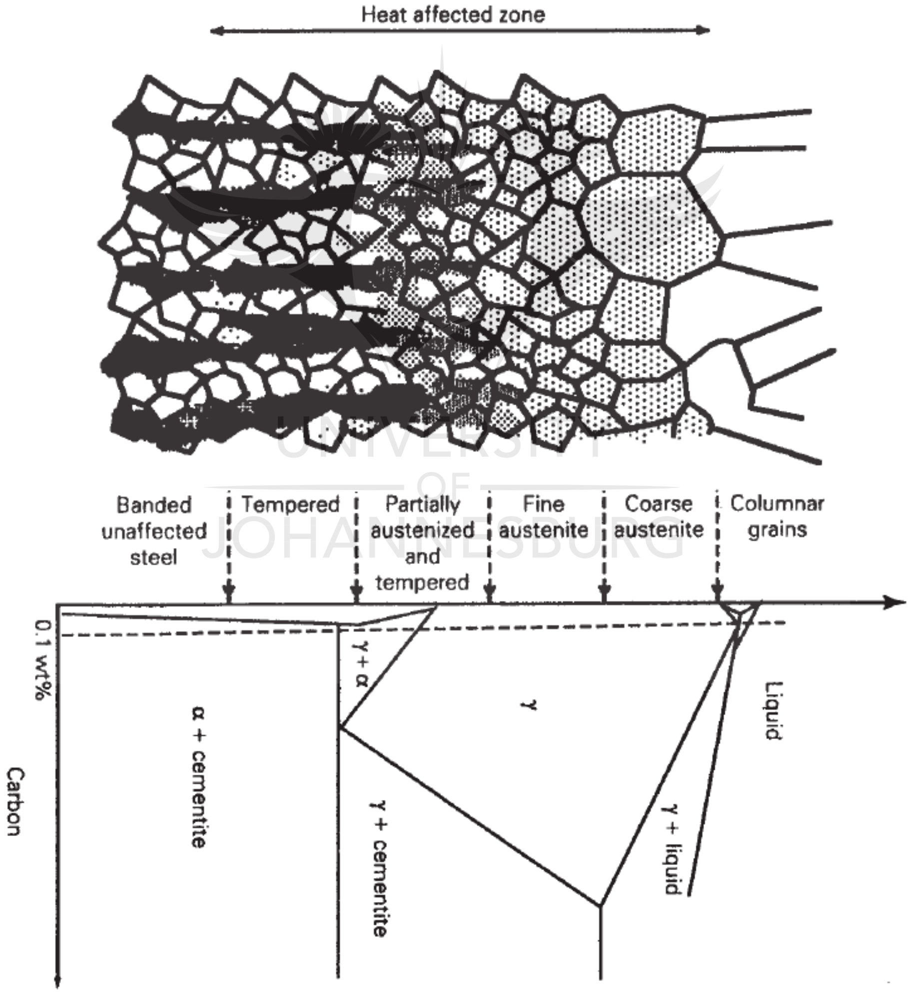

Figure 2-28: Illustration of microstructural variation typically obtained in steel welds [77]

The maximum temperature in the HAZ very close to the fusion boundary usually exceeds the A_{c3} temperature, resulting in the annealing of austenite. This, in turn, results in the formation of very coarse grain structures called "coarse-grained austenite zone" [93] (Figure 2-29). As the distance increases away from the fusion boundary zone, the austenite grain sizes sharply decrease until the fine-grained zone. The properties in the fine-grained zone are usually superior to that of the coarse zone [77].

At the farther regions away from the fusion boundary zone, but within the HAZ, these areas become only partially austenitic during heating and this is due to the peak temperature being lower in this region [93] (Figure 2-30). The austenitic phases in this region have high carbon concentration because of the higher solubility of carbon in austenite at relatively lower temperatures. The areas of the HAZ that do not transform to austenite are tempered [77] (Figure 2-31).

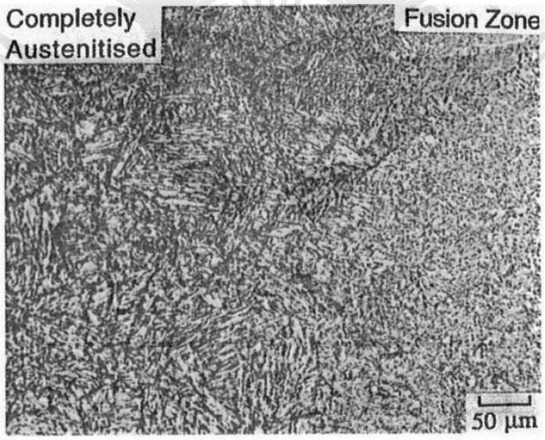

Figure 2-29: Fully austenitised region of steel welds [77]

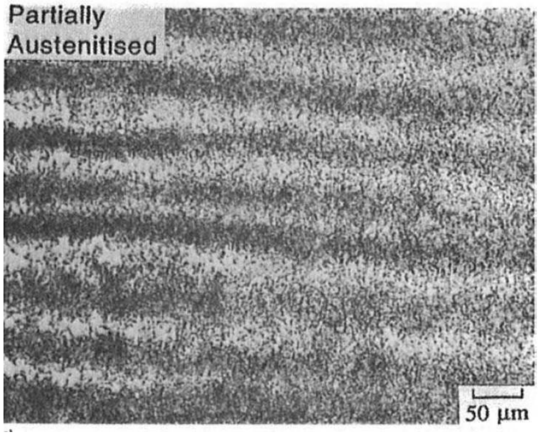

Figure 2-30: Partially Austenitised region of steel welds [77]

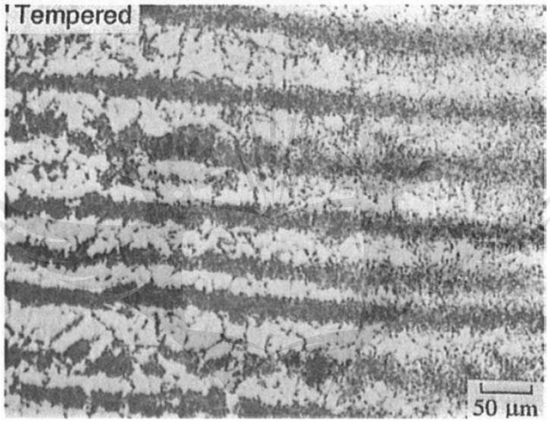

Figure 2-31: Tempered region of steel welds [77]

2.9.2 **Scholastic Review on the Microstructure of Steel Welds**

This section of the review aims at understanding the relationship between microstructural evolution in GMAW and the mechanical properties of selected grades of steel.

Nathan *et. al.* [30] carried out a comparative analysis on the effect of GMAW, SMAW and FSW on mechanical properties and microstructure of HSLA (High Strength Low Alloy) naval grade steel. Their results showed better tensile strength and hardness properties for FSW over SMAW and GMAW, while the GMAW joint showed higher toughness. The FSW samples resulted in properties of 664 MPa, 410 HV and 48J for tensile strength, microhardness and impact energy respectively. GMAW showed results of 580 MPa, 304 HV and 69J, while SMAW showed 578 MPa, 3125 HV and 62 J for tensile strength, weld metal microhardness and impact energy respectively. Also noteworthy in their work was that the GMAW samples depicted higher ductility than the samples of other processes as can be concluded from the percentage elongation results in Table 2-1

Table 2-1: Mechanical Properties of Parent Metal and welded joints [30]

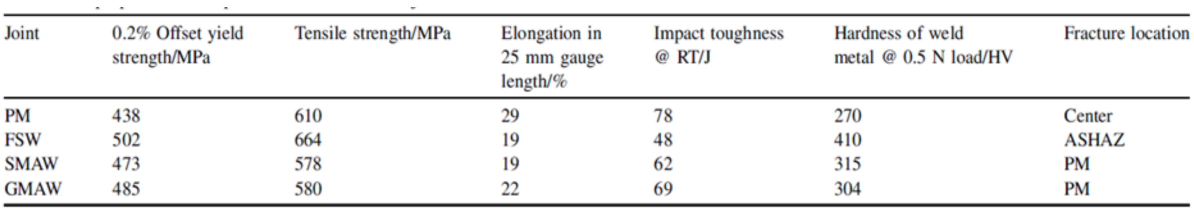

Joint	0.2% Offset yield strength/MPa	Tensile strength/MPa	Elongation in 25 mm gauge length/%	Impact toughness @ RT/J	Hardness of weld metal @ 0.5 N load/HV	Fracture location
PM	438	610	29	78	270	Center
FSW	502	664	19	48	410	ASHAZ
SMAW	473	578	19	62	315	PM
GMAW	485	580	22	69	304	PM

An understanding of the differences in microstructure in all three processes provides a better explanation for the significant differences in mechanical properties. As shown in the figure below, the macrostructure of the SMAW weld joint depicts a wider WZ (weld zone) than is visible in the GMAW weld joint. This is due to the higher energy density in the GMAW process and a resulting high self-quenching rate both of which are responsible for a narrower fusion zone in the SMAW sample. The grains of the SMAW samples (Figure 2-32) were coarser than that of the GMAW samples (Figure 2-33), this is due to higher heat input and a resulting slower cooling rate in the SMAW process [91].

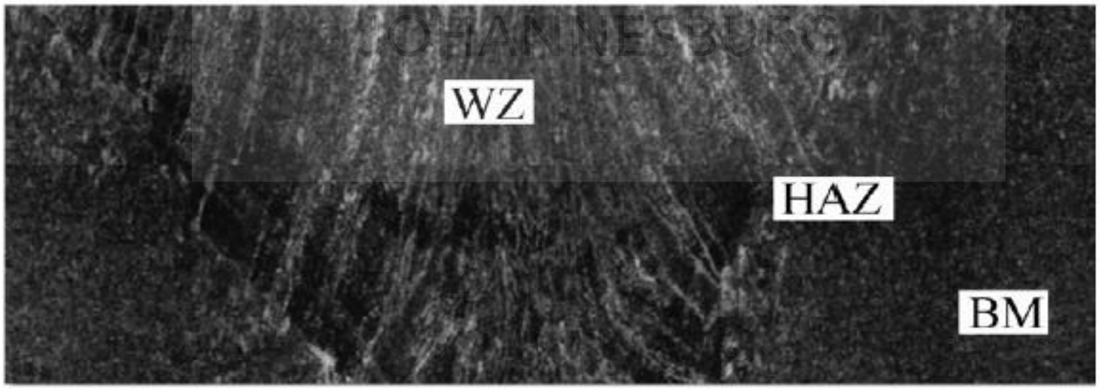

Figure 2-32: Fusion Zone for SMAW sample [30]

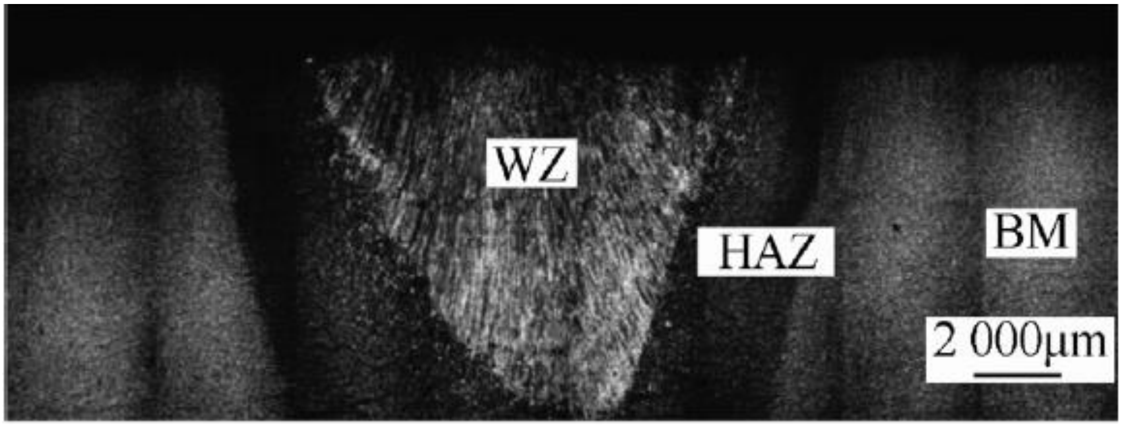

Figure 2-33: Fusion Zone for GMAW sample [30]

Nathan *et. al.* [30] reported that the hardness values of both SMAW and GMAW samples were highest in the heat-affected zones as shown in Figure 2-34 and Figure 2-35 respectively.

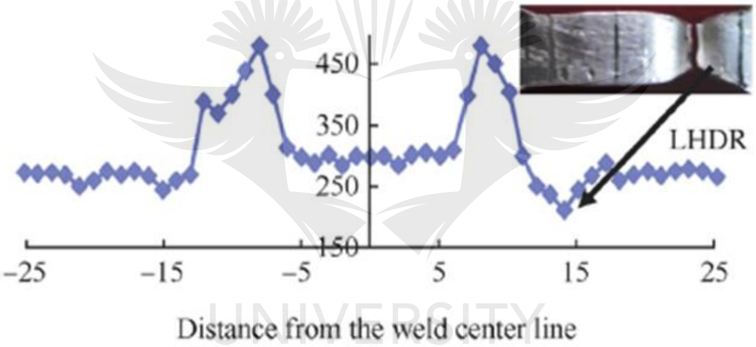

Figure 2-34: SMAW Hardness profile for HSLA Naval Grade Steel [30]

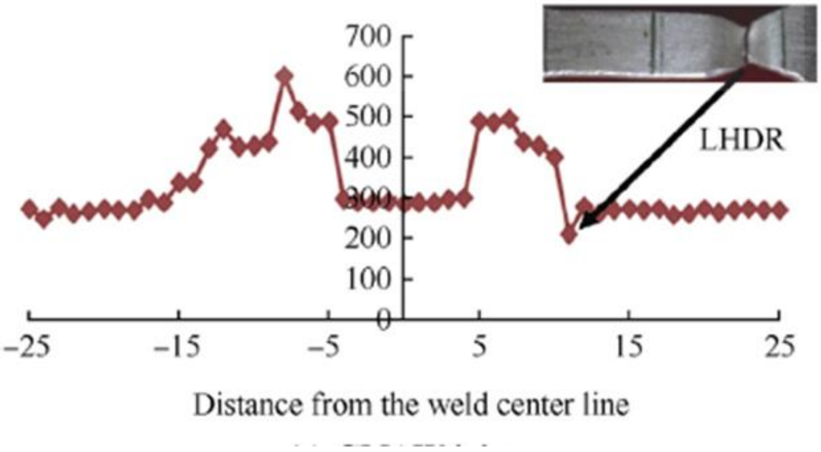

Figure 2-35: GMAW Hardness profile for HSLA Naval Grade Steel [30]

The hardness profile of the FSW sample, however (Figure 2-36), showed the highest hardness values in the weld metal region. This was attributed to the formation of typically harder phases in the FSW weld metal sample as was confirmed from the SEM images.

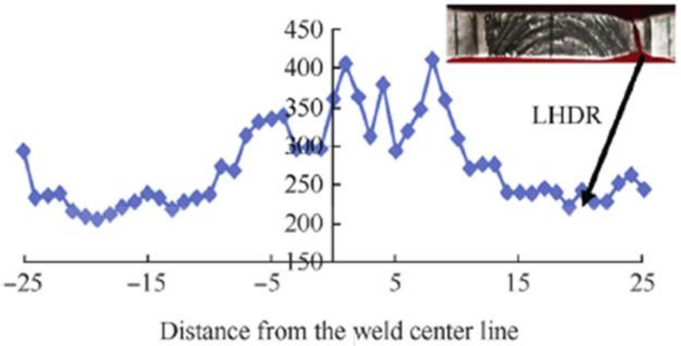

Figure 2-36: FSW Hardness profile for HSLA Naval Grade Steel [30]

The failure of the material for all three samples occurred in the lowest hardness distribution region (LHDR), which is consistent with their hardness profiles.

The SEM micrographs showed that the microstructure of the weld metal of the GMAW sample contained acicular ferrite and martensite structures (Figure 2-37).

The considerable difference in microhardness of the FSW samples and GMAW samples could be explained due to the presence of acicular ferrite and upper bainite in the FSW samples (Figure 2-38), which clearly explains higher microhardness values in the FSW samples [30]. The SMAW samples were found to contain retained austenite, acicular ferrite and carbides within the weld metal (Figure 2-39).

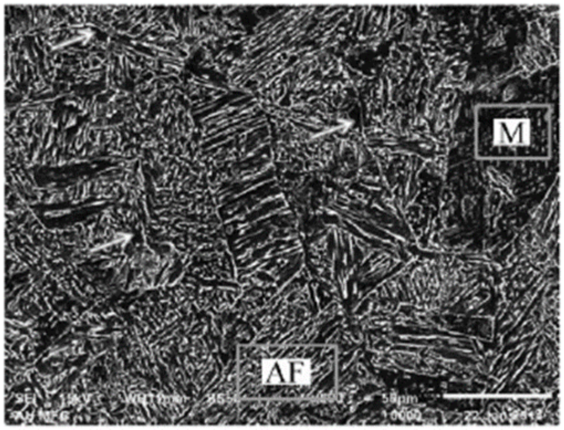

Figure 2-37: SEM Micrograph for GMAW HSLA naval grade steel sample, Weld Metal [30]

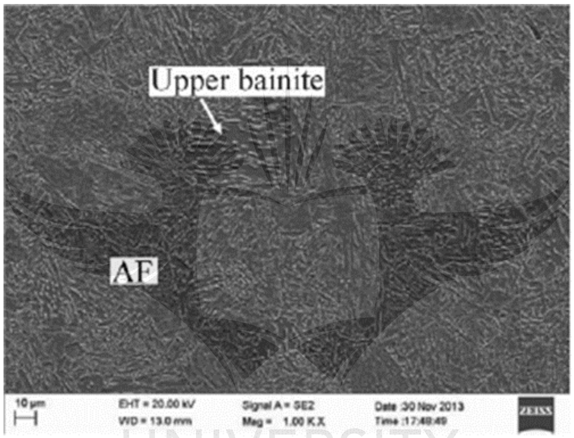

Figure 2-38: SEM Micrograph for FSW HSLA naval grade steel sample, Weld Metal [30]

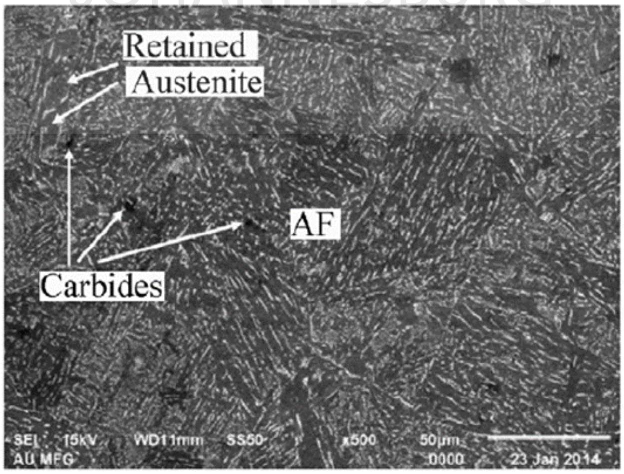

Figure 2-39: SEM Micrograph for SMAW HSLA naval grade steel sample, Weld Metal [30]

With respect to the GMAW sample, due to the relatively high heat input associated with GMAW, coarse-grains were formed in the weld metal. The authors concluded that it is practically impossible to produce a homogenous weld by fusion processes. [30]

In another related work, the effect of selected GMAW welding parameters on the microstructure HAZ and FZ of 10 mm thick industrial low carbon steel plates was carried out [95]. The effect of the wire feed rate on the grains in the HAZ of the material is shown in Figure 2-40.

As can be seen, the original pearlite and ferrite structures of the parent material were significantly altered with dendritic coaxial structures obtained at a wire feed rate of 7m/min. [95].

In the weld metal or fusion zone, the result is quite similar to what is obtained in the HAZ. It was also noted that the grain structures seem to get denser with an increase in wire feed rate (Figure 2-41).

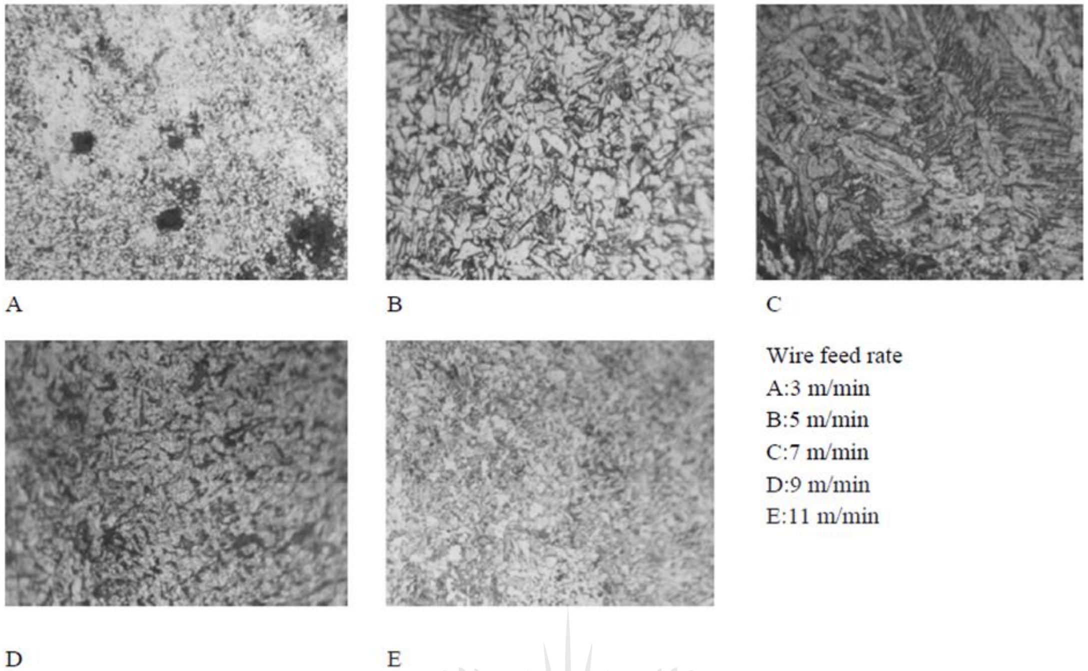

Figure 2-40: Effect of wire feed rate on grains in the HAZ of industrial low carbon steel [95]

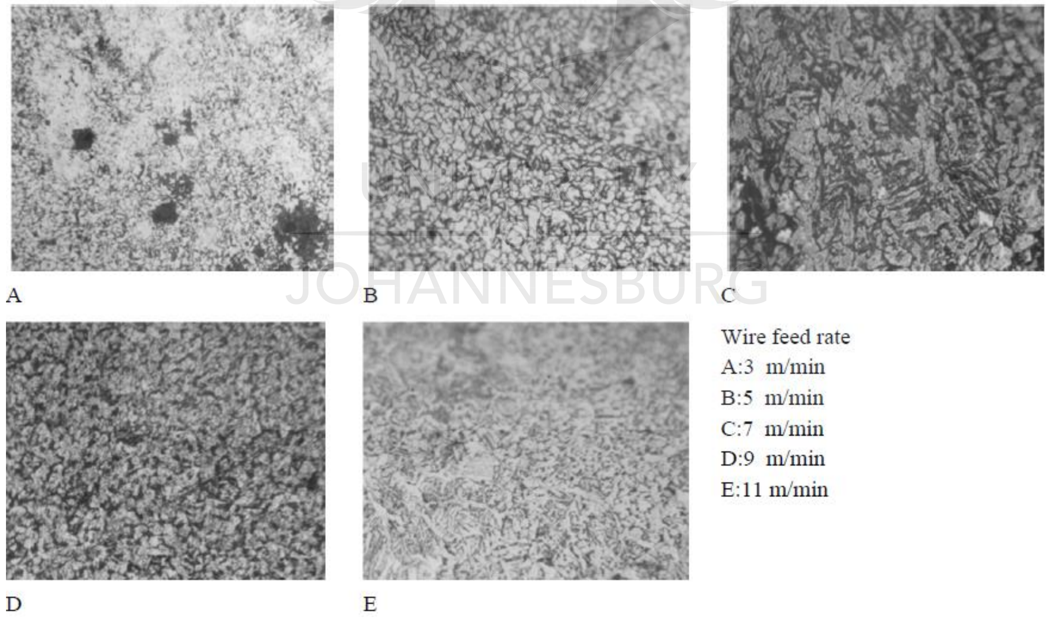

Figure 2-41: Effect of wire feed rate on grains in the FZ of industrial low carbon steel [95]

When the welding voltage was varied, the microstructure in the weld metal showed a formation of lamellar structures at 35V as shown in Figure 2-42. This was attributed to the high heat input at such a high voltage, causing recrystallizaton of the grains. [95]

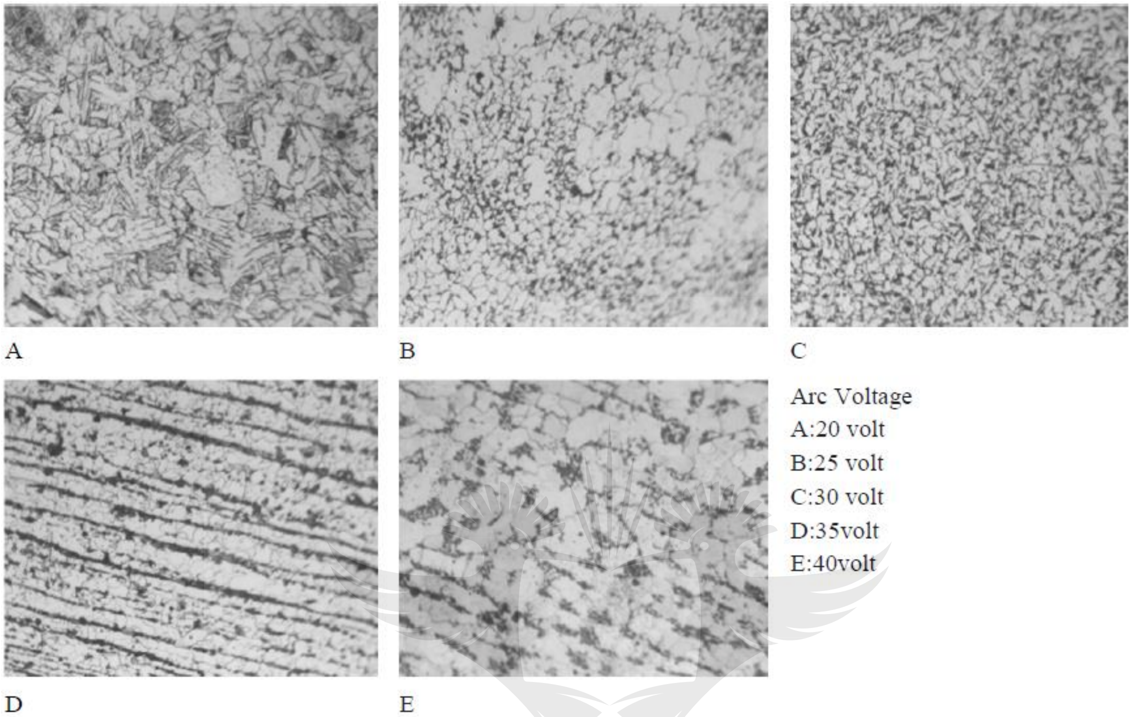

Figure 2-42: Effect of voltage on grains in the FZ of industrial low carbon steel [95]

Varying the welding speed in the weld metal and heat-affected zones of the material did not show as much significant change in microstructure as when the wire feed rate was varied. This led to the conclusion that the wire feed rate and voltage were the most significant factors affecting the microstructural evolution of mild steel weldments in GMAW [95]. It was deduced that the wire feed rate was responsible for the size of the HAZ [95], [96]

It was also pointed out that the amount of heat input plays a significant role in microstructural evolution as high heat input will lead to slow cooling rates and a consequent formation of acicular ferrite and martensite structures with the possibility of some austenite retained in the weld metal [95], [96]. Acicular ferrite microstructure is usually associated with good strength and toughness of the weld metal. [95]

The increase in hardness in both the WM and HAZ compared to the parent metal was attributed to the diffusion of a large number of carbon atoms from the cementite phase [95], [96] The effect of welding parameters on heat input and grain growth as well as the significance of grain size on the hardness and toughness of mild steel has also been studied by Gharibshahiyan *et. al.* [97]. As shown in Figure 2-43, high heat input and slow cooling rates result in wider HAZ and increased grain size. Lower cooling rates are also responsible for the increase in the size of austenite phases in the microstructure of the weld joint [98].

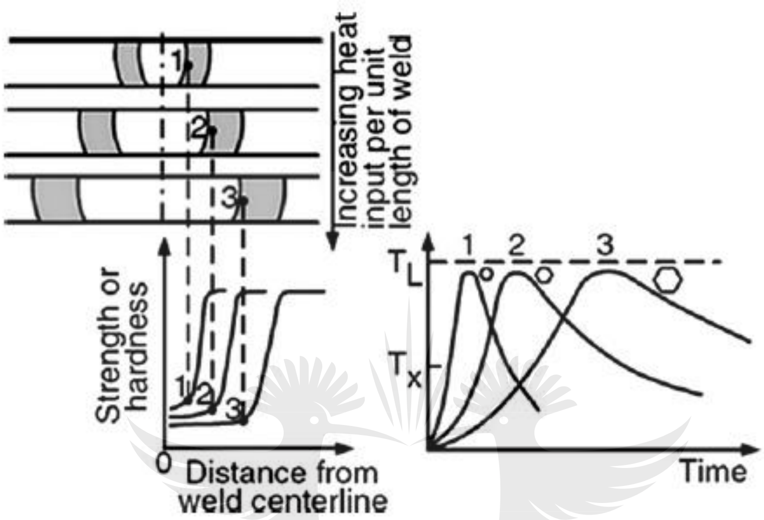

Figure 2-43: Effect of heat input per unit length on (i) width of HAZ, (ii) strength and hardness profiles and (iii) thermal cycles near the fusion boundary [97]

A relationship between Heat input and welding voltage is given by the following Equation 2.1:

$$H = \frac{60.E.I}{1000.S} \qquad (2.1)$$

Where H is the heat input in J/mm. E represents the welding voltage and S is the travel speed. Also, a relationship between grain boundary migration energy and grain boundary size is given by the following Equation 2.2:

$$\frac{d\overline{D}}{dt} = \frac{2\gamma}{\overline{D}} \qquad (2.2)$$

Where $\overline{D}$ represents mean grain size and γ represents grain boundary migration energy. Grain boundary migration and grain size enlargement are directly related to high heat input. At low welding speeds as well, it is expected that there is an increase in grain boundary energy which in turn leads to grain growth. [99]

Figure 2-44 shows the difference in grain size in the WM and the HAZ across a variety of welding voltages.

As can be seen in the Figure 2-44, the grain sizes in both the WM and HAZ increase with an increase in welding voltage [97]. According to the ASTM E 112-96 standard, the relationship between grain size number and grain size is given by Equation 2.3 [100]:

$$N = 2^{n-1} \qquad (2.3)$$

Where N represents grain size number and n represents grain size. The above equation shows an inversely proportional relationship between both properties, this simply implies a drop in the number of grains per square area as the grain size increases.

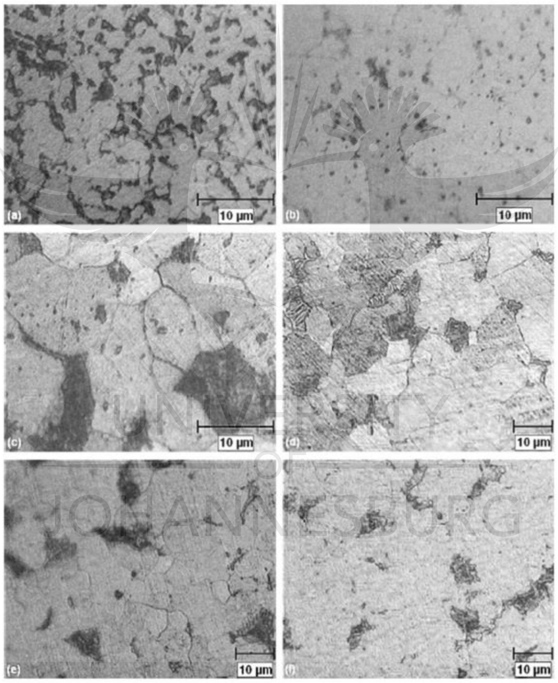

Figure 2-44: Optical micrographs (a–c) for specimens with voltage 20, 25, 30 V, (d–f) for heat affected zone for the same specimens

As shown in Figure 2-45, in a statistical verification of Figure 2-44, the grain size number in the weld metal at 30V is smaller than at 20V. This confirms the increase in grain size with an increase in voltage or heat input.

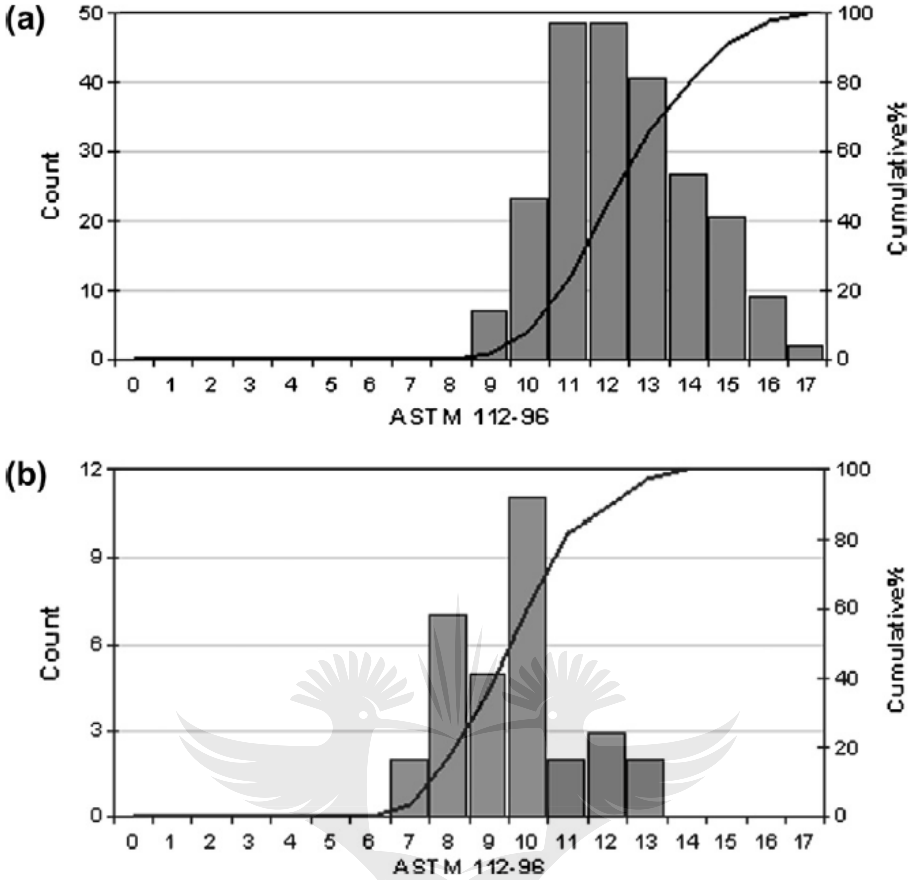

Figure 2-45: Comparison of the grain size number in the WM: (a) welding voltage 20 V and (b) welding voltage 30 V. [97]

Table 2-2 gives a summary of the grain size number in the different zones of the weldment at various voltage levels.

Table 2-2: Variety of number and area of grains in the WM and HAZ of GMAW mild steel [97]

	Voltage (V)	Grain size number	Max. area (μm^2)	Min. area (μm^2)	Ave. area (μm^2)
WM	20	288	221	0.3	28.5
	25	63	420	1.7	116.7
	30	46	691.7	9.6	217.7
HAZ	20	69	1897	10.9	397.6
	25	59	2107	39.7	436.9
	30	32	5882	9	607

It was also noted that grains in the HAZ are larger in size than grains in the WM of the same weld joint across all voltage levels.

Gharibshahiyan *et. al* [97] also observed that the amount of pearlite in the weld joint was inversely proportional to the heat input. They found a reduction from 17.8 % to 7.4 % when heat input was increased from 5.4 kJ/cm to 8.1 kJ/cm. This was attributed to the amount of carbon diffusion at different temperature levels.

The authors also showed that in the HAZ, the hardness of the material decreases with high heat input. Figure 2-46 depicts this phenomenon.

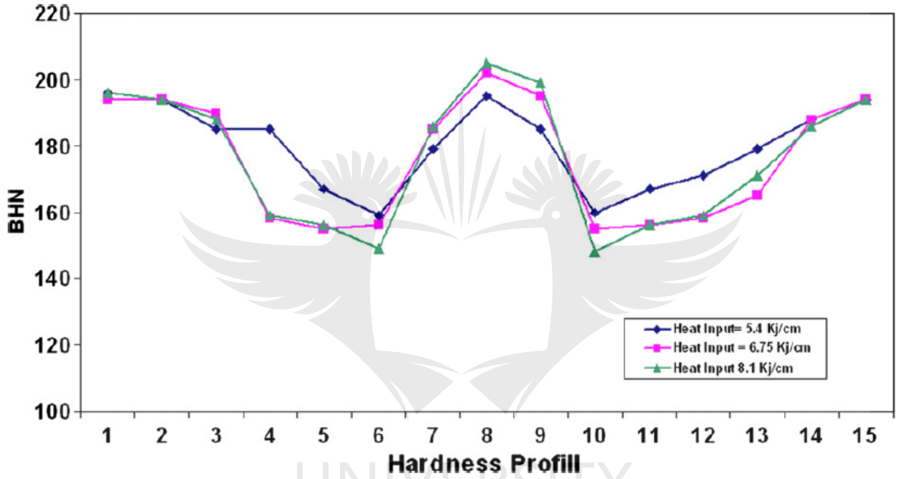

Figure 2-46: Hardness profile of Mild steel GMAW samples [97]

In the weld metal, however, high heat input produced higher hardness values. This high hardness in the weld region is said to be possibly attributed to finer grain sizes, needle-shaped ferrite grains or the presence of widmanstatten in the ferrite grains [101]. Hardness is inversely proportional to grain size as shown in Equation 2.4 [102].

$$H = H_0 + \frac{K}{\sqrt{d}} \qquad (2.4)$$

Where H is hardness, K is a proportionality constant and d is grain size.

Previous authors [88], [103] have reported the presence of ferrite grains in the HAZ and could be responsible for lower hardness in this region. The occurrence of grain growth in this region is also said to be responsible for lower hardness value in this region [88], [103].

Toughness reduced with increase in welding voltage. This can be attributed to the formation of coarse pearlite and planar ferrite, ultimately formed from the austenite grain growth due to low heat input. It has been observed that the presence of an increased amount of acicular ferrite in the weld metal increases the toughness of the material. This is because the fine grain size and interlocking nature of acicular ferrite greatly limit crack propagation and cleavage fracture [104].

Conversely, in a high input situation, ferrite grains are more predominant than austenite grains, which results in grain boundary growth [89]. The predominance of ferrite grains, coupled with its lower yield strength when compared with pearlite, easily allows crack initiation and crack growth. Also responsible for reduced toughness is the increase in grain size due to high heat input. Larger grains allow for easy movement of dislocations which in turn reduces ductility [101].

2.10 Titanium and its Alloys

2.10.1 Titanium

Titanium, like some other metals, can crystallize in different crystal structures. Each variation of the crystal structure is, however, only stable within a defined temperature range [105]. A total transformation from one crystal structure to another is called an allotropic transformation and the temperature at which a transformation occurs is called the tranus temperature [106].

Pure titanium, like most of its alloys, crystallizes at low temperature as α-titanium which is a modified ideally hexagonal close-packed (HCP) structure [107]. At higher temperatures, β-titanium which is a body-centred cubic structure (BCC), is stable. The tranus temperature, for pure titanium to β-titanium is 822 ± ^{0}C. α and β-titanium crystal structures are very significant as they determine the range of properties exhibited by titanium alloys [107].

Diffusion of atoms in BCC β-titanium is considerably higher than in HCP α-titanium, this is due to more densely packed atoms in HCP α-titanium. This limited volume diffusion in α-titanium is responsible for better creep properties and α-titanium and its alloys than in β-titanium [105].

Fast cooling of titanium usually results in very fine lamellar structures; however, coarse lamellar structures are obtained upon slow cooling. This is because time and temperature-dependent diffusion processes are significantly slower below the β-tranus temperature [106].

Acicular or fine plate-like, as well as martensitic structures, can be obtained at high cooling rates from temperatures that are above the martensite start temperature. Under these conditions, BCC β-titanium undergoes a diffusion-less transformation process to HCP α-titanium [105]. The martensitic structure obtained is characterized by a very fine basket-weave structure. Due to its diffusion-less nucleation process, the basket-weave structure depicts needle-like characteristics [106].

2.10.2 **Classification of Titanium Alloys**

Titanium alloys have been widely used in engineering due to their high specific strength and exceptional corrosion resistance. These properties have allowed the use of titanium alloys in aerospace, automotive and biomedical fields [108], [109]. Ti-6Al-4V (which contains 6% Aluminium, 4% Vanadium, 0.25% iron and 0.2% oxygen) is the most popular titanium alloy and it covers up to 50% of world consumption of titanium alloys [110]. Due to an impressive combination of mechanical and corrosive properties, this alloy enjoys a widespread application in the manufacture of biomedical components such as dental implants, prosthetic femoral components, surgical instruments, amongst others. [75]

Alloying elements of titanium are classified as neutral additions, α-stabilizers or β-stabilizers [106]. α-stabilizers extend the α-phase filed to higher temperatures. On the other hand, β-stabilizers shift the β-phase to lower temperatures. Neutral alloy elements have very minimal influence on the β-tranus temperature [105].

Amongst all the α-stabilizers, aluminium is the most important alloying element. Other interstitial elements such as oxygen, nitrogen and carbon are also α-stabilizers [111]. α-stabilizers also result in the development of a two-phase α+β field [112]. Titanium alloys are typically broadly classified into α, α+β, and β alloy [111]. These could be further subdivided into near-α and metastable β-alloys [112].

A three-dimensional phase diagram schematically describes the various titanium alloys (Figure 2-47)

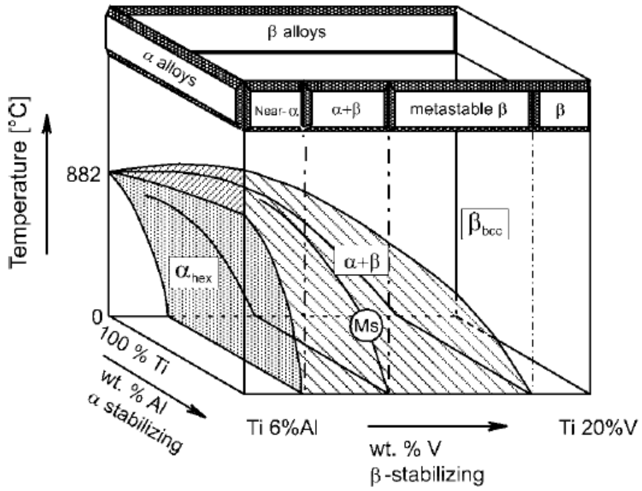

Figure 2-47: Schematic three-dimensional representation of the classification of Titanium alloys [112]

There are two-phase diagrams depicted in Figure 2-47 with α-stabilizing and β-stabilizing elements respectively.

The diagram shows that α-alloys majorly comprise commercially pure titanium and other alloys with either α-stabilizing or neutral elements as alloying elements. Where minor fractions of β-stabilizing are added, the alloys are referred to as near α-alloys. β-stabilizing elements include Molybdenum, Vanadium, Tantalum, Niobium, Iron, Manganese, Chromium, Cobalt, Nickel, Copper, Silicon and Hydrogen [105].

α+β alloys are the most widely used alloy group [105] . Metastable β-alloys are formed in a situation where β-titanium no longer transforms to martensite during fast quenching due to an increased level of β-stabilising elements [113].

The most important titanium phase diagram is the Ti-Al system (Figure 2-48)

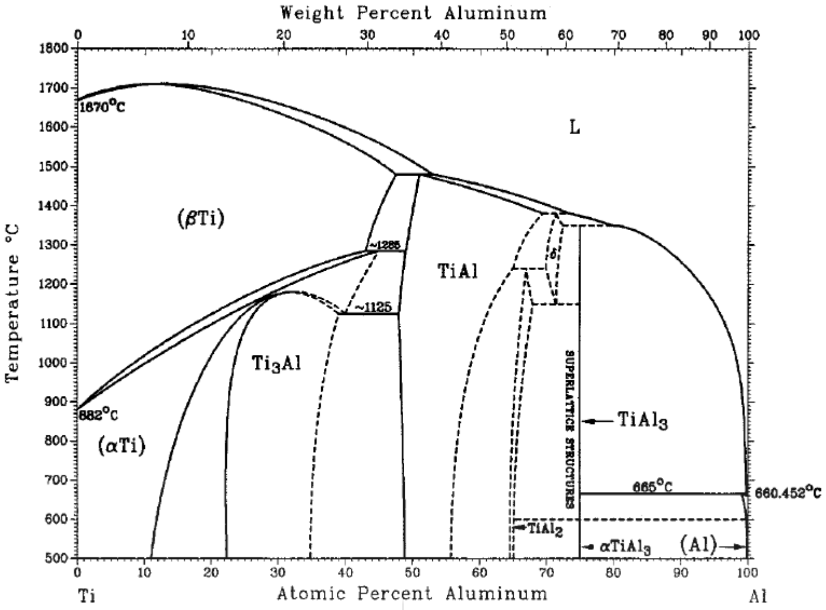

Figure 2-48: Ti-Al Phase diagram. [114]

This diagram shows the occurrence of several intermetallic phases due to the presence of aluminium as an α-stabilizing element. These intermetallic phases include α_2-Ti_3Al, γ-$TiAl_2$ and $TiAl_3$ [114].

2.10.3 The Microstructure of Titanium Alloys.

Microstructures have a substantial influence on the properties of titanium alloy as shown in Table 2-3.

Table 2-3: Influence of microstructure on some properties of titanium alloys.

fine	*coarse*	*Property*	*lamellar*	*equiaxed*
○	○	Elastic modulus	○	+/– (texture)
+	–	Strength	–	+
+	–	Ductility	–	+
–	+	Fracture toughness	+	–
+	–	Fatigue crack initiation	–	+
–	+	Fatigue crack propagation	+	–
–	+	Creep strength	+	–
+	–	Superplasticity	–	+
+	–	Oxidation behavior	+	–

The microstructure of titanium alloys is characterized by the arrangement of the α and β phases. Lamellar structures are generated during cooling from the β-phase field while equiaxed microstructures form due to recrystallization [106]. Both microstructures are the two extreme cases of phase arrangements in the microstructure of Ti-alloys. Also, both microstructures can have fine or coarse arrangements in their two phases [112].

Different microstructures can also be generated through thermo-mechanical treatments. Thermo-mechanical treatments are a complex sequence of solution heat treatment, deformation, recrystallization, ageing and annealing [115].

In the formation of lamellar structures, α-titanium nucleates at the grain boundaries once the temperature falls below the β-transus temperature. These grains grow as lamellae into the prior β grains [116]. The cooling rate determines the fineness or coarse nature of the lamellae. Slow cooling rates lead to the formation of pure lamellar structure (Figure 2-49). Much reduced cooling rates result in coarser lamellae [116].

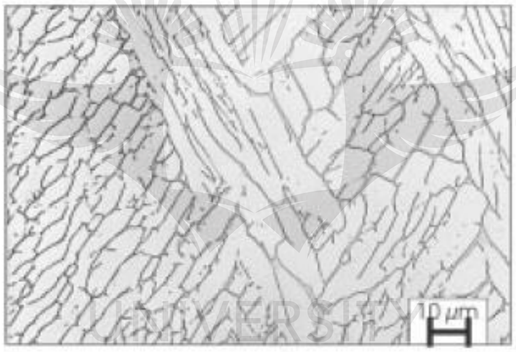

Figure 2-49: Lamellar structures of Ti-6Al-4V alloy after slow cooling from 1050 ^{0}C. [112]

Rapid quenching results in martensitic transformation, with very needle-like microstructures (Figure 2-50) [116]. Unlike in steels, the hardening effect of martensite structures in titanium is moderate [112]

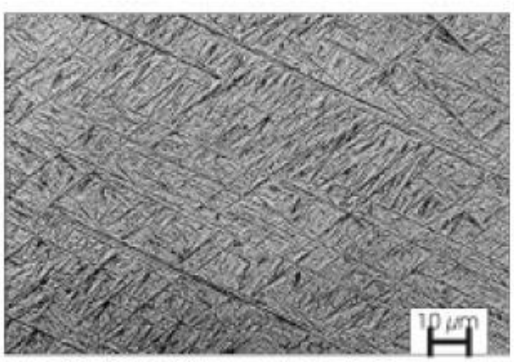

Figure 2-50: Martensite structures of Ti-6Al-4V alloy after rapid water quenching from 1050 0C

Equiaxed microstructures are a product of a recrystallization process. The alloy is first deformed in the α+β field, then subjected to solution heat treatments at temperatures in the two-phase field [116]. This generates recrystallized and equiaxed microstructure (Figure 2-51a) [112]. Further annealing results in coarser microstructure (Figure 2-51b).

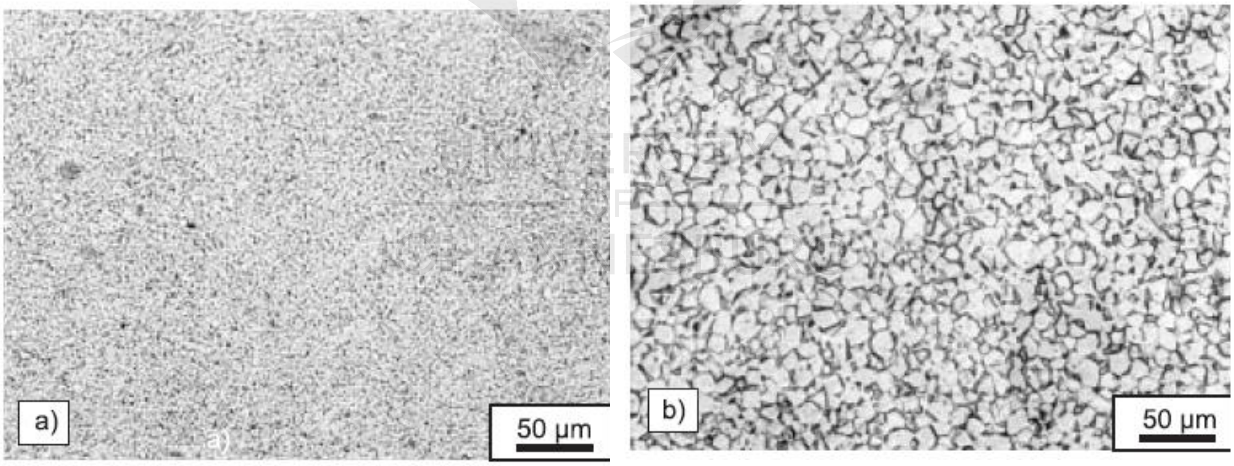

Figure 2-51: Microstructure of equiaxed Ti-6Al-V via recrystallizaton. (a) fine equiaxed grains (b) coarse equiaxed grains

2.10.3.a Properties of Titanium Alloy Classes

Table 2-4 shows the difference in physical, mechanical and technological properties between the three major classes of titanium alloys. (α, α+β and β).

Table 2-4: Properties of α, β and α+β titanium alloys [112]

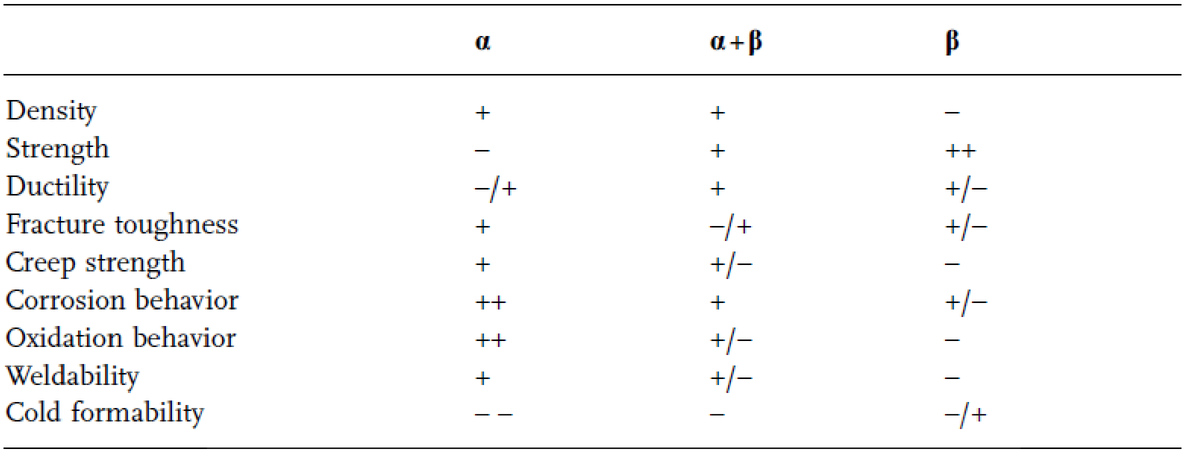

	α	**α+β**	**β**
Density	+	+	–
Strength	–	+	++
Ductility	–/+	+	+/–
Fracture toughness	+	–/+	+/–
Creep strength	+	+/–	–
Corrosion behavior	++	+	+/–
Oxidation behavior	++	+/–	–
Weldability	+	+/–	–
Cold formability	– –	–	–/+

The properties of titanium alloys are significantly influenced by the arrangement, volume fraction and properties of the α and β phases [116]. α-titanium generally has a higher resistance to plastic deformation, reduced ductility and higher creep resistance than β-titanium alloys [117]. α-alloys typically have a lower density than β-alloys, due to the fact that the major α-stabilizing element; aluminium, is half the specific weight of titanium [112].

α+β alloys and metastable β alloys can be hardened to higher strength levels than α-alloys. While metastable β-alloys can be hardened to very high levels of strength, it is usually accompanied by low ductility [96]. Fracture toughness is primarily dependent on microstructure and ageing conditions. There is, therefore, no substantial difference in fracture toughness between the classes of alloys [112].

While all the classes of titanium alloys show excellent corrosion resistant behaviour due to the easy formation of TiO_2 oxide layer, α-alloys show the most excellent corrosion [118] behaviour [112]. In terms of weldability, α and α+β alloys are easier to weld than β alloys. The high reactivity of titanium with oxygen and hydrogen in the atmosphere leads to embrittlement in the alloys[112], [119].

2.11 Metal Matrix Composites

A composite is an artificially made multiphase material whose constituent phases, which are chemically dissimilar and separated by a distinct interface, combine to exhibit significantly better properties than those of the individual constituent phase [120]. Most composite materials are composed of just two phases; a matrix phase (which is continuous and surrounds the other phase) and a dispersed phase [120].

This resultant superiority in property is responsible for the high interest in composite materials for engineering applications. For instance, the automobile industry is in search of alternative materials that are lighter and stronger than steel but still suitable in automobile applications [121]. The classification of composite materials can be done based on the composite structure or based on the matrix material. On the basis of the matrix material, composites can be classified into Metal Matrix Composites (MMC), where the matrix phase is a metal; Polymer Matrix Composites (PMC), where the matrix is a polymer and Ceramic Matrix Composites (CMC), where the matrix is a ceramic material [121]. When classified based on the nature of reinforcements, composites can be subdivided into as shown in Figure 2-52;

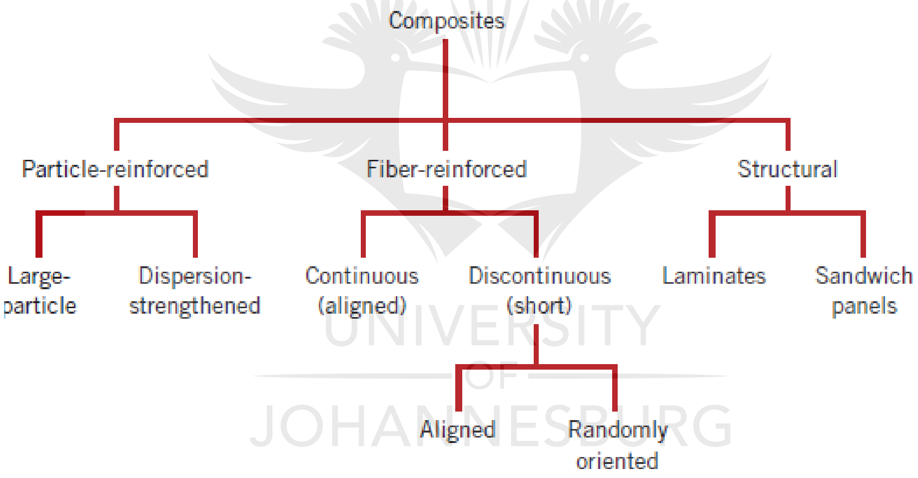

Figure 2-52: Classification of Composite materials

Particle-reinforced composites contain particulate materials in its reinforcement phase, they could be large particles or dispersion strengthened, where the particulate reinforcements are uniformly dispersed within the matrix. Fibre-reinforced composites have continuous or discontinuous fibres as reinforcements. Structural composites depend not only on the properties of the constituent phases but on the geometrical design of the phases. This is usually in a laminate or sandwich panel configuration [120].

The ability of MMCs to resist high temperatures, radiation and moisture, coupled with zero outgassing at vacuum, improved mechanical properties, as well as thermal and electrical conductivities give MMCs an advantage over other composites [122]. MMCs are usually a combination of a ductile metal or an alloy matrix reinforced with other metal, organic or non-metallic compounds [123]. They are usually produced by implanting the reinforcements into the metal matrix phase [124]. Properties such as specific strength, specific stiffness, wear resistance, corrosion resistance and high elastic modulus are improved on when high strength reinforcement materials are implanted into the metal matrix [124]. Commonly used metal matrices are Aluminium, Magnesium, Copper, Iron and Titanium. However, Aluminium and Titanium are the most commonly used metal matrices [121]. The use of iron as a matrix is usually problematic due to its brittleness and relatively low impact strength when compared with other composites [121].

Steel-based metal matrix composites only show great promise for wear-resistant applications and are not suitable for marine environment applications [125]. Studies have shown that the application of ceramic particles into a steel-based metal matrix results in improved mechanical properties, particularly wear resistance [126]-[127]. Chang *et al.* [128] used Titanium and Molybdenum coated SiC particles as reinforcements in Iron-based matrix and compared the mechanical properties of both composites. They found out that the Iron-based composite with Mo-coated SiC particles was more effective in improving mechanical properties than the Ti-coated SiC particles. They attributed this to the higher interfacial energy between the Mo-coated SiC particles and the Fe-matrix [128].

A novel semi powder metallurgy method inculcating spark plasma sintering (SPS) and solution assisted wet mixing was used to make steel matrix composite – 316L/poly carbo silane (PCS) [129]. The authors reported improved yield strength (YS) and ultimate tensile strength (UTS) values with increasing volume fractions of PCS. According to the authors, this improvement in strength was due to the network structure, refined microstructure and solid solution effects [129].

2.12 **Numerical Modelling**

The use of numerical modelling to describe the thermal and material properties of welding processes is known to date back to the 1970s [130]. This is the area of analysis that deals with thermo-mechanical responses and changes in material properties due to welding processes, with the aid of computer simulation, is called Computational Welding Mechanics (CWM) [130].

Figure 2-53 describes the finite element modelling process

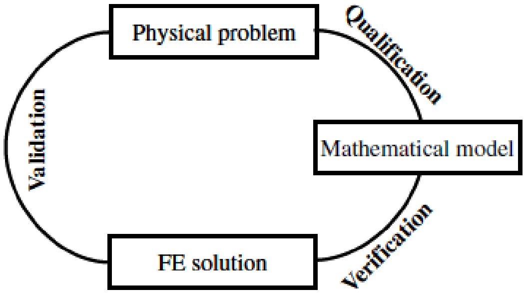

Figure 2-53: Finite element modelling process [131]

2.12.1 Finite Element Modelling (FEM) Process

A physical problem (such as a welding problem), is converted to a conceptual or mathematical model, through a process called qualification [131]. In the case of a welding problem, for instance, the mathematical model will be a collection of governing equations, defined with corresponding elements and boundary conditions. The mathematical model goes through a verification process to determine the accuracy of the model in describing the physical problem. After the process of verification, the mathematical model is solved as a finite element model. The solution of the finite element model is then validated through experimentation. A validated solution in close accuracy with the experimental results can then be used to predict the solutions of other mathematical models, similar in scope with the initial mathematical model [130] .

2.12.1.a Mathematical Model Describing Fusion Welding Process

A non-linear heat transfer equation is sufficient to describe the transient heat source that is present in fusion welding processes [132]. This general equation is given as shown in Equation 2.5 [133]:

$$c\rho\frac{\partial T}{\partial t} = k\left(\frac{\partial^2 T}{\partial x^2}\right) + k\left(\frac{\partial^2 T}{\partial y^2}\right) + k\left(\frac{\partial^2 T}{\partial z^2}\right) + Q \qquad (2.5)$$

Where:

c = heat capacity (J/Kg^{0}C)

ρ = density (Kg/m^3)

T= temperature (^{0}C)

t = time (s)

Q = internal heat generation (W/m^3)

k = thermal conductivity (W/m^{0}C)

This equation (2.5) could be re-written as follows [133];

$$\frac{\partial T}{\partial t} = \frac{k}{c\rho}\left[\left(\frac{\partial^2 T}{\partial x^2}\right) + \left(\frac{\partial^2 T}{\partial y^2}\right) + \left(\frac{\partial^2 T}{\partial z^2}\right)\right] + \frac{Q}{c\rho} \qquad (2.6)$$

Since the property; thermal diffusivity can be introduced into the above equation (2.6), we have Equation 2.7 [133];

$$\frac{\partial T}{\partial t} = \alpha\left[\left(\frac{\partial^2 T}{\partial x^2}\right) + \left(\frac{\partial^2 T}{\partial y^2}\right) + \left(\frac{\partial^2 T}{\partial z^2}\right)\right] + \frac{Q}{c\rho} \qquad (2.7)$$

Where α, represents thermal diffusivity of the material. This governing equation shows that the rate of heat distribution with respect to time is a function of the thermal conductivity, heat capacity and density of the material.

The total heat input supplied to the weld region is described as a volumetric heat flux as shown in Equation 2.8 [134];

$$q = \frac{\eta VI}{v} \qquad (2.8)$$

Where:

η = arc efficiency

V = welding voltage (V)

I = welding current (A)

v = volume (m^3)

q = volumetric heat flux (W/m^3)

The arc efficiency of Gas Metal Arc Welding is commonly found to be between 0.7-0.9.

Also worth considering in the simulation of the fusion welding process is the amount of heat loss due to convection. This is described by the following Equation 2.9 [135];

$$q_c = -h(T_s - T_T) \qquad (2.9)$$

Where;

h = heat transfer coefficient (W/m^2 ^{0}C)

T_s = surface temperature of the material (^{0}C)

T_T= ambient temperature (^{0}C)

Heat loss during transient heat analysis for fusion welding also includes heat loss via radiation. However, such losses are usually ignored during analysis as they are known to have insignificant effects on the overall outcome.

In the thermal analysis for the GMAW process, the description of the heat source is critical to obtaining accurate results. The most well-known method of describing the heat source for this fusion process is called the double ellipsoid Goldark method [136]. In this method, the shape of the weld pool is described by a double ellipsoid with a welding power input given as Equation 2.10 [134]:

$$Q = \eta V I \qquad (2.10)$$

Where;

η= arc efficiency, which is between 0.7 - 0.9 for GMAW

V= welding voltage (V)

I= welding current (I)

The power of the welding arc in the Goldark double ellipsoid model is distributed or described by a Gaussian function of a radial distance from the centre to the interior of the double ellipsoid [136]. The Goldark double ellipsoid model is defined by the following Equation 2.11 [137]:

$$q(x,y,z,t) = \frac{6\sqrt{3Q}}{abc\pi\sqrt{\pi}} e^{\left(\frac{-3x^2}{a^2}\right)} e^{\left(\frac{-3y^2}{b^2}\right)} e^{\frac{-3[z+v+(\tau-t)]^2}{c^2}} \qquad (2.11)$$

Where;

x, y, z is the coordinate system

t is time (s)

Q is heat input rate (W)

$a, b, c,$ are ellipsoid dimension parameters (m)

v is the velocity (m/s)

τ is a lag factor.

A sketch of the ellipsoidal heat source with the ellipsoid dimensional parameters in Figure 2-54 [132];

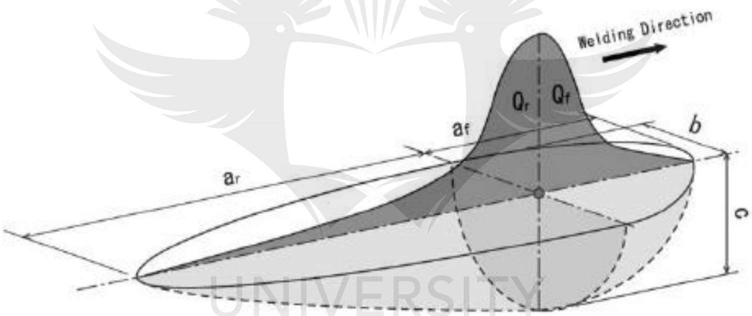

Figure 2-54: Ellipsoidal heat source dimensional parameters [132]

2.12.2 Application of Finite Element Analysis and Simulation to Welding Processes

In the modelling of fusion welding processes, the simultaneous solution of thermal and mechanical fields is usually not recommended, due to the high computational costs [130]. It is more common to solve both fields separately whilst modelling the welding process in a method that is called a staggered solution procedure [137]. This approach splits the modelling process into a thermal analysis, which is followed by mechanical analysis and is usually referred to as a thermo-mechanical analysis [130].

Another procedure of computational welding mechanics which includes a model of the microstructure of the welded materials is called a thermo-metallurgical-mechanical (TMM) analysis [138], [139]. This type of simulation, however, usually ignores the effect of stress and strains on the microstructure [130].

2.12.2.a Residual Stress Determination

One of the most common reasons for welding simulation is to determine the residual stresses and deformations present in a welded sample [130]. This information could, in turn, be used to determine the risk of buckling, fatigue, stress-corrosion cracking etc. [130]. Residual Stresses are simply defined as the presence of stresses within a material in the absence of external load [140]. Residual stresses could be tensile or compressive nature (Figure 2-55), and this largely depends on the location from the heat source and the volumetric changes which could occur due to variation in heating and cooling rates during a welding process [141],[142].

During the welding process, as the heat source approaches a specific point on the material, the increase in temperature leads to an increase in compressive residual stresses. As the heat source reaches the specific point on the materials, the compressive residual stresses decrease and could eventually disappear [143]. As the heat source crosses the specific point of interest on the material, the temperature of the base material gradually begins to reduce, which causes shrinkage in the HAZ of the material [143]. As a result, the highest tensile residual stress values occur along the weld metal zone [143].

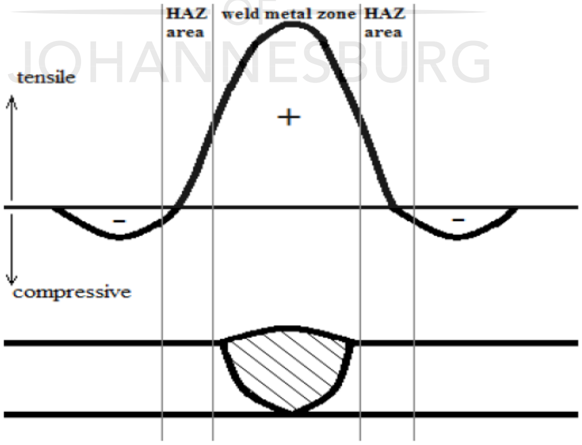

Figure 2-55: Distribution of weld residual stresses in a weldment [143]

The rate of cooling after heat input during the welding process also contributes to the formation of residual stresses within a welded component. Typically, the top and bottom areas of a welded sheet are exposed to high cooling rates either due to forced or natural convection. However, the inner parts of the material are subjected to lower cooling rates (Figure 2-56). These difference in rates of cooling could be responsible for thermal expansions and contractions that may also lead to compressive stresses at the surface and residual stresses in the inner sections of the material. [144]

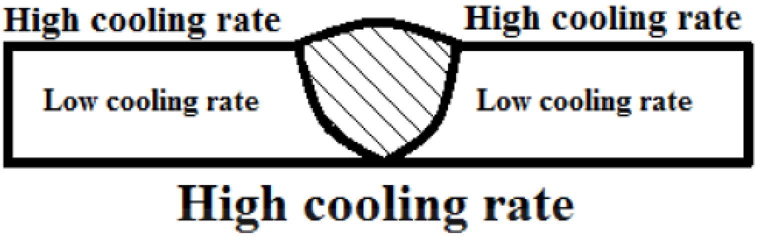

Figure 2-56: Cooling rate in a weldment [143]

2.12.2.b Application of Welding Simulations

Although Radaj [145] in his review of residual stress results obtained from welding simulations, submitted that the use of these results was not as beneficial in some regards, it is still worth considering some applications of welding simulation analysis to solve typical welding problems.

Crack propagations in the presence of residual stresses due to circumferential welds in a core shroud have been studied [146]. It was assumed that initial cracks occurred due to intergranular stress corrosion cracking. The authors computed the stress intensity factors within the weld to determine crack growth. Teng *et. al.* [147]-[148] used finite element analysis of multi-pass welds to obtain residual stresses and subsequently used the results for fatigue analysis in critical areas of the weld. Zhou *et. al.* [149] performed thermo-mechanical finite element analysis to predict the residual stress distribution in a single U-butt weld of 2.25Cr-1Mo-0.25V steel. This was carried out using ANSYS finite element software. The distribution of welding residual stress in the multi-pass weld was shown to be complex [149]. They also showed that the creep damage of the welded joint could be accelerated when the residual stress levels are lowered [149].

Ogino [150] *et. al.* developed a unified numerical model to investigate the influence of shielding gas on metal transfer in GMAW processes. They determined that globular metal transfer occurs when argon shielding gas is used with an arc current less than 230 A, while at higher currents, spray transfer occurred [150]. However, when Ar + 18 % CO_2 gas was used as shielding gas, the transition from globular to spray transfer occurred around 280 A [150]. The authors concluded that this difference was due to the change in the driving force applied to the molten metal by the arc plasma [150].

In another simulation involving metal transfer, Velumani *et. al.* [151] developed a model for a multi-pass GMAW welding process using ANSYS, such that the model accommodates metal transfer and the finite elements “grow” to simulate this transfer (Figure 2-57). The model included temperature-dependent thermo-mechanical properties, convective and radiative boundary conditions, as well as the effect of latent heat [151]. The numerical results were confirmed by experimental results and they were able to demonstrate the application of FEA models to understand multi-pass welding processes [151].

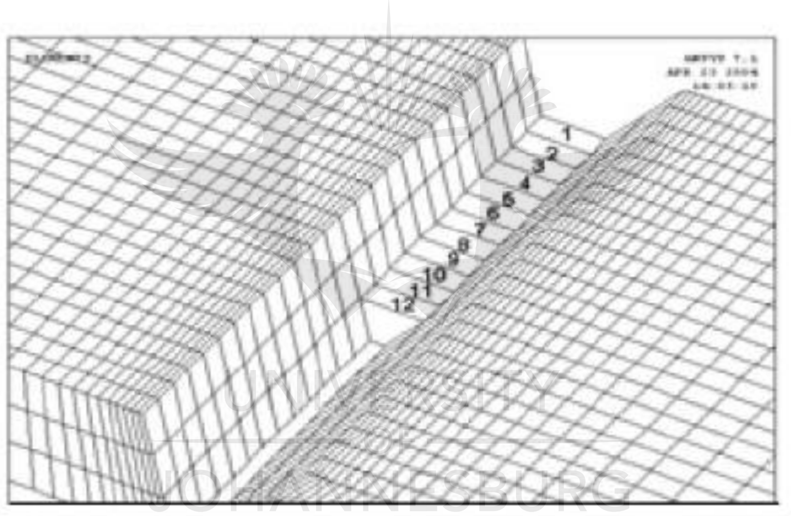

Figure 2-57: Metal deposition of the 12th element step during the first pass of the simulated GMAW process [151]

Velmanaboina *et. al.* [152] developed a 3-D finite element model to simulate the hybrid laser-TIG welding process for SS316L butt joints. The heat flux models were simulated using double ellipsoidal surface heat flux for the TIG process and lateral heat to the thickness face for the laser process [152]. Transient thermal heat analysis was performed to obtain temperature distribution during the fusion process and subsequently to evaluate mechanical stresses and distortion. The work showed that structural integrity with a minimum factor of safety of 1.3 was maintained with the amount of residual stresses calculated [152].

2.13 Conclusion

This review gives an in-depth consideration of the research done so far in improving the weld integrity of steel materials in MIG welding. Evidently, the application of Taguchi's method of orthogonal arrays to optimize process parameters is a popular idea in improving steel weld integrity and has been applied with huge success.

In the specific area of improving the mechanical properties of mild steel welds in MIG welding, quite a lot of work has also been done, such that optimum parameters can be gleaned from literature for certain output characteristics. Despite this, it remains to be seen if the mechanical properties of MIG welded mild steel sheets can be improved beyond what optimum parameters derived from Taguchi's methods, will give. Kathuria and Gupta's [41] work on SAW of mild steel sheets, along with Lin *et. al.'s* [74] work strongly suggest that titanium alloy powder can be added to improve mild steel sheet weldments, this time, in MIG welding. The mechanical properties of titanium alloy powder already suggest that it can act as a good reinforcement of steel welds.

This research could further test for the effect of titanium powder addition, on mechanical properties such as tensile strength and hardness in MIG welding of mild steel sheets. Such research will significantly contribute to the body of literature in this research field and potentially push the boundary for achieving optimum mechanical integrity in weld joints of mild steel sheets.

An in-depth review of the microstructures of iron, steel and typical microstructural evolution in steel due to heat input during welding processes has been discussed. The relationship between microstructural evolution in steel welds and the mechanical properties have been discussed. Titanium alloys and their microstructures have been discussed to understand their possible property contribution in steel-titanium composites when steel welds are reinforced with titanium.

Finally, a brief review of the numerical modelling of welding processes and their usefulness in predicting temperature distribution and residual stresses in weldments have been highlighted and discussed in this chapter.

3. Experimental Methodology

3.1 Introduction

This chapter covers the experimental procedure for this study. The material used in the experimental study is AISI 1008 Mild steel. Experimental MIG welding of mild steel was conducted. The design of experiment adopted for the welding experiment is Taguchi's Orthogonal array. The adoption and implementation of Taguchi's DoE are discussed in this chapter. The characterization tests which include optical microscopy, SEM analysis, XRD and mechanical tests such as tensile and Vickers microhardness tests and their respective equipment are discussed.

3.2 Materials Description

The parent material was 3mm-thick AISI 1008 steel. The reinforcement metallic powders used in the experiment were commercially pure Titanium and Ti 6-2-2-2-2 Titanium alloy. The chemical composition of the parent material is given in Table 3-1.

Table 3-1: Chemical composition of parent material AISI 1008 steel.

Elements	C	Si	Mn	P	S	Cr	Mo	Ni	Al	Fe
% by wt.	0.072	0.068	0.320	0.0098	0.0091	0.042	0.0050	0.0064	0.042	Balance

The electrode used for the MIG welding process is MIG 6000 Plus from Afrox Company in Johannesburg, South Africa. It is an ER 70S-6 copper-coated wire electrode. Its chemical composition is given in Table 3-2.

Table 3-2: Chemical composition of ER 70S-6, MIG 6000 wire electrode

Elements	C	Mn	Si	Cu	Fe
% by wt. (max)	0.15	1.85	1.15	0.5	Balance

3.3 Development of Experimental Design

The experimental work employs parametric optimization to attain welds joint quality. Taguchi's method of Design of Experiments was adopted to carry out the first stage of experiments for this study. This design method involves selecting a pre-determined orthogonal array which is derived from a selection of chosen factors and levels. This orthogonal array selection allowed for the efficient combination of varied parameters. The experimental design was followed by a signal-to-noise ratio analysis and then the analysis of variance (ANOVA) to determine the significance of titanium powder addition to the welded mild steel joints if any. The experiments were carried out on two weld joint configurations; butt joint and lap joints.

In the second stage of the experimental work, optimized welding runs were carried out with titanium powder reinforcement. These were compared with specimens welded with the same optimized parameters but without titanium powder reinforcements. The comparison of both sets of weldments provided the required data to conclude on the effect of the metallic powder reinforcement on the mechanical properties of the weldment.

3.3.1 Weld Joint Design

In this study, seventy-two (72) mild steel sheets were cut using a Guillotine machine. Thirty-six (36) of the specimens were prepared for lap-joint configuration with dimensions of 100mm x 40mm x 3mm. The other thirty-six (36) specimens were reserved for butt-joint welding configuration with dimensions of 150mm x 40mm x 3mm. The samples reserved for butt-joint configuration were milled to create a 45^0 groove (Figure 3-1). The samples reserved for lap joint welding were milled using a 2-mm end mill to create a groove 40 mm x 2 mm x 0.5 mm (Figure 3-1). These grooves were filled with the titanium powders before welding was done. All specimens were mechanically cleaned with sandpaper and treated with acetone to ensure clean surfaces for welding.

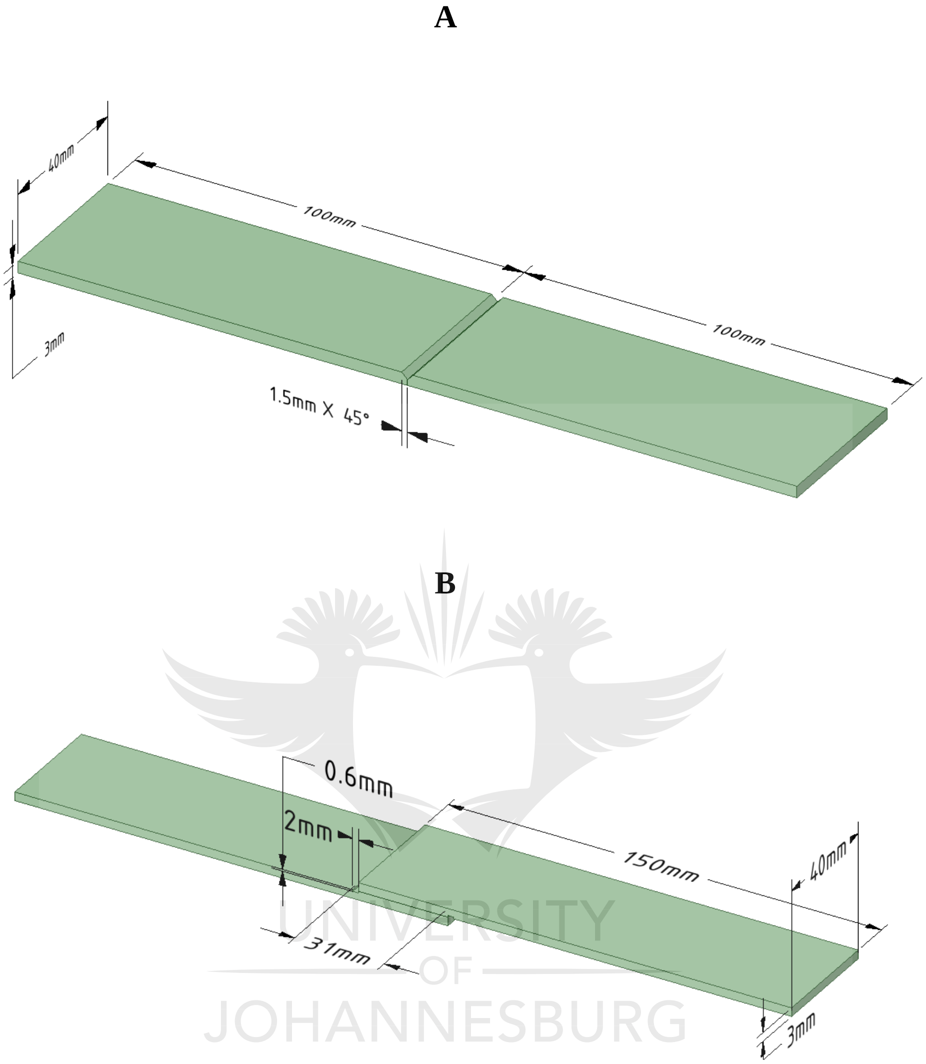

Figure 3-1: Dimensions of (a) butt and (b) lap joint steel sheets

3.3.2 Taguchi Methods

Taguchi's Design of Experiment method is one amongst other types of experimental design methods used to plan experimental studies. Other common experimental design methods are full factorial method and response surface methodology (RSM), which has been mentioned in the preceding chapter. The Taguchi's design of experiment method was preferred for this study because of its efficient and economical approach. This method cuts down the number of experimental runs required for experimental studies and still gives excellent results due to its robust design. [50]

The application of Taguchi's design method is summarized in three basic steps. First, an orthogonal array was selected from a set of predefined arrays based on the selected experimental factors and levels. This orthogonal array defined the conditions for each experimental run. After the experiments were carried out, a signal-to-noise ratio analysis was carried out to determine the optimum input parameters. Lastly, the analysis of variance was used to determine the significant factors responsible for a defined output response.

3.3.3 Selection of Orthogonal Array

The selected design factors for optimization were the welding voltage, welding current and reinforcement powder. The factors were each given two levels. This was decided to reduce the number of experiments considering that the same experiments were to be carried out for butt and lap configurations.

Table 3-3 shows a design matrix for a two-level, three-factor experiment.

Table 3-3: Experimental Parameters in notation form

Factors	A	B	C
Level 1	1	1	1
Level 2	2	2	2

To determine the number of runs for the experimental procedure, the total degrees of freedom for the experiment was first determined as illustrated in Equation (3.1).

$$Degree\ of\ Freedom, DOF = No.of\ Levels - 1\ -----------(3.1)$$

The Degree of Freedom (DOF) is defined as the number of ways a system can independently vary when a constraint is imposed. In the case of a three-level factor, the DOF is given in equation (3.1) for each factor. The total DOF for the experiment is given by Equation (3.2):

$$\sum\nolimits_{i=1}^{k}(L_k - 1)\ -----------------\ (3.2)$$

Where L represents each level, and k is the number of levels. Using equations (3.1) and (3.2), the total degrees of freedom is given as shown in Table 3-4;

Table 3-4: Determination of Degrees of Freedom

Factors	Levels (L)	Degrees of Freedom ($DOF = L - 1$)
Welding Voltage	2	1
Welding Current	2	1
Powder Reinforcement	2	1
	Total DOF $\sum_{i=1}^{k}(L_k - 1)$	3

The total number of experiments required is given by the Equation 3.3:

$$T_{experiments} = 1 + \sum_{i=1}^{k}(L_k - 1) - - - - - - - - - - - -(3.3)$$

This gives us, $3 + 1 = 4$

Therefore, the selected orthogonal array should accommodate a 3-factor, 2-level experiment with a minimum of 4 experimental runs (Equation 3.4), i.e.

$$Selected\ number\ of\ experimental\ runs\ \geq 4 - - - - - - - - - - - -(3.4)$$

From the standard orthogonal arrays, the most suitable selection is an L_4 array. It allows for a maximum of three factors at two levels, with four experimental runs as presented in Table 3-5.

Table 3-5: L4 Orthogonal Array

Experiments	A	B	C
1	1	1	1
2	1	2	2
3	2	1	2
4	2	2	1

Therefore, the adopted orthogonal array with the relevant parameters for the butt joint configuration is given in Table 3-6. Final experimental values were derived by a combination of consultation from welding handbooks and direct observation of weld quality during pilot runs.

Table 3-6: Orthogonal Array with Experimental Values for Butt joints

Experiments	Voltage (V)	Current (A)	Reinforcement Powder
1	22	120	Commercially pure Titanium
2	22	130	Ti-2-2-2-2 alloy
3	24	120	Ti-2-2-2-2 alloy
4	24	130	Commercially pure Titanium

The butt joint experiments were first carried out. Microstructural observation of defects in these welds informed the decision to increase welding parameters for the lap joints. Table 3-7 gives the parametric values used for the lap welds.

Table 3-7: Orthogonal Array with Experimental values for lap joints

Experiments	Voltage (V)	Current (A)	Reinforcement Powder
1	23	215	Commercially pure Titanium
2	23	240	Ti-2-2-2-2 alloy
3	26	215	Ti-2-2-2-2 alloy
4	26	240	Commercially pure Titanium

Welding speed was kept at approximately 24 cm/min and the gas flow rate was kept constant at 15 L/mm. The difficulty in keeping welding speed constant is due to the semi-automatic arc welding machine used. The experiments were conducted randomly, and each experimental run was repeated three times to account for errors.

3.4 Experimental Setup for MIG Welding of Steel

The welding was conducted using a Miller XMT-400 series model MIG welding machine set up at South African Institute of Welding, Johannesburg (Figure 3-2). For the butt-joint weldment, two workpieces, each of dimensions 100 x 40 x 3 mm with a 45^0 groove machined across its width, were clamped together (Figure 3-3). The selected titanium powder was introduced into the groove and the welding operation was done in one pass using direct current electrode positive (DCEP). Twelve experimental runs were carried out for this joint configuration.

Figure 3-2: Miller XMT-400 series MIG welding machine

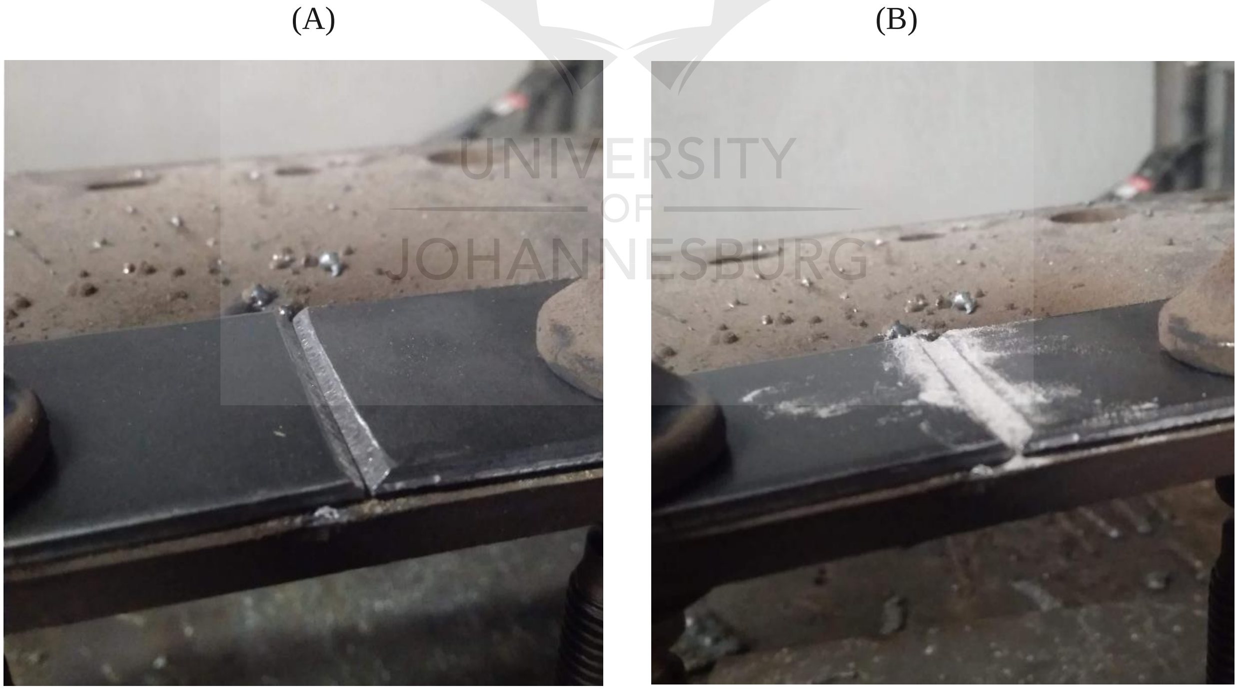

Figure 3-3: Set up for butt joint configuration, A) before introducing titanium powder B) after introducing titanium powder

For the lap welding configuration, two workpieces of dimensions 150 x 40 x 3 mm were clamped with an overlap of 30 mm allowed to create the lap joint (Figure 3-4). A groove 0.4 mm deep, 2 mm wide and 40 mm across the width of the sheet was machined on each sheet. The selected titanium powder was introduced to the groove and the welding operation was conducted in one pass also using direct current electrode positive (DCEP). Twelve experimental runs were also conducted for this configuration.

Figure 3-4: Set up for lap joint configuration

For both joint configurations, the shielding gas used was Agroshield 5 shielding gas supplied from Afrox company, South Africa. It is made up of a combination of Argon, CO_2 and O_2 gases. This shielding gas is specifically prepared for MIG welding of mild steel. The electrode used for both experiments was MIG 6000 Plus supplied from Afrox company in Johannesburg, South Africa. It is a type ER70S-6, 1.2 mm thick wire electrode designed for MIG welding of mild steel sheets.

3.5 Material Characterization Methods

The purpose of characterization tests is to determine the physical and metallographic properties of the samples. This is also done to obtain data that can be statistically analyzed to determine the effects of the process parameters on the quality of the samples. Before characterization tests were carried out, the samples were prepared according to ASTM E3-11 [153] standard for metallographic sample preparation.

3.5.1 Test Sample Preparation

A) Cutting: The samples were cut using a Mecatome T300 cut-off machine; a wet abrasive cut off machine which is shown in Figure 3-5. The samples were cut using a consumable SiC abrasive cut off wheel. The wheel was first inserted into the machine and tightened properly. The already marked out samples were inserted and clamped appropriately. The cut-off machine hood was closed, and the coolant tap turned on. The coolant was fed at 90^0 to the cut-off wheel for optimal cooling. By carefully applying pressure using the cutting handle, sample sizes of 20mm x 10mm were cut for microhardness testing and microstructural examination.

Figure 3-5: Mecatome T300 wet abrasive cut-off machine

B) Mounting: For the samples to be properly ground and polished before microstructural characterization, they had to be mounted. Mounting was done using pneumatic water-cooled automated hot compression mounting press supplied by Struers (Figure 3-6). In the mounting process, heat and pressure are applied to melt the resin around the sample and then subsequently cooled for solidification. Black Polyfast was used as mounting resin because it is preferred for subsequent scanning electron microscopy (SEM) tests. Each mounted specimen was then properly labelled before grinding and polishing. The parameters used for the mounting process are given in Table 3-8.

Figure 3-6: Struers Cito-Press Automated Mounting Press

Table 3-8: Mounting Parameters

Mounting Parameters	
Resin	Polyfast
Heating Time	3.5 mins
Temperature	180^0 C
Pressure	250 bar
Cooling Time	1.5 mins
Rate	High

C) Grinding and Polishing: The mounted specimens were first subjected to plane grinding and then fine grinding (Figure 3-7). The purpose of fine grinding is to rid the sample of any damage that might have occurred during cutting. Fine grinding reduces the surface roughness to a degree that is suitable for polishing. After grinding was completed, the samples were polished as per specifications. Diamond polishing removes scratches introduced to the sample during grinding. Table 3-9: Grinding and Polishing process gives details of the grinding and polishing processes.

Figure 3-7: Labopol 25 Grinding and Polishing machine

Table 3-9: Grinding and Polishing process

Step	**Plane Grinding**			**Fine Grinding**	**Diamond Polishing**	**Oxide Polishing**
Surface	FEPA SiC Paper 320	FEPA SiC Paper 500	FEPA SiC Paper 800	FEPA SiC Paper 1200	MD Dac	MD Chem
Suspension	-			-	DiaPro Dac 3µm	OP-S
Lubricant	water	water	water	water	-	-
Speed (rpm)	300	300	300	300	150	150
Force (N)/sample	25	25	25	25	20	20
Time	Until plane	4 mins	4 mins	2 mins	2 mins	1 min

D) Etching: The samples were etched to reveal the microstructures. The etchant used for the specimens was 3% Nital. This was made by mixing 3 ml of nitric acid in 100 ml of ethanol. Nital was applied to the specimen surface for 15 seconds using absorbent cotton buds, until a cloudy surface was observed, signalling the corrosion of the surface by the etchant. After this observation was made, the samples were immediately dipped in water, rinsed with acetone and subsequently dried with a hand dryer.

3.5.2 Optical Microscopy

Samples of the welded specimens were subjected to microstructural examination using an Optical microscope Olympus BX 51M (Figure 3-8). The microscope has two lenses; objective lens and eyepiece lens. The product of the magnification of both lenses is the final magnification of the sample. Optical microscopy was done to investigate the various welding zones, the shape of the weld and variation in grain sizes at different weld zones.

Figure 3-8: Olympus BX 51M Optical Microscope

3.5.3 Scanning Electron Microscopy (SEM)

Further microstructural examinations were carried out using a TESCAN scanning electron microscope (SEM) is shown in Figure 3-9. The TESCAN SEM which was equipped with Energy Dispersive Spectroscopy (EDS) was used to study the chemical composition and morphology of the reinforcing titanium. It was also used for failure analysis of the optimized butt samples after fracture takes place. The working principle of SEM involves a release of high-intensity electron beams resulting in the reflection of electrons from the sample, which are captured as high-resolution images. In the case of EDS, characteristic x-rays are reflected from the sample and captured to identify the chemical elements present and their distribution within the sample.

Figure 3-9: TESCAN Scanning Electron Microscope

3.5.4 X-Ray Diffraction Analysis (XRD)

The optimized specimens were also subjected to X-ray diffraction analysis. The purpose of this analysis was to further study the structure, composition and phase purity of the optimized weldments. XRD works by shooting an incident x-ray beam on the sample, which diffracts to many directions. The angle and intensity of diffraction are captured and used to map the crystallographic structures within the specimen. Figure 3-10 shows the Rigaku Ultima IV X-ray Diffractometer, used for characterization in this study.

Figure 3-10: Rigaku Ultima IV X-ray Diffractometer

3.6 Mechanical Testing

To determine the mechanical properties of each experimental specimen, mechanical tests were carried out. The tests conducted are standardized mechanical tests as prescribed by ASTM testing standards. For this study, the following mechanical tests were carried out;

1. Tensile Strength Testing
2. Vickers Hardness Testing

3.6.1 Tensile Strength Testing

The specimens were prepared for tensile strength testing on Zwick Roell 2250 tensile testing machine (Figure 3-11). Each sample was prepared according to standard ASTM E8/E8M-16a [154] dimensions for tensile testing of metallic materials. The dog-bone shaped test sample was machined to standard dimensions. The dimensions are summarized in Table 3-10;

Figure 3-11: Zwick Roell 2250 tensile testing machine

Table 3-10: Standard ASTM E8/E8M-13a Tensile test sample dimensions

Standard ASTM E8/E8M-13a	Dimensions (mm)
Gauge Length	50
Width	12.5
Radius of fillet	12.5
Overall Length	200
Length of Reduced Section	57
Length of Grip Section	50
Width of Grip Section	20

The tests were conducted using an apex load of 100KN and at a crosshead rate of 3 mm/min, which is prescribed by the ASTM E8/E8M-13a testing standard. Each sample was subjected to tensile forces until failure occurred. The tensile machine recorded digitally, in real-time the required stress and strain data for further analysis. These values were collected and recorded for statistical analysis. For the final stage of the welding, the lap shear tensile shear test of the lap joint was carried out using ASTM D1002 [155] prescribed standards.

3.6.2 Microhardness Indentation Testing

A digital indenter microhardness tester was used to determine the hardness quality of the welded joints (Figure 3-12). It reveals the resistance of the material to plastic deformation. The test was conducted according to ASTM E384 [156] testing standard for Vickers Microhardness testing.

Figure 3-12: Digital Vickers Micro hardness Testing Machine

To obtain microhardness values, a force of 300 g was applied to make a diamond-shaped indentation on the sample with a dwell time 15 seconds. The dimensions of the diamond-shaped indentation were measured by the digital indenter and used to calculate the value of microhardness at the indented point. This is achieved by dividing the applied load with the surface area created by the indentation. The indentations were made across the fusion zone, through the heat-affected zone and to the base metal to understand the microhardness profile of the specimen.

The hardness values obtained were recorded for statistical analysis.

3.7 Numerical Analysis

The methodology of the finite element analysis of the MIG welding process is discussed in the section with respect to the governing equations, temperature-dependent properties, geometry and analysis settings.

3.7.1 Finite Element Analysis: Governing Equations

A non-linear transient heat conduction analysis was carried out using the Finite Element Analysis software, ANSYS. Certain mathematical equations were used to model the heat conduction within the material, boundary conditions of the welding heat source and convective heat loss. These equations are highlighted in this section.

The non-linear heat conduction is governed by the three-dimensional Fourier Heat Conduction Equation 3.5 [133] given below ;

$$\frac{dT}{dt} = \frac{k}{\rho C_p}\left[\frac{\delta^2 T}{\delta x^2} + \frac{\delta^2 T}{\delta y^2} + \frac{\delta^2 T}{\delta z^2}\right] + \frac{q}{\rho C_p} - - - - - - - - - (3.5)$$

Where k represents thermal conductivity; ρ represents the density; C_p represents specific heat capacity at constant pressure; q represents the heat energy generated from the domain, t represents time and T represents temperature. This equation describes the heat flow in three-dimensions along the x, y and z axes. When applied to welding, the heat generation term q is zero, as no heat is generated by the welded material.

Natural convective heat flow, which is one of the boundary conditions governing heat loss from the domain to the surroundings is defined by Equation 3.6 [135] below;

$$q = h(T - T_\infty) - - - - - - - - - - - (3.6)$$

q represents the convective heat flux in Wm^{-2}. h represents the heat transfer coefficient of the surrounding, which is not a material property, rather, it is calculated. T and T_∞ represent the temperature of the domain and ambient temperature respectively.

The convective heat transfer coefficient of air is determined by Equation 3.7 [149];

$$h_c = 10.45 - v + 10v^{\frac{1}{2}} \qquad 2 \leq v \leq 20\,\frac{m}{s} - - - - - - - - - - (3.7)$$

For this analysis, forced convection due to the shielding gas and radiative heat loss were assumed to be negligible and therefore not considered.

The thermal heat-source for the MIG welding process was described using a modified gaussian distribution equation [134] as shown in Equation 3.8;

$$q(x, y, t) = \frac{3Q}{\pi r_0^2} e^{\left(-3\frac{r^2}{d_0^2}\right)} - - - - - - - - - - - (3.8)$$

Where Q represents the heat input rate. r_0 represents the effective radius of the welding arc and d_0 represents the diameter of the welding arc.

r is defined by Equation 3.9

$$r(x, y, t) = (x - x_0)^2 + (y - vt - y_0)^2 \; - - - - - - - - - - (3.9)$$

Where x_0 and y_0 represent the distance of the heat source from the origin of the reference coordinate system along the x-axis and y-axis respectively. v is the travel speed of the welding arc and t is the time.

The heat input rate Q in equation 10 is given by Equation 3.10 [134]

$$Q = \frac{\eta V I}{v} - - - - - - - - - - - (3.10)$$

Where η represents the thermal efficiency of the welding process and is typically given as 0.9 for MIG welding. V represents the welding voltage in Volts. I represents the welding current in Amps and v is the welding speed given in mm/s. Heat input rate, Q, is given in J/mm.

3.7.2 Temperature-Dependent Properties

Thermal conductivity and specific heat capacity are material properties that vary with temperature. These temperature-dependent properties for low carbon mild steel (Table 3-11) and typical $\alpha + \beta$ titanium alloys (Table 3-12) were sourced from literature. Due to unavailable data, the density of mild steel was kept constant, despite being a temperature-dependent property. The increase in specific heat capacity beyond the melting point of the material is applied to make up for the convective heat flow in the melting pool [157].

Table 3-11: Temperature-dependent properties of mild steel [158]

T (^{0}C)	**Thermal Conductivity (W/m K)**	**Specific Heat (J/Kg K)**
0	51.9	450
100	51.1	499.2
300	46.1	565.2
450	41.05	630.5
550	37.5	705.5
600	35.6	773.3
720	30.64	1080.4
800	26.0	931
1450	29.45	437.93
1510	29.7	400
1580	29.7	735.25
5000	42.2	400

Table 3-12: Temperature-dependent properties of titanium [157]

Temperature (^{0}C)	**Density (Kg/m^3)**	**Thermal Conductivity (W/m ^{0}C)**	**Specific Heat (J/Kg ^{0}C)**
20	4420	7	546
500	4350	12.6	651
995	4282	22.7	753
1100	4267	19.3	641
1200	4262	21	660
1600	4198	25.8	732
1700	3886	83.5	831
1800	3818	83.5	831

3.7.3 Geometry

Two geometries were created for each butt and lap joint configuration (Figure 3-13a-b); one geometry had titanium reinforcement and the other did not. The space occupied by titanium in the reinforced weldments were replaced by the weld metal in the unreinforced weldment. For ease of computation, the titanium powder particles were collectively modelled as a single solid.

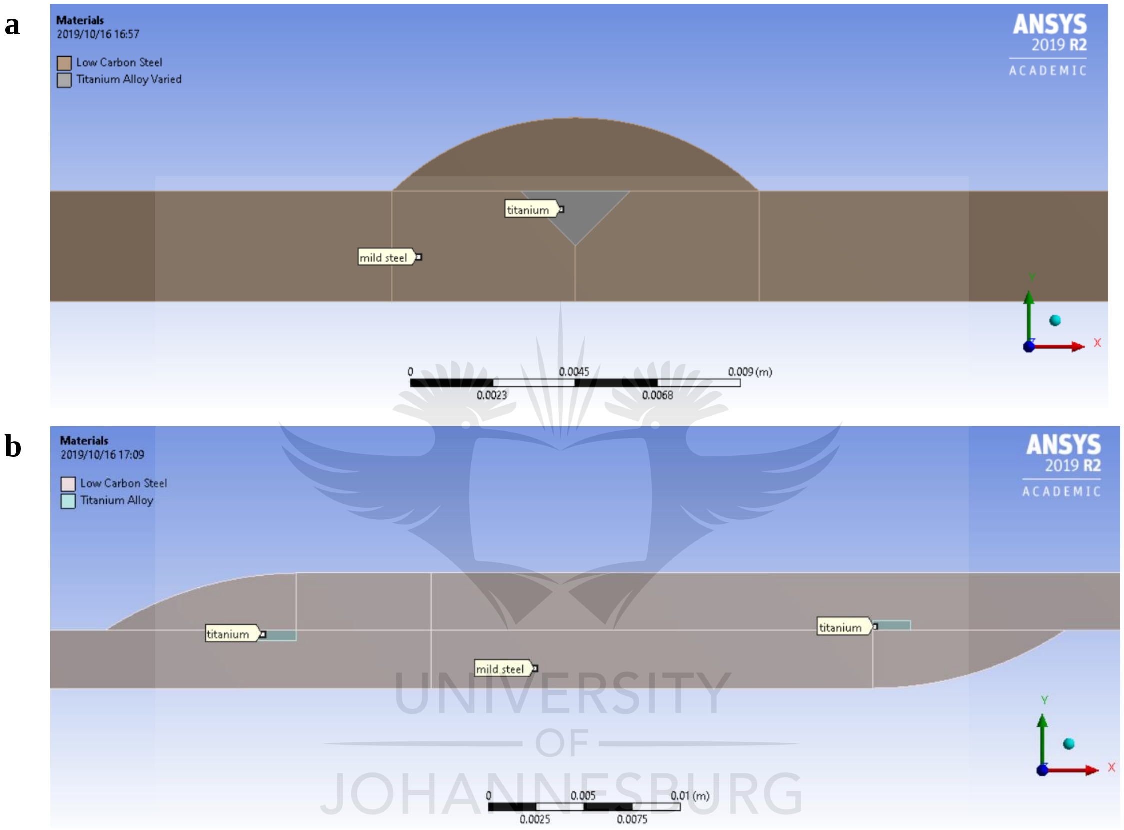

Figure 3-13: Weld geometry of reinforced (a) butt weld joint and (b) lap joint

Figure 3-14 shows the meshing of the butt and lap joints. To ensure accuracy, the elements in the weld metal (WM) region and heat-affected zone (HAZ) were made finer due to the sensitivity of the temperature gradient in these regions. Predominantly hexagonal elements were used for the mild steel plates while tetrahedral elements were used in the WM region due to its curvature. All elements were of the quadratic order.

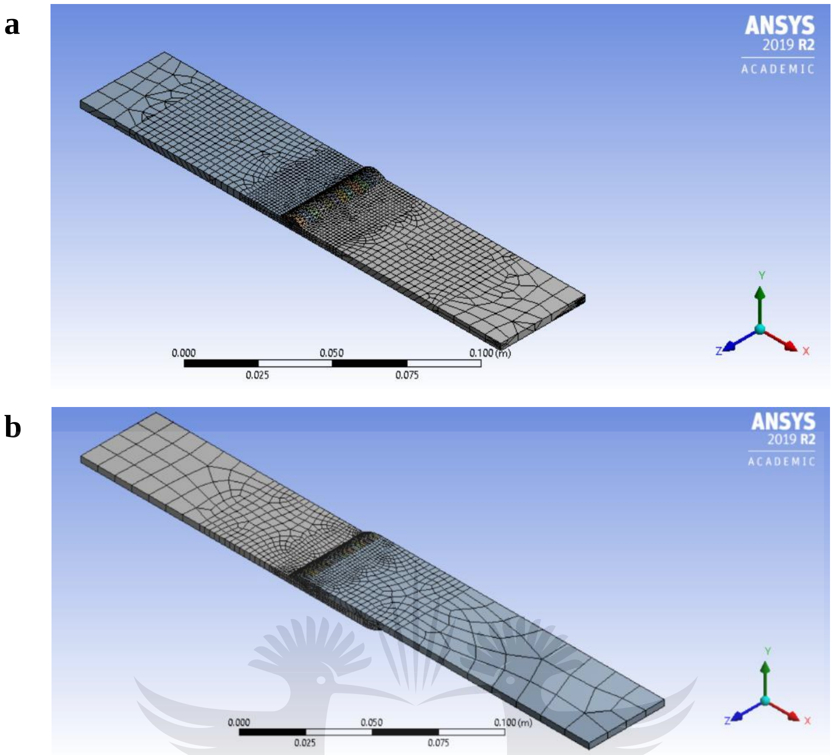

Figure 3-14: Mesh of (a) butt joint and (b) lap joint

The meshing statistics are given in Table 3-13. The nodes and elements for the reinforced joints are slightly more than their unreinforced counterparts, due to the finer mesh of the titanium reinforcement.

Table 3-13: Meshing statistics of butt and lap joints

	Butt Joints		Lap Joints	
	Reinforced	Unreinforced	Reinforced	Unreinforced
Nodes	30 336	29 638	31 585	29 949
Elements	8 617	8 317	7 352	7 124

To simulate the metal deposition of the weld metal, the weld metal geometry was subdivided into 12 and each subdivision was sequentially activated using “element birth and death” method. The time of activation of each subdivision of the weld metal was in sync with the total time taken during the welding experiment, which was an average of 6 seconds.

3.7.4 Boundary Conditions and Analysis

The modified Gaussian equation used to model the heat source from the welding torch was defined using ANSYS APDL's function editor and was imported from its command window into ANSYS Mechanical as a command script. The convective heat loss boundary condition was applied on all side surfaces and the bottom surface of the joints. Applying the heat source and convective heat loss boundary conditions to the lap joints was more complicated because the welding was done at the top and bottom of the sheets. To simulate this, two transient thermal models were created and linked in ANSYS workbench as shown in Figure 3-15

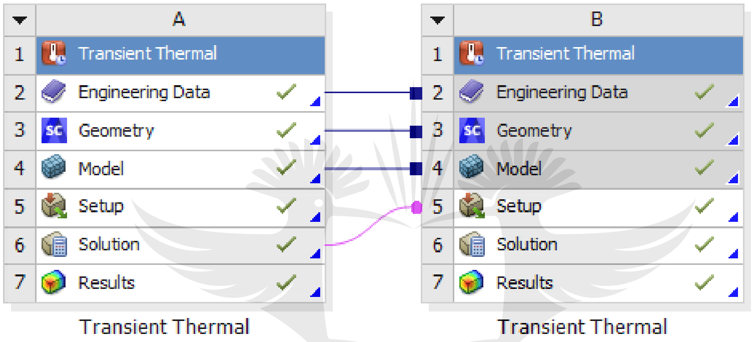

Figure 3-15: ANSYS Workbench layout for lap joint analysis

The temperature field solution from the application of the first heat source was linked to the setup of the second heat source. The same method of application of boundary conditions for the butt joints was implemented for both transient thermal objects in Figure 3-15. The convective film coefficient of air for indoor conditions was calculated to be 22.5 W/m^2 ^{0}C, using Equation 7. The ambient temperature of the room was set at 25 ^{0}C.

The simulation for the butt joints was done for 2000 s till the sheets reached ambient temperature. For each transient thermal object of the lap joint simulation, the analysis was done for 1600 s, resulting in a total analysis time of 3200 s. The temperature field and temperature history at selected points in the domain were obtained from the analysis and correlated with the microstructures observed across the weld zones.

3.8 Summary

This chapter discussed the experimental design of the study which includes the full application of parametric optimization using Taguchi’s Design of Experiment Method. The experimental setup and execution of MIG welding were discussed. The material characterization and mechanical properties tests were discussed, detailing the specimen preparation for the tests and the equipment used to carry out characterization tests. The governing equations and methodology for numerical analysis of the welding process using ANSYS Mechanical FEA software have been discussed.

With the purpose of this study being to determine the effect of titanium powder reinforcements on MIG welding of steel sheets, the methodology discussed in this chapter allows for the obtainment of the necessary results required for analysis, which is discussed in the following chapter.

4. Results and Discussions

4.1 Introduction

In this chapter, the results of parametric optimization of butt and lap MIG welded joints using Taguchi's DoE are presented and discussed in detail, with respect to ultimate tensile strength performance. Microhardness and optical microscopy characterization of the samples used for optimization are also presented and discussed. The mechanical testing and characterization results of the final welding of the optimized samples vis-a-vis the effect of titanium powder reinforcement is presented and discussed in detail.

FEA results from ANSYS are also presented, discussed and correlated with the microstructural evolution across the weld zones. Finally, the temperature field obtained from the numerical analysis is used to predict the weld pool (weld bead) geometry and compared with experimentally obtained weld bead dimensions for process validation.

4.2 Parametric Optimization Results

As earlier discussed in the previous chapter, process optimization was carried out with the adoption of Taguchi's DoE and an L4 orthogonal array for both butt and lap joints configuration.

4.2.1 Visual Weld Observation

Figure 4-1 depicts the top surface visual appearance of the butt joints and the description is given in Table 4-1

A.

B.

C.

D.

Figure 4-1: Visual Inspection of Butt Joint Welds

A) Sample B1, welded at 22V, 120A with commercially pure titanium reinforcement.

B) Sample B2, welded at 22V, 130 A with Ti 6-2-2-2-2 reinforcement

C) Sample B3, welded at 24V, 120A with Ti 6-2-2-2-2 reinforcement.

D) Sample B4, welded at 24V, 130 A with commercially pure Titanium reinforcement

Table 4-1: Visual description of butt joint welds

Sample No.	Description/Observation
B1	**22V, 120A, Commercially Pure Titanium**
a	Normal bead width, Good weld, no spatter
b	Normal bead width, Okay weld, Some spatter visible
c	Okay weld, spatter present
B2	**22V, 130A, Ti 6-2-2-2-2 Alloy**
a	Normal bead width, Good weld, minimal spatter, small crater present.
b	Normal bead width, Good weld, no spatter, small crater present.
c	Normal bead width, Good weld, no spatter, small crater present.
B3	**24V, 120A, Ti 6-2-2-2-2 Alloy**
a	Wide and flat bead, good weld, no spatter, small crater present.
b	Wide and flat bead, okay weld, very little spatter, small crater present.
c	Wide and flat bead, good weld, very little spatter
B4	**24V, 130A, Commercially Pure Titanium**
a	Normal bead width, Good weld, very little spatter.
b	Normal bead width, Good weld, very little spatter, small crater present.
c	Normal bead width, Good weld, very little spatter, small crater present.

The visual appearance of the lap joints weldments is shown in Figure 4-2

A) Sample L1, welded at 23V, 215A with commercially pure Ti reinforcement.

B) Sample L2, welded at 23V, 240A with titanium 6-2-2-2-2 alloy reinforcement

C) Sample L3, welded at 26V, 215A with Titanium 6-2-2-2-2 alloy reinforcement

D) Sample L4, welded at 26V, 240 A with commercially pure Ti reinforcement

Figure 4-2: Visual Inspection of Lap Joint Welds

Table 4-2 presents the visual inspection report for the lap joint weldments shown in Figure 4-2

Table 4-2: Visual observation of lap joint welds

Sample No.	**Description/Observation**
L1	**22V, 215A, Commercially Pure Titanium**
a	Top: fairly good weld, lack of fusion at the toe, little spatter. Bottom: Okay weld, little spatter present.
b	Top: Good weld, little spatter. Bottom: Good weld, no spatter.
c	Top: Okay weld, little spatter. Bottom: Good weld, spatter present.
L2	**23V, 240A, Ti 6-2-2-2-2 Alloy**
a	Top: Good weld, little spatter. Bottom: Good weld, no spatter.
b	Top: Good weld, little spatter. Bottom: Good weld, no spatter.
c	Top: Good weld, no spatter. Bottom: Good weld, no spatter.
L3	**26V, 215A, Ti 6-2-2-2-2 Alloy**
a	Top: Good weld, wide bead, no spatter, small crater present. Bottom: Good weld, wide bead, no spatter, small crater present.
b	Top: Good weld, wide bead, no spatter. Bottom: Good weld, wide bead, no spatter.
c	Top: Good weld, wide bead, no spatter. Bottom: Good weld, wide bead, no spatter.
L4	**26V, 240A, Commercially Pure Titanium**
a	Top: Good weld, no spatter, small crater present. Bottom: Good weld, no spatter, very small crater present.
b	Top: Good weld, no spatter, very small crater present. Bottom: Good weld, no spatter.
c	Top: Good weld, no spatter, very small crater present. Bottom: Okay weld, no spatter, minimal lack of fusion at the top toe.

It was clearly observed that wider beads were obtained at B3 and L3 samples for the butt and lap joints respectively. This could be attributed to higher welding voltage and appropriate corresponding welding current. Srivastava and Garg [44] in the GMAW welding of mild steel showed that higher voltage and wire feed rate, which is directly proportional to the current (when using a constant voltage semi-automatic welding machine), results in wider and higher beads. Jahanzaib *et al.* [159] also showed that weld bead width and penetration are mostly influenced by current. In the samples with higher currents, but the same welding voltage (B4 and L4), the beads are not as wide. This suggests that there could be an optimum range of welding current during which wider beads are produced. However, this cannot be ascertained from these results due to a non-linear increase in the welding parameters over successive experimental runs. For this same reason, the role of the metallic powder reinforcements on the bead shape can also not be definitively ascertained from these results.

The presence of spatter in some of the welds could be attributed to the mode of metal transfer during the welding process. A globular metal transfer is known to contribute to the formation of spatter, while spray transfer typically does not form spatter [26]. Craters are typical features that occur at the end of a weld run, there was no crater crack present in all the craters seen on the weldment. None of the weldments had surface porosity. This testifies to the effective supply of inert gas during the welding process.

4.2.2 Morphology of Titanium Powder Reinforcements

Commercially pure titanium and Ti 6-2-2-2-2 alloy were used as metallic powder reinforcements during the optimization process, their morphologies and elemental composition are given hereafter.

4.2.2a Commercially Pure Titanium

Figure 4-3a shows the morphology of Commercially Pure Titanium under SEM. The size of the powder particles ranges from ≈ 40.54µm to 95.12µm (Figure 4-3b).

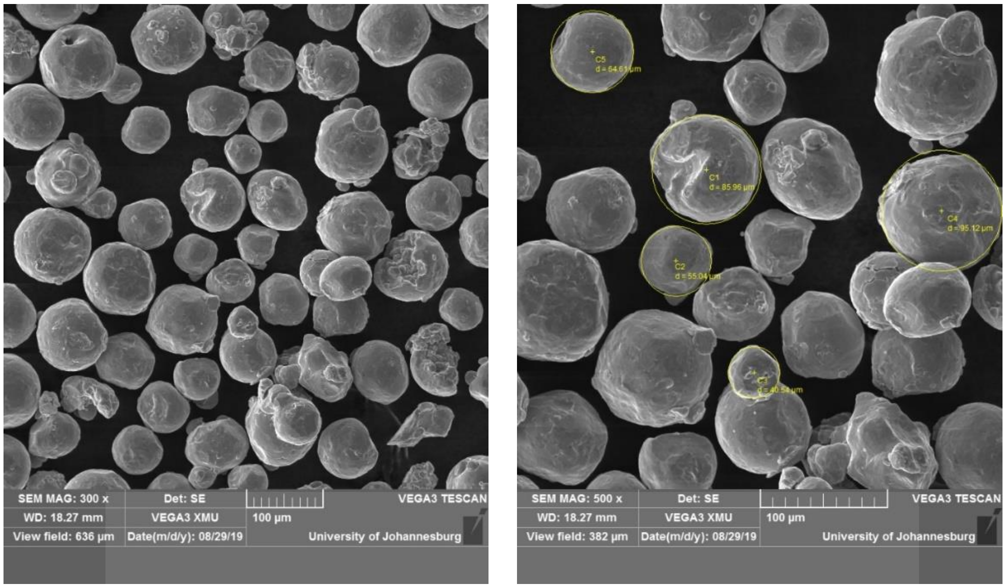

(a) **(b)**

Figure 4-3: Morphology of commercially pure Titanium

An EDS of a sample of the powder is given in Figure 4-4. The elemental composition shows the purity of the titanium powder. This is further highlighted in Table 4-3, which shows the chemical composition of the powder titanium to be 100 %.

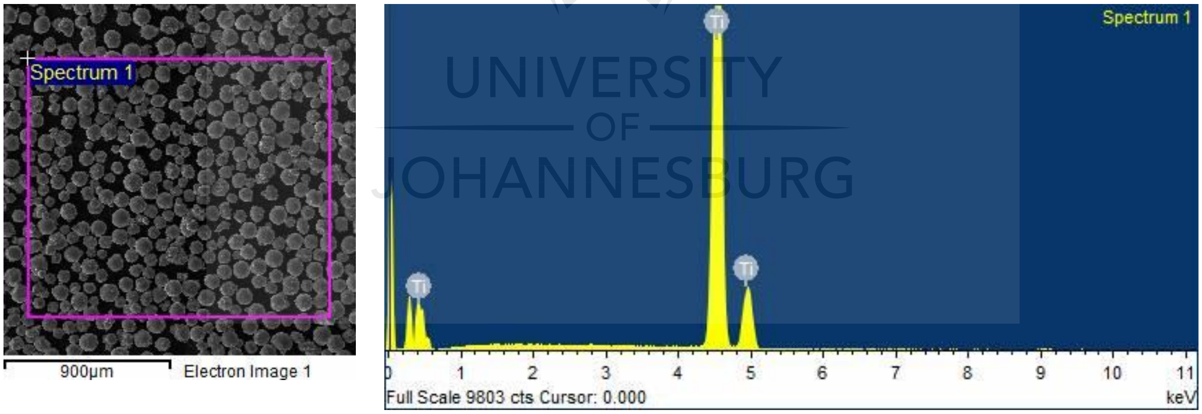

Figure 4-4: EDS of commercially pure titanium

Table 4-3: Chemical Composition of CP Titanium powder from EDS

Element	Weight %	Atomic %
Titanium	100	100
Total	100	

4.2.2b Ti 6-2-2-2-2 Alloy

Figure 4-5a shows the morphology of Ti 6-2-2-2-2 alloy as revealed under SEM. The size of the powder particles is shown to range from ≈19.88µm to 83.34µm (Figure 4-5b)

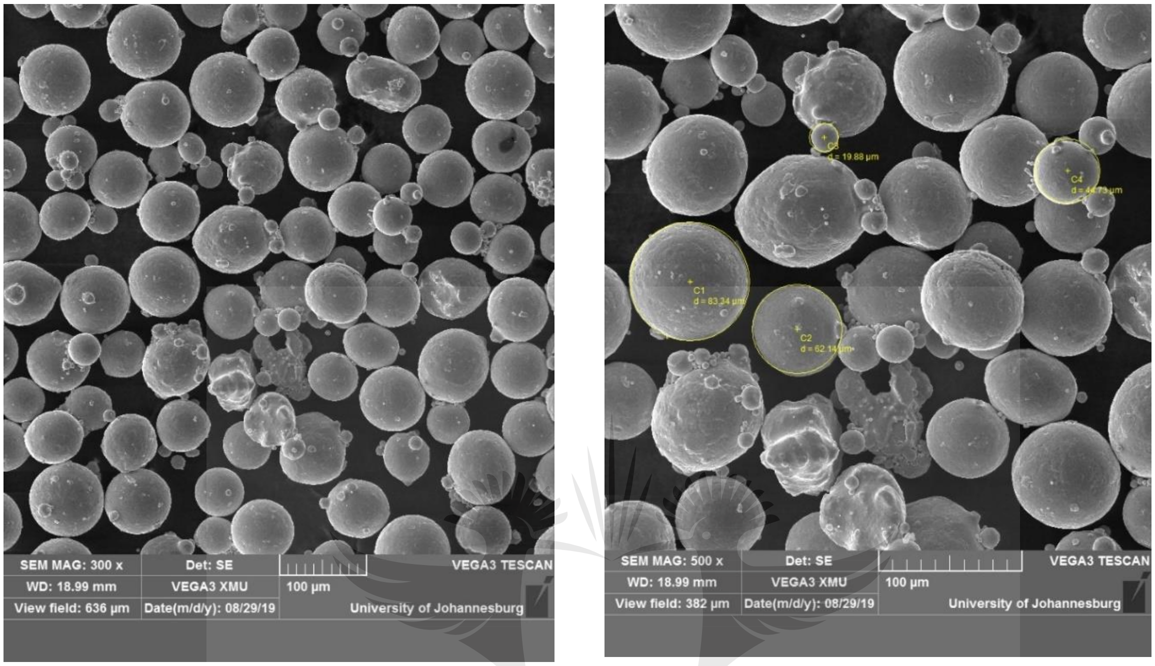

(a) **(b)**

Figure 4-5: Morphology of Ti 6-2-2-2-2 alloy

An EDS of a sample of the alloy powder is also given in Figure 4-6 The elemental amount of Tin and Chromium in the analysis fell way below what is normally expected (Table 4-4). However, considering only a small portion of the powder was taken, an explanation for this could be due to a degree of inhomogeneity in the powder.

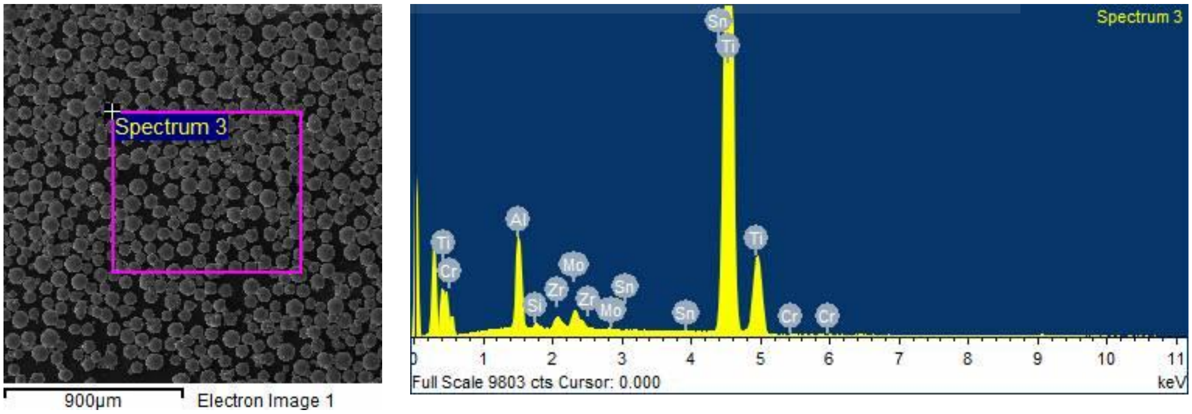

Figure 4-6: EDS of commercially pure titanium

Table 4-4: Chemical Composition of Ti 6-2-2-2-2 powder.

Element	Weight %	Atomic%
Aluminium	6.20	10.76
Silicon	0.32	0.54
Titanium	87.94	85.94
Chromium	0.04	0.03
Zirconium	2.17	1.11
Molybdenum	3.26	1.59
Tin	0.07	0.03

4.2.3 Vickers Hardness Results

The microhardness values of weldments are known to vary across weld zones due to the non-homogenous microstructural evolution across the zones. Consequently, microhardness profiling across the weld zones was done to adequately describe the hardness behaviour of the material. Figure 4-7 shows the hardness profile of the butt joint weldments.

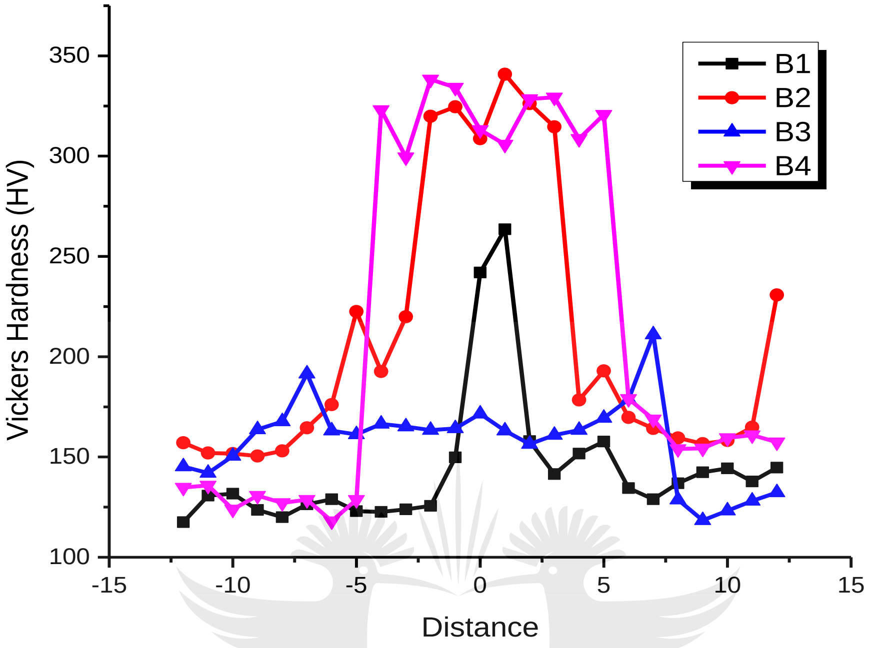

Figure 4-7: Vickers Hardness profiles of butt joints.

The hardness profile of sample B1 is somewhat unexpected. In the HAZ there is a slight increase in the microhardness and a consequent decrease in the WM. The hardness values in the WM fall in the range between 150 and 170. The microstructure phases formed in the weld zone in this sample could explain the low hardness values and this will be considered in a further section of this chapter. Samples B1 and B3 show the lowest hardness values in the WM, while samples B2 and B4 gave similarly high hardness in this zone. This is somewhat interesting considering samples B2 and B4 were both welded at 130A but with sample B2 with 24V and Ti 6-2-2-2-2 alloy while sample B2 was done with 22V and commercially pure titanium. This seems to suggest a significant role of welding current in the value of the hardness property of the material in the WM.

Figure 4-8 below depicts the hardness profile of the lap welded joints.

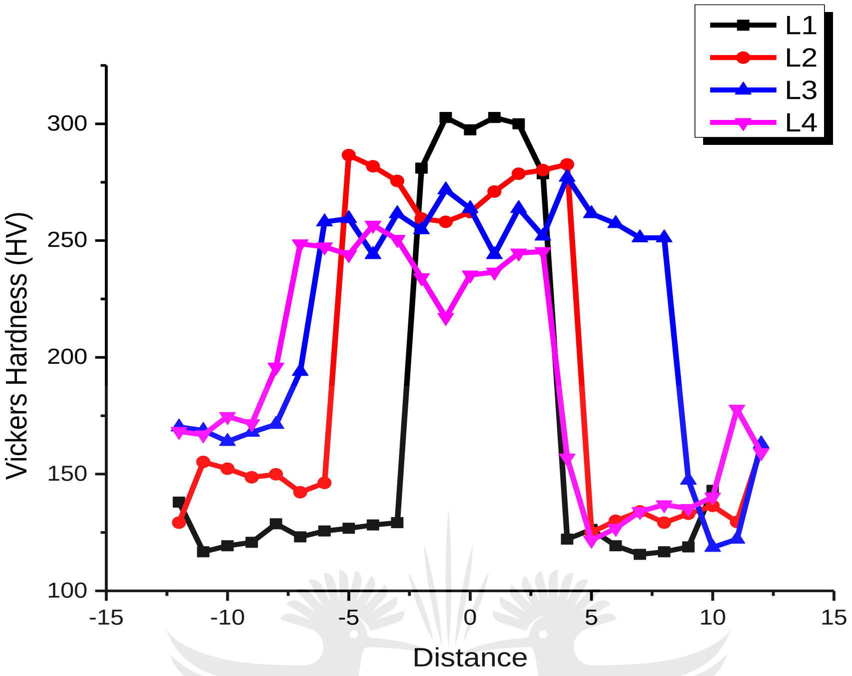

Figure 4-8: Vickers Hardness profiles of lap joints

Sample L1 shows the highest hardness values in the WM. It is worth noting that unlike the hardness profile of B3 discussed earlier, none of such profiles is observed with the lap joints. This might give credence to the suspicion that welding current plays a significant role in the microhardness in the weld metal. Welding currents in the lap joint range from 215A-240A unlike in the butt joints where the current range is from 120A-130A. These profiles seem to suggest that at high current and medium voltage range, optimum hardness value in the weld metal is observable.

Sample L3 has a wider bead than the others which explains the significantly more points with high hardness in the WM.

4.2.4 Tensile Strength Result Analysis Methodology: S/N Ratios and Analysis of Variance

With the adoption of Taguchi Design of Experiment Method, the mechanical test results for Tensile Strength were analyzed. The objective of the analysis was first, to determine optimum process parameters required to obtain optimum output responses. Secondly, the analysis was done to determine the significance of each varied experimental factor, which in this study are welding voltage, welding current and titanium powder reinforcements.

To achieve both objectives, signal-to-noise ratio analysis and analysis of variance (ANOVA) were carried out. For a static design, which is used in this study, there are three possible optimization scenarios. These are

1. The smaller-the-better: this is chosen when a smaller output response is desired. For instance, in a situation where cost is to be minimized. The S/N ratio for this scenario is given by Equation 4.1:

$$[S/N]_s = -10.\log_{10}[MSD] - - - - - - - - - - - (4.1)$$

Where MSD is Mean Square Deviation. Equation (4.1) can be written as given in Equation 4.2,

$$[S/N]_s = -10.\log_{10}\left[\frac{\sum \mu^2}{n}\right] - - - - - - - - - - (4.2)$$

Where μ is the output mean, and n is the number of trial runs for each level.

2. Nominal-the-best: this is chosen when neither a smaller or larger response value is desired. For instance, it is used when a fixed output value is most desired. The S/N ratio for this scenario is given in Equation 4.3:

$$[S/N]_n = 10.\log_{10}\frac{\mu^2}{\sigma^2} - - - - - - - - - - - (4.3)$$

Where μ is the output mean and σ^2 is the standard deviation.

3. The larger-the-better: This is chosen when a larger output response is desired. The S/N ratio for this scenario is given in Equation 4.4:

$$[S/N]_l = -10.\log_{10}[MSD] - - - - - - - - - - (4.4)$$

Where MSD is Mean Square Deviation. This equation is written as in Equation 4.5;

$$[S/N]_l = -10.\log_{10}\left[\frac{\sum \frac{1}{\mu^2}}{n}\right] - - - - - - - - - - - - (4.5)$$

Where μ is the output mean and n is the number of trial runs.

For this study, the larger-the-better S/N ratio scenario was selected for output responses for tensile strength. The signal-to-noise ratios for each experiment were calculated using Equation 4.5.

4.2.5 Ultimate Tensile Strength Test Results

The focus of the parametric optimization using Taguchi's DoE was for ultimate tensile strength. Each experimental run was repeated three times to ensure the robustness of the optimization process, yielding three samples per experimental run. The average UTS of the three samples was used to calculate S/N ratios and obtain optimum parameters. The tensile behaviour of the parent material is given in Figure 4-9. The average UTS of the parent material is calculated to be 388.46 MPa.

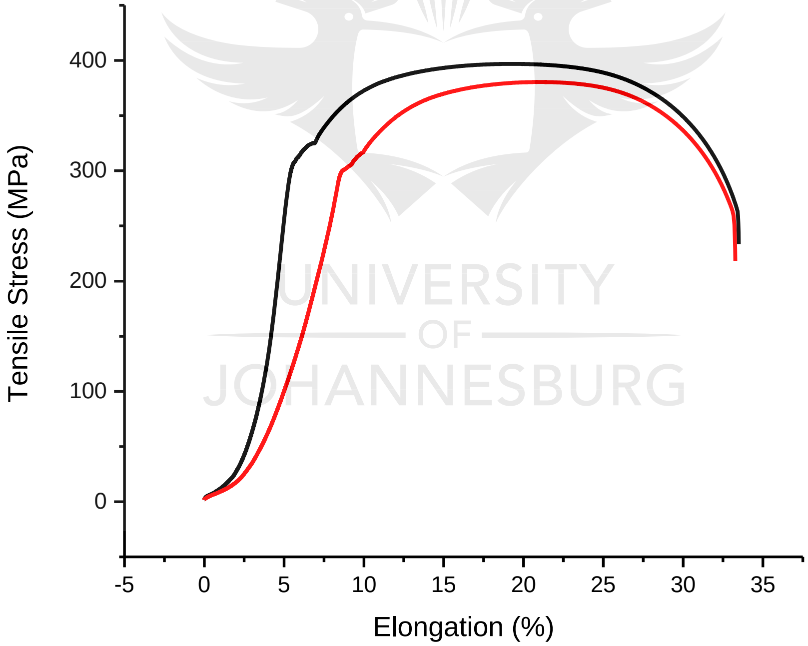

Figure 4-9: Tensile Stress-strain curve of AISI 1008 steel, as received.

Table 4-5 gives the output response for Ultimate tensile strength of the samples.

Table 4-5: Response table for Ultimate Tensile Strength of Butt Joints.

Weld Number	**Voltage (V)**	**Current (A)**	**Powder Reinforcement**	**Heat Input J/mm**	**Ultimate Tensile Strength (MPa)**			**Avg. UTS (MPa)**
					A	**B**	**C**	
B1	22	120	Pure Titanium	535.14	307.21	374.88	285.69	322.59
B2	22	130	Ti 6-2-2-2-2	579.73	339.34	368.66	470.44	392.81
B3	24	120	Ti 6-2-2-2-2	583.78	356.16	338.40	371.93	355.50
B4	24	130	Pure Titanium	632.43	371.05	362.04	363.25	365.45

Sample C of B2 produced an atypical result of 470 MPa which is more than the ultimate tensile strength of the parent material and deviates largely from the average of the other two samples. However, in order to maintain the orthogonality of the design, this sample result was not ruled out. It was also determined that the outlying nature of the result of B2 C does not significantly affect the outcome of the optimization process.

The S/N ratio depicts the degree of the desirability of the output response. For this analysis, larger-the-better was chosen as the preferred desirability. Table 4-6 shows the S/N ratios of the ultimate tensile strength of the butt joint samples for each experimental run.

Table 4-6: S/N ratios of UTS for butt joints

Weld Number	Voltage (V)	Current (A)	Powder Reinforcement	Avg. UTS (MPa)	S/N Ratio
B1	22	120	Pure Titanium	322.59	50.01
B2	22	130	Ti 6-2-2-2-2	392.81	51.64
B3	24	120	Ti 6-2-2-2-2	355.50	50.99
B4	24	130	Pue Titanium	365.45	51.25

The S/N ratio for each level of selected factors (voltage, current and powder reinforcement) was also calculated and has as a response table, Table 4-7. This is possible due to the orthogonality of the experimental design. The response table suggests that current is the most significant of the three selected factors for this process.

Table 4-7: S/N Ratio response table for UTS of butt joints

Level	Voltage	Current	Powder
1	50.82	50.50	50.63
2	51.13	51.45	51.62
Delta	0.30	0.95	0.69
Rank	3	1	2

The main effects plot provides the optimum parameters for optimum ultimate tensile strength of the butt joints as shown in Figure 4-10.

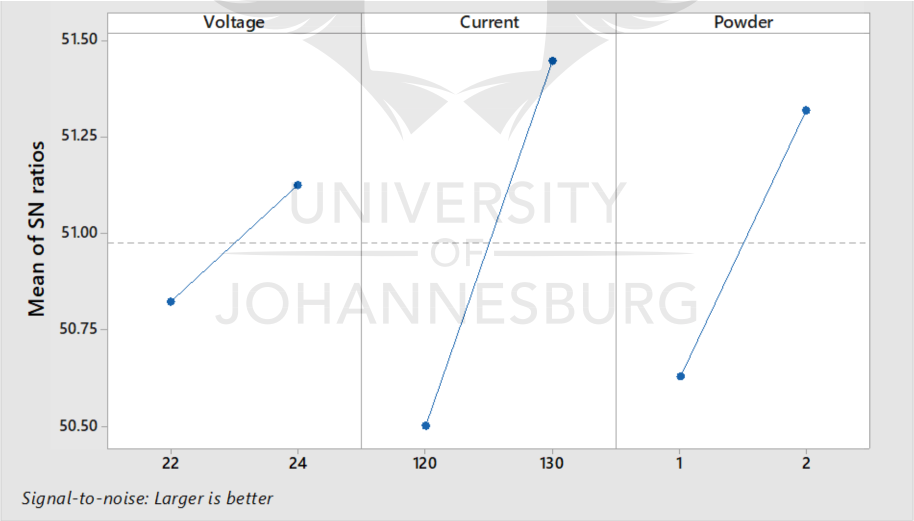

Figure 4-10: Main effects plot for S/N ratios of Ultimate Tensile Strength for Butt Joints

The main effects plot indicate that the optimum parameters are 24V, 130A and Ti 6-2-2-2-2 alloy. All selected parameters are from a higher level of all three factors. ANOVA was also conducted on the tensile test results and is given in Table 4-8.

Table 4-8 ANOVA for Ultimate Tensile Strength of Butt Joints

Source	**Degree of Freedom**	**Adj. SS**	**Adj. MS**	**F-Value**	**P-value**
Voltage	1	23.0	22.99	0.01	0.913
Current	1	4820.4	4820.42	2.68	0.141
Powder	1	2724.35	2724.35	1.51	0.254
Error	8	14411.7	1801.46		
Total	11	21979			

In the ANOVA table, the P-value indicates the significance of a group of data (in this case parametric factors) on the output response (in this case, Ultimate tensile strength). A P-value of 0.05 or less indicates a significant factor. In Table 4-8 none of the three factors is shown to be statistically significant. This analysis indicates that within the selected range of values of the process parameters, the output response (Ultimate Tensile Strength) does not vary significantly.

4.2.6 Joint Efficiency of Butt Joints

The joint efficiency of a weld joint is defined as the ratio of the tensile strength of the weld joint to the tensile strength of the parent material and is given in percentage. Table 4-9 shows the joint efficiency of all butt welds. The Joint efficiency of sample B2 is beyond 100% because of an outlying (unrealistic) UTS result from sample B2 C. The strength of the joints is within an acceptable range with respect to the parent material. The ductility of the sample also appears to increase with an increase in heat input as the heat input increases from B1 to B4 as shown earlier (Table 4-5).

Table 4-9: Joint efficiency of welded butt joints

Weld Number	**Avg. UTS (MPa)**	**Joint Efficiency (%)**	**Percentage Elongation (%)**			**Average Percentage Elongation (%)**
			A	**B**	**C**	
B1	322.59	82.99	2.99	1.99	1.67	6.65
B2	392.81	101.01	3.89	15.9	12.94	10.91
B3	355.50	91.46	16.20	3.20	16.29	11.89
B4	365.45	94.02	16.05	26.76	7.5	17.77

4.2.7 Tensile Lap-Shear Strength for Lap Joints

For the lap joints, tensile-shear strength tests were conducted. Each experimental run replicated three times yielded three samples for the tensile shear strength testing. Table 4-10 gives the output response of the tests. The tensile shear stress is the tensile force divided by the overlap area (45 x 12.25 mm^2, for these samples).

Table 4-10: Response table for Lap-Shear Strength

Weld Number	**Voltage (V)**	**Current (A)**	**Powder Reinforcement**	**Heat Input J/mm**	**Ultimate Tensile Strength (MPa)**			**Avg. UTS (MPa)**
					A	**B**	**C**	
L1	23	215	Pure Titanium	890.1	23.47	23.33	22.88	23.23
L2	23	240	Ti 6-2-2-2-2	993.6	23.66	23.45	23.76	23.62
L3	26	215	Ti 6-2-2-2-2	1006.2	28.88	23.67	23.77	25.44
L4	26	140	Pure Titanium	1123.2	23.05	23.13	24.18	23.45

The average values of all lap joint samples don't vary much. Sample L3 had the highest tensile shear strength with 25.44 MPa, while sample L1 had the lowest tensile shear strength with 23.23 MPa. The S/N Ratios for Taguchi's DoE for these samples are given in Table 4-11 and the S/N ratios response output table for each level of each parametric factor is given in Table 4-12. The response table shows current to be the most significant of the three factors.

Table 4-11: S/N Ratios for Lap-Shear Strength

Weld Number	Voltage (V)	Current (A)	Powder Reinforcement	Avg. UTS (MPa)	S/N Ratio
L1	23	215	Pure Titanium	23.23	27.32
L2	23	240	Ti 6-2-2-2-2	23.62	27.47
L3	26	215	Ti 6-2-2-2-2	25.44	28.00
L4	26	240	Pue Titanium	23.45	27.40

Table 4-12: S/N Ratio Response table for Lap-Shear Strength

Level	Voltage	Current	Powder
1	27.39	27.66	27.36
2	27.70	27.43	27.73
Delta	0.31	0.23	0.38
Rank	2	3	1

S/N ratios given in Table 4-12 were used to generate the main effects plot in Figure 4-11

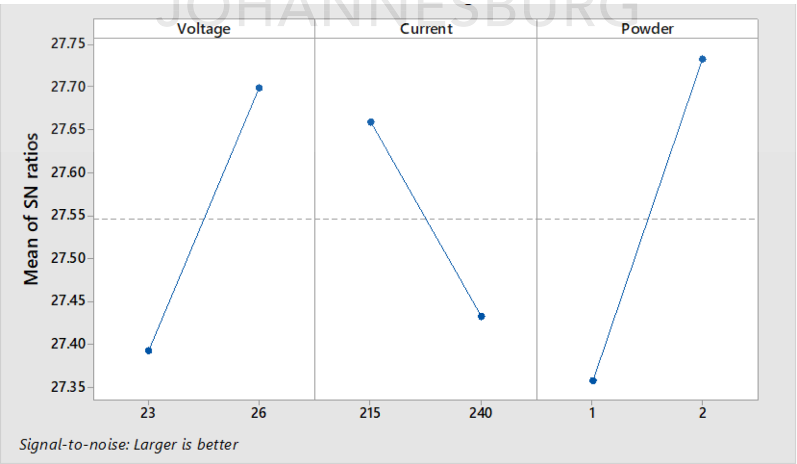

Figure 4-11: Main effects plot for Lap-Shear Strength

The main effects plot shows the optimum welding parameters to be at 26V, 215A and Ti 6-2-2-2-2 powder. The ANOVA table for this data is given in Table 4-13

Table 4-13: ANOVA for Lap-Shear Strength

Source	Degree of Freedom	Adj. SS	Adj. MS	F-Value	P-value
Voltage	1	3.131	3.131	1.33	0.282
Current	1	1.896	1.896	0.81	0.395
Powder	1	4.260	4.260	1.81	0.215
Error	8	18.791	2.349		
Total	11	28.078			

As was the case for the butt joints, the ANOVA data shows that none of the selected process parameters is statistically significant for the range of values selected. This suggests that an L4 orthogonal array may not be suitable to sufficiently determine the statistical significance of process parameters. However, using a wide range of values across levels in the design matrix might improve variance. An L9 orthogonal array will be more suitable to determine statistical significance and is more prevalent in literature [49]-[53]. Nonetheless, for the purpose of process optimization, which was the main objective for this portion of this work, the selected L4 orthogonal array is effective, especially since the estimation of the typical optimum parametric range is known. The stress-strain curves of UTS and Lap Shear Strength of the butt joints and lap joints can be found in Appendix A

4.2.8 Failure Mode of Butt Joints and Lap Joints

The failure modes of the butt and lap welded joints were observed and are presented in

Table 4-14;

Table 4-14: Failure mode of Butt Joints

Butt Joints	**Ultimate Tensile Strength (MPa)**	**Heat Input J/mm**	**Failure Mode**	**Region of Failure**
	B1			

A	307.21	535.14	Brittle	Weld Metal
B	374.88	535.14	Brittle	Weld Metal
C	285.69	535.14	Brittle	Weld Metal
	B2			
A	339.34	579.73	Brittle	Weld Metal
B	368.66	579.73	Ductile	Base Metal
C	470.44	579.73	Brittle	Weld Metal
	B3			
A	356.16	583.78	Ductile	Base Metal
B	338.40	583.78	Brittle	Weld Metal
C	371.93	583.78	Ductile	Base Metal
	B4			
A	371.05	632.43	Ductile	Base Metal
B	362.04	632.43	Ductile	Base Metal
C	363.25	632.43	Brittle	Weld Metal

Seven of the twelve butt welds under-went brittle failure at the weld metal. This suggests a compromise of structural integrity in the weld joint. The microstructural evolution in the weld metal and the existence of possible defects in that region could explain the reason for brittle failure. Table 4-14 already suggests that the heat input could be a factor for the failure mode. Samples B1 A, B and C, which have the lowest heat input, all underwent brittle failure. The number of samples with ductile failure increases as heat input increases.

The failure modes of the lap joints are presented in Table 4-15. All lap welds exhibited ductile failure away from the weld joint and closer to the base metal area.

Table 4-15: Failure Mode of Lap Joints

Butt Joints	**Ultimate Tensile Strength (MPa)**	**Heat Input J/mm**	**Failure Mode**	**Region of Failure**
	L1			
A	23.47	890.1	Ductile	Base Metal

B	23.33	890.1	Ductile	Base Metal
C	22.88	890.1	Ductile	Base Metal
	L2			
A	23.66	993.6	Ductile	Base Metal
B	23.45	993.6	Ductile	Base Metal
C	23.45	993.6	Ductile	Base Metal
	L3			
A	28.88	1006.2	Ductile	Base Metal
B	23.67	1006.2	Ductile	Base Metal
C	23.77	1006.2	Ductile	Base Metal
	L4			
A	23.13	1123.2	Ductile	Base Metal
B	24.18	1123.2	Ductile	Base Metal
C	23.45	1123.2	Ductile	Base Metal

The pictures of the samples after failure are presented in appendix B.

4.2.9 Optical Microscopy of Butt and Lap Joint Weldments

In this section, the microstructure of the butt and lap joint weldments as revealed under the optical microscope are briefly discussed in view of the optimization process. Firstly, the microstructure of the parent material is presented in Figure 4-12. Its microstructure reveals the dominance of ferrite with small regions of pearlite. This is due to the low weight percentage of carbon present in the parent material. The large lighter grains are ferrite grains, while the smaller darker grains are pearlite.

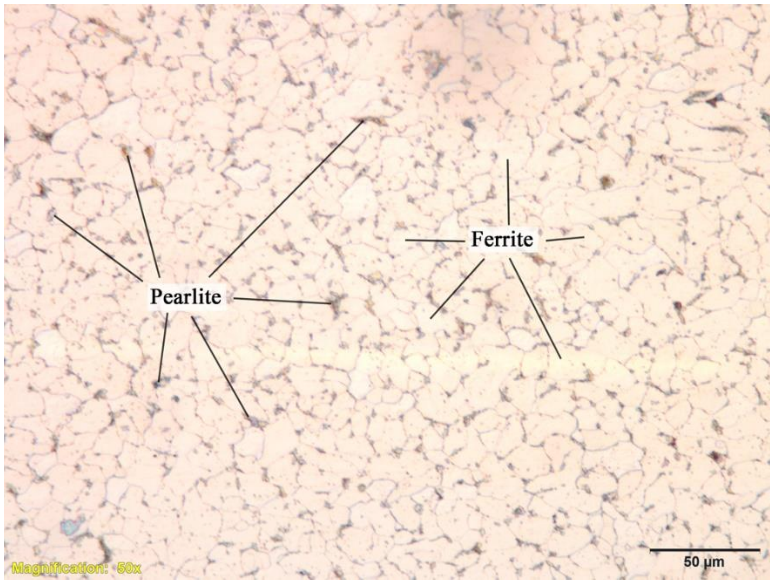

Figure 4-12: Microstructure of parent material

4.2.9a Butt Joints

Figure 4-13 gives the microstructural phases in the WM and HAZ of the butt joint samples. All pictures presented here were taken at 20x magnification.

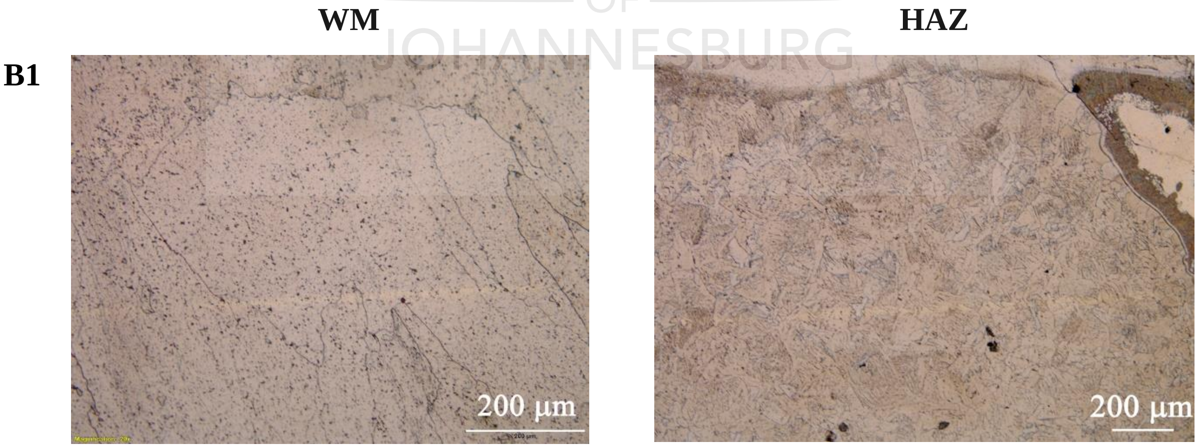

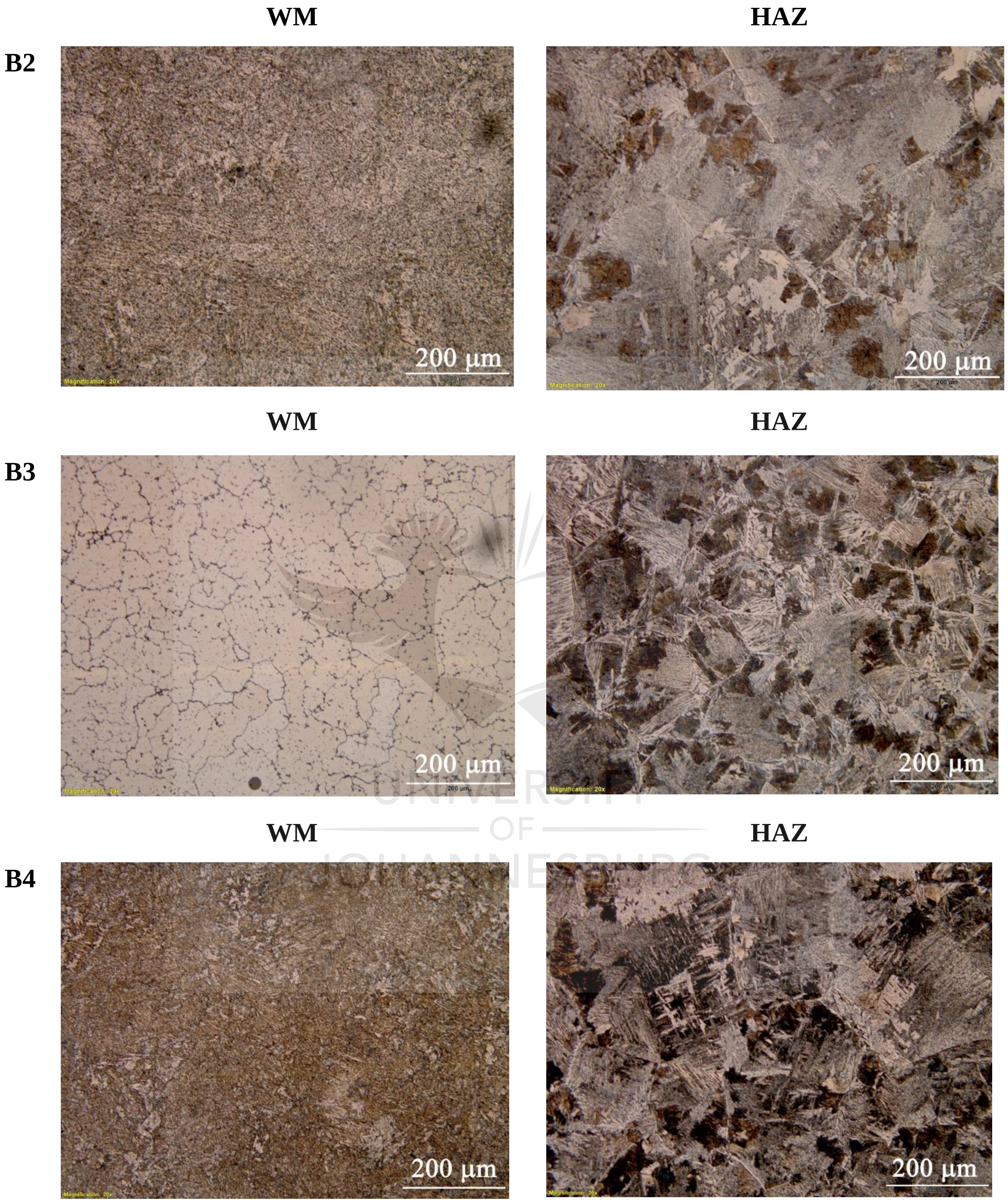

Figure 4-13: Micrographs of Butt joints in the WM and HAZ. All pictures are in 20x magnification.

Cellular grain growth is evident at the fusion boundary of sample B1 with predominantly ferritic grains present in the weld metal (Figure 4-13). The presence of coarse grain sizes in the WM of B1 and B3 explains the relatively lower hardness values in this region compared to other samples as seen in Figure 4-7, as hardness has been reported to be inversely proportional to grain size [102]. Larger grain sizes also allow easy movement of dislocations, resulting in reduced ductility [97]. This could explain the predominantly brittle failure observed in sample B1 (Table 4-14). In the coarse-grained (High temperature) HAZ of B1, allotriomorphic and widmanstatten ferrite are dominant with some acicular ferrite present.

The formation of acicular ferrite and allotriomorphic ferrite in the WM of B2 could explain the higher hardness values observed in this region in Figure 4-7. Similar microstructural phases were also found in B4, which also possesses higher hardness values in the WM. The formation of fine acicular ferrite in the weld metal is typically desirable and is known to contribute to the strength of the weld metal [77]. Allotriomorphic and widmanstatten ferrite grains dominate the coarse grain HAZ of B2, B3 and B4. Coarse pearlite grains are also observed in the HAZ of these three samples. B3 just like B1 has predominantly coarse regular ferritic grains in the weld metal and this could be due to slower cooling rates than usual [77].

There was a lack of fusion observed in sample B1 and this could be due to insufficient heat input. Sizeable gas pores were also visible at the root of the fusion zone (Appendix C). The presence of huge gas pores in B1 and B4 are defects that could be due to surface contamination or too high shielding gas flow rate. These possibilities were addressed in the second subsequent and final welding phase.

4.2.9b Lap Joints

Figure 4-14 shows the microstructural phases in the WM and HAZ of the lap joint samples. Coarse-grained widmanstatten ferrite dominates the coarse-grained high-temperature HAZ of all four samples (L1 – L4). Degenerate pearlite coarse grains are also observed in the HAZ for samples L3 and L4. In the WM regions, allotriomorphic ferrite, acicular and widmanstatten ferrite are dominant and this is typical of WM region of steel welds [77]. This combination of microstructures could explain the relatively higher microhardness values observed in Figure 4-8. The diffusion of carbon atoms from cementite, which typically occurs in the WM during solidification, contributes to high hardness in this region [95].

Sample L1 shows very fine acicular ferrite grain formation and could explain why this sample had the highest range of microhardness values in the WM.

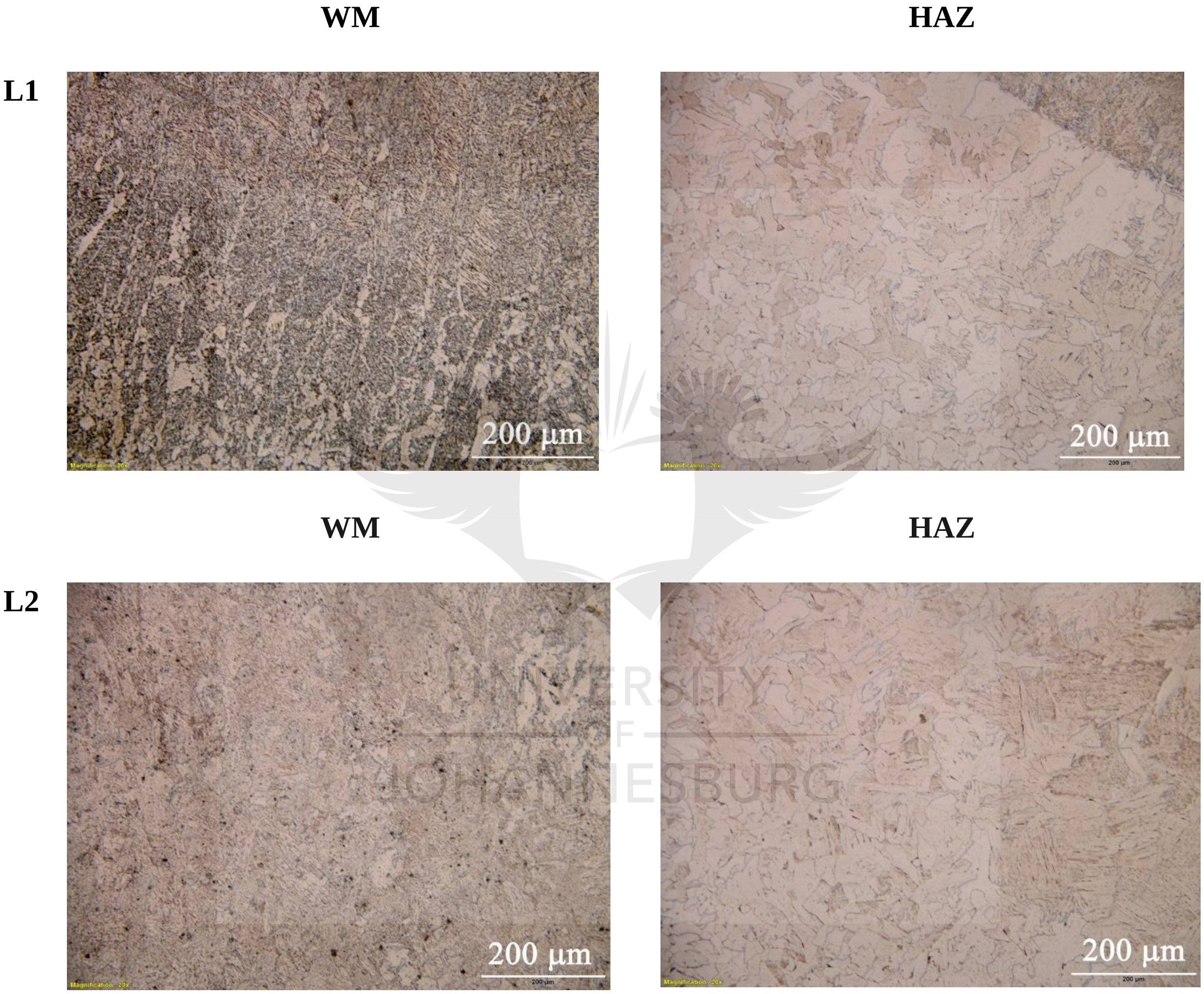

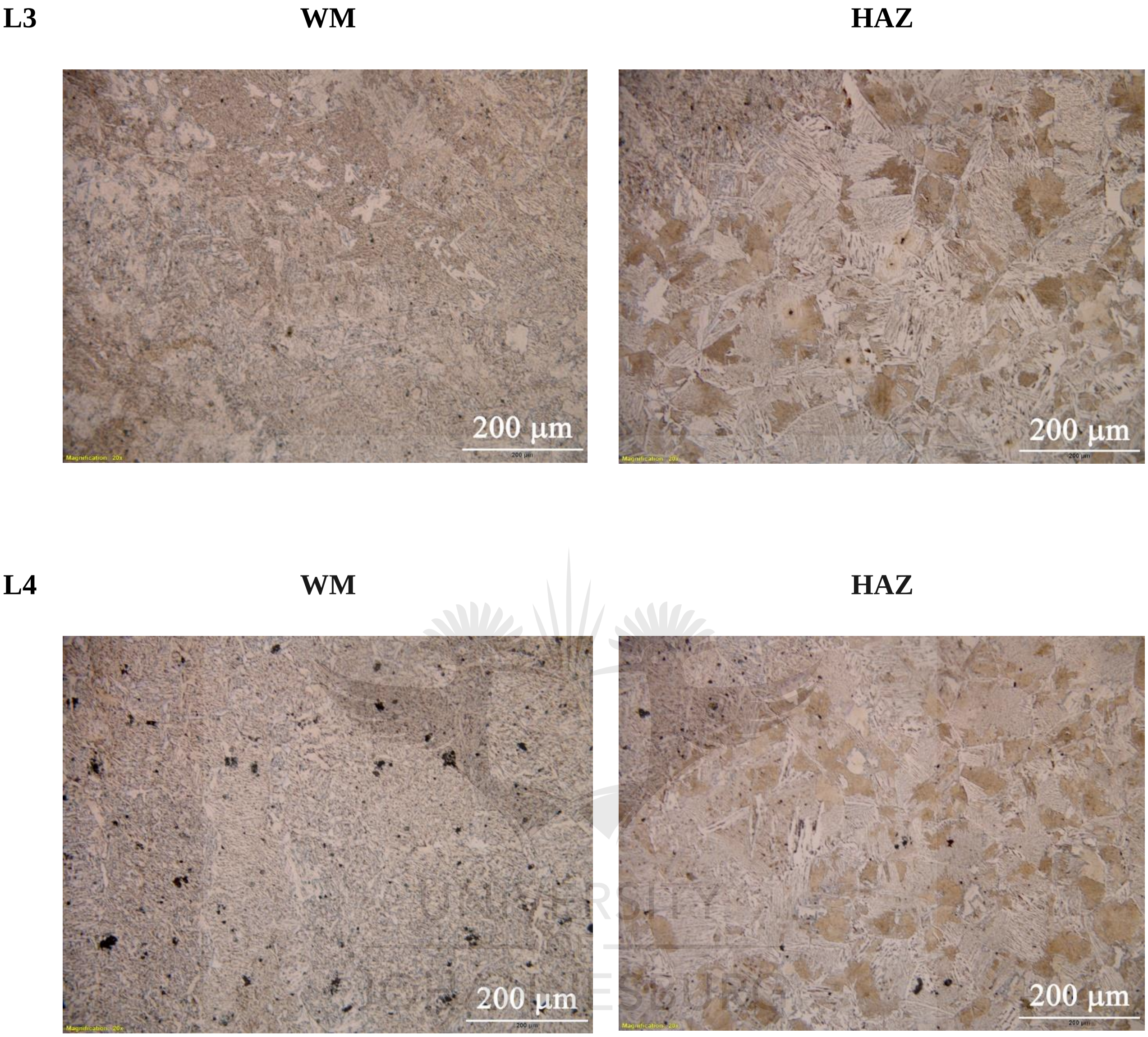

Figure 4-14: Micrographs of Lap joints in the WM and HAZ. All pictures are at 20x magnification

4.2.10 Optimization Process Conclusion

The optimized parametric values for tensile strength of the butt joints were calculated to be at 24V, 130A and with Ti 6-2-2-2-2 Alloy powder. However, considering the brittle failure of 58% of the welds in the WM region, the current was increased to 220A for the final welding phase. This increased the heat input to the weld region and was also expected to induce spray metal transfer mode and increase the depth of penetration. It should be noted that this temperature range used for the lap joints, all of which recorded no brittle failure at the WM.

The optimized parameters for tensile shear strength of the lap joints, calculated at 26V, 215A with Ti 6-2-2-2-2 were retained for the final welding phase.

4.3 Final Welding

In the final welding stage, the optimized process parameters were used to run two sets of weldments for both the butt and lap joints. One set was reinforced with Ti 6-2-2-2-2 powder while the other set was not reinforced. A direct comparison of the micro-hardness, tensile strength and failure analysis of both sets of weldments for the butt and lap joints were carried out.

4.3.1 Vickers Hardness

The microhardness profiles across the weld zones of the butt joints are given in Figure 4-15. The sample reinforced with Ti 6-2-2-2-2, sample BP, showed higher hardness values in the weld metal region of the material than that of the sample without titanium reinforcement (BN) in the same region. The presence of titanium particles could be responsible for the formation of finer grains in the WM and consequently higher hardness values. The hardness values in the HAZ of both samples fall between the range of 120 – 170 HV. The lower hardness in the reinforced sample at distance 5 could be due to the dominance of coarse Widmanstatten grains in that region as observed in Figure 4-20b.

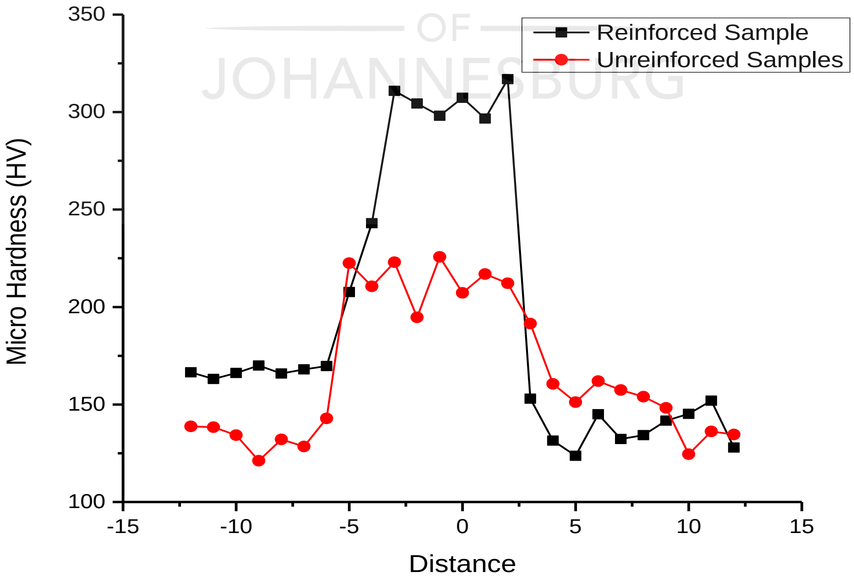

Figure 4-15: Vickers Hardness Profile for optimized butt joints

The microhardness profiles of the optimized welded lap joints are given in Figure 4-16. The titanium reinforced sample, LP, also shows higher hardness values in the WM region than in the unreinforced sample. This could be attributed to the addition of Ti 6-2-2-2-2 powder as was the case for the butt joints.

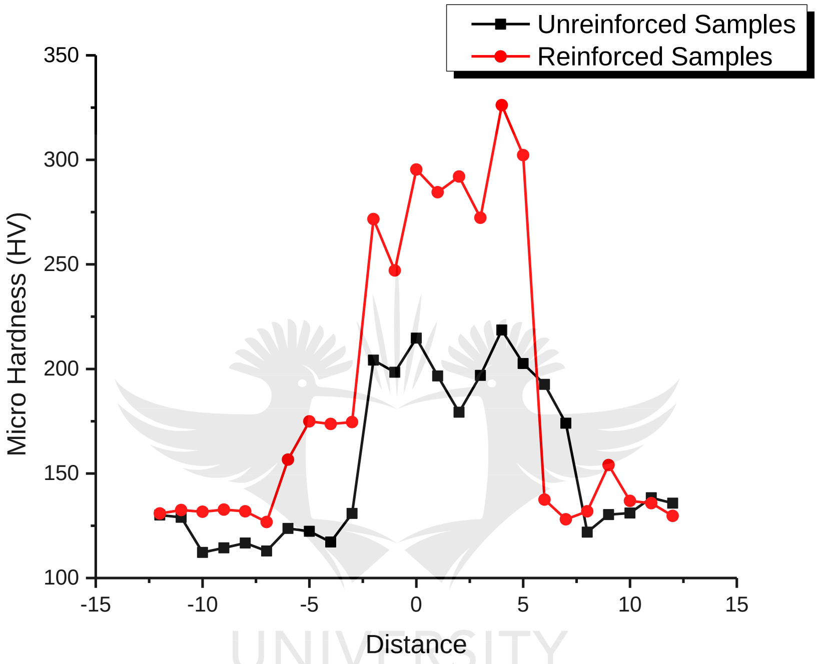

Figure 4-16: Vickers Hardness Profile for optimized lap joints

4.3.2 Tensile Strength

The behaviour of the optimized butt welds under tensile loading is given in Figure 4-17

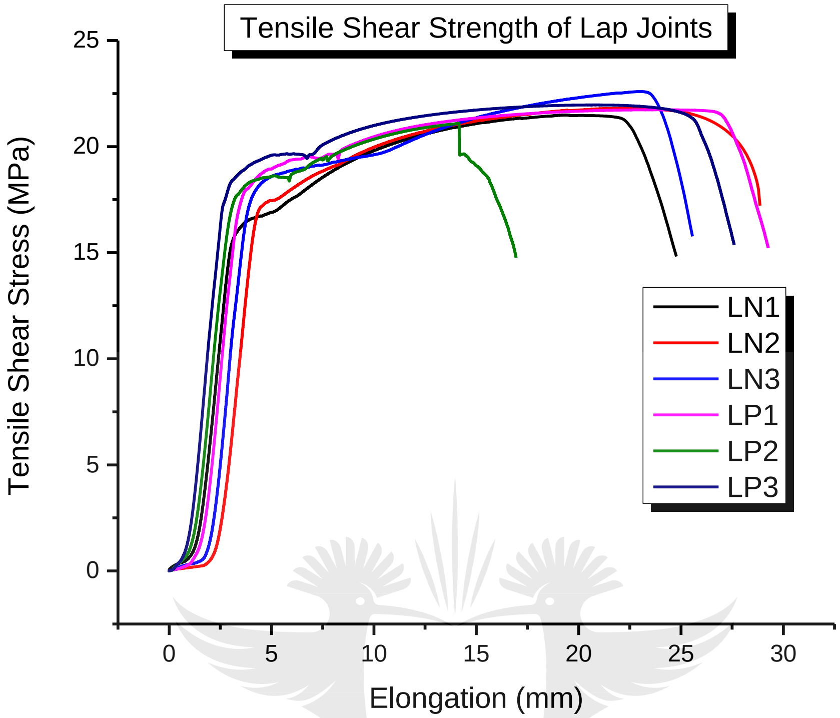

Figure 4-17: Tensile Strength of optimized butt-welded samples.

Samples designated as BP refer to titanium-reinforced samples while BN refers to the unreinforced samples. The stress-strain curves of the samples are similar and there isn't any significant difference in UTS of the reinforced and unreinforced samples. Table 4-16 gives the average values of both sets of samples.

Table 4-16: Joint efficiency of optimized butt welds

Weld Number	**UTS (MPa)**			**Avg UTS (MPa)**	**Joint Efficiency**
	1	**2**	**3**		
BN	362.17	373.56	-	367.87	94.64
BP	372.18	381.39	377.68	376.75	96.92

While the average UTS value of the reinforced sample is higher than that of the unreinforced sample, the individual UTS of the samples all fall within a close range. In fact, sample BN2 has a slightly higher UTS than BP1. Consequently, the powder reinforcement cannot be definitively said to have improved the tensile strength of the weldment. However, this data shows promise for future research work which will be discussed in the subsequent chapter. Notwithstanding, it can be concluded that the titanium alloy powder reinforcement does not adversely affect the tensile strength of the welded material.

The effect of the titanium alloy reinforcement on the ductility of the welded material appears insignificant as well. It is also evident that the ductility of the welded material is lower than that of the parent material which is at 34% elongation. The per cent elongation of the welded samples ranges from 15 – 23%. The high joint efficiency observed in Table 4-16 is in agreement with the study of Kumar and Singh [160] who optimized process parameters for mild steel plates.

The behaviour of the optimized lap welded joints under tensile shear loading is given in Figure 4-18. There is no real significant difference in tensile shear strength between the reinforced and unreinforced samples. Table 4-17 gives the average values of both sets of samples. The results show that the addition of titanium alloy powder does not improve the tensile shear strength of the lap welded joint.

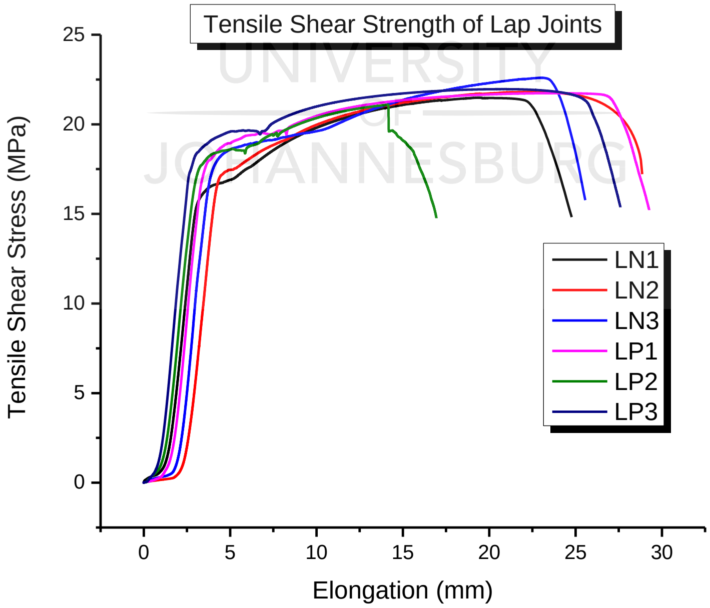

Figure 4-18: Tensile Shear-Strength of optimized lap-welded samples.

Table 4-17: Tensile Shear Strength of optimized lap joints

Weld Number	**UTS (MPa)**			**Avg. UTS (MPa)**
	1	**2**	**3**	
LN	21.49	21.82	22.59	21.97
LP	21.74	21.09	21.96	21.59

4.3.3 Optical Microscopy of optimized butt and lap joint weldments.

4.3.3a Butt Joints

In the WM region, allotriomorphic ferrite is more prominent in the unreinforced sample while acicular ferrite is more prominent in the reinforced sample (Figure 4-19). This could explain the higher hardness values of the reinforced samples and it also suggests that the reinforced samples could have better toughness due to the higher prominence of acicular ferrite. This is because acicular ferrite is known to improve material toughness, due to its interlocking needle-like shape which inhibits crack propagation and cleavage fracture [104], [161]. The presence of titanium alloy reinforcement could be responsible for a slightly slower cooling rate, resulting in larger prior austenite grains. This is known to result in reduced allotriomorphic and widsmanstatten ferrite growth and induced acicular ferrite growth [77].

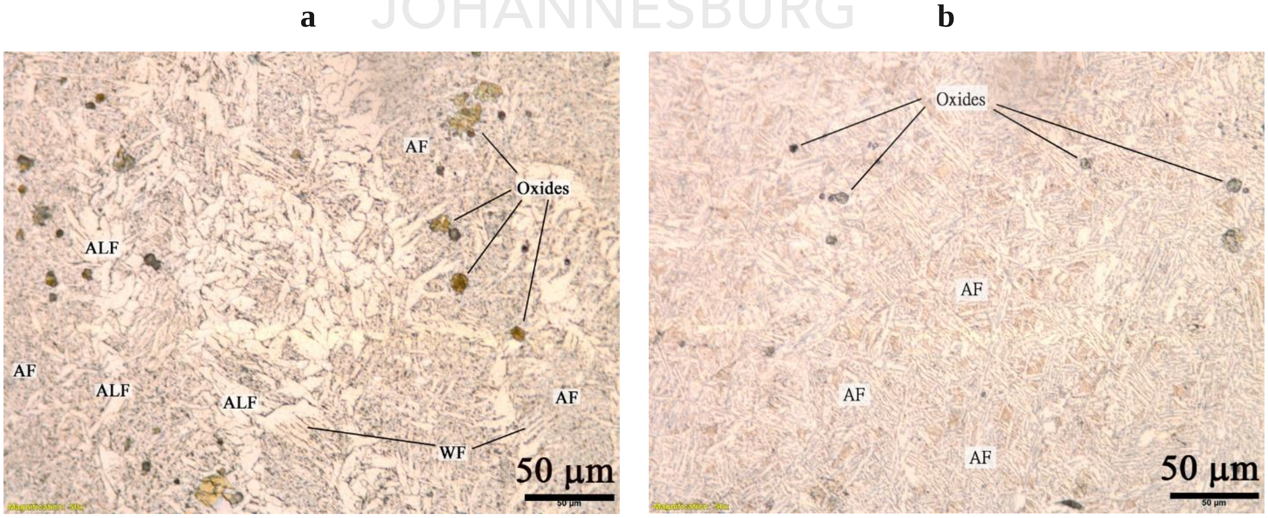

Figure 4-19: Micrographs Weld Metal of butt joints a) unreinforced sample b) reinforced sample

In the HAZ (Figure 4-20), both samples have widmanstatten ferrite grains formed over the coarse prior austenite grains. Some allotriomorphic ferrite is present in the unreinforced samples and less so in the reinforced samples. The darker coarse grains could be degenerate pearlite and less likely to be martensite, due to the lower hardness values observed in this region. Coarse ferrite grain growth observed in this region has been reported to be responsible for low hardness in the HAZ as seen in Figure 4-15 [88], [103].

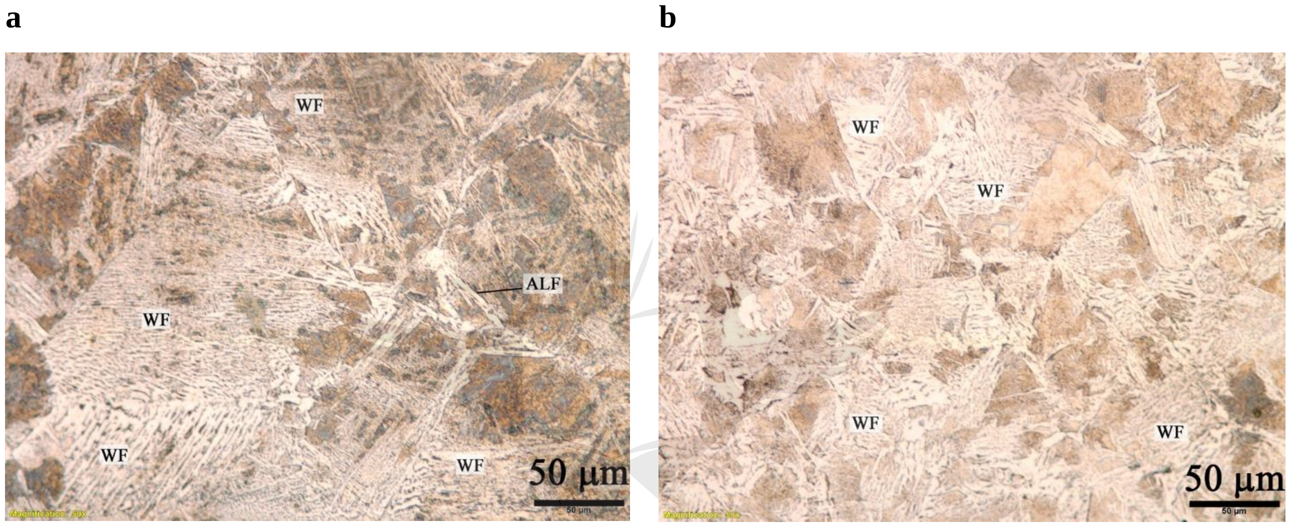

Figure 4-20: Micrographs of HAZ of butt joints a) unreinforced sample b) reinforced sample

4.3.3b Lap Joints

As was the case with the butt joints, the WM of the reinforced samples shows the dominance of acicular ferrite (Figure 4-21b), while relatively wide widmanstatten and polygonal ferrite are more dominant in the unreinforced sample (Figure 4-21a). The finer acicular ferrite grains in the reinforced sample could be due to the presence of titanium powder in the WM. It has been reported that titanium-rich inclusions in steel welds are very effective in acicular ferrite formation [77].

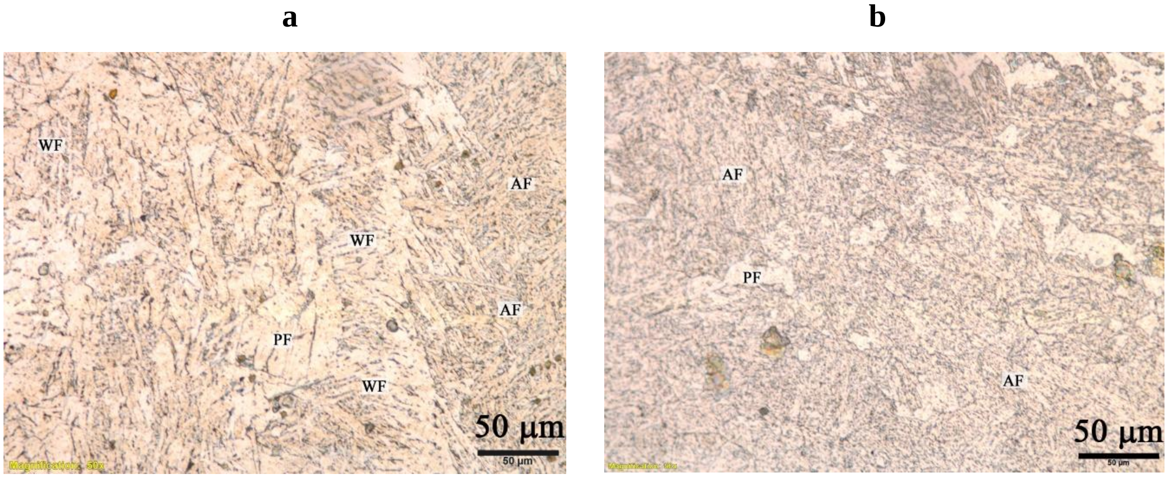

Figure 4-21: Micrographs Weld Metal of lap joints a) unreinforced sample b) reinforced sample

In the HAZ both reinforced and unreinforced samples showed the same microstructure (Figure 4-22 a-b). Wide widmanstatten ferrite grains can be seen to have grown across the prior austenite grains, yielding to a coarse ferritic microstructure in the HAZ. The larger widths of the widmanstatten ferrite in the lap joint compared with the butt joint could be due to the difference in welding geometry and its effect on the cooling rate in the HAZ. The reheating of the HAZ during the second stage of the lap welding could lead to slow cooling rates and consequently coarser grains.

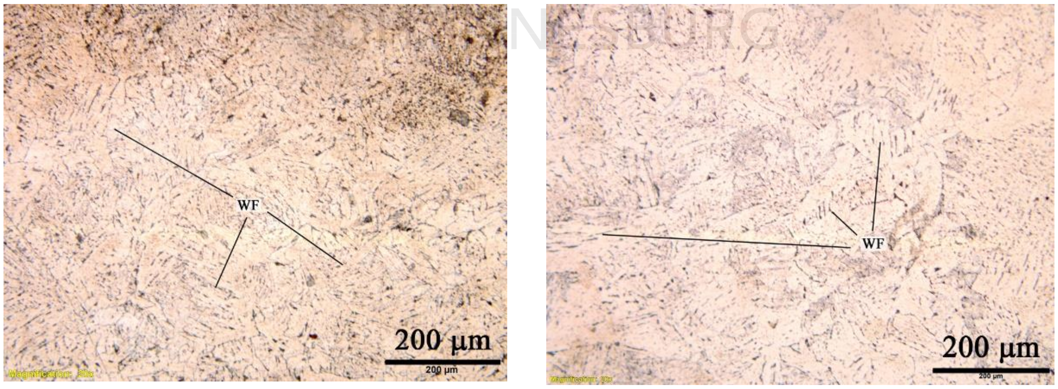

Figure 4-22: Micrographs HAZ of lap joints a) unreinforced sample b) reinforced sample

4.3.4 XRD of optimized butt and lap joint weldments.

XRD analysis was carried out to identify the microstructural phases present and their purity in the weld metal region of the reinforced and unreinforced lap and butt joint samples. These results indicated the presence of crystalline phases in the samples as expected. Firstly, the diffraction pattern of the parent material is given in Figure 4-23.

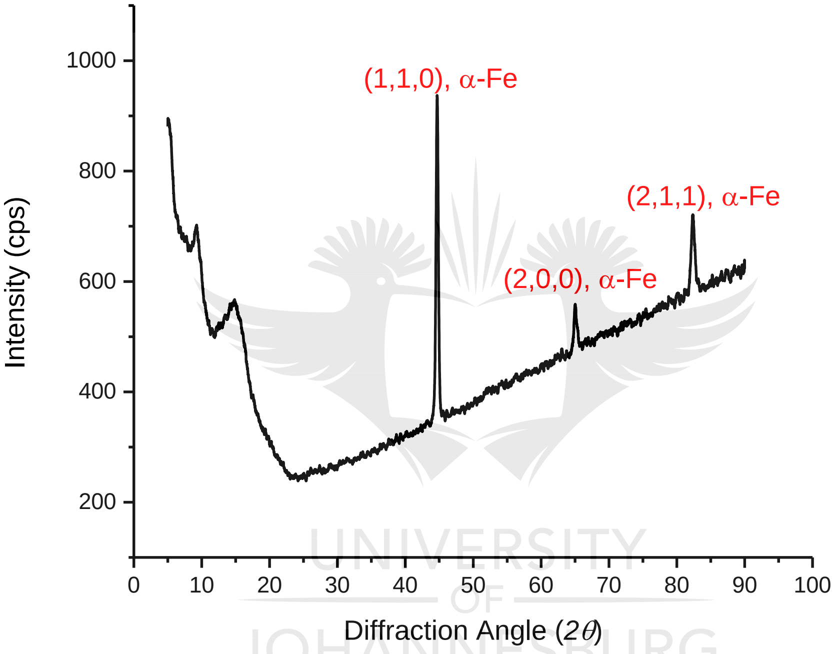

Figure 4-23: XRD Diffractogram of AISI 1008 Mild Steel (Parent material)

In the parent material, α-ferrite diffracts strongly at 44.6^0. Other less intense diffractions of α-ferrite are observed at 64.9^0 and 82.4^0. This indicates the dominance of α-ferrite in the parent material as has been pointed out in Figure 4-12 and is expected of low carbon steels with less than 1% carbon.

In Figure 4-24-Figure 4-25, the diffractograms of the optimized butt and lap joints are presented respectively. The reinforced butt joint (Figure 4-24a) is characterized by a strong peak at 44.4^0, indicating an iron-titanium intermetallic phase being dominant. Martensite phase is also identified to diffract at this peak. The iron-titanium intermetallic phase also occurs, albeit not as intensely at 64.7^0 and 82.1^0, martensite is suspected to be present at 64.7^0 but not at 82.1^0.

A

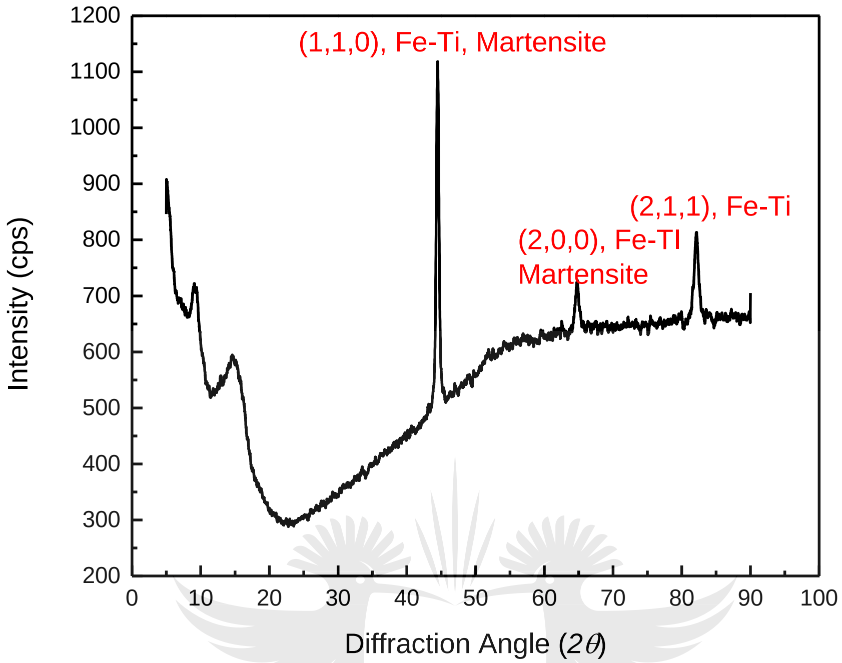
(1,1,0), Fe-Ti, Martensite
(2,1,1), Fe-Ti
(2,0,0), Fe-TI
Martensite
Intensity (cps)
1200
1100
1000
900
800
700
600
500
400
300
200
0
10
20
30
40
50
60
70
80
90
100
Diffraction Angle (2θ)

B

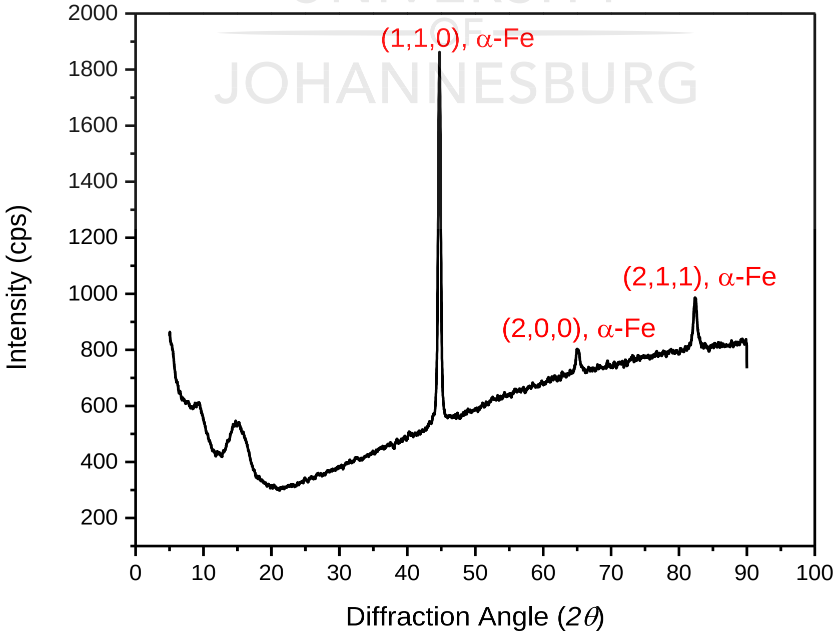
(1,1,0), α-Fe
(2,1,1), α-Fe
(2,0,0), α-Fe
Intensity (cps)
2000
1800
1600
1400
1200
1000
800
600
400
200
0
10
20
30
40
50
60
70
80
90
100
Diffraction Angle (2θ)

Figure 4-24: Diffractogram of (A) reinforced butt joint (B) unreinforced butt joint

The unreinforced butt joint shows a similar diffractive pattern as the parent material, with α-ferrite diffracting at 44.6^0, 65.1^0 and 82.3^0, the strongest peak occurring at 44.6^0 (Figure 4-24b). This indicates phase purity in the unreinforced butt welds, as there is an absence of intermetallic compounds. It also suggests that the titanium alloy powder reinforcement induces iron-titanium intermetallic compounds and possibly martensite microphases.

In the reinforced lap joint, the same iron-titanium intermetallic compound observed in the reinforced butt joint also diffracts strongly at 44.96^0 and less intensely at 65.1^0 and 82.4^0. A suspected martensitic microphase also diffracts at the same angles as the Fe-Ti intermetallic compound (Figure 4-25a).

Like the unreinforced butt joint, the unreinforced lap joint showed the same diffractive pattern as the parent material, with peaks at 41.6^0, 64.6^0 and 82.1^0 of α-Fe (Figure 4-25b). This also shows phase purity in the unreinforced lap joint and an absence of intermetallic compounds.

A

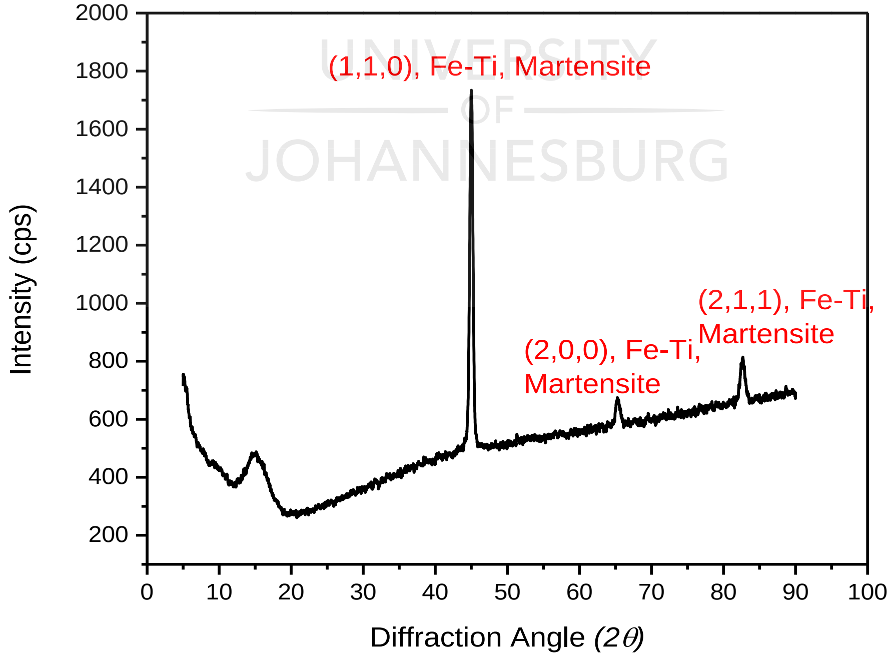

B

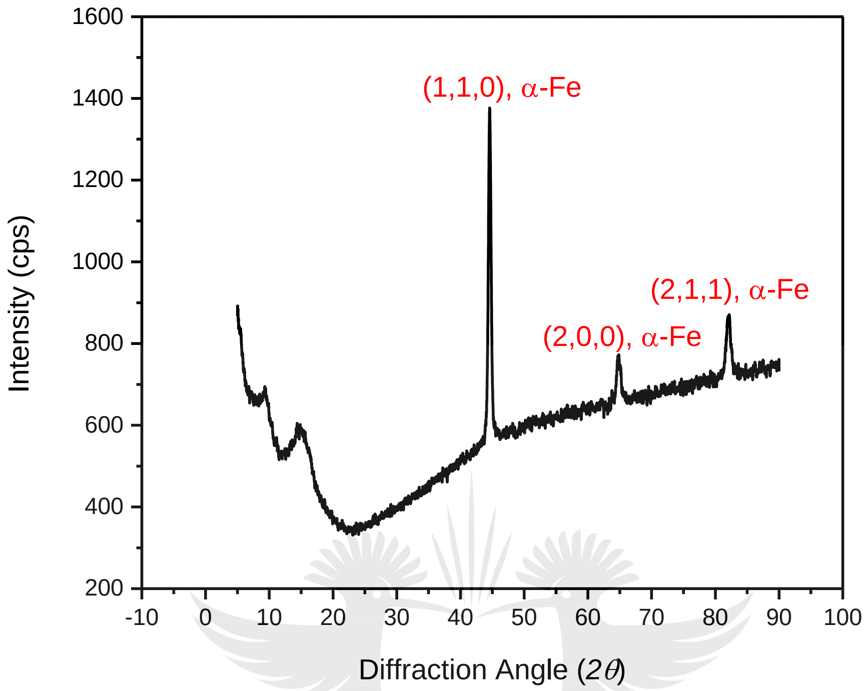

Figure 4-25: Diffractogram of (A) reinforced lap joint (B) unreinforced lap joint

The occurrence of suspected martensite phases in the reinforced samples is not captured in the microhardness results and optical microscopy analysis of these samples. However, the XRD analysis also indicates that martensite could be present as a microphase. The quantitative analysis results of the diffractograms showed the weight per cent of martensite to be 18.8 % in the reinforced butt joint and 10.8 % in the reinforced lap joint (Figure 4-26).

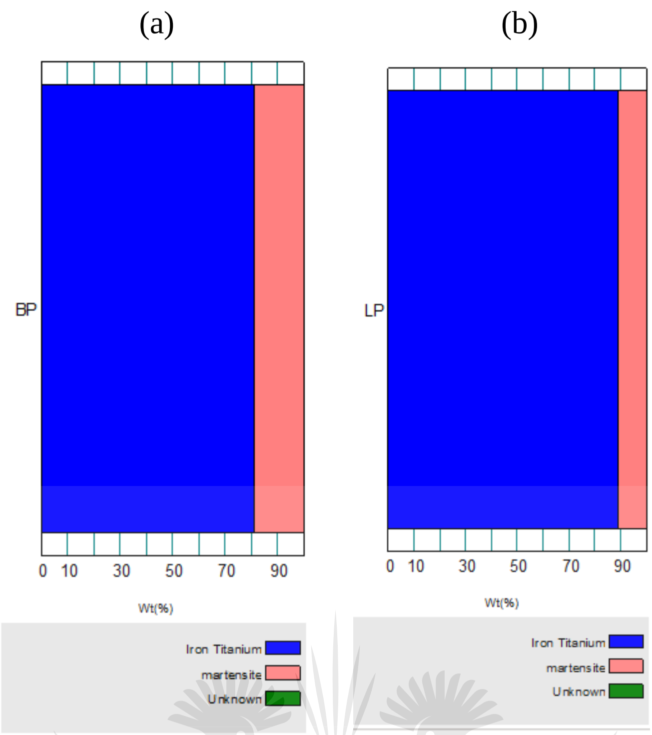

Figure 4-26: Qualitative analysis of phases in XRD results of reinforced (a) butt joint (b) lap joint

It is possible that microphases of martensite exist within the reinforced weldments as this has been reported to occur in typical steel welds [77]. Nano-indentation in the weld metal could be carried out to confirm the presence of martensite, as higher hardness values than what has been observed in the WM of the reinforced samples, is expected for martensite phase in steel. However, the formation of acicular ferrite with martensite structures is typical of GMAW welded steels as reported by Nathan *et. al.* [30]

Table 4-18 summarises the phases observed in the reinforced joints with their chemical formulae.

Table 4-18: XRD Phase Analysis of optimized butt and lap joints

Sample	**Identified Phase**	**Miller's Indices**	**Chemical Formula**	**Weight %**
Butt Unreinforced	α-Iron	(110), (200), (211)	Fe	100.0
Butt Reinforced	Iron-Titanium	(110), (200), (211)	$Fe_{0.975}Ti_{0.025}$	81.2

	Martensite	(110), (200)	$C_{0.12}Fe_{1.88}$	18.8
Lap Unreinforced	α-Iron	(110), (200), (211)	Fe	100.0
Lap Reinforced	Iron-Titanium	(110), (200), (211)	$Fe_{0.975}Ti_{0.025}$	89.2
	Martensite	(110), (200), (211)	$C_{0.055}Fe_{1.945}$	10.8

The chemical formula of the suspected martensite phase in the lap joints is different from that of the butt joint. This could be due to the difference in heat input between the two samples. A similar observation was made by Oyama [162] where the author studied the microstructural phases formed in copper reinforced aluminium welds. The author reported variations in the chemical formula of Al-Cu intermetallic compounds formed. Intermetallic compounds are typically known to be very hard and brittle [162], this high hardness is most likely, contributes to the higher microhardness values previously reported in the weld metal of the reinforced samples in Figure 4-15 and Figure 4-16.

4.3.5 Failure Analysis of Optimized Butt and Lap Joint Weldments

4.3.5a Butt Welds

The fracture of the butt welds due to failure during tensile loading is shown in Figure 4-27

Figure 4-27: Fracture of butt welds a) unreinforced samples b) reinforced samples

Sample BN 1 (unreinforced) underwent brittle failure at the fusion zone while sample BN 2 underwent ductile failure in the base metal. Failure analysis of BN 1 using SEM (Figure 4-28) showed predominantly brittle fracture as cleavage fracture was observed. The elemental analysis at spectrum 2 in Figure 4-28a revealed the presence of an oxide compound, that could be responsible for high stress concentration leading to failure in that region

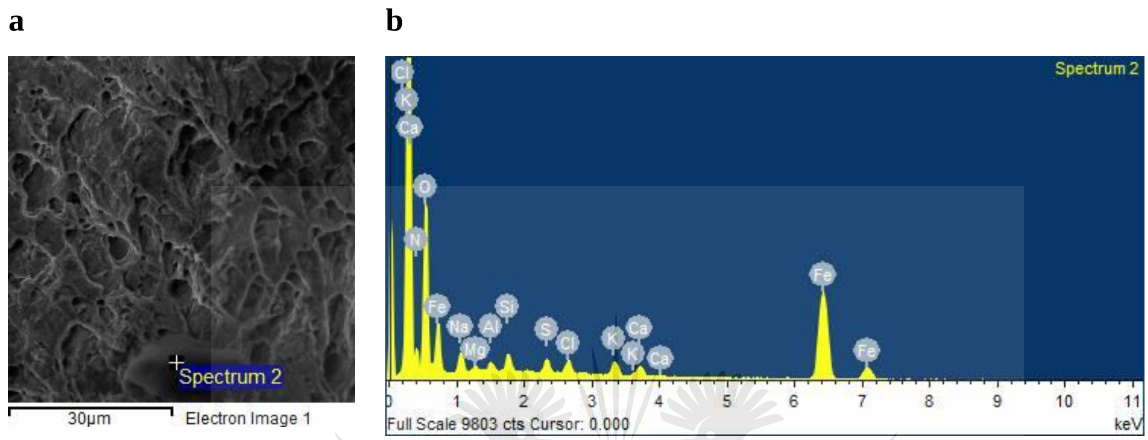

Figure 4-28: SEM image of fracture region of sample BN1 and its corresponding spectrum

The elemental composition of the oxide located on spectrum 2 is given in appendix D1.

Sample BN 2 underwent ductile failure in the base metal region as depicted by the dimples in Figure 4-29a. Elemental analysis carried out on spectrum 2 (Figure 4-29a) revealed the presence of an oxide and possibly potassium chloride. These impurities could be responsible for inducing stress concentrations and ultimately crack growth. Elemental composition of the impurity at spectrum 2 is given in appendix D2.

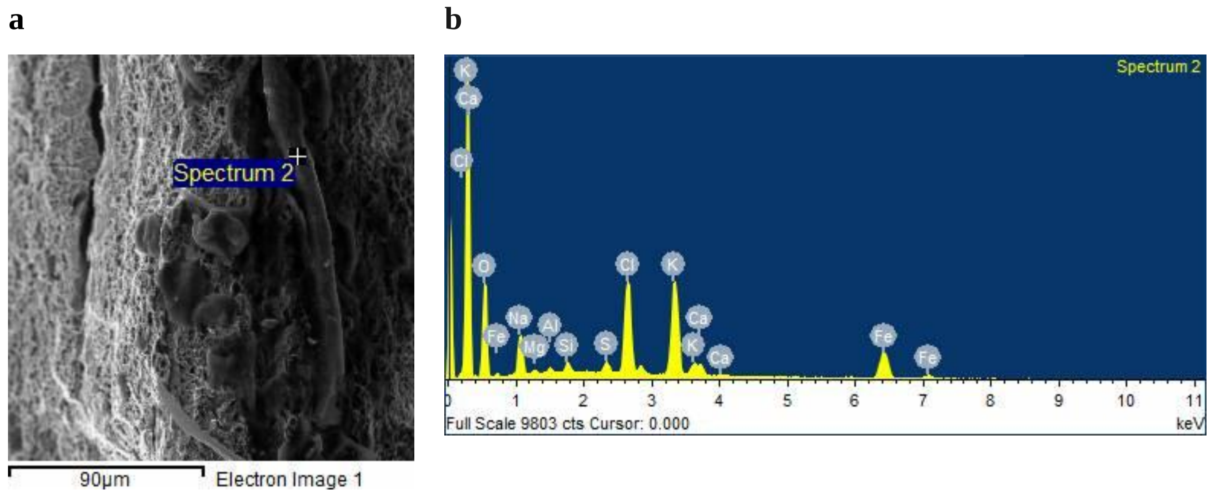

Figure 4-29: SEM image of fracture region of sample BN 2 and its corresponding spectrum

All reinforced samples underwent ductile failure in the base metal region. Sample BP2 was taken as a representative sample for fractography analysis. The presence of a relatively large oxide impurity in spectrum 1 (Figure 4-30) is most likely responsible for high stress concentration and consequent crack propagation in this region during tensile loading. Elemental composition of the impurity at spectrum 1 is given in appendix D3.

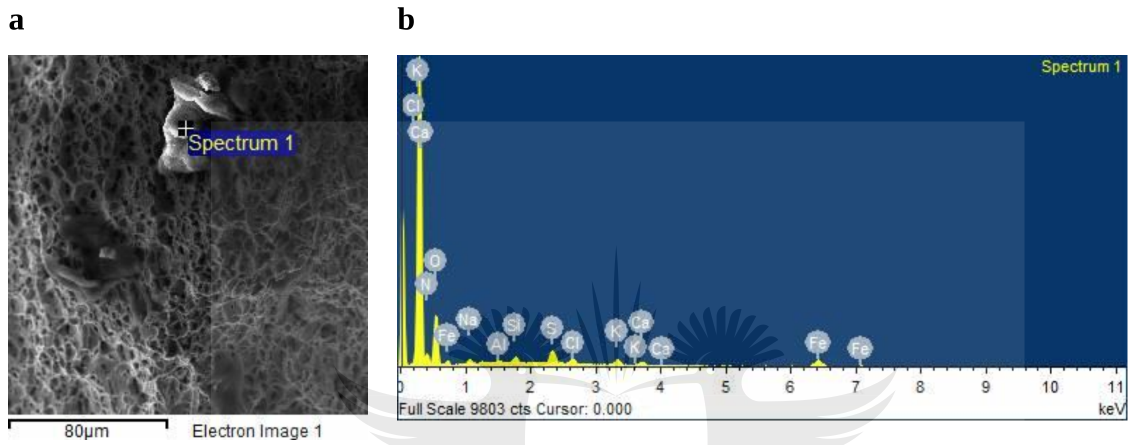

Figure 4-30: SEM image of fracture region of sample BP 2 and its corresponding spectrum

It can be concluded that none of the reinforced samples failed at the weld zone and it follows that the weakest region of the material was in areas where material impurities might have created very high stress concentrations, thereby, weakening the area.

4.3.5b Lap Welds

The fracture of the lap welds due to failure during tensile shear loading is shown in Figure 4-31

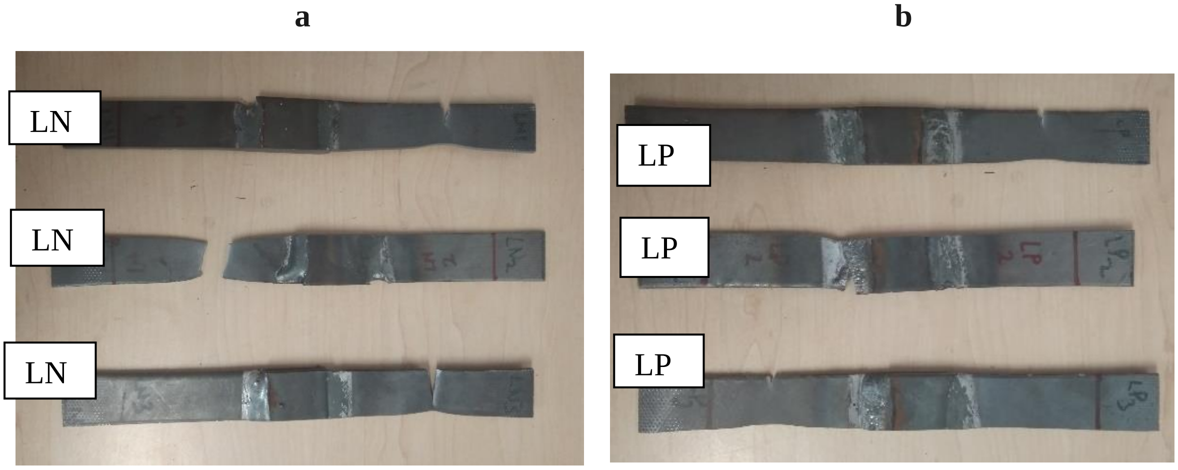

Figure 4-31: Fracture of lap welds a) unreinforced samples b) reinforced samples

Failure in all the unreinforced samples occurred at the base metal region. All unreinforced welds underwent ductile failure. Sample LN2 underwent complete transverse fracture across the base metal (Figure 4-31a). Amongst the reinforced samples, LP1 and LP3 underwent ductile failure, however, crack propagation in both samples were not as long as those of the unreinforced samples. Sample LP2, despite undergoing ductile failure, failed in the weld metal region, thus, elongation in this sample was smaller than in samples LP1 and LP3 as seen in Figure 4-31b.

4.4 Numerical Analysis of Thermal Field Distribution in Butt and Lap Welds

A three-dimensional transient thermal analysis was conducted in ANSYS Workbench to obtain the temperature distribution history across the weld zone of the material. To do this, temperature probes were inserted at specific distances from the weld centre, across the weld zones during the simulation. Experimental temperature history data was unavailable; however, the simulated temperature history has been correlated with the microstructure evolution across the weld zones and with the weld pool geometry to provide some degree of validation. Sun *et al.* [135] also correlated the temperature history data derived from FEA with the microstructure evolution across the weld zones and reported a good agreement.

Figure 4-32a-b shows snapshots of the FEA simulation for the butt and lap joints at 1.8s and 16s respectively. Figure 4-32 shows the simulation for the lap joint at 16.1s just after the second heat source has been applied, and the second weld bead of the lap is created. Figure 4-32 highlights the expected temperature field observed during welding and the simulation of metal deposition modelled using element "birth and death" technique in ANSYS Mechanical.

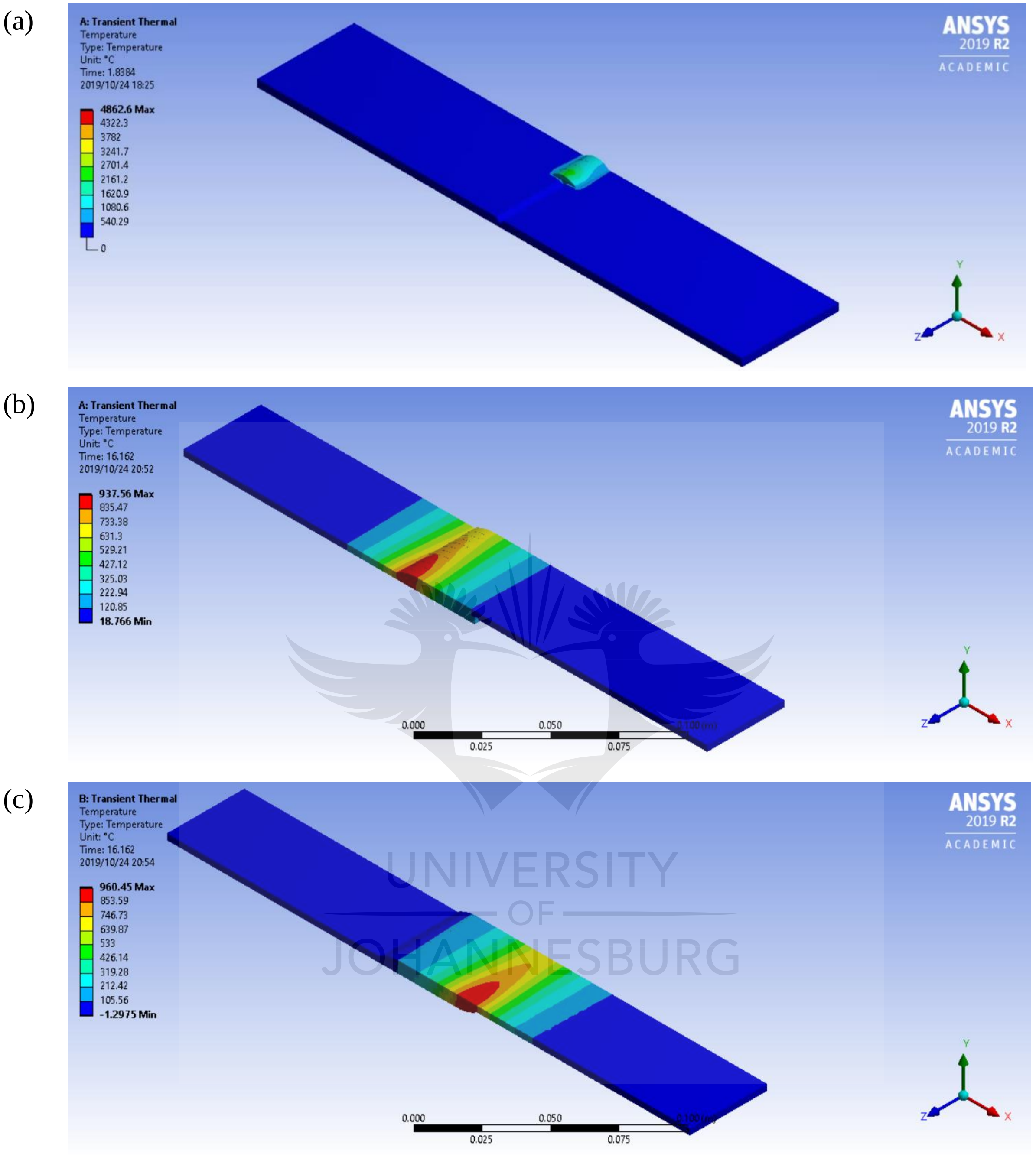

Figure 4-32: FEA simulation of MIG welding process for (a) butt joint (b) lap joint and (c) second welding of the lap joint.

4.4.1 Butt Joints

4.4.1a Unreinforced Butt Joint

Figure 4-33 shows the temperature history of the unreinforced butt joint at the weld centre, 5 mm, 8 mm, 10 mm, 12 mm and 15 mm away from the centre. In the weld centre, temperatures reach ≈2300 ^{0}C. This confirms melting in the weld pool, as the peak temperature exceeds the melting point of the parent material (1426 ^{0}C). The cooling rate in the weld pool is faster than in regions farther away, and this is evident from the steepness of the temperature curve over time.

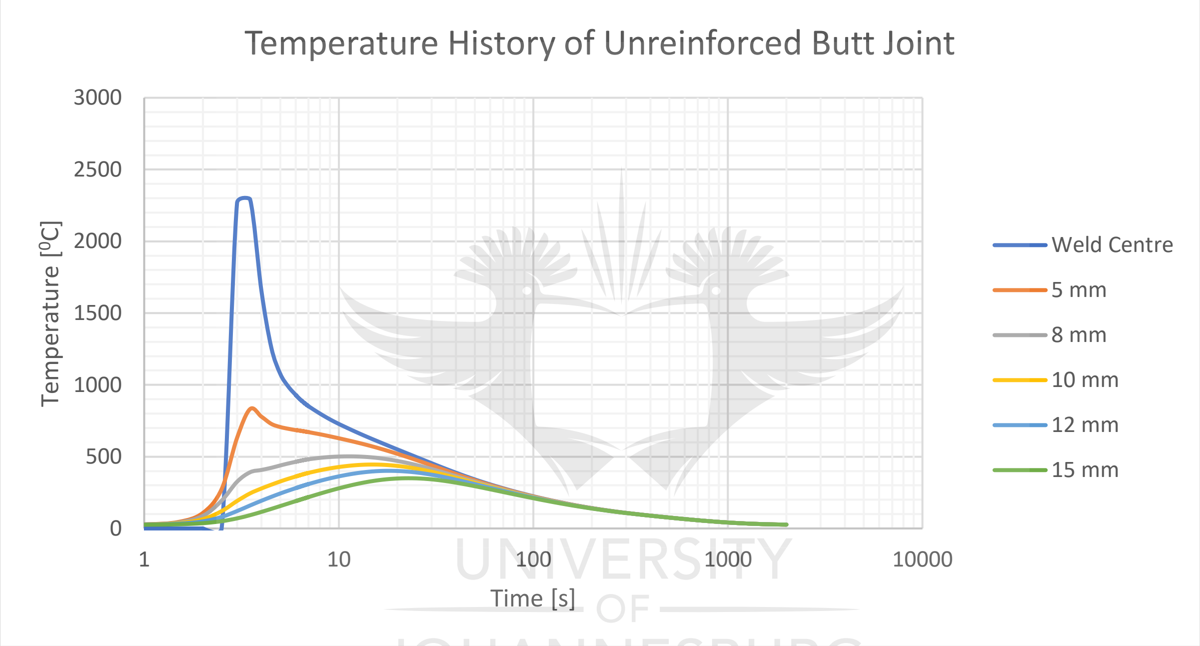

Figure 4-33: Temperature-Time history of Unreinforced butt joint.

For instance, in the weld centre, the time taken to cool over the temperature range from 800 ^{0}C to 500 ^{0}C, is 13 seconds while the time which was taken to cool over a temperature range from 800 ^{0}C to 500 ^{0}C, 5mm away from the weld centre is 21 seconds. At critical temperature A_{c1} (723^0 C) eutectoid reaction occurs, and all remaining austenite transforms to α-ferrite. Thus, grain growth takes place as the metal cools from >910 ^{0}C, where austenite begins to transform to α-ferrite. Fast cooling rates usually leads to finer grains, while slow cooling rates leads to coarser grains [26]. Thus, coarser grains are observed 5 mm away from the weld centre, which is just outside the weld pool as shown in Figure 4-34.

5 mm away from the weld centre, melting does not take place, but the grains are heated above the A_{C1} critical point (723 ^{0}C), and to form a combination of austenite and ferrite grains. Upon slow cooling, coarse ferrite grains are formed resulting in the coarse grain heat-affected zone (CGHAZ) as in Figure 4-34. Further away from the weld pool, >8 mm, the grains are not heated beyond 500 ^{0}C and are only tempered. Between 5-8 mm away from the weld centre, the fine grain heat-affected zone (FGHAZ) consisting of partially austenised grains are observable. Therefore, the temperature history of the weld joint generated in the FEA correlates with the microstructure observed in the HAZ.

In the WM, the cooling rate is not fast enough to form the metastable martensite phase, and as has been seen in the XRD results, no martensite is present (Figure 4-24b).

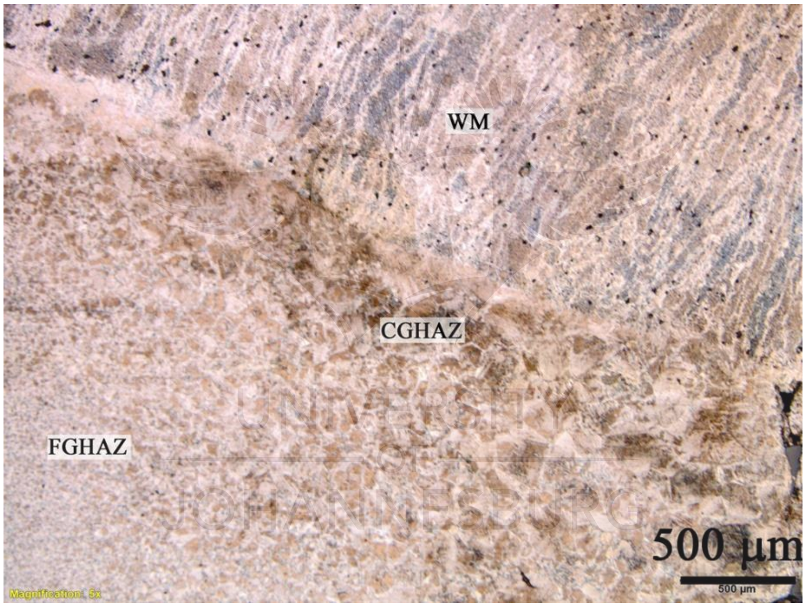

Figure 4-34: Weld zones of the unreinforced butt joint

4.4.1b Reinforced Butt Joint

The temperature history of the reinforced butt joint is presented in Figure 4-35. The temperature history follows the same pattern as that of the unreinforced butt joints. However, the cooling rate in the weld centre is observed to be slower in the reinforced sample. The weld centre in the reinforced sample cools from 2000 ^{0}C – 500 ^{0}C in 47.5 seconds. This is possibly due to the titanium powder reinforcement in the weld pool.

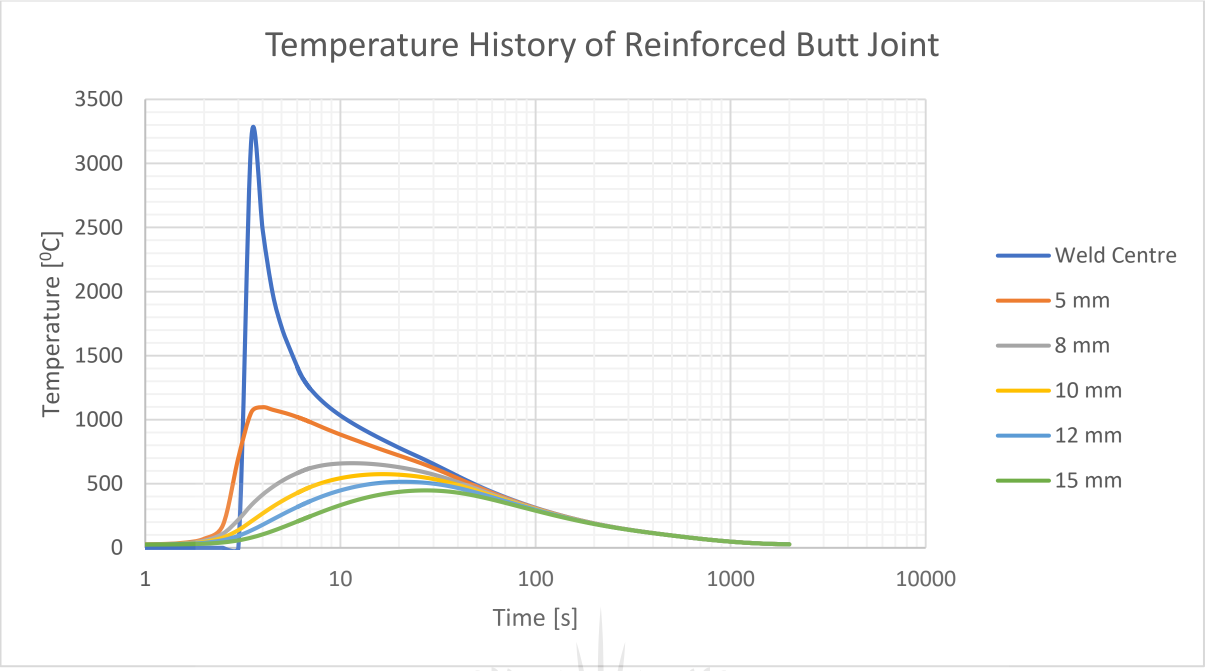

Figure 4-35: Temperature-Time history of Reinforced butt joint.

The titanium alloy powder, which has a lower thermal conductivity than the parent material, possibly retains heat for a longer period, thus slowing down the cooling rate. This is expected to result in an increase in the prior austenite grain sizes. However, increased austenite grain sizes, coupled with titanium powder inclusions favours the formation of acicular ferrite [77], as acicular ferrite nucleates on intragranular inclusions. The formation of acicular ferrite in the WM has been shown to be more dominant in the reinforced butt weld than in the unreinforced counterpart as previously discussed from Figure 4-19a-b. Figure 4-36 shows the presence of acicular ferrite in the WM.

As was the case in the unreinforced butt joint, 5 mm away from the weld centre, the temperature history shows that the grains adjacent to the WM were completely austenised, and slowly cooled, resulting in the formation of CGHAZ.

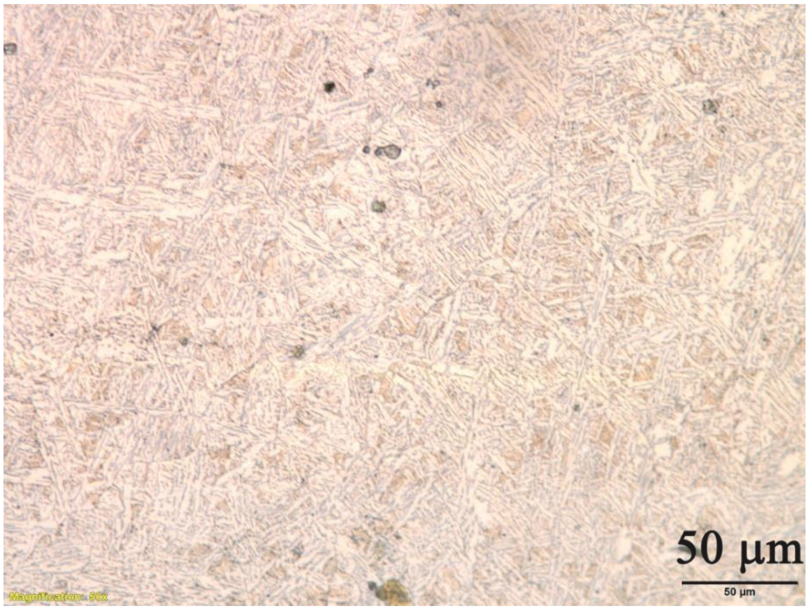

Figure 4-36: Weld Metal region of reinforced Butt joint showing acicular ferrite microstructures

The slower cooling rate of the reinforced butt joint due to the presence of titanium reinforcement is reflected in Figure 4-37. Figure 4-37 shows the locus of peak temperatures at distances away from the weld pool. This peak temperature difference and consequently reduced cooling rates predicted by the simulation correlates with the microstructures formed in the weld metal.

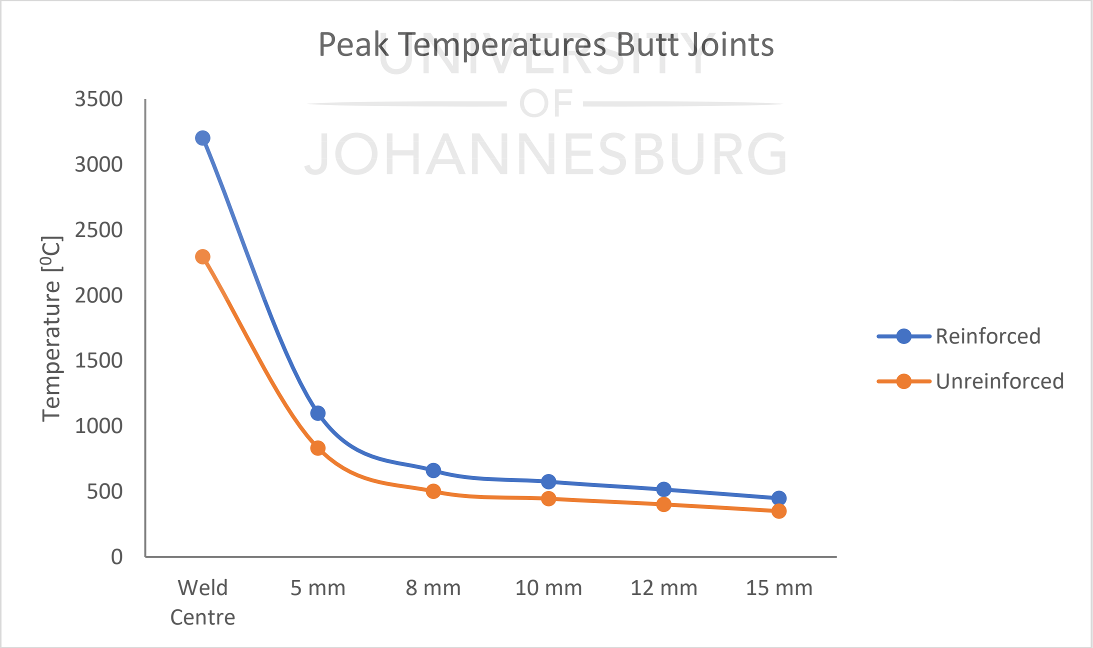

Figure 4-37: Locus of Peak temperatures in optimized butt joints

4.4.2 Lap Joints

In analyzing the temperature distribution of the lap joints, temperature data were obtained from the overlapping and underlapping sheets (Figure 4-38), due to the asymmetric nature of heat distribution in a lap joint longitudinally, when considering the weld pool as the centre point. For simplification of analysis, attention was paid to the heat distribution with reference to only one of the two weld pools on each lap geometry.

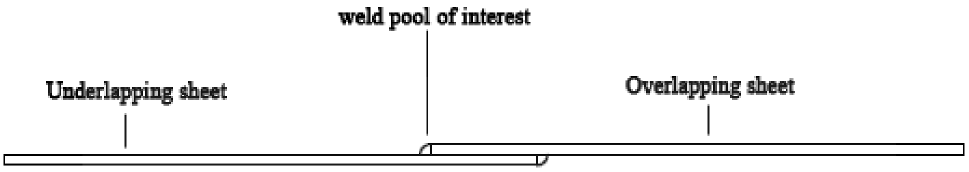

Figure 4-38: Lap Joint Geometry

4.4.2a Unreinforced Lap Joints

Figure 4-39 gives the heat distribution of the underlapping sheet in the unreinforced lap joint. The simulations estimate that temperatures reach $\approx$3100 ^{0}C in the weld pool, confirming molten metal in the weld pool. 5 mm away from the weld pool, temperatures go beyond the A_{c3} critical temperature (910 ^{0}C) and become fully austenised before cooling begins.

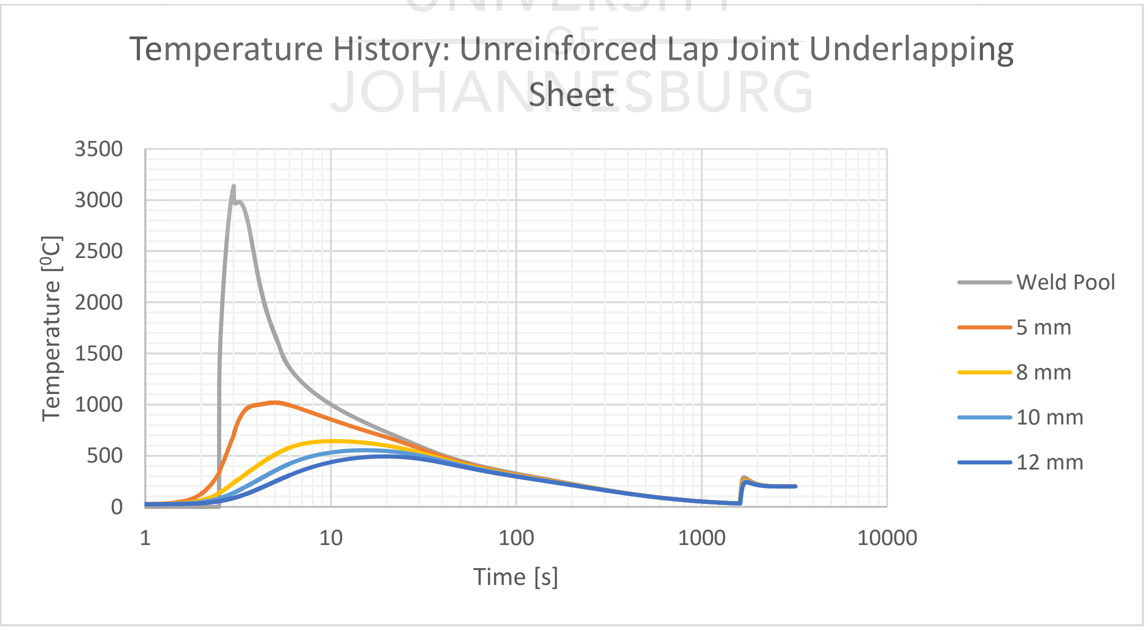

Figure 4-39: Temperature history of the underlapping sheet of the unreinforced lap joint.

The relative slow cooling in this region results in the formation of the CGHAZ. 8 mm away from the weld centre, temperatures reach within the neighbourhood of A_{c1} when the eutectoid reaction occurs. Regions farther away from this point are only tempered. Therefore between 5-8 mm away from the weld centre, on the underlapping plate, the FGHAZ is formed. Figure 4-40 shows the FGHAZ and CGHAZ of the underlapping sheet.

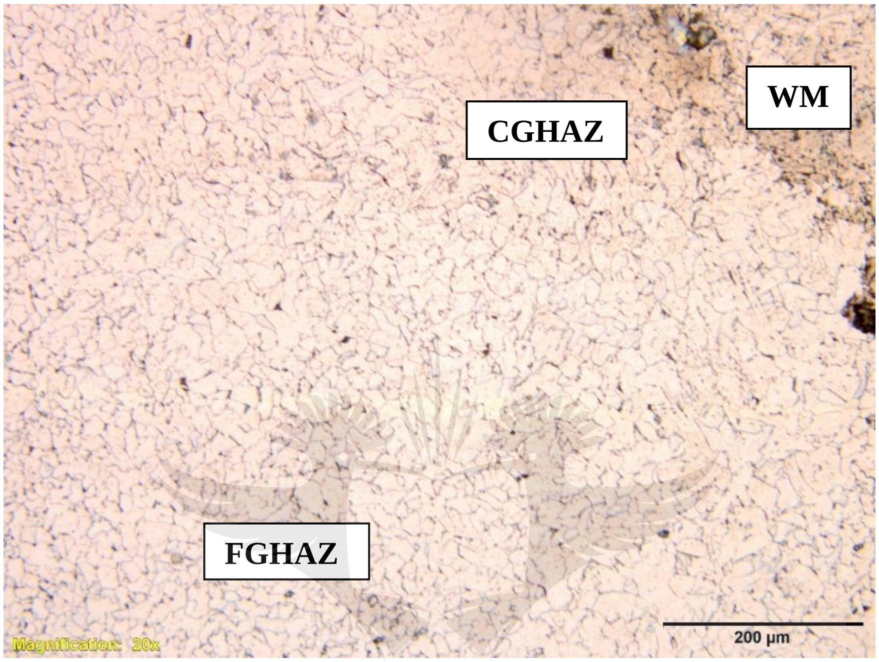

Figure 4-40: Underlapping sheet of unreinforced lap joint, showing FGHAZ and CGHAZ

The temperature history of the overlapping sheet of the unreinforced lap joint is given in Figure 4-41. It is immediately noticeable that the temperature peak, 5 mm away from the weld centre reaches ≈ 2100 ^{0}C indicating that the weld pool continues to this region and a portion of the overlapping sheet undergoes melting as well. The peak temperatures 8 mm and 10 mm away from the welding centre are also higher in the overlapping sheet than in the underlapping sheet. The microstructural evolution in the overlapping sheet is expected to be like that of the underlapping sheet, except that the CGHAZ and FGHAZ will be farther away from the weld centre in the underlapping sheet.

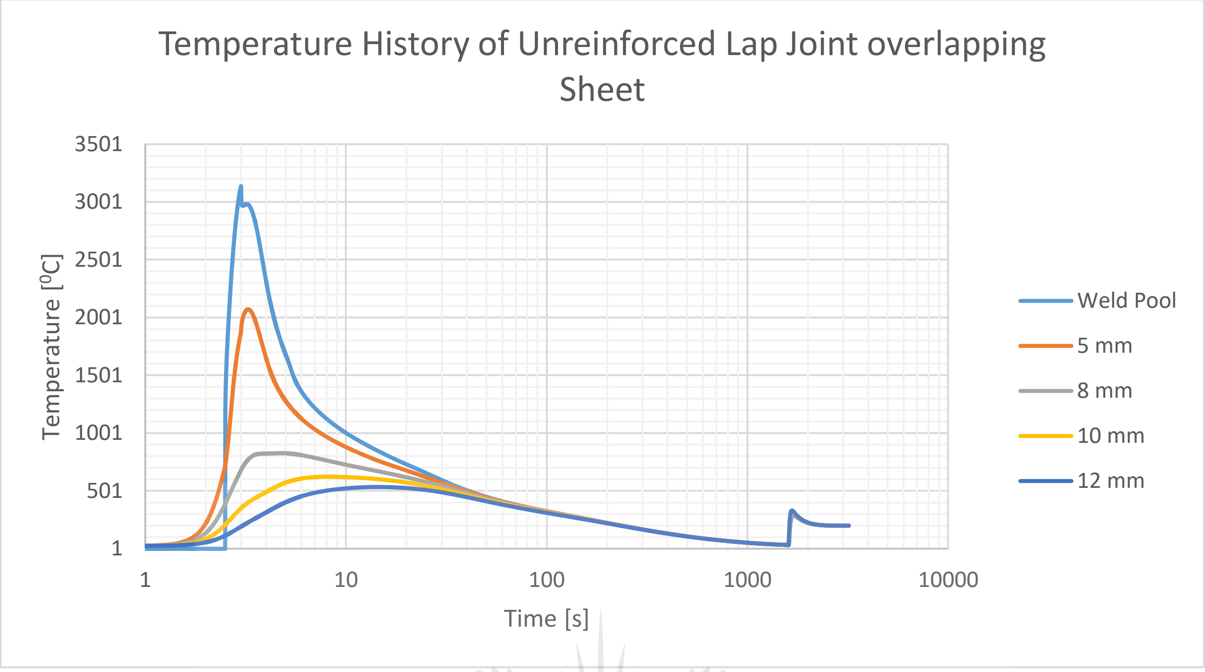

Figure 4-41: Temperature history of the overlapping sheet of the unreinforced lap joint.

4.4.2b Reinforced Lap Joints

The temperature history of the underlapping sheet of the reinforced lap joint is given in Figure 4-42. The analysis estimates a peak temperature of ≈ 3100 ^{0}C in the weld pool, indicating the melting of the parent metal and titanium powder reinforcement. As was the case in the unreinforced lap joint, temperatures 5 mm away from the weld centre exceed the A_{c3} temperature indicating a fully austenised zone during heating.

In this region, CGHAZ is expected to form upon cooling due to a relatively slow cooling rate from its prior austenite phase. Beyond this point, FGHAZ is expected to be formed, as was the case in the unreinforced joint. The cooling rates of both the reinforced and unreinforced samples in the weld metal appear to be the same as both take an estimated 37s to cool from 3000 ^{0}C to 500 ^{0}C. We do not see a prominent effect of titanium reinforcement on the cooling rate as was the case in the butt weld, this could be due to the geometry of the lap weld being more significant in affecting the cooling rate.

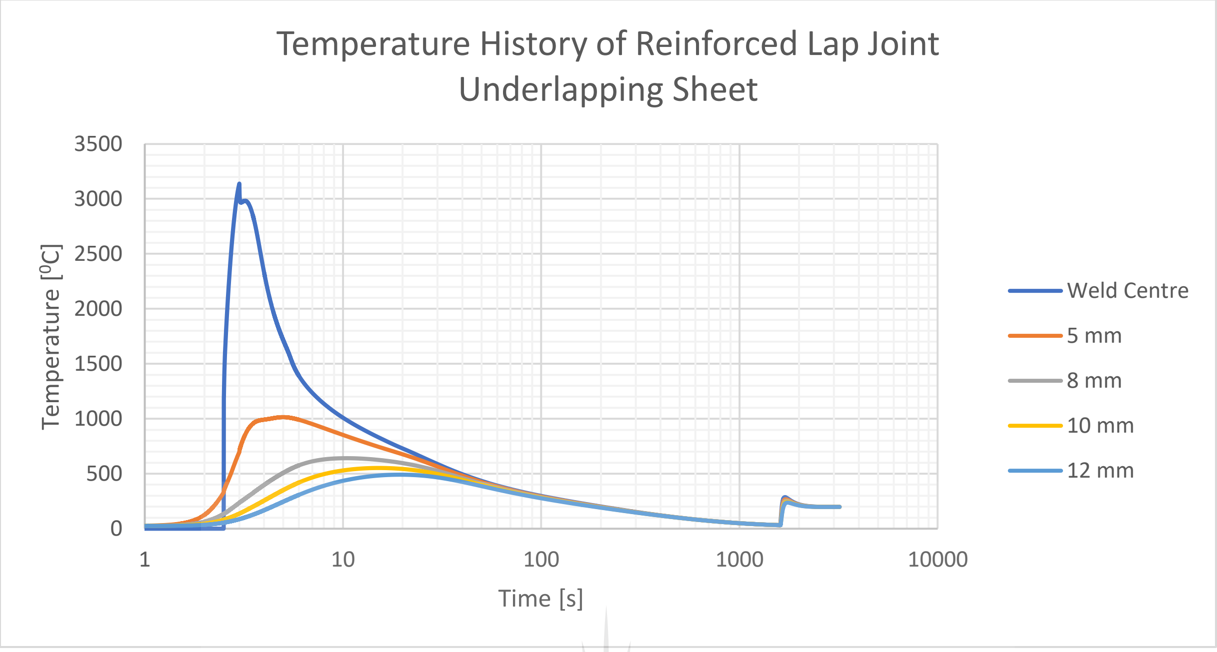

Figure 4-42: Temperature history of the underlapping sheet of the reinforced lap joint.

The temperature history of the overlapping sheet of the reinforced lap weld is given in Figure 4-43. The same pattern observed in the unreinforced lap weld is seen here, with the weld pool extending to 5 mm away from the weld centre on the overlapping sheet. CGHAZ are expected to form just beyond 5 mm, from the weld centre, with FGHAZ also forming between 5 and 8 mm from the weld centre.

The XRD results suggest the presence of martensite in the WM of the reinforced lap joint. However, the cooling rate does not support this. Furthermore, if martensite phases exist in the WM of the reinforced lap joint this could be in form of microphases, which might only be observable using SEM. Notwithstanding, the presence of titanium, will aid the formation of acicular ferrite as earlier seen in Figure 4-21.

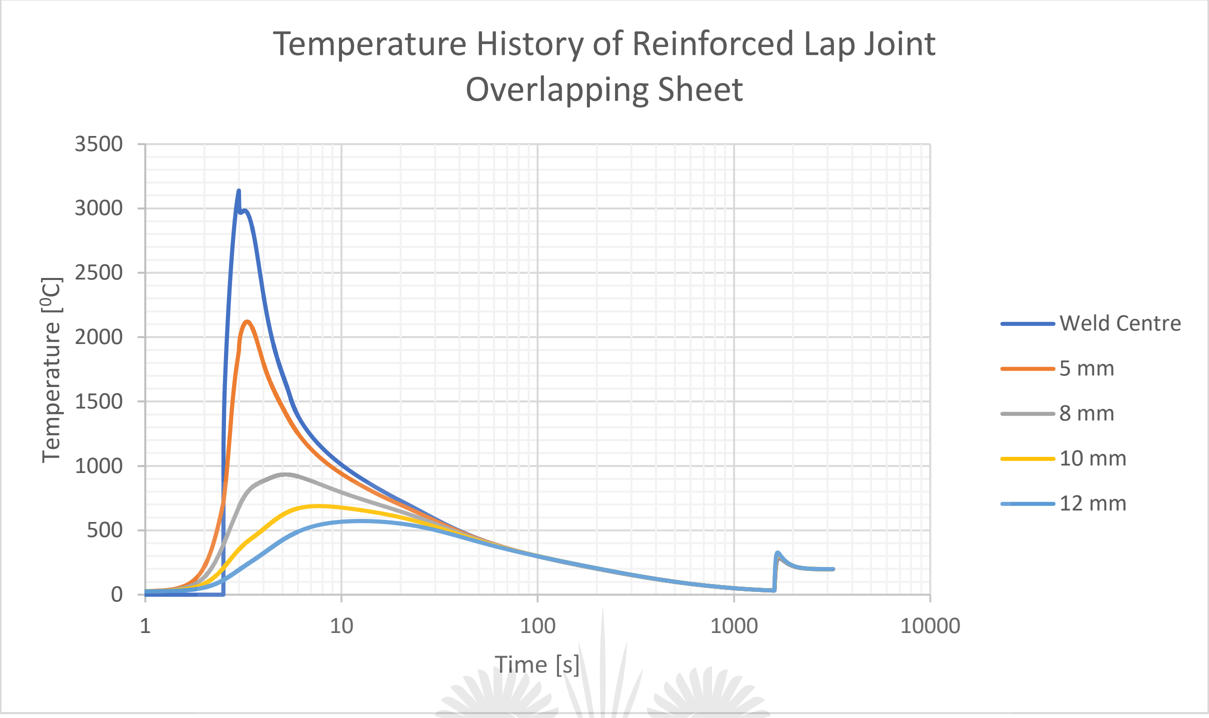

Figure 4-43: Temperature history of the underlapping sheet of the reinforced lap joint.

Lastly, Figure 4-44 compares the locus of peak temperatures of the reinforced and unreinforced lap joints on the underlapping and overlapping plates of each. The figure shows that peak temperatures in the underlapping sheets of both lap joints are almost equal. While in the overlapping sheets, peak temperatures are slightly higher for the reinforced joints. This implies that the peak temperatures in the reinforced lap joints may be affected by the titanium reinforcement, due to its lower conductivity.

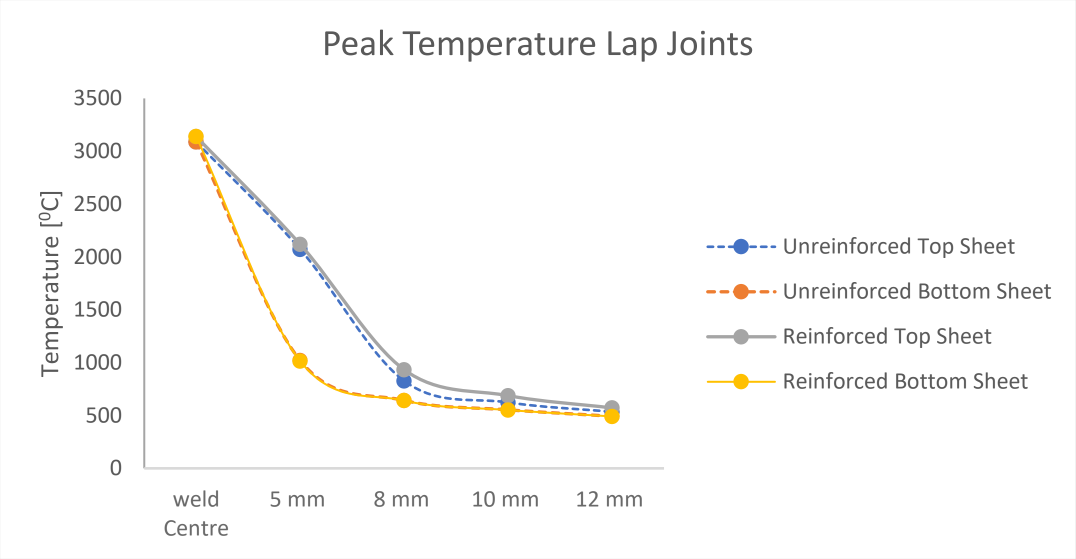

Figure 4-44: Locus of Peak temperatures in optimized lap joints

4.5 Numerical Analysis of Weld Pool Geometry in Butt and Lap Welds

The three-dimensional transient thermal analysis also predicts the weld geometry of the weld pool and could also serve as an alternative method of simulation validation [135],[163]. Piekarska *et al.* [164] have shown that the weld pool can be defined from thermal simulations by the based on the temperature field in the cross-section of the weld. To obtain the simulated weld pool geometry, the cross-section of the weld pool at a point when the heat source is overhead is captured and the temperature contours are used to determine the weld pool dimension. All areas of the weld pool equal to or greater than the melting point of steel are assumed to be part of the weld pool. In regions where titanium reinforcement is present, the areas equal to and above the melting point of titanium were considered to be part of the weld pool. The simulated weld pool dimensions and experimental weld pool dimensions are compared for validation.

The weld pool width and depth of penetration of the are the two dimensions that have been used for comparison in this study. Figure 4-45 shows these dimensions as measured from both the lap and butt joints. *a* represents the depth of penetration and *b* represents the width of the weld pool.

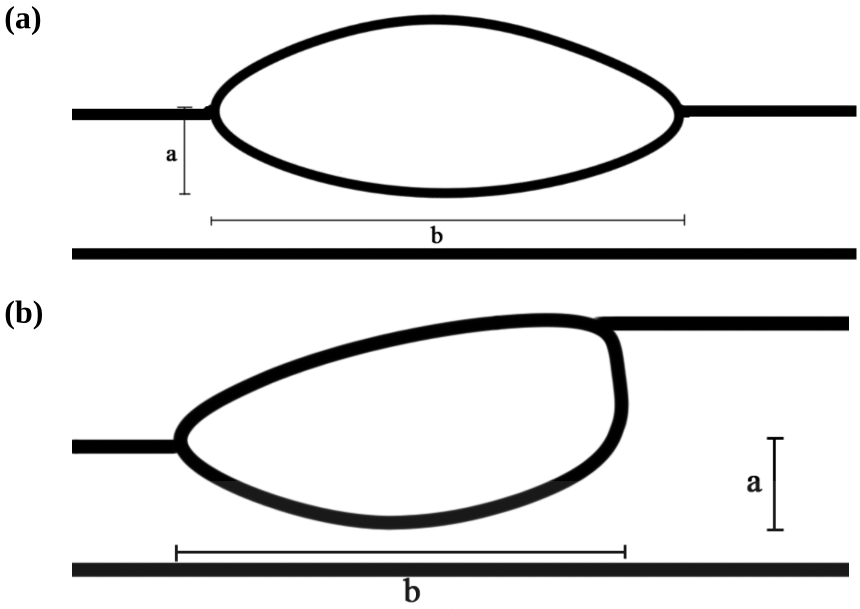

Figure 4-45: Weld pool dimensions of (a) butt joint and (b) lap joints.

The mash-ups of the simulated and experimental weld pool geometries, given to scale are shown in Figure 4-46 a-d.

(a) Butt Unreinforced

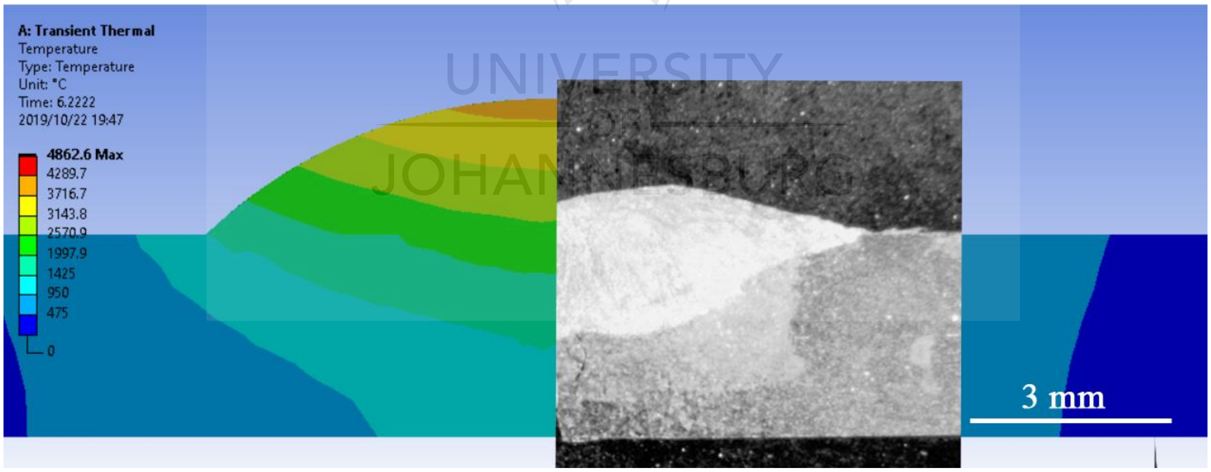

(b) Butt Reinforced

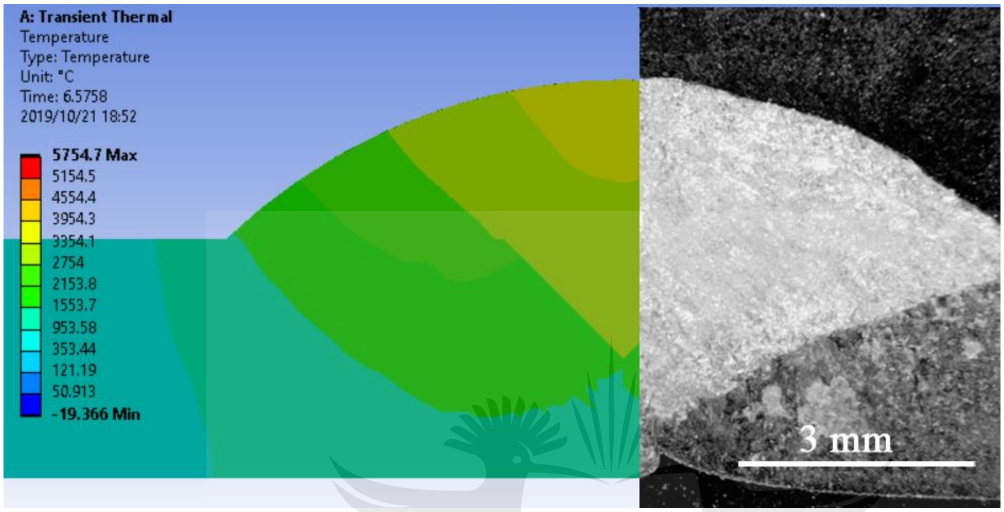

(c) Lap Unreinforced

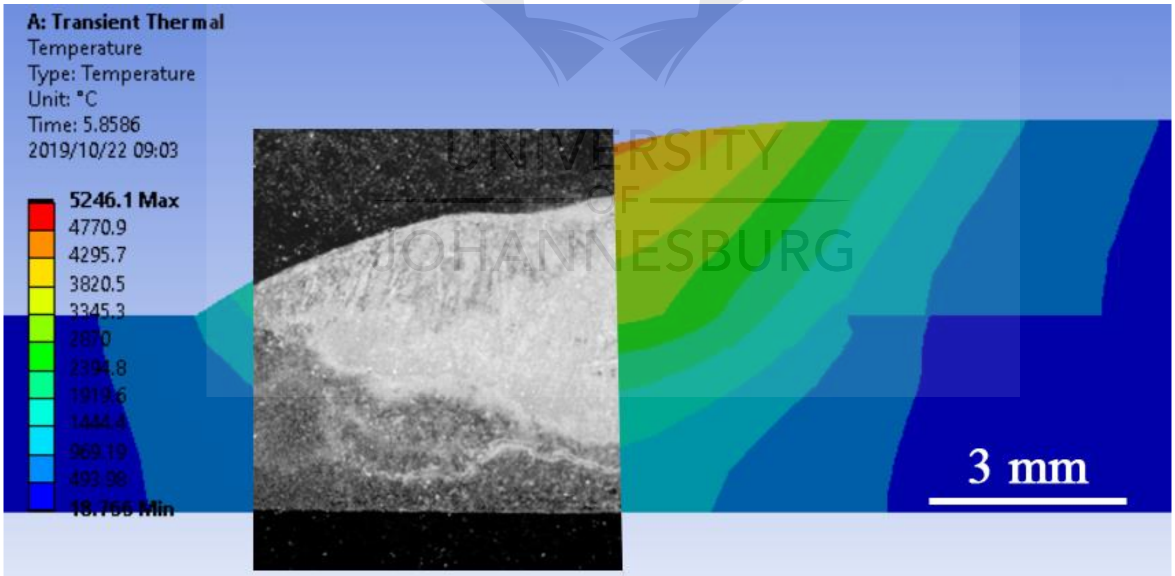

(d) Lap Reinforced

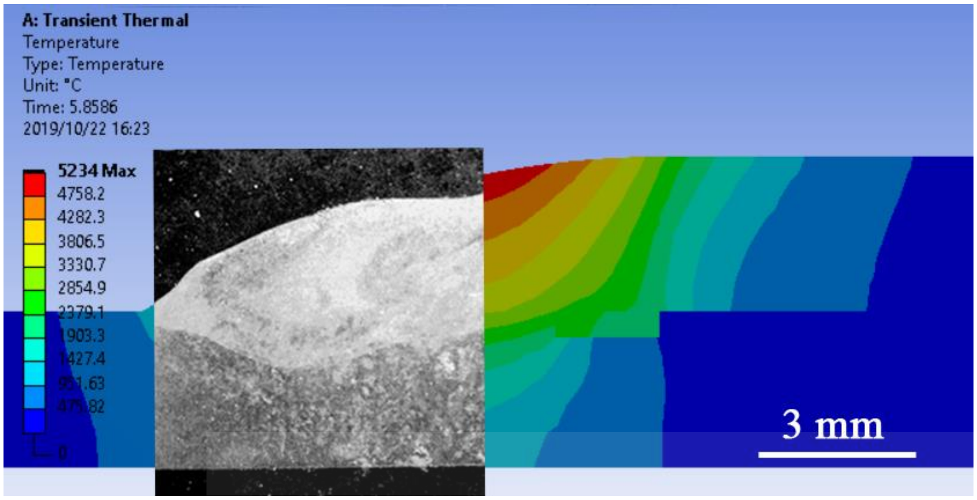

Figure 4-46: Comparison of experimental and simulated weld pool geometries

Figure 4-46 shows there is good agreement between the simulated and experimental weld pool dimensions with respect to its width and depth of penetration. However, the bead height only shows excellent agreement with the reinforced butt joint (Figure 4-46 b). It should be noted that an estimated bead height of 2 mm was put into the simulation set up, therefore it is not expected that the simulated bead height would be wholly accurate. The estimated bead height of 2mm was based on the bead height of the reinforced weldments obtained during the optimization process. Notwithstanding, the depth of penetration and pool width are expected to closely simulate the experimental dimensions.

Table 4-19 shows the experimental and simulated bead with and depth of penetration for the butt joints. The difference between the simulation and experimental results are given as the relative error in percentage. The simulated results for the depth of penetration are in good agreement with the actual dimensions for the butt joints, with a percentage error of less than 10. The agreement between the simulated and experimental results for the bead width of the unreinforced butt joint is only fair, with 15.1 % error. The reason for this error could be due to the difficulty in capturing the complex material behaviour at very high temperatures during simulation [165]. It could also be due to inconsistency in the welding parameters of the actual experiment since a semi-automatic constant voltage MIG machine was used. Nevertheless, the simulated bead width for the reinforced butt joint was in very good agreement with the actual measurement. This shows that this simulation method can be recommended for reinforced weld pool geometry predictions for butt joints.

Table 4-19: Measured and Simulated weld pool dimensions of butt joints.

Butt Joints				
Comparison	**Bead Width**		**Depth of Penetration**	
	Unreinforced	**Reinforced**	**Unreinforced**	**Reinforced**
Experiment (mm)	8.25	9.31	1.67	1.80
Simulation (mm)	9.50	9.81	1.69	1.63
Relative Error (%)	15.1	5.3	1.2	9.4

Table 4-20 shows the experimental and simulated bead width and depth of penetration for the lap joints. The variables in Table 4-20 as same as in Table 4-19. The results in Table 4-20 show that experimental and simulated results for bead width and depth of penetration of the lap joints are in good agreement. Discrepancies between actual and simulated results are within the acceptable error range. The relative error range is similar to those obtained in similar FEA studies [135],[163]. The simulation method is therefore suitable and recommended for predicting the weld pool geometry for lap joints, for both reinforced and unreinforced materials.

Table 4-20: Measured and Simulated weld pool dimensions of lap joints

Lap Joints				
Comparison	**Bead Width**		**Depth of Penetration**	
	Unreinforced	**Reinforced**	**Unreinforced**	**Reinforced**
Experiment (mm)	9.35	11.38	1.93	1.54
Simulation (mm)	10.07	11.33	2.07	1.69
Relative Error (%)	7.1	0.4	7.3	9.7

4.6 Summary

In this chapter, the results of Taguchi's DoE for process optimization were presented. The optimum parameters derived for both the lap and butt joints were used in the final welding stage and compared with unreinforced weldments. Titanium 6-2-2-2 alloy turned out to be the powder reinforcement of choice from the optimization process. ANOVA results of the optimization process did not point out any of the selected parameters as statistically significant.

The microstructures of the weldments obtained during the optimization process were discussed and correlated with the microhardness values measured across the weld zones of the samples. Relatively large gas pores and lack of fusion were observed in some butt welds in the optimization stage. These defects were addressed in the final welding stage.

Mechanical test results from the final welding stage were presented in this chapter and higher microhardness values were found in the reinforced weldments than in their unreinforced counterparts. With regards to microstructure, it was observed that acicular ferrite was more prominent in the weld metal of the reinforced samples. XRD characterization identified the presence of martensite micro-phases in the reinforced samples. The XRD samples also reflected phase purity in the unreinforced samples.

There was no significant difference between the ultimate tensile strength of the reinforced and unreinforced samples. All reinforced and unreinforced optimized samples underwent ductile fracture. Failure analysis for the butt joint samples using SEM and EDS was also carried out and reported.

FEA results have been presented in this chapter. The temperature history of butt and lap; reinforced and unreinforced samples were discussed and correlated with microstructural evolution across the weld zones. The weld pool dimensions of the optimized samples were simulated using FEM and validated with experimental results. The simulated weld pool geometries all showed good agreement, except for the bead width of the unreinforced butt joint which only showed a fair agreement with 15.1 % error.

5. Conclusions and Recommendations

5.1 Introduction

The aim of this research work was to investigate the effect of titanium powder reinforcement on the MIG welding of low carbon steels. Titanium reinforced AISI 1008 steel weldments have been designed using MIG welding and optimized using Taguchi's L4 orthogonal array as a DoE method. This was done for both butt and lap weld configurations. The weldments were characterised for tensile strength and microhardness. Other methods of characterization carried out were optical microscopy, XRD Analysis, EDS and SEM for failure analysis.

The effect of thermal loading during welding, with respect to microstructural evolution, has been simulated using ANSYS Mechanical. The simulation results have been presented and discussed in the preceding chapter. The aim and objectives of this research work have been achieved and well documented in the preceding chapters. In this chapter, the conclusions of this investigation and recommendations for future research work are presented.

5.2 Conclusions

The optimum welding parameters (with respect to tensile strength) for titanium-reinforced 3-mm thick mild steel welds, using MIG welding process, was calculated to be in the region of 24 V and 215 A for butt joints; 26 V and 220 A for lap joints. The gas flow rate was kept constant at 15 lpm. Taguchi's L4 orthogonal array is effective for parametric optimization. However, for more robust optimization processes, an L9 orthogonal array is recommended.

The addition of titanium powder reinforcement resulted in an increase in microhardness within the WM of the mild steel weldments. Microhardness values in the WM of unreinforced samples were lower than their reinforced counterparts, and this was the case for both butt and lap joints. XRD Analysis of the weld zones of the reinforced weldments confirmed the presence of iron-titanium inter-metallic formation. $Fe_{0.975}Ti_{0.025}$ was identified in the reinforced butt welds, while $Fe_{0.975}Ti_{0.025}$ was identified in the reinforced lap welds. The difference in chemical formulae was attributed to the higher heat input in the lap welds. Suspected microphases of Martensite were also identified in the WM of the reinforced samples. The presence of these inter-metallics and martensite microphases could explain the increased microhardness in the WM of the reinforced weldments.

There was no significant difference in tensile strength between the reinforced and unreinforced samples of both butt and lap joints. However, the reinforced butt joint had a higher average tensile strength of 376.75 MPa compared to 367.87 MPa of the unreinforced butt joint. Nevertheless, the tensile strengths of the individual samples fall within a narrow range, such that it is too close to ascertain a definite influence of titanium reinforcement on the tensile strength of the weldments. It can be concluded that despite increasing the hardness of the weldments, titanium reinforcement does not adversely affect nor improve the strength of the weld.

Acicular ferrite was found to be prominent in the reinforced samples for both butt and lap joints than in their unreinforced counterparts. This was attributed to the presence of titanium particles which possibly induced acicular ferrite nucleation on inclusions present in the weld zone. The prominence of acicular ferrite in the reinforced samples suggests an improvement of impact toughness. However, this test could not be carried out to due specimen size and unavailability of testing equipment.

The failure analysis of the butt welds revealed that failure occurred in the base metal for all reinforced samples. SEM and EDS analysis revealed the presence of large impurities in the base metal, which could have resulted in increased stress concentrations and ultimately, failure. In the lap joints, failure occurred in the base metal region for two of the three reinforced samples; and in the weld metal region for the third sample. However, all butt and lap weldments in the final welding stage underwent predominantly ductile failure.

Using ANSYS FEA software, the temperature history at certain points away from the weld centre were calculated and correlated with the microstructure revealed via optical microscopy. In the butt joints, it was deduced that titanium reinforcement could be responsible for a slower cooling rate due to its lower thermal conductivity. However, this was not as pronounced in the lap joints, despite the peak temperatures on the top sheet being higher in the reinforced samples than in the unreinforced samples.

FEA was used to predict the weld pool geometry of lap and butt joints (reinforced and non-reinforced) and validated from the experimental measurements of the weld bead dimensions. The comparison of simulated and experimental results showed generally good agreement. It can be concluded that the adoption of a modified Gaussian distribution equation as the welding heat source sufficiently estimates the weld bead geometry of powder reinforced mild steel welded sheets. This could help to ascertain the weldability of metallic powder reinforced welds.

The aims and objectives of this research work have been achieved and discussed in detail. Despite the promising outlook of the effect of titanium powder reinforcement on the mechanical properties of mild steel welds, evidence from this research work shows that further research is required to fully exhaust the possibilities of this approach.

5.3 Future Work

Despite the body of research work carried out in this study, this study creates a hotbed of possible future research work regarding the use of titanium powders as weld reinforcements in mild steel. Further studies that could be done are highlighted below;

- Process parametric optimization involving varying amounts of titanium powder, using an L9 orthogonal array should be considered. Varying the amount of titanium powder reinforcement could determine the extent to which titanium could improve the tensile strength of the weldments.
- Response surface methodology combined with regression analysis could be used as a statistical tool to develop mathematical models to predict output responses due to various parametric combinations.
- The dominance of acicular ferrite due to titanium reinforcements suggests an improvement of impact toughness. Therefore, impact toughness testing should be done on titanium-reinforced mild steel welds.
- The temperature history calculated from FEA could be validated by redoing the experiments with thermocouples.
- Goldark’s double ellipsoidal heat source can be used to simulate the welding process to check if more accurate weld pool geometries can be obtained.
- Residual stress testing using XRD can be carried out to determine the residual stresses obtained in the welding process of reinforced weldments and compared with their unreinforced counterparts. FEA can also be used to predict the residual stresses introduced to the material during welding.

- The effect of titanium reinforcement of mild steel weldments on the corrosion and wear properties of the weldment can be investigated, considering that titanium has good anti-corrosion properties

It is recommended that future experimental work on this study be carried out with automated welding equipment. This will ensure repeatability in the results obtained from the welding experiment. Parametric stability whilst using semi-automatic welding machines can be complicated and requires excellent welding skills.

References

[1] P. Kumar, A. K. Dhingra and P. Kumar, "Optimization of process parameters for machining of mild steel EN18 by response surface methodology," *Advances in Engineering: An International Journal*, vol. 1, *(1)*, .

[2] (Feb 9,). *5 Contemporary uses of mild steel*. Available: http://www.austenknapman.co.uk/blog/uses-of-metal/5-contemporary-uses-of-mild-steel.

[3] S. Helzer, "Welding metallurgy part 1: Understanding mechanical principles," in Anonymous Inspection Trends, 2006, .

[4] T. Odiaka, N. Madushele and S. Akinlabi, "Improvement of joint integrity in MIG welded steel: A review," in *ASME 2018 International Mechanical Engineering Congress and Exposition*, 2018, .

[5] T. Nam *et al*, "Effect of Post Weld Heat Treatment on the Microstructure and Mechanical Properties of a Submerged-Arc-Welded 304 Stainless Steel," *Metals*, vol. 8, *(1)*, pp. 26, 2018.

[6] X. Li *et al*, "Effect of post weld heat treatment on the microstructure and properties of Laser-TIG hybrid welded joints for CLAM steel," *Fusion Eng. Des.*, vol. 128, pp. 175-181, 2018.

[7] C. Sawanishi *et al*, "Mechanical properties and microstructures of resistance spot welded DP980 steel joints using pulsed current pattern," *Science and Technology of Welding and Joining*, vol. 19, *(1)*, pp. 52-59, 2014.

[8] R. Lokesh *et al*, "Optimization of process parameters tool pin profile, rotational speed and welding speed for submerged friction stir welding of AA6063 alloy," *International Journal of Technical and Research Applications12*, pp. 35-38, 2015.

[9] S. P. Chavda, J. V. Desai and T. M. Patel, "A review on optimization of MIG Welding parameters using Taguchi's DOE method," *International Journal of Engineering and Management Research*, vol. 4, *(1)*, pp. 16-21, 2014.

[10] J. Shah, G. Patel and J. Makwana, "Optimization and Prediction Of MIG Welding Process Parameters Using ANN," *International Journal of Engineering Development and Research*, vol. 5, *(2)*, 2017.

[11] (Mar 21,). *Gas Metal Arc Welding (GMAW)- Components and working principles*. Available: http://www.zoombd24.com/gas-metal-arc-welding-gmaw-components-and-working-principles/.

[12] S. Angaria, P. S. Rao and S. S. Dhami, "Optimization of MIG Welding Process Parameters: A Review," *Research Journal of Engineering and Technology*, vol. 8, *(3)*, pp. 273-276, 2017.

[13] J. P. Ganjigatti, D. K. Pratihar and A. RoyChoudhury, "Modeling of the MIG welding process using statistical approaches," *The International Journal of Advanced Manufacturing Technology*, vol. 35, *(11-12)*, pp. 1166-1190, 2008.

[14] T. Bell. (Mar 2,). *All About Steel*. Available: https://www.thebalance.com/metal-profile-steel-2340175.

[15] D. Johnson. (Feb 26,). *Properties & Uses of Steel*. Available: https://sciencing.com/properties-uses-steel-7271721.html.

[16] T. Bell. (July 1,). *What Are the Different Types of Steel?*. Available: https://www.thebalance.com/steel-grades-2340174.

[17] Worldsteel. (). *About worldsteel statistics*. Available: http://www.worldsteel.org/faq/about-worldsteel-statistics.html.

[18] American Iron and Steel Institute. (). *Making Steel: How It's Made | AISI - American Iron & Steel Institute*. Available: http://www.steel.org/steel-technology/how-its-made.aspx.

[19] D. R. H. Jones and M. F. Ashby, *Engineering Materials 2: An Introduction to Microstructures, Processing and Design*. 2005.

[20] J. Fu *et al*, "Effect of Nb addition on the microstructure and corrosion resistance of ferritic stainless steel," *Applied Physics A*, vol. 126, *(3)*, pp. 1-12, 2020.

[21] American Iron and Steel Institute. (). *Steel Glossary P-T*. Available: http://www.steel.org/steel-technology/glossary/glossary-p-t.aspx.

[22] J. Kim *et al*, "An Experimental study on Prediction of Back-bead Geometry in Pipeline Using the GMA Welding Process," *Journal of the Korean Society of Manufacturing Technology Engineers*, vol. 20, *(1)*, pp. 74-80, 2011.

[23] J. Kazi *et al*, "A Review on Various Welding Techniques," *International Journal of Modern Research*, vol. 5, *(2)*, pp. 22-28, 2015.

[24] K. Singh and A. Anand, "Safety Considerations In A Welding Process: A Review," *International Journal of Innovative Research in Science, Engineering and Technology*, vol. 2, *(2)*, pp. 341-350, 2013.

[25] C. M. Chen and R. Kovacevic, "Finite element modeling of friction stir welding—thermal and thermomechanical analysis," *Int. J. Mach. Tools Manuf.*, vol. 43, *(13)*, pp. 1319-1326, 2003.

[26] S. Kou, *Welding Metallurgy*. (Second ed.) Hoboken, New Jersey: John Wiley & Sons, Inc., 2003.

[27] A. Hooda, A. Dhingra and S. Sharma, "Optimization of MIG welding process parameters to predict maximum yield strength in AISI 1040," *International Journal of Mechanical Engineering and Robotics Research,* vol. 1, *(3),* 2012.

[28] A. Pal, "MIG Welding Parametric Optimisation Using Taguchi's Orthogonal Array and Analysis of Variance," *International Journal of Research Review in Engineering Science and Technology,* vol. 4, *(1),* pp. 211-217, 2015.

[29] P. Yayla, E. Kaluc and K. Ural, "Effects of welding processes on the mechanical properties of HY 80 steel weldments," *Mater Des,* vol. 28, *(6),* pp. 1898-1906, 2007.

[30] S. R. Nathan *et al*, "Effect of welding processes on mechanical and microstructural characteristics of high strength low alloy naval grade steel joints," *Defence Technology,* vol. 11, *(3),* pp. 308-317, 2015.

[31] S. P. Tewari, A. Gupta and J. Prakash, "Effect of welding parameters on the weldability of material," *International Journal of Engineering Science and Technology,* vol. 2, *(4),* pp. 512-516, 2010.

[32] M. B. Raut and S. N. Shelke, "Optimization of Special Purpose Rotational MIG Welding by Experimental and Taguchi Technique," *International Journal of Innovative Technology and Exploring Engineering (IJITEE),* vol. 4, *(6),* pp. 39-46, 2014.

[33] D. Ramos-Jaime, I. L�pez-Ju�rez and P. Perez, "Effect of process parameters on robotic GMAW bead area estimation," *Procedia Technology,* vol. 7, pp. 398-405, 2013.

[34] G. Ramakrishna, P. S. Rao and P. G. Rao, "Methods To Improve Mechanical Properties of Welded Joints: View Point," *International Journal of Mechanical Engineering and Technology,* vol. 7, *(6),* pp. 309-314, 2016.

[35] J. I. Lee and K. W. Um, "A prediction of welding process parameters by prediction of back-bead geometry," *J. Mater. Process. Technol.,* vol. 108, *(1),* pp. 106-113, 2000.

[36] B. C. Patel and J. Gandhi, "Optimizing and analysis of parameter for pipe welding: a literature review," *Int J Eng Res Technol (IJERT),* vol. 2, *(10),* pp. 229-234, 2013.

[37] L. S. Kumar, D. S. Verma and D. V. Satyanarayana, "Impact Of Voltage On Austenitic StainlessSteel for The Process Of TIG And MIG Welding," *International Journal of Mechanical Engineering and Technology,* vol. 1, *(1),* pp. 60-75, 2010.

[38] K. Kishore *et al*, "Analysis of defects in gas shielded arc welding of AISI1040 steel using Taguchi method," *ARPN Journal of Engineering and Applied Sciences,* vol. 5, *(1),* pp. 37-41, 2010.

[39] N. S. Patel and P. B. Rahul, "A review on parametric optimization of tig welding," *International Journal of Computational Engineering Research,* vol. 4, *(1),* pp. 27-31, 2014.

[40] U. Eşme, "Application of Taguchi method for the optimization of resistance spot welding process," *Arabian Journal for Science and Engineering,* vol. 34, *(2),* pp. 519, 2009.

[41] A. Kathuria and D. Gupta, "Effect of Titanium Powder Addition on Tensile Strength in Submerged Arc Welding," *International Journal of Engineering Sciences Research and Technology,* vol. 5, *(1),* pp. 882-828, 2016.

[42] V. Pandhare *et al*, "Determination Of Significant Factors Affecting The Bending Strength Of Weld Joint Prepared by Gas Metal Arc Welding," *International Journal of Mechanical Engineering Research and Technology,* vol. 2, *(1),* pp. 1-10, 2016.

[43] E. G. Akpabio *et al*, "Process optimization for the application of carbon from plantain peels in dye abstraction," *Journal of Taibah University for Science,* vol. 11, pp. 173-185, 2017.

[44] S. Srivastava and R. K. Garg, "Process parameter optimization of gas metal arc welding on IS:2062 mild steel using response surface methodology," *Journal of Manufacturing Processes,* vol. 25, pp. 296-305, 2017. Available: http://0-www.sciencedirect.com.ujlink.uj.ac.za/science/article/pii/S1526612516301888. DOI: //doi.org/10.1016/j.jmapro.2016.12.016.

[45] B. A. Shukla and N. G. Phafat, "Experimental Study of CO2 Arc Welding Parameters on Weld Strength for AISI 1022 Steel Plates Using Response Surface Methodology," *Internatial Journal of Mechanical Engineering and Technology,* vol. 4, *(6),* pp. 37-42, 2013.

[46] M. Singla, D. Singh and D. Deepak, "Parametric Optimisation of Gas Metal Arc Welding Processes using Factorial Design Approach," *Journal of Minerals and Materials Characterisation and Engineering,* vol. 9, *(4),* pp. 353, Apr 20, 2010.

[47] I. A. Ibrahim *et al*, "The Effect of Gas Metal Arc Welding (GMAW) Processes on Different Welding Parameters," *Procedia Engineering,* vol. 41, pp. 1502-1506, 2012. Available: http://0-www.sciencedirect.com.ujlink.uj.ac.za/science/article/pii/S1877705812027427. DOI: //doi.org/10.1016/j.proeng.2012.07.342.

[48] K. C. Harshal, D. S. Gunwant and M. S. Kadam, " Finite Element Model to Predict Residual Stresses in MIG Welding." *International Journal Mechanical Engineering and Technology,* vol. 3, *(3),* pp. 350-361, Sep, 2012.

[49] K. B. Pipavat, D. Pandya and M. V. Patel, "Optimization of MIG welding Process Parameter using Taguchi Techniques," *Optimization,* vol. 1, *(5),* 2014.

[50] S. V. Sapakal¹ and M. T. Telsang, "Parametric optimization of MIG welding using Taguchi design method," *Int J Adv Eng Res Stud,* vol. 1, *(4),* pp. 28-30, 2012.

[51] V. Singh, "An Investigation for Gas Metal Arc Welding optimum Parameters of Mild Steel AISI 1016 using Taguchi‟ s Method," *International Journal of Engineering and Advanced Technology (IJEAT),* vol. 2, *(6),* pp. 407-409, 2013.

[52] R. R. Patil and M. V. Kavade, "Parametric Optimization of Gas Metal Arc Welding for S355J2N by Using Design of Experiment," *Journal of Material Science and Mechanical Engineering,* vol. 2, *(10),* pp. 44-48, 2015.

[53] S. Utkarsh *et al,* "Experimental investigation of MIG welding for ST-37 using design of experiment," *International Journal of Scientific and Research Publications,* vol. 4, *(5),* pp. 1, 2014.

[54] K. A. Rajagopal, K. Balakrishnan and I. M. Chandran, "Optimization of Process Parameters by Taguchi Methods in Gas Metal Arc Welding of AISI 1042 Steel," *Proceedings of International Conference on Materials for the Future - Innovative Materials, Processes, Products and Applications,* pp. 56-59, 2013.

[55] M. A. Dinesh, C. Vedansh and V. Jyoti, "Parametric Optimization of MIG Process Parameters Using Taguchi and Grey Taguchi Analysis." *International Journal of Research in Engineering and Applied Sciences.,* vol. 3, *(6),* pp. 1-17, 2013.

[56] S. R. Meshram and N. S. Pohokar, "Optimization of process parameters of Gas Metal Arc Welding to improve Quality of Weld bead geometry," *International Journal of Engineering, Business and Enterprise Applications,* pp. 46-52, 2013.

[57] G. Kocher, S. Kumar and G. Singh, "experimental analysis in MIG welding with is 2062e250 a steel with various effects," *International Journal of Advanced Engineering Technology,* vol. 3, pp. 158-162, 2012.

[58] S. K. Rakesh, "Determination of Significant Process Parameter in Metal Inert Gas Welding of Mild Steel by using Analysis of Variance (ANOVA)," *International Journal of Engineering and Management Research,* vol. 4, *(2),* pp. 271-276, 2014.

[59] J. Ding *et al*, "Effect of post weld heat treatment on properties of variable polarity TIG welded AA2219 aluminium alloy joints," *Transactions of Nonferrous Metals Society of China,* vol. 24, *(5),* pp. 1307-1316, 2014.

[60] S. R. Ahmed, L. A. Agarwal and B. Daniel, "Effect of Different Post Weld Heat Treatments on the Mechanical properties of Cr-Mo Boiler Steel Welded with SMAW Process," *Materials Today: Proceedings,* vol. 2, *(4-5),* pp. 1059-1066, 2015.

[61] T. Ibrahim, D. S. Yawas and S. Y. Aku, "Effects of gas metal arc welding techniques on the mechanical properties of duplex stainless steel," *Journal of Minerals and Materials Characterization and Engineering,* vol. 1, *(05),* pp. 222, 2013.

[62] R. Ahmad and M. A. Bakar, "Effect of a post-weld heat treatment on the mechanical and microstructure properties of AA6061 joints welded by the gas metal arc welding cold metal transfer method," *Mater Des,* vol. 32, *(10),* pp. 5120-5126, 2011.

[63] J. An *et al*, "Improvement of mechanical properties of stainless maraging steel laser weldments by post-weld ageing treatments," *Mater Des*, vol. 40, pp. 276-284, 2012.

[64] J. Mao *et al*, "Microstructure and mechanical properties of GTA weldments of titanium matrix composites prepared with or without current pulsing," *Transactions of Nonferrous Metals Society of China*, vol. 24, *(5)*, pp. 1393-1399, 2014.

[65] V. Balasubramanian, V. Ravisankar and G. M. Reddy, "Effect of pulsed current welding on mechanical properties of high strength aluminum alloy," *The International Journal of Advanced Manufacturing Technology*, vol. 36, *(3-4)*, pp. 254-262, 2008.

[66] A. Raveendra and B. R. Kumar, "Experimental study on Pulsed and Non-Pulsed Current TIG Welding of Stainless Steel sheet (SS304)," *International Journal of Innovative Research in Science, Engineering and Technology*, vol. 2, *(6)*, pp. 2337-2344, 2013.

[67] X. Dai *et al*, "Microstructure and properties of Mg/Al joint welded by gas tungsten arc welding-assisted hybrid ultrasonic seam welding," *Mater Des*, vol. 77, pp. 65-71, 2015.

[68] P. Leo *et al*, "Effect of power distribution on the weld quality during hybrid laser welding of an Al–Mg alloy," *Optics & Laser Technology*, vol. 73, pp. 118-126, 2015.

[69] C. Li and L. Liu, "Investigation on weldability of magnesium alloy thin sheet T-joints: arc welding, laser welding, and laser-arc hybrid welding," *The International Journal of Advanced Manufacturing Technology*, vol. 65, *(1-4)*, pp. 27-34, 2013.

[70] P. K. Singh, D. Patel and S. B. Prasad, "Optimization of process parameters during vibratory welding technique using Taguchi's analysis," *Perspectives in Science*, vol. 8, pp. 399-402, 2016. Available: http://0-www.sciencedirect.com.ujlink.uj.ac.za/science/article/pii/S2213020916301100. DOI: //doi.org/10.1016/j.pisc.2016.04.088.

[71] L. Qinghua, C. Ligong and N. Chunzhen, "Effect of vibratory weld conditioning on welded valve properties," *Mech. Mater.*, vol. 40, *(7)*, pp. 565-574, 2008.

[72] P. Ambroza, L. Kavaliauskiene and E. Pupelis, "Automatic arc welding and overlaying welding of steel using waste materials powder/Lankinis automatinis plieno suvirinimas ir apvirinimas naudojant antriniu medziagu miltelius," *Mechanika*, vol. 2, *(82)*, pp. 75-80, 2010.

[73] B. Singh *et al*, "Effect of CaF2, FeMn and NiO additions on impact strength and hardness in submerged arc welding using developed agglomerated fluxes," *J. Alloys Compounds*, vol. 667, pp. 158-169, 2016.

[74] Z. Lin, P. Chuan and Z. TIAN, "Influence of Ti on Weld Microstructure and Mechanical Properties in Large Heat Input Welding of High Strength Low Alloy Steels," *Journal of Iron and Steel Research, International*, vol. 22, *(5)*, pp. 431-437, 2015.

[75] J. Tušek and M. Suban, "High-productivity multiple-wire submerged-arc welding and cladding with metal-powder addition," *Journal of Materials Processing Technology*, vol. 133, *(1)*, pp. 207-213, 2003. Available: http://0-www.sciencedirect.com.ujlink.uj.ac.za/science/article/pii/S0924013602002352. DOI: //doi.org/10.1016/S0924-0136(02)00235-2.

[76] Y. Li *et al*, "Effect of oxides on nucleation of ferrite: first principle modelling and experimental approach," *Materials Science and Technology*, vol. 32, *(1)*, pp. 88-93, 2016.

[77] H. Bhadeshia and R. Honeycombe, *Steels: Microstructure and Properties*. 2017.

[78] R. N. Wright, "Chapter 14 - Relevant Aspects of Carbon and Low-Alloy Steel Metallurgy," *Wire Technology (Second Edition)*, pp. 201-233, 2016. Available: http://www.sciencedirect.com/science/article/pii/B9780128026502000145. DOI: https://doi.org/10.1016/B978-0-12-802650-2.00014-5.

[79] J. W. Christian, *The Theory of Transformations in Metals and Alloys*, . (3rd ed.) UK: Pergamon Press, Oxford, 2002.

[80] C. Suryanarayana, "Microstructure: An introduction," in *Aerospace Materials and Material Technologies*Anonymous 2017, .

[81] E. Gamsjäger, J. Svoboda and F. D. Fischer, "Austenite-to-ferrite phase transformation in low-alloyed steels," *Computational Materials Science*, vol. 32, *(3)*, pp. 360-369, 2005. Available: http://www.sciencedirect.com/science/article/pii/S0927025604002150. DOI: https://doi.org/10.1016/j.commatsci.2004.09.031.

[82] D. A. Laughlin and Hono Kazuhiro, *Physical Metallurgy*. (5th Edition ed.) Massachusetts, USA: Elsevier, 2014*2*.

[83] W. Plieth, "10 - Corrosion and Corrosion Protection," *Electrochemistry for Materials Science*, pp. 291-321, 2008. Available: http://www.sciencedirect.com/science/article/pii/B9780444527929500129. DOI: https://doi.org/10.1016/B978-044452792-9.50012-9.

[84] R. E. Smallman and A. H. W. Ngan, "Chapter 2 - Phase Diagrams and Alloy Theory," *Modern Physical Metallurgy (Eighth Edition)*, pp. 43-91, 2014. Available: http://www.sciencedirect.com/science/article/pii/B978008098204500002X. DOI: https://doi.org/10.1016/B978-0-08-098204-5.00002-X.

[85] R. Schmid-Fetzer, "Phase diagrams: the beginning of wisdom," *Journal of Phase Equilibria and Diffusion*, vol. 35, *(6)*, pp. 735-760, 2014.

[86] P. J. Ennis, "7 - Ferritic and martensitic steels for power plants," *Structural Alloys for Power Plants*, pp. 188-220, 2014. Available:

http://www.sciencedirect.com/science/article/pii/B9780857092380500073. DOI: https://doi.org/10.1533/9780857097552.2.188.

[87] Z. Yang and H. Fang, "An overview on bainite formation in steels," *Current Opinion in Solid State and Materials Science*, vol. 9, *(6)*, pp. 277-286, 2005. Available: http://www.sciencedirect.com/science/article/pii/S1359028606000490. DOI: https://doi.org/10.1016/j.cossms.2006.06.005.

[88] A. J. Loureiro, "Effect of heat input on plastic deformation of undermatched welds," *J. Mater. Process. Technol.*, vol. 128, *(1-3)*, pp. 240-249, 2002.

[89] W. W. Xu *et al*, "Effect of welding heat input on simulated HAZ microstructure and toughness of a VN microalloyed steel," *Journal of Iron and Steel Research, International*, vol. 14, *(5)*, pp. 234-239, 2007.

[90] K. P. Kolhe and C. K. Datta, "Prediction of microstructure and mechanical properties of multipass SAW," *J. Mater. Process. Technol.*, vol. 197, *(1-3)*, pp. 241-249, 2008.

[91] Y. Zhang *et al*, "Effect of heat input on microstructure and toughness of coarse grain heat affected zone in Nb microalloyed HSLA steels," *J. Iron Steel Res. Int.*, vol. 16, *(5)*, pp. 73-80, 2009.

[92] R. Singh, "Chapter 3 - Physical Metallurgy," *Applied Welding Engineering (Second Edition)*, pp. 13-26, 2016. Available: http://www.sciencedirect.com/science/article/pii/B9780128041765000037. DOI: https://doi.org/10.1016/B978-0-12-804176-5.00003-7.

[93] Z. Boumerzoug, C. Derfouf and T. Baudin, "Effect of welding on microstructure and mechanical properties of an industrial low carbon steel," *Engineering*, vol. 2, *(07)*, pp. 502, 2010.

[94] J. Laitila and J. Larkiola, "Effect of enhanced cooling on mechanical properties of a multipass welded martensitic steel," *Weld. World*, vol. 63, *(3)*, pp. 637-646, 2019.

[95] T. Tawfeek, "Study the Influence of Gas Metal Arc Welding Parameters on the Weld Metal and Heat Affected Zone Microstructures of Low Carbon Steel," .

[96] T. Tawfeek, A. Hemaid and O. A. Gaheen, "An Investigation into Effect of Butt Welding Parameters on Weldment Mechanical Properties," *American Journal of Mechanical Engineering*, vol. 4, *(3)*, pp. 92-98, 2016.

[97] E. Gharibshahiyan *et al*, "The effect of microstructure on hardness and toughness of low carbon welded steel using inert gas welding," *Mater Des*, vol. 32, *(4)*, pp. 2042-2048, 2011.

[98] M. Shome, "Effect of heat-input on austenite grain size in the heat-affected zone of HSLA-100 steel," *Materials Science and Engineering: A*, vol. 445, pp. 454-460, 2007.

[99] D. A. Porter, K. E. Easterling and M. Sherif, *Phase Transformations in Metals and Alloys, (Revised Reprint).* 2009.

[100] E. Gharibshahiyan, A. H. Raouf and N. Parvin, "Microstructural evolution in friction stir welded API 5L-X52 steel," *International Advanced Research Journal in Science, Engineering and Technology*, pp. 2-11, 2013.

[101] Muda, Wan Shaiful Hasrizam Wan *et al*, "Effect of welding heat input on microstructure and mechanical properties at coarse grain heat affected zone of ABS grade A steel," *ARPN Journal of Engineering and Applied Sciences*, vol. 10, *(20)*, pp. 9487-9495, 2015.

[102] R. Abbaschian and R. E. Reed-Hill, *Physical Metallurgy Principles.* 2008.

[103] R. Kaçar and K. Kökemli, "Effect of controlled atmosphere on the mig-mag arc weldment properties," *Mater Des*, vol. 26, *(6)*, pp. 508-516, 2005.

[104] S. D. Bhole *et al*, "Effect of nickel and molybdenum additions on weld metal toughness in a submerged arc welded HSLA line-pipe steel," *J. Mater. Process. Technol.*, vol. 173, *(1)*, pp. 92-100, 2006.

[105] W. Ahmed *et al*, "2 - Precision machining of medical devices," *The Design and Manufacture of Medical Devices*, pp. 59-113, 2012. Available: http://www.sciencedirect.com/science/article/pii/B9781907568725500029. DOI: https://doi.org/10.1533/9781908818188.59.

[106] F. H. Froes, *Titanium: Physical Metallurgy, Processing, and Applications.* 2015.

[107] S. K. Nayak *et al*, "Insight into point defects and impurities in titanium from first principles," *Npj Computational Materials*, vol. 4, *(1)*, pp. 1-10, 2018.

[108] C. Veiga, J. P. Davim and A. Loureiro, "Properties and applications of titanium alloys: a brief review," *Rev.Adv.Mater.Sci*, vol. 32, *(2)*, pp. 133-148, 2012.

[109] M. V. Ribeiro, M. Moreira and J. R. Ferreira, "Optimization of titanium alloy (6Al–4V) machining," *J. Mater. Process. Technol.*, vol. 143, pp. 458-463, 2003.

[110] (Sep 19,). *Titanium and titanium alloys: Fundamentals and Applications*.

[111] R. E. Smallman and A. H. W. Ngan, "Chapter 14 - Selected Alloys," *Modern Physical Metallurgy (Eighth Edition)*, pp. 529-569, 2014. Available: http://www.sciencedirect.com/science/article/pii/B9780080982045000146. DOI: https://doi.org/10.1016/B978-0-08-098204-5.00014-6.

[112] Leyens Christoph and Peters Manfred, *Titanium and Titanium Alloys: Fundamentals and Applications.* Weinheim, Germany: Wiley-VCH, 2003.

[113] J. Stráský *et al*, "4.5 - Microstructure and lattice defects in ultrafine grained biomedical α+β and metastable β Ti alloys," *Titanium in Medical and Dental Applications*, pp. 455-475, 2018. Available: http://www.sciencedirect.com/science/article/pii/B9780128124567000202. DOI: https://doi.org/10.1016/B978-0-12-812456-7.00020-2.

[114] N. Kosova *et al*, "The preparation of the ti-al alloys based on intermetallic phases," in *IOP Conference Series: Materials Science and Engineering*, 2016, .

[115] G. Lütjering and J. C. Williams, *Titanium.* 2007.

[116] J. Sieniawski *et al*, "Microstructure and mechanical properties of high strength two-phase titanium alloys," *Titanium Alloys-Advances in Properties Control*, pp. 69-80, 2013.

[117] I. Chattoraj, "10 - Stress corrosion cracking (SCC) and hydrogen-assisted cracking in titanium alloys," *Stress Corrosion Cracking*, pp. 381-408, 2011. Available: http://www.sciencedirect.com/science/article/pii/B9781845696733500109. DOI: https://doi.org/10.1533/9780857093769.3.381.

[118] N. J. Hallab and J. J. Jacobs, "Chapter II.5.6 - Orthopedic Applications," *Biomaterials Science (Third Edition)*, pp. 841-882, 2013. Available: http://www.sciencedirect.com/science/article/pii/B9780080877808000735. DOI: https://doi.org/10.1016/B978-0-08-087780-8.00073-5 ".

[119] D. Prando *et al*, "Corrosion of titanium: Part 1: Aggressive environments and main forms of degradation," *Journal of Applied Biomaterials & Functional Materials*, vol. 15, *(4)*, pp. e291-e302, 2017.

[120] W. D. Callister and D. G. Rethwisch, *Materials Science and Engineering: An Introduction.* 20077.

[121] A. Ramanathan, P. K. Krishnan and R. Muraliraja, "A review on the production of metal matrix composites through stir casting–Furnace design, properties, challenges, and research opportunities," *Journal of Manufacturing Processes*, vol. 42, pp. 213-245, 2019.

[122] K. K. Ekka and S. R. Chauhan, "Dry sliding wear characteristics of SiC and Al 2 O 3 nanoparticulate aluminium matrix composite using Taguchi technique," *Arabian Journal for Science and Engineering*, vol. 40, *(2)*, pp. 571-581, 2015.

[123] K. Ekka and S. Chauhan, "Dry Sliding Wear Characteristics of SiC and AlO Nanoparticulate Aluminium Matrix Composite Using Taguchi Technique." *Arabian Journal for Science & Engineering (Springer Science & Business Media BV)*, vol. 40, *(2)*, 2015.

[124] M. Kok, "Production and mechanical properties of Al2O3 particle-reinforced 2024 aluminium alloy composites," *J. Mater. Process. Technol.*, vol. 161, *(3)*, pp. 381-387, 2005.

[125] R. Acker *et al*, "Casting of Fe–CrMnNi and ZrO2-Based Metal–Matrix Composites and Their Wear Properties," *Steel Research International*, vol. 87, *(8)*, pp. 1111-1117, 2016.

[126] J. W. Kaczmar, K. Pietrzak and W. Włosiński, "The production and application of metal matrix composite materials," *J. Mater. Process. Technol.*, vol. 106, *(1-3)*, pp. 58-67, 2000.

[127] S. C. Tjong and Z. Y. Ma, "Microstructural and mechanical characteristics of in situ metal matrix composites," *Materials Science and Engineering: R: Reports*, vol. 29, *(3-4)*, pp. 49-113, 2000.

[128] R. Chang *et al*, "Comparison study of Fe-based matrix composites reinforced with Ti-coated and Mo-coated SiC particles," *Mater. Chem. Phys.*, vol. 204, pp. 154-162, 2018.

[129] D. Guan *et al*, "Microstructure and tensile properties of in situ polymer-derived particles reinforced steel matrix composites produced by powder metallurgy method," *Materials Science and Engineering: A*, vol. 705, pp. 231-238, 2017.

[130] L. Lindgren, "Numerical modelling of welding," *Comput. Methods Appl. Mech. Eng.*, vol. 195, *(48-49)*, pp. 6710-6736, 2006.

[131] W. L. Oberkampf and T. G. Trucano, "Verification and validation in computational fluid dynamics," *Prog. Aerospace Sci.*, vol. 38, *(3)*, pp. 209-272, 2002.

[132] J. Katsuyama, K. Masaki and K. Onizawa, "Effect of partial welding on the residual stress and structural integrity of piping welds," *Journal of Pressure Vessel Technology*, vol. 135, *(6)*, pp. 061403, 2013.

[133] J. Ahn *et al*, "Prediction and measurement of residual stresses and distortions in fibre laser welded Ti-6Al-4V considering phase transformation," *Mater Des*, vol. 115, pp. 441-457, 2017.

[134] M. Hashemzadeh, B. Q. Chen and C. G. Soares, "Comparison between different heat sources types in thin-plate welding simulation," *Developments in Maritime Transportation and Exploitation of Sea Resources*, pp. 329-335, 2013.

[135] G. F. Sun *et al*, "Numerical and experimental investigation of thermal field and residual stress in laser-MIG hybrid welded NV E690 steel plates," *Journal of Manufacturing Processes*, vol. 34, pp. 106-120, 2018.

[136] T. F. Flint *et al*, "Extension of the double-ellipsoidal heat source model to narrow-groove and keyhole weld configurations," *J. Mater. Process. Technol.*, vol. 246, pp. 123-135, 2017.

[137] C. A. Felippa, K. C. Park and C. Farhat, "Partitioned analysis of coupled mechanical systems," *Comput. Methods Appl. Mech. Eng.*, vol. 190, *(24-25)*, pp. 3247-3270, 2001.

[138] L. Borjesson and L. Lindgren, "Simulation of multipass welding with simultaneous computation of material properties," *Journal of Engineering Materials and Technology*, vol. 123, *(1)*, pp. 106-111, 2001.

[139] J. Ronda and G. J. Oliver, "Consistent thermo-mechano-metallurgical model of welded steel with unified approach to derivation of phase evolution laws and transformation-induced plasticity," *Comput. Methods Appl. Mech. Eng.*, vol. 189, *(2)*, pp. 361-418, 2000.

[140] J. Mackerle, "Finite element analysis and simulation of welding-an addendum: a bibliography (1996-2001)," *Modell Simul Mater Sci Eng*, vol. 10, *(3)*, pp. 295, 2002.

[141] Z. Barsoum and I. Barsoum, "Residual stress effects on fatigue life of welded structures using LEFM," *Eng. Failure Anal.*, vol. 16, *(1)*, pp. 449-467, 2009.

[142] E. Kula, *Residual Stress and Stress Relaxation.* 2013*28.*

[143] D. Fu *et al*, "Effect of welding sequence on residual stress in thin-walled octagonal pipe–plate structure," *Transactions of Nonferrous Metals Society of China*, vol. 24, *(3)*, pp. 657-664, 2014.

[144] N. S. Rossini *et al*, "Methods of measuring residual stresses in components," *Mater Des*, vol. 35, pp. 572-588, 2012.

[145] D. Radaj, "Integrated finite element analysis of welding residual stress and distortion," *Book-Institute of Materials*, vol. 784, pp. 469-490, 2002.

[146] J. Zhang *et al*, "Modeling of weld residual stresses in core shroud structures," *Nucl. Eng. Des.*, vol. 195, *(2)*, pp. 171-187, 2000.

[147] T. Teng, C. Fung and P. Chang, "Effect of weld geometry and residual stresses on fatigue in butt-welded joints," *Int. J. Pressure Vessels Piping*, vol. 79, *(7)*, pp. 467-482, 2002.

[148] T. Teng and P. Chang, "Effect of residual stresses on fatigue crack initiation life for butt-welded joints," *J. Mater. Process. Technol.*, vol. 145, *(3)*, pp. 325-335, 2004.

[149] Y. Zhou *et al*, "Finite Element Modelling of Welding Residual Stress and Its Influence on Creep Behavior of a 2.25 Cr-1Mo-0.25 V Steel Cylinder," *Procedia Engineering*, vol. 130, pp. 552-559, 2015.

[150] Y. Ogino, Y. Hirata and A. B. Murphy, "Numerical simulation of GMAW process using Ar and an Ar–CO 2 gas mixture," *Weld. World*, vol. 60, *(2)*, pp. 345-353, 2016.

[151] T. Velumani, V. V. Murugan and N. Kuppuswamy, "Optimization of multi-pass GMAW of steel structures using Ansys and Lab VIEW," *Advances in Natural and Applied Sciences*, vol. 9, *(2)*, pp. 18-29, 2015.

[152] H. Vemanaboina *et al*, "SIMULATION OF HYBRID LASER-TIG WELDING PROCESS USING FEA," *Journal of Engineering Science and Technology*, vol. 13, *(6)*, pp. 1782-1792, 2018.

[153] ASTM International, *ASTM E3-11(2017), Standard Guide for Preparation of Metallographic Specimens.* West Conshohocken, PA: 2017.

[154] ASTM International, *ASTM E8 / E8M-16a, Standard Test Methods for Tension Testing of Metallic Materials.* West Conshohocken, PA: 2016.

[155] ASTM International, *ASTM D1002-10(2019), Standard Test Method for Apparent Shear Strength of Single-Lap-Joint Adhesively Bonded Metal Specimens by Tension Loading (Metal-to-Metal).* West Conshohocken, PA: 2019.

[156] ASTM International, *ASTM E384-17, Standard Test Method for Micro Indentation Hardness of Materials.* West Conshohocken, PA: 2017.

[157] X. Lu *et al*, "Finite element analysis and experimental validation of the thermomechanical behavior in laser solid forming of Ti-6Al-4V," *Additive Manufacturing*, vol. 21, pp. 30-40, 2018.

[158] S. H. Zargar, M. Farahani and M. K. B. Givi, "Numerical and experimental investigation on the effects of submerged arc welding sequence on the residual distortion of the fillet welded plates," *Proc. Inst. Mech. Eng. Pt. B: J. Eng. Manuf.*, vol. 230, *(4)*, pp. 654-661, 2016.

[159] M. Jahanzaib *et al*, "Modeling of weld bead geometry on HSLA steel using response surface methodology," *The International Journal of Advanced Manufacturing Technology*, vol. 89, *(5-8)*, pp. 2087-2098, 2017.

[160] S. Kumar and R. Singh, "Optimization of process parameters of metal inert gas welding with preheating on AISI 1018 mild steel using grey based Taguchi method," *Measurement*, vol. 148, pp. 106924, 2019.

[161] M. Mirzaei *et al*, "Study of welding velocity and pulse frequency on microstructure and mechanical properties of pulsed gas metal arc welded high strength low alloy steel," *Mater Des*, vol. 51, pp. 709-713, 2013.

[162] Oyama Cynthia, "Reinforcement of Aluminium AA1100 MIG Welds using Copper Powder." , University of Johannesburg, 2017.

[163] T. Zhang *et al*, "Thermomechanical analysis for laser GMAW-P hybrid welding process," *Computational Materials Science*, vol. 47, *(3)*, pp. 848-856, 2010.

[164] W. Piekarska and M. Kubiak, "Three-dimensional model for numerical analysis of thermal phenomena in laser–arc hybrid welding process," *Int. J. Heat Mass Transfer*, vol. 54, *(23-24)*, pp. 4966-4974, 2011.

[165] Y. Rong *et al*, "Numerical simulation and experiment analysis of angular distortion and residual stress in hybrid laser-magnetic welding," *J. Mater. Process. Technol.*, vol. 245, pp. 270-277, 2017.

Appendix

Appendix A: Stress Strain Curves of Butt and Lap Joints for Optimization

i) Butt Joints

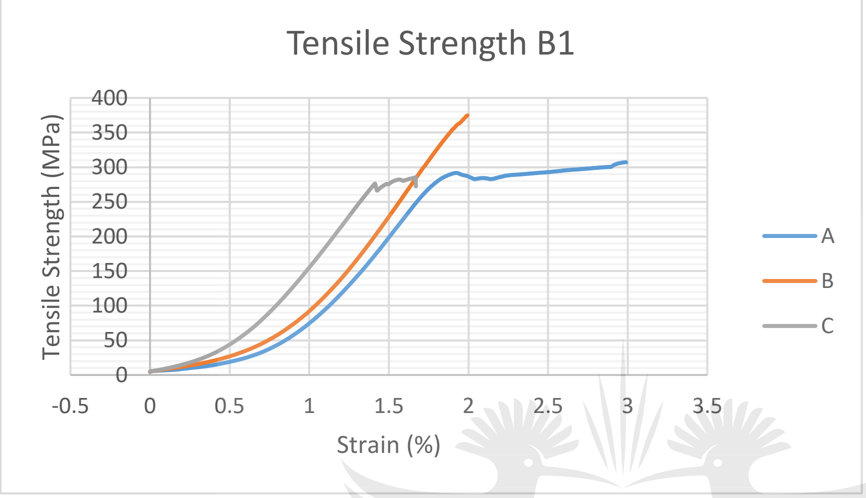

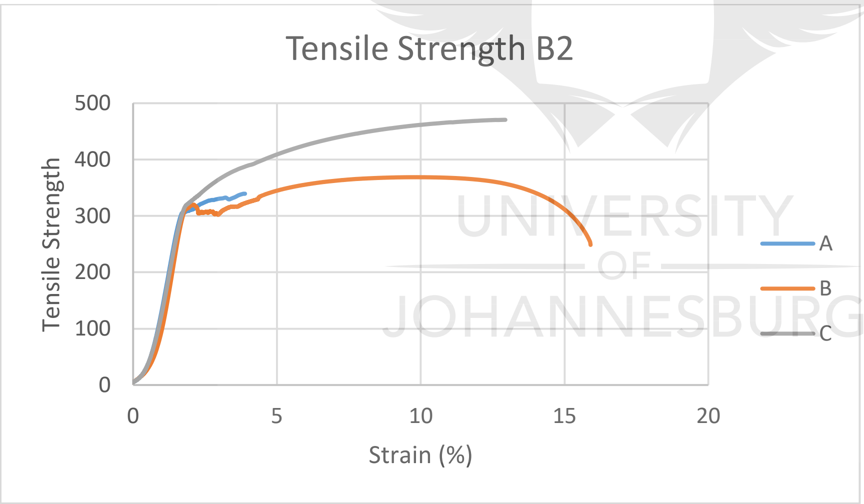

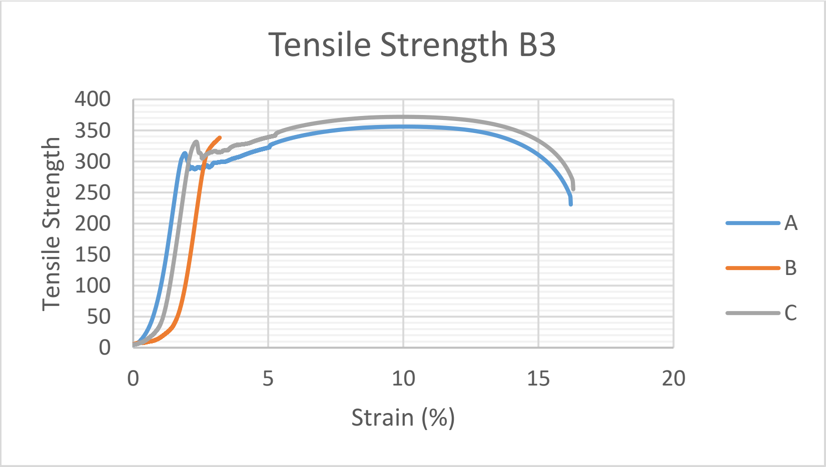

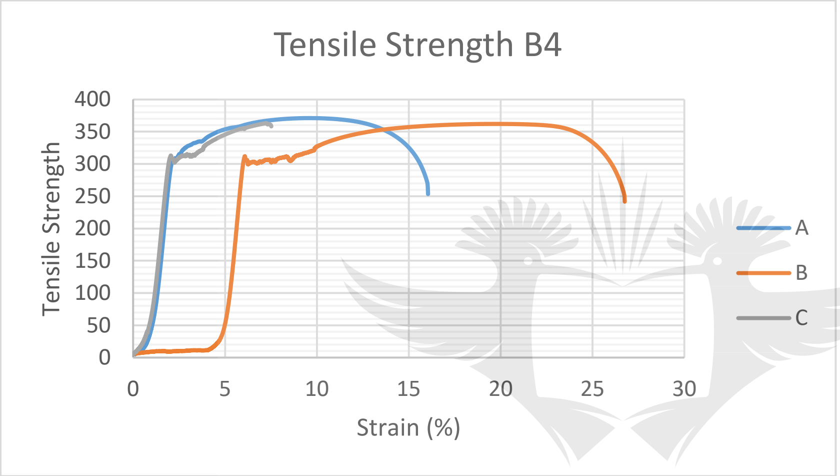

ii) Lap Joints

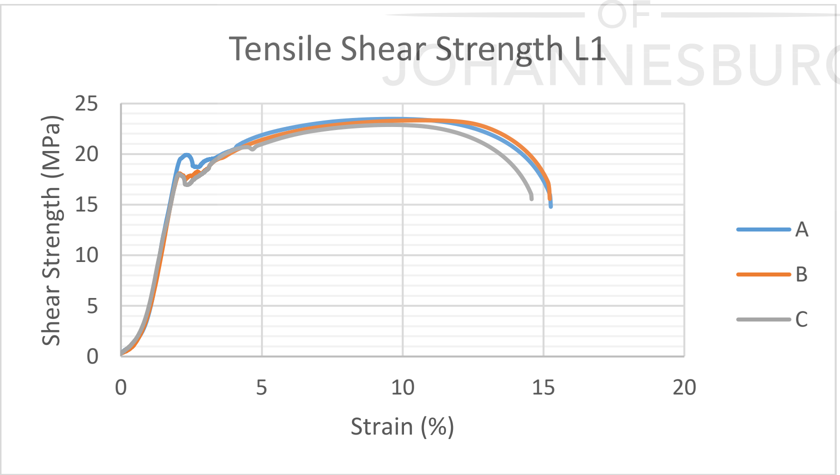

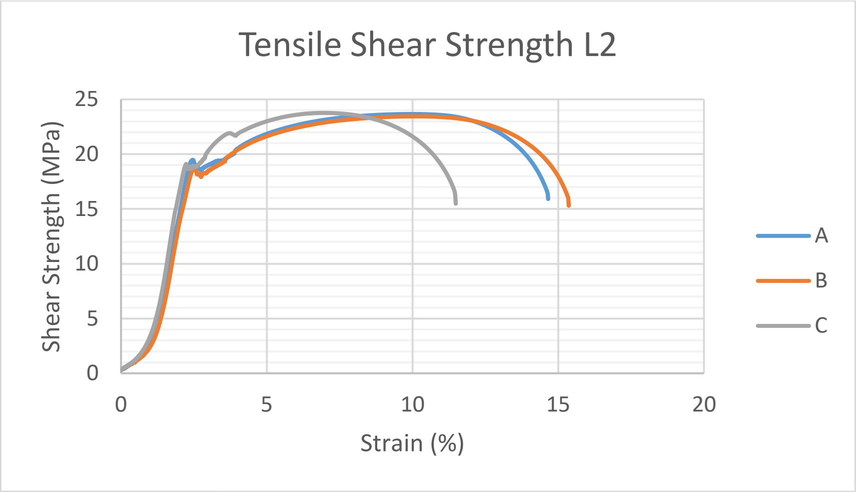
Tensile Shear Strength L2
Shear Strength (MPa)
25
20
15
10
5
0
0
5
10
15
20
Strain (%)
A
B
C

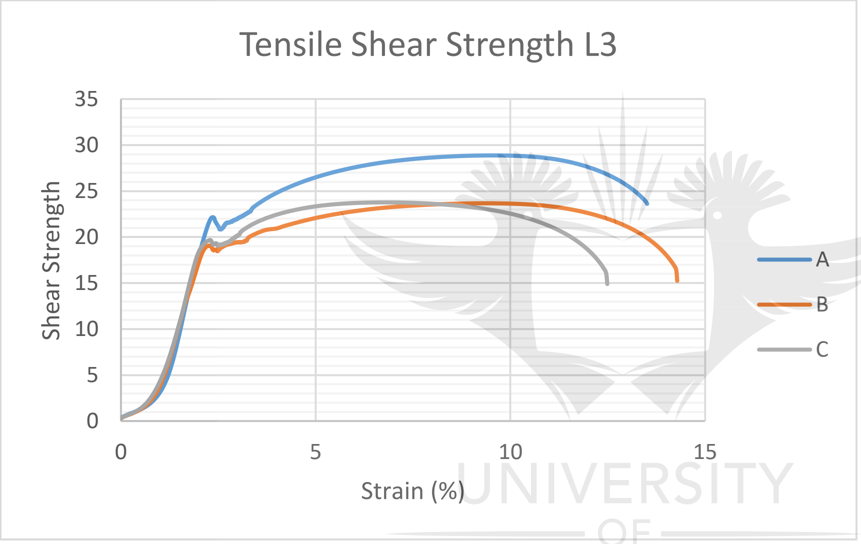
Tensile Shear Strength L3
Shear Strength
35
30
25
20
15
10
5
0
0
5
10
15
Strain (%)
A
B
C

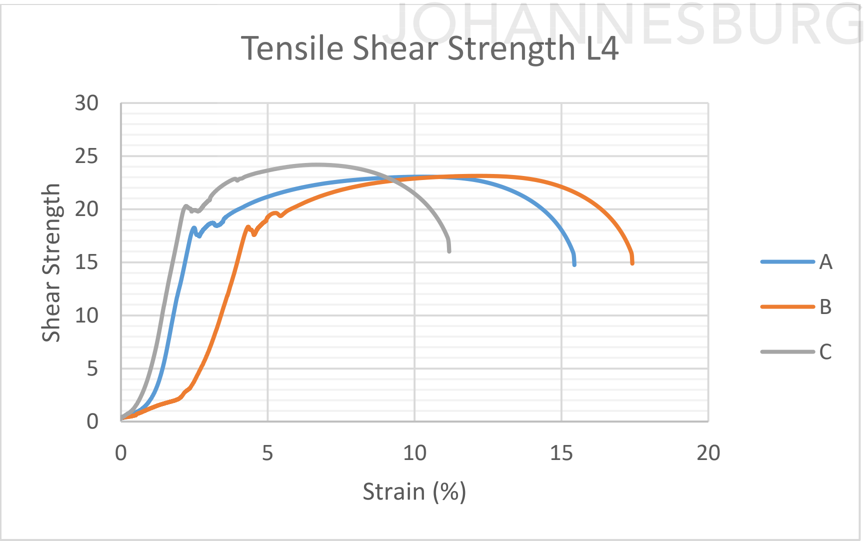
Tensile Shear Strength L4
Shear Strength
30
25
20
15
10
5
0
0
5
10
15
20
Strain (%)
A
B
C

Appendix B: Failure of Butt and Lap Joints for Optimization

i) Butt Joints

ii) Lap Joints

Appendix C: Microstructure of Sample B1 and B4

B1

B4

Appendix D: EDS of Optimized Butt Joint Samples

i) BN1 (Spectrum 2)

Element	Weight %	Atomic %
N	28.34	38.29
O	41.52	49.12
Na	2.17	1.79
Mg	0.32	0.25
Al	0.54	0.38
Si	0.97	0.66
S	0.88	0.52
Cl	0.94	0.50
K	1.07	0.52
Ca	0.80	0.38
Fe	22.44	7.60
Total	**100.00**	

ii) BN2 (Spectrum 2)

Element	Weight %	Atomic %
O	46.33	66.26
Na	7.57	7.53
Mg	0.54	0.51
Al	0.51	0.44
Si	1.12	0.91
S	1.30	0.93
Cl	12.56	8.11
K	15.38	9.00
Ca	1.90	1.09
Fe	12.78	5.23
Total	**100.00**	

iii) BP2 (Spectrum 1)

Element	Weight %	Atomic %
N	38.22	44.75
O	48.11	49.32
Na	1.20	0.86
Al	0.37	0.23
Si	0.93	0.55
S	2.54	1.30
Cl	1.12	0.52
K	1.28	0.54
Ca	1.00	0.41
Fe	5.21	1.53
Total	**100.00**	